Anode Interfaces in All-Solid-State Batteries

Varnika Agarwal

Department of Materials, University of Oxford

A thesis submitted for the degree of
Doctor of Philosophy
Michaelmas 2024
Supervised by Prof. Sir Peter Bruce

Declaration of Originality

I, Varnika Agarwal, hereby declare that this doctoral thesis, which is approximately 40,039 words in length (including captions), has been written by me and is the record of work carried out by me.

Acknowledgments

First, I would like to thank my supervisor, Prof. Sir Peter G. Bruce, for his supervision and great support throughout my DPhil study to make this thesis possible. I will be forever grateful for his guidance and the great example of the scientist he set with his dedication, devotion, and contribution to science. I would like to thank the Faraday Institution and the Henry Royce Institute. I must extend my appreciation towards my assessors, Prof. Chris Governor, and Prof. Susie Speller, who have generously shared their wealth of knowledge and expertise during the completion of my studies. I would like to offer my special thanks to Dr Paul Adamson for his help with my research and thesis revision. Moreover, I would also like to thank Prof. Hazel Assender for her support. I owe my deepest gratitude to all my group members, both past and present, for their support and all the good times. I would like to thank Dr Dominic Spencer Jolly for all the invaluable discussions, guidance, and supervision he gave me during my DPhil study. For carrying out XPS and PFIB experiments for me. For guiding throughout my DPhil journey. I would also like to give a special mention to Dr Hui Gao, for all the support she gave me during our lunch time talks whether it was professional or personal. I would like to thank Dr Xiangwen Gao, Dr Boyang Liu, Dr Gareth O. Hartley, Dr Dominic Melvin, Dr Longlong Wang, Shengming Zhang, Dr Bingkun Hu, Bartholomew Payne and Lechen Yang for their help and the fruitful discussions we have had, which helped advance my understanding of alloys in all-solid-state batteries. My greatest appreciation also goes to Dr Stephen Turrell and Marco Siniscalchi for all their assistance with PVD experiments. Special thanks to Dr Robert House for carrying *operando* XRD experiments and to Dr Joshua Gibson for conducting XPS experiments. I would like to thank Dr Oxana V. Magdysyuk from Diamond Science Park for helping with the *operando* XCT experiments at I12 (JEEP). I would also like to thank my other group members for their support, Dr Tammy, Dr Ceren, Dr Shengda Pu, Dr Sofia, Dr Mikkel, Rui, Ziuxan, and Hang.

To my parents, Vishal and Meenu; and my uncle and aunt, Vikas and Dipti. I owe you everything and thank you so much. Words fail to express how lucky I am to be your daughter. Your constant love and support at every stage of my life has made me what I am today. I would always be grateful to you for believing me and pushing me to be the best version of myself. I would like to thank my brothers, Rachit and Achin, for bearing all my calls when I was stressed. To my sister-in-law's, Sakshi, Rishieka and sister, Vanya for giving me all the emotional support I needed. Thank you for your selfless love, your understanding, and all the sacrifices you made for me along the way. Without your support, I know I would not have got to where I am.

I would like to thank all my friends, whether they were in Oxford or in India, for being always with me.

Abstract

Solid-state batteries have the potential to transform the transportation industry but there are substantial hurdles to overcome before fully realising their benefits. This thesis primarily addresses the challenges associated with Li-free or so called anodeless solid-state cells. One of the most significant issues is the morphological instability observed at the interface between the metal anode and solid electrolyte during charging and discharging, which leads to cell shorting.

Chapter 3 describes investigation of the use of a silver metal interlayer in Li-free all-solid-state batteries. The chapter focusses on the cycling performance with a sulphide solid electrolyte and employs techniques such as PEIS, SEM/EDX, PFIB and XPS. These techniques help to understand the role of the silver metal interlayer during charge and discharge, thereby mitigating contact loss. Moreover, the interfacial reactivity between the lithiated silver and the sulphide solid electrolyte reveals the presence of interfacial by-products.

Chapter 4 investigates the mechanisms underpinning the operation of a graphite-silver composite interlayer in a Li-free solid-state setup using various techniques such as *operando* XRD, SEM/EDX and electrochemical lithiation. The investigation reveals the structural changes occurring in the composite interlayer at different rates of charge and discharge. The critical current density with the composite interlayer was determined to be 2 mA cm^{-2} and strategies to improve it are explored. Additionally, the role of silver nanoparticles in the composite interlayer is discussed.

Finally, **Chapter 5** explores plasma cleaning as a surface treatment technique to remove impurities from the air exposed surface of Na-β”-Alumina (NBA) solid electrolyte. Optimising conditions for the plasma treatment results in a relatively low interfacial resistance of NBA against a Na metal anode at room temperature. SEM and XPS techniques provide insight on the effects of plasma cleaning.

List of Publications

1. Spencer-Jolly, Dominic, Varnika Agarwal, Christopher Doerrer, Bingkun Hu, Shengming Zhang, Dominic LR Melvin, Hui Gao et al. "Structural changes in the silver-carbon composite anode interlayer of solid-state batteries." *Joule* 7, no. 3 (**2023**): 503-514.[1] (First co-authors)

   This publication was published as first joint co-authors with Dr Dominic Spencer Jolly and forms a major part of Chapter 4. Collaborative work is mentioned in the footnotes of the respective pages and acknowledged in the text.

List of Conferences

1. Poster presentation in MRS Spring **2023** titled “Structural changes in the silver-carbon composite anode interlayer of solid-state batteries”.

List of Abbreviations

2D	Two dimensional
3D	Three dimensional
ASSBs	All-solid-state batteries
BE	Binding energy
BEV	Battery Electric Vehicle
BSE	Back-scattered electron
CCD	Critical current density
CE	Counter electrode
CEI	Cathode electrode interphase
CT	Charge transfer
DMC	Dimethyl carbonate
EC	Ethyl carbonate
EDX/EDS	Energy-dispersive X-ray Spectroscopy
EIS	Electrochemical impedance spectroscopy
ESCA	Electron spectroscopy for chemical analysis
EV	Electric vehicle
FIB	Focussed ion beam
ICE	Internal combustion engines
ISE	Inorganic solid electrolyte
KE	Kinetic energy
PXRD	Powder X-ray diffraction
PFIB	Plasma focussed ion beam
HOMO	Highest Occupied Molecular Orbital
NBA	Na-β”-Alumina
LAGP	$Li_{1-x}Al_xGe_{2-x}(PO_4)_3$
LE	Liquid electrolyte
LIB	Lithium-ion battery
LLTO	$Li_{3x}La_{2/(3-x)}TiO_3$
LLZO	$Li_7La_3Zr_2O_{12}$
LUMO	Lowest Unoccupied Molecular Orbital
MCIs	Mixed conducting interphases
NCA	Nickel cobalt aluminium oxide
NiCd	Nickel-cadmium
NiMH	Nickel-metal hydride
NMC	Nickel manganese cobalt oxide
NMR	Nuclear magnetic resonance
OCV	Open circuit voltage
PEEK	Polyether ether ketone
PEIS	Potentiostatic electrochemical impedance spectroscopy
PEO	Polyethylene oxide
PTFE	Polytetrafluoroethylene
PVD	Physical vapour deposition

PVdF	Polyvinylidene fluoride
R/C element	Resistor/Capacitor element
RE (or Ref)	Reference electrode
RT	Room temperature
SE	Solid electrolyte
SEI	Solid electrolyte interphase
SEM	Scanning electron microscope/microscopy
SHE	Standard hydrogen electrode
SIMS	Secondary ion mass spectrometry
SSBs	Solid-state batteries
WE	Working electrode
XCT	X-ray computed tomography
XPS	X-ray photoelectron spectroscopy
XRD	X-ray diffraction
UV	Ultraviolet

Table of Contents

1 Chapter 1: Introduction 1

1.1 Introduction to batteries 1

1.1.1 Overview 1

1.1.2 Background of Li-ion batteries 2

1.1.3 The lithium-ion battery and beyond 5

1.1.4 Limitations of the Li-ion battery 8

1.2 Solid-state batteries 10

1.2.1 Overview 10

1.2.2 Solid electrolytes properties and different types 12

1.2.3 Challenges in ASSBs 22

1.3 Li-free or anodeless solid-state battery 29

1.3.1 Overview 29

1.3.2 Factors Influencing Coulombic Efficiency (CE) and cycle life 31

1.3.3 Current research trends and developments to tackle morphology instability 36

1.4 Summary and Aim of the work 40

2 Chapter 2: Experimental Techniques 42

2.1 Overview 42

2.2 Sample Preparation 42

2.2.1 Cell Fabrication 42

2.2.2 Physical Vapor Deposition (PVD) 44

2.2.3 Plasma Cleaning 46

2.3 Structural Characterisation 48

2.3.1 X-ray diffraction (XRD) 48

2.3.2 Scanning electron microscopy (SEM) 51

2.3.3 Focused Ion Beam (FIB) 54

2.4 Chemical characterisation 56

2.4.1 Energy dispersive X-ray (EDX) 56

2.4.2 X-ray Photoelectron Spectroscopy (XPS) 58

2.5 Electrochemical Testing 60

2.5.1 Electrochemical Impedance Spectroscopy (EIS) 60

2.5.2 Galvanostatic Cycling 64

3 Chapter 3: Silver metal anode interlayers for Li-free all-solid-state batteries. 66

3.1 Overview 66

3.2 Introduction 66

3.3 Experimental Methods 69

3.3.1 Preparation of Li_6PS_5Cl disks 69

3.3.2 Preparation of metal interlayers on sulphide solid electrolyte for half-cell experiments 69

3.3.3 Preparation of full cells 71

3.3.4 Structural and electro-chemical characterisation 72

3.4 Results and Discussion 74

3.4.1 Full cell performance 75

3.4.2 Electrochemical first charging profiles 76

3.4.3 Morphology after charging 78

3.4.4 Low CE during full cell cycling 84

3.4.5 Role of silver as an interlayer during charge and discharge 96

3.4.6 Problems associated with metal interlayers 98

3.5 Conclusion 101

3.6 Future work 102

4 Chapter 4: Mechanistic understanding of graphite and graphite-silver anode interlayers for all-solid-state batteries 103

4.1 Overview 103

4.2 Introduction 104

4.3 Experimental Methods.. 106

4.3.1 Fabrication of interlayers and cells.. 106

4.3.2 Electrochemical Testing.. 111

4.3.3 Chemical Characterisation... 112

4.3.4 Structural Characterisation 112

4.3.5 *Operando* XCT 113

4.4 Results and Discussion 114

4.4.1 Critical Current Densities of graphite and graphite-silver composite interlayers 114

4.4.2 Charging graphite-silver interlayer at low rate using *operando* XRD 115

4.4.3 Discharging graphite-silver interlayer at low rate using *operando* XRD............................ 122

4.4.4 Charging the graphite-silver interlayer at high rate with *operando* XRD and XCT 125

4.4.5 The role of silver nanoparticles in composite interlayers.. 129

4.4.6 Full cell performance of graphite-silver composite interlayers.. 134

4.4.7 Strategies to improve full cell performance of graphite-silver composite interlayer cells... 136

4.5 Conclusions 138

4.6 Future work 139

4.6.1 Investigating the role of Li behind these interlayers 139

4.6.2 Exploring different carbons and metal nanoparticles 140

4.6.3 Other areas to investigate 141

5 Chapter 5: Surface treatment of Na-β”-Alumina solid electrolyte by plasma cleaning 142

5.1 Overview 142

5.2 Introduction 142

5.3 Experimental Methods.. 145

5.3.1 Cell Fabrication 145

5.3.2 Electrochemical Testing of 2-electrode cells 146
5.3.3 Plasma Cleaner 146
5.3.4 Heat Treatment 147
5.3.5 Impedance *vs* time 147
5.3.6 Wettability test 147
5.3.7 Characterisation 148

5.4 Results and Discussions 149

5.4.1 Surface treatment of NBA Disks 149
5.4.2 Comparative study of different surface treatment techniques 150
5.4.3 Optimisation of plasma cleaning conditions 156
5.4.4 Morphology 164
5.4.5 Wettability 165
5.4.6 Problems with Plasma Cleaning 167

5.5 Conclusions 169

6 Chapter 6: Conclusions and Outlook 170

7 References 173

8 Appendix 200

1 Chapter 1: Introduction

1.1 Introduction to batteries

1.1.1 Overview

Climate change poses a major threat to the world, with glaciers melting, water level rising, unpredictable weather etc.[2,3] For humankind to reduce its greenhouse gas emissions and to slow global warming, electric vehicles (EVs) will have a major role to play as 26% of the greenhouse gas emissions are from the transportation industry.[4] To reduce these emissions, the transport industry needs to move away from internal combustion engines (ICEs) to electric based transportation. Many governments have passed legislation to go fully electric from 2035 by banning the sale of ICE-based vehicles to promote greener alternatives.[5–7] The demand for EVs is increasing tremendously as it is a great alternative to ICEs, keeping the carbon footprint low.[8]

With rapid growth in the market of Battery Electric Vehicles (BEV), the range of EVs is gradually increasing as the battery technology progresses with companies like CATL announcing “Shenxing PLUS” with over 1000 km range.[9] Additionally, increasing the lifetime of batteries is very important for the sustainability of EVs and batteries. They need to be able to handle harsh weather conditions, with battery packs that can operate at very low and high temperatures with minimal degradation to enhance safety. The current cells, with intercalation electrodes and liquid electrolytes (LE), will soon reach their theoretical limits.[10,11] Hence, new alternative anode and cathode materials should be investigated as, there is a constant need to make batteries safe and long lasting with high energy density.[12]

Currently, graphite is used as an anode material, which has a specific capacity of 372 mAh g^{-1}.[10] Li metal, however, has a roughly ten times higher specific capacity of 3840 mAh g^{-1}.[13] Nevertheless, Li metal cannot be directly used in a cell with a liquid electrolyte as the two continually react and failure can occur very easily during operation due to the formation of Li dendrites that short-circuit the cell.[14] Hence, all-solid-state battery (ASSBs) for which the liquid electrolyte is replaced with a mechanically strong solid electrolyte (SE) and a metal anode are promising paths towards high energy densities.[15]

This thesis presents strategies to improve interfaces between the solid electrolyte and metal anode in an ASSB and an "anodeless" or so called "Li-free" battery. Additionally, strategies to reduce interfacial resistance of the solid electrolyte by different surface treatments are explored. This chapter provides a summary of different types of batteries, solid electrolytes and anodes. Moreover, the advantages, disadvantages and challenges are explored and existing work describing methods to overcome interfacial issues are discussed.

1.1.2 Background of Li-ion batteries

Electrochemical energy storage was developed in the 19th century with one of the first practical examples being the Daniell Cell in 1836.[16] Advances in the following centuries allowed batteries to become one of the key energy storage technologies of our time. Different types of batteries are shown in Figure 1.1 with their timeline.[16]

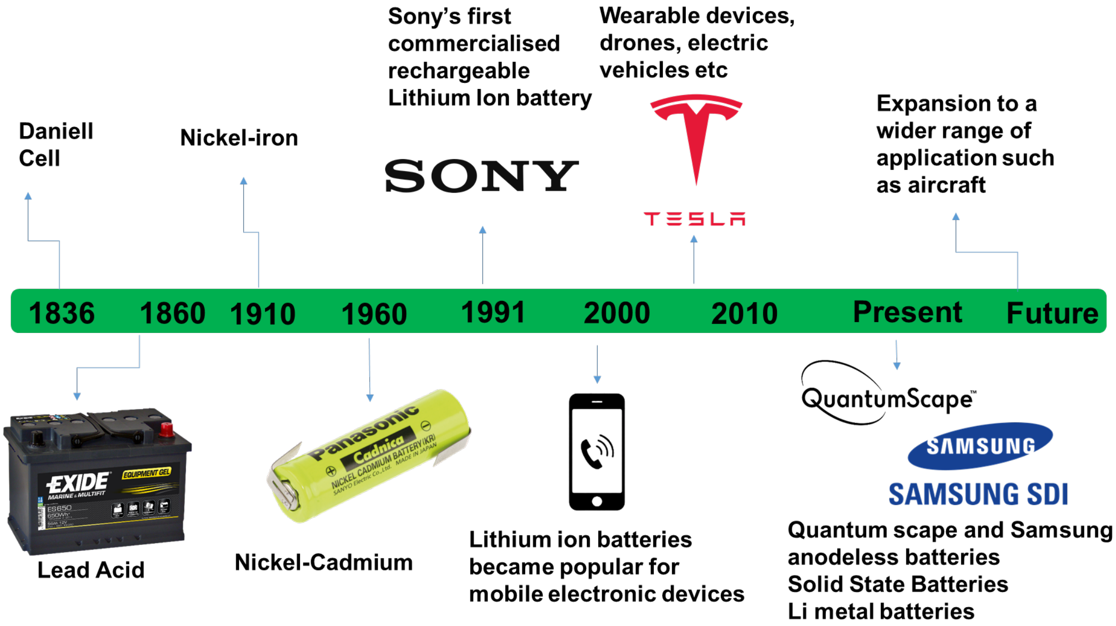

Figure 1.1. Schematic showing the history of invention of different types of batteries.

Batteries have three main components: a positive electrode, a negative electrode, and an electrolyte. Electrodes are responsible for the conversion of chemical energy into electrical energy and vice-versa. The positive and negative electrode work together to facilitate the movement of charge and enable the battery to store and release electrical energy efficiently.[17] Electrolytes provide ionic conduction while blocking electronic conduction which prevents self-discharging by isolating the half-cells electronically.[18,19]

1.1.2.1 Primary Batteries

Primary batteries are non-rechargeable due to their irreversible electrochemical reaction. Common examples of primary cells are alkaline, lithium iron disulphide and zinc-carbon batteries also known as the Leclanchè battery.[20]

Primary batteries have long shelf lives and low initial cost, hence used in several single use devices.[20] They are commonly used in sensors, watches, smoke detectors and hearing aids.[21] Over the past three decades, the global demand for batteries has increased primarily due to the demand for reversible high-performance applications. Therefore, the market share of primary batteries has significantly reduced in comparison to secondary batteries.[22]

1.1.2.2 Secondary Batteries

Secondary batteries are more commonly known as rechargeable batteries. They are electrically recharged after discharge by passing current in opposite direction to bring them to their initial pre-discharge state to be used again with a minimal capacity loss. When a reverse potential is applied, electrons are forced to flow back from the positive electrode to the negative electrode. Common examples of secondary batteries are lead-acid, zinc-air, Li-ion, nickel-cadmium, nickel-metal hydride (NiMH) and lithium-ion polymer.[23] In 1859, the lead-acid battery was developed by Gaston Plantè as the first secondary battery and is still used as a starting power source for automotive engines today.[24] Nickel-cadmium (NiCd) batteries were the first small rechargeable batteries that could be used in handheld devices. NiCd batteries have a low cell voltage, but they can charge very quickly with low localised heating. Due to minimal heating, effects such as volume expansions and other stresses are reduced. However, their maximum capacity decreases over time and were therefore replaced by nickel-metal hydride battery and eventually the Li-ion battery.[23,25]

Sony commercialised the first rechargeable Li-ion battery in 1991.[16,26] Recently, Li-ion demand crossed 1 TWh across all energy storage applications.[27] They are the most successful battery of all time and will be discussed in more detail in the following sections.[9,16,28]

1.1.3 The lithium-ion battery and beyond

This section aims to summarise the basics of the Li-ion battery and discusses its limitations. As shown in Figure 1.2, batteries with Li-based chemistries can theoretically offer both higher specific energy and power densities, which explains their popularity.

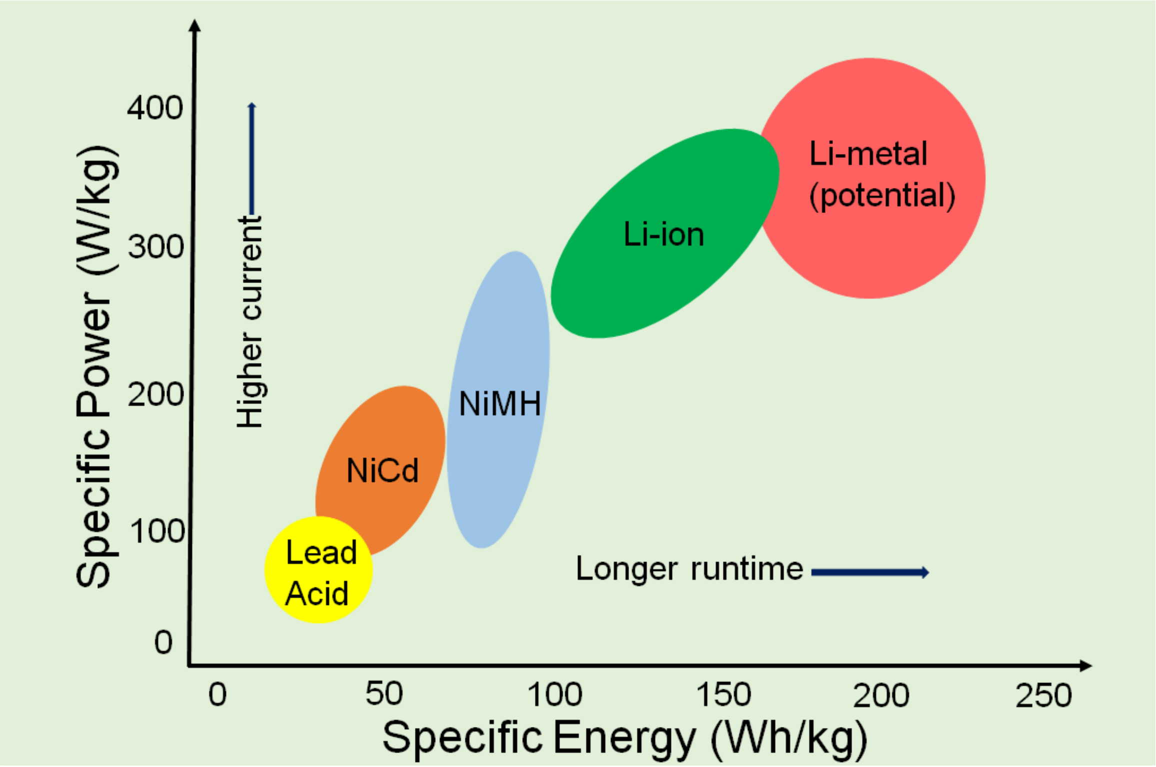

Figure 1.2. Specific energy density of Li metal battery compared to other battery systems. This figure is reproduced with permission from Issues and challenges facing rechargeable lithium batteries. Nature ***414****, 359–367 (2001).*[29] *Copyright 2001 Nature.*

A Li-ion secondary battery operates in two modes: Charging and discharging. During discharge, Li-ions diffuse from the anode (its active material is oxidised, electrode with high chemical potential of Li i.e., negative electrode) to the cathode to reduce its active material (electrode with low chemical potential of Li i.e., positive electrode) through the electrolyte medium and separator, which conducts Li-ions but not electrons as shown in Figure 1.3. To maintain the electrical neutrality, electrons flow from negative to positive electrode through an external circuit. Charging the battery by an external power source reverses both the ionic and electronic processes. During charging, the reverse process takes place in which the anode active material is reduced and cathode active material is oxidised.[17] A separator provides a physical barrier between the anode and cathode and therefore prevents short circuiting in the cell and ensures higher safety.[16,30–32] As discussed in the review by Dang et al.[33] LIB are connected either in series (to increase voltage) or in parallel (to increase current) or in mixed configuration to make a battery module. Multiple modules are subsequently stacked together to form a battery pack. For example, the 24 kWh battery pack of the Nissan LEAF consists of 192 prismatic Li-ion cells, organised into 48 modules, with each module containing 4 cells.[34,35] The current trend is to increase the battery pack size to achieve greater EVs range.[36]

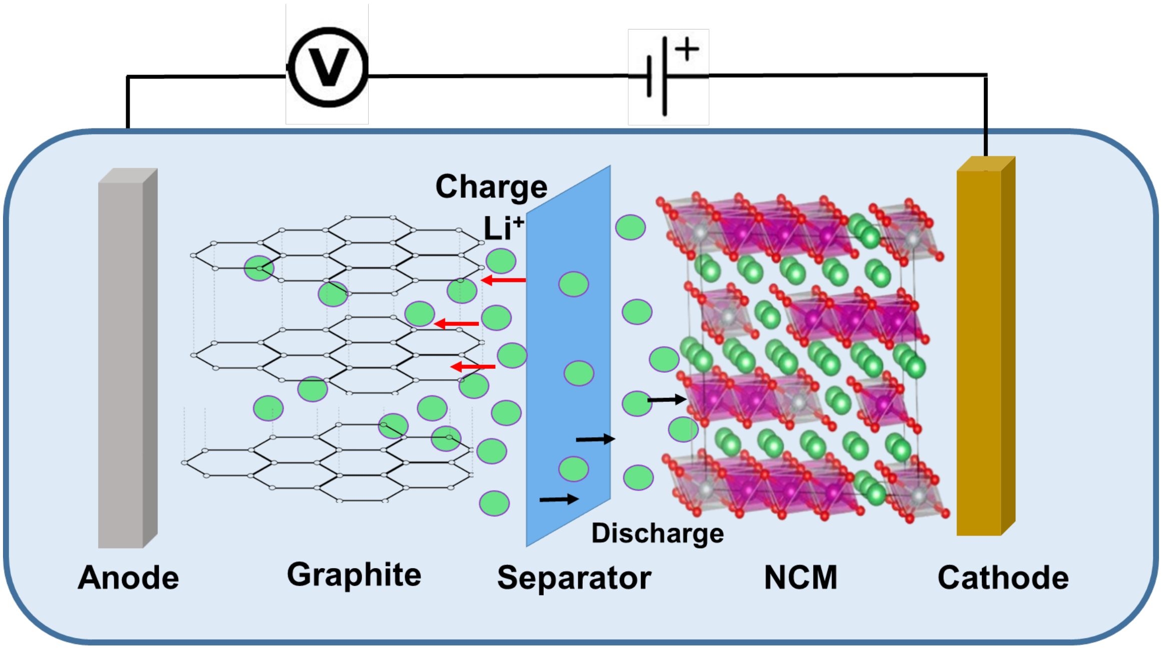

Figure 1.3. Schematic representation of a working lithium-ion battery. Adapted from[12]*. This graphite structure is an open access article distributed under the terms and conditions of the Creative Commons Attribution (CC BY) license and NMC structure adapted with permission from*[37,38] *is Copyright 2018 Wiley.*

Rechargeable battery performance is measured in terms of safety, energy density, charge/discharge rates, cycle life, and cost. Materials play an important role to achieve these.[12] Currently, in a traditional Li-ion battery, graphite is used as an anode material, a lithium transition metal oxide such as $LiCoO_2$ as a cathode material and a lithium salt (e.g. $LiPF_6$) dissolved in dimethyl carbonate (DMC) and ethyl carbonate (EC) is used as the liquid electrolyte.[39] Graphite is favourable due to its high surface area, low manufacturing costs and its porous structure. It has good rate capability and low irreversible capacity.[40]

Commonly used cathode materials are Lithium Cobalt Oxide (LCO: $LiCoO_2$)[31], Lithium Iron Phosphate (LFP: $LiFePO_4$)[41], Nickel Cobalt Aluminum Oxide (NCA: $LiNi_{0.8}Co_{0.15}Al_{0.05}O_2$)[42], and Lithium Nickel Manganese Cobalt Oxide (NMC: $LiNi_xMn_yCo_zO_2$, where $x+y+z=1$)[43]. This is due to their advantages and disadvantages shown in the Table 1 below.[44]

Cathode Material	**Specific capacity (Ah kg^{-1})**	**Mid-Voltage (V)**	**Advantage**	**Disadvantage**	**Application**
LCO	155	3.9	High cycle stability	Expensive	Portables
NCA	180	3.7	High energy density, power capability and cycle life	Expensive, moderate charge thermal stability	Premium EVs
NMC*	160	3.8	High energy density, cycle life and thermal stability	Moderate priced	EVs
LFP	160	3.4	High thermal stability and cycle life. Cheap	Low energy density	EVs and ESS

Table 1: Advantages and disadvantages of commonly used applications with potential applications areas. [44]

** NMC advantages and disadvantages can vary depending on the composition. For example, NMC811 gives higher energy density compared to NMC111 but is more expensive.*

A separator soaked in highly conducting organic liquid electrolyte is used to separate the anode and cathode from each other. To improve the columbic efficiency (CE) of $LiPF_6$, it is dissolved in a mixture of organic solvents. They are cheap and highly conducting, allowing flow of Li-ions between electrodes but not electrons. They are easily wettable against electrode materials.[45]

The operating voltage of a cell is determined by the overall compatibility of its components such as anode, cathode, and electrolyte. It is defined as the difference in the chemical potential between the cathode (μ_c) and anode (μ_A), which determines the open-circuit voltage (V_{oc}) of the system:

$$Voc = \frac{(\mu\mathrm{A}) - \mu\mathrm{c}}{e}$$

Where e is the electronic charge. This open-circuit voltage (Voc) is constrained by the electrochemical stability window of the electrolyte.[12,46] Electrochemical stability window of the electrolyte is explained as the energy gap between its Lowest Unoccupied Molecular Orbital (LUMO) and Highest Occupied Molecular Orbital (HOMO) and determines the operating voltage window. For stable cycling, the anode's potential must stay below the electrolyte's LUMO, and the cathode's above its HOMO, Otherwise, reactions may form an interphase layer, which, if stable, allows ion flow. An unstable interphase increases resistance, leading to reduced performance and shorter battery life.[12] This is discussed in more detail in Section 1.2.3.2.

1.1.4 Limitations of the Li-ion battery

Since the inception of LIBs three decades ago, significant research on the development of new materials has enabled Li-ion batteries to double in energy density, leading to their domination of the secondary battery market.[47] The current market expansion due to a surge in demand for EVs[48] has led to tremendous interest in increasing the energy density further as well as also improving the power of LIBs whilst also making them safer to use.[49–51] However, there are some challenges associated with current LIBs, as discussed below:

- A significant safety concern from both the industry and public to using current LIB chemistries in EVs. Reports of electric cars[52] catching fire and smart phones[53,54] bursting into flames have highlighted the need to make these batteries safer. This safety issue is primarily due to the presence of a flammable, highly toxic and volatile organic liquid electrolyte. One primary concern related to battery fires is the occurrence of the thermal runaway due to an internal electrical short-circuit which can result from fast charging[55], manufacturing faults[53], or other reasons.[53,56,57] If an electrical short-circuit occurs between the anode and cathode, it can easily lead to the ignition of the flammable liquid electrolyte.[55]
- LIB have additional battery packaging to avoid leakage and ensure safety but that adds to extra weight and cost. This leads to extra volume and a decrease in specific energy (amount of energy a battery can store per unit mass, Wh/kg) and power density (power delivered per unit mass, W/kg). A tremendous effort is being made to make batteries safer as this is important for the automotive sector by introducing thermal management techniques such as water cooling plates in the battery pack.[55,58]
- Another limitation is the gradual buildup of side products especially at high temperatures and voltages which leads to the formation of interphase such as LiF, Li_2CO_3 and Li_2O.[59] While research indicates that interphases can sometimes enhance cell performance, its breakdown and the associated interfacial reactions can initially cause a rapid temperature rise, increasing the risk of thermal runaway.[29,60] Moreover, over time the interphase layer thickens, which limits the Li^+ intercalation and hence leads to cell failure.[61–65]

- At the cathode, under high-temperature and high-voltage conditions, Li loss and capacity fade is observed due to factors such as the decomposition of the SEI film, oxygen release, which leads to thermal runaway of the battery.[55,66,67]
- Graphite has a low theoretical capacity of 372 mAh g^{-1} (LiC_6), because of limited Li-ion storage sites within a sp^2 hexagonal carbon structure.[68] Therefore, to meet the ever-increasing demand for high-energy materials, researchers are investigating new materials for anode[69] and cathodes[70]. Many alkali metals, intermetallic compounds have been studied as anode materials especially focusing on group 4 elements (Si[71–74], Ge[75], Al[76,77], Sn[78]) and group 5 (Sb[79], Bi[80], In[81–83]) elements due to their high reactivity with lithium.[84,85]

Li metal is considered the 'holy grail' of anodes. Li metal batteries using Li metal as anode holds a strong promise for next generation batteries due to its low redox potential (-3.04 V *vs* Standard hydrogen electrode (SHE)) and high theoretical capacity of 3860 mAh g^{-1}.[86] However, the development of Li-metal batteries is challenged by low CE and cycle life.[86–90] This is primarily driven by dendrite formation[88], unwanted SEI growth[91], uneven deposition of Li metal.[89] A common concern is that Li dendrites might physically puncture the separator, leading to a short circuit within the cell, which could potentially trigger thermal runaway and cause an explosion. To overcome some of the challenges associated with Li metal liquid LIB, solid state batteries have been considered as a potential solution. These are discussed in detail in further sections.

1.2 Solid-state batteries

1.2.1 Overview

In a solid-state battery (SSB), the flammable organic liquid electrolyte is replaced by a solid non-flammable solid electrolyte.[1] SSBs work on the same principle as Li-ion battery. Most researched solid electrolytes (SE) are inorganic or organic. They act as a dense physical barrier, between the anode and cathode, while also meeting the Li^+ ionic conductivity requirements (1-10 mS cm^{-1} at room temperature), which has led to the speculation that they could offer a promising route to mitigating the Li dendrite problem.[92,93] Hence, making the batteries safer.[94,95] Moreover, it is considered that a Li metal anode can be used with solid-state batteries, giving it the ultimate push in terms of energy density.[96]

Solid state batteries can be categorised as semi-solid state and all-solid-state battery (ASSB). In a "semi"[97], or "quasi"[98], or "hybrid", there is some liquid present in one or more components, while in an ASSB, all the components are solid.[99] In this thesis, solid-state refers to ASSB, potentially using Li-metal as the anode. While there have been several announcements by OEM's announcing EVs powered by SSBs, those exclusively refer to semi-solid batteries.[100,101] Li-metal ASSBs are still few years away from commercialisation due to the challenges involved in its development.[102] Currently, they suffer from challenges such as poor cycle life, low CE, undesirable solid electrolyte interphase (SEI) growth and Li dendrite formation as discussed in several reviews.[103–105] This is discussed in detail in Section 1.2.3. Companies like Prologium[106], Samsung SDI[107] and Factorial[108] opened pilot facilities for SSB with plans to mass produce by 2026-2027.[109,110]

While Li metal has attracted the most attention for the use in SSBs due to its high theoretical capacity, sodium metal also shows a high theoretical capacity compared to hard carbons (1166 mAh g^{-1} compared to 300 mAh g^{-1} for hard carbons) and a potential of -2.71 vs SHE for sodium ion batteries.[112,113] Researchers have been exploring Na based technology to replace Li, especially for large-scale grid storage application as sodium is low cost, naturally abundant and easily accessible.[113–116] However, solid-state sodium batteries suffer from similar challenges as Li-metal ASSBs, which is hindering its commercialisation as discussed in various recent reviews.[118,119]

This thesis primarily focusses on Li-ion conducting electrolytes and Li metal in solid-state batteries. However, Chapter 5 focusses on surface treatment of a Na-ion conducting electrolyte as a model system and its use with a Na metal anode for Na metal ASSB.

1.2.2 Solid electrolytes properties and different types

1.2.2.1 Overview

As discussed in Section 1.2.1, ASSB research has been driven by the goal of enhancing the energy density by using Li metal as an anode material, whilst making them safer, with the use of SEs. The growing interest in SE materials is largely driven by their potential to provide significant mechanical strength[119,120], robust enough to withstand high critical current densities without being penetrated by lithium metal[121,122], which is crucial for preventing dendrite formation.

Beyond mechanical properties, SE are expected to provide enhanced electrochemical stability, particularly when interfacing with Li metal anodes and high-voltage (>5 V) cathodes to prevent degradation and ensure battery safety.[37,61,124] Moreover, some SEs like Li_6PS_5Cl, LATP exhibits high ionic conductivity at room temperature[96,125] with minimal electronic conductivity and form a stable interfacial layer with the lithium metal anode[19]. Another advantage of SEs is their high Li^+ transference number, close to unity.[125] It is considered that a higher transference number leads to low concentration gradients during high-rate cycling, resulting in reduced polarisation and dendrite formation.[126,127]

Despite these promising attributes, several different types of solid electrolyte have been reported in the literature which possess one or more of these features as shown in

Figure 1.4. Yet, no solid electrolyte possesses all the properties and the search for an ideal solid electrolyte is being carried out around the world.

1.2.2.2 Different types of solid electrolyte

Solid electrolytes are generally of three types: Inorganic ceramic solid electrolytes, solid polymer electrolytes and composite polymer solid electrolytes. Advantages and disadvantages are summarised in Figure 1.4.

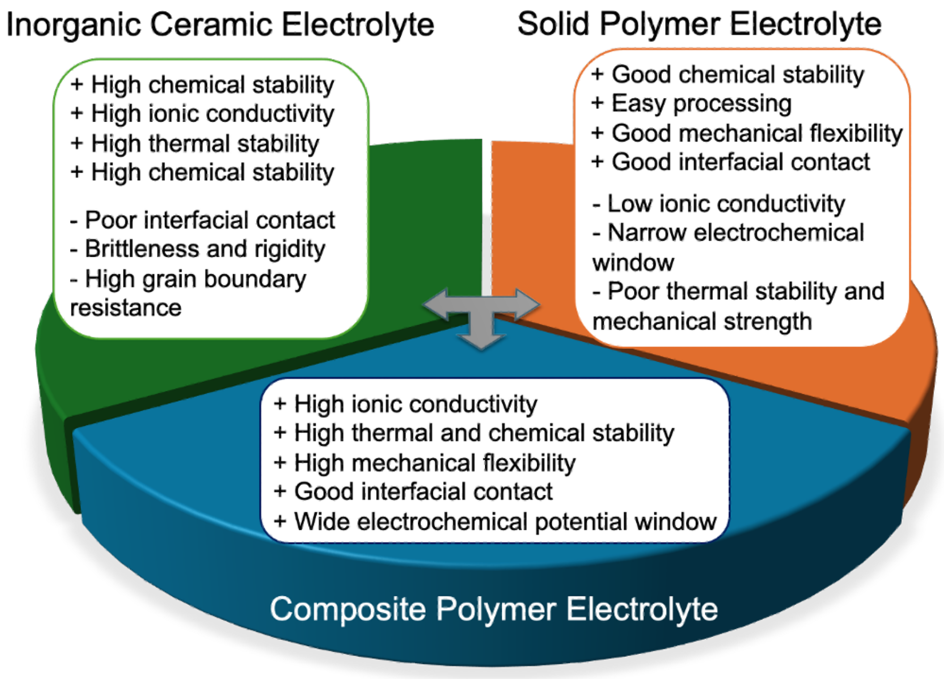

Figure 1.4. Schematic showing different solid electrolyte properties for consideration with advantages and disadvantages. Adapted with permission from Adv Compos Hybrid Mater ***5****, 2651–2674 (****2022****).*[126] *Copyrights Springer Nature 2022.*

Organic solid electrolytes, composed of polymers, offer promising advantages such as ease of manufacturing and the flexibility to accommodate volume changes in anodes and cathodes, ensuring good interfacial contact.[128] However, their low conductivity compared to liquid electrolytes, requires cells to operate at around 80°C[129] for reasonable charge and discharge speeds. Additionally, their poor mechanical strength fails to prevent Li dendrite formation at low charging currents.[127,131,132] Moreover, Cao et al.[132] discuss that most organic polymer solid electrolytes usually show low transference number, which leads to dendrite formation.

In contrast, inorganic solid electrolytes (ISEs) offer higher ionic conductivity[96,125,134,135], better mechanical and chemical stability[120,136], and compatibility with a wide range of electrode materials[37,124] compared to organic solid electrolytes. These advantages make ISEs more suitable for preventing dendrite growth and handling the harsh conditions within batteries.[136] They are typically categorised based on their chemistry, with oxides and sulphides being the two primary classes of materials, discussed in the next section.

Composite polymer SE are usually a combination of ISE and a solid polymer SE.[137] It combines the advantages of inorganic and organic solid electrolyte to provide a close to an ideal solid electrolyte. They can offer high ionic conductivity with high chemical and thermal stability. Moreover, due to the presence of polymers, they can also provide high mechanical flexibility. Furthermore, a wide electrochemical potential window can be achieved by selecting the right materials, which also helps to increases the interfacial contact between electrolyte and electrodes.[126] They are however not discussed in this thesis, as it is beyond the scope of this work.

1.2.2.2.1 Sulphide solid electrolyte

Sulphide solid electrolytes include thio-phosphates based on the Li-P-S system. They are thio-LISICON (Li_2S-MS_2-M'_xS_y,where M=Si, Ge; M'=P, Sb, Al etc), $Li_{10}GeP_2S_{12}$ (LGPS, 8.4 ± 2.7 mS cm^{-1})[138], β-Li_3PS_4 (0.16 mS cm^{-1})[95] and $Li_7P_3S_{11}$ glass ceramic (16 mS cm^{-1})[139]. They show high ionic conductivity and are easy to process[140], without the need for high sintering temperatures, which makes them an attractive SE for ASSB.

As discussed in a recent review from Hu et al.[141], based on their structural states, sulphide SEs are generally classified into three types: amorphous glass, glass-ceramic, and crystalline electrolytes[143,144]. The first category, amorphous sulphide glass electrolytes like $Li_2S–P_2S_5$, have an internal structure with no distinct crystalline order, exhibiting complete disorder. In contrast, glass-ceramic electrolytes, such as $Li_7P_3S_{11}$, combine both crystalline and glass phases. These electrolytes are usually obtained by heat-treating the glass phase, introducing crystalline regions that enhance their ionic conductivity over purely amorphous glass. Materials like argyrodite Li_6PS_5Cl, thio-LISICON, and LGPS, fall under the crystalline sulphide category and exhibits highest ionic conductivity among the categories mentioned. This increased conductivity is due to the presence of continuous Li^+ conduction channels within their ordered crystalline frameworks[145,146].

A detailed study on sulfide-based ISEs assessed their mechanical stability using first-principles calculations[146]. The results showed bulk moduli ranging from 23.3 to 32.9 GPa, shear moduli between 7.9 and 11.3 GPa, and Young's moduli in the range of 21.7–33.4 GPa. These values are considerably lower compared to those reported for oxide-based ISEs but higher than polymer SEs. Experimental validation showed slightly lower but similar ranges for Young's modulus on hot-pressed $Li_2S–P_2S_5$ pellets, while cold-pressed samples showed even lower values of Young's modulus.[147] This can be due to lower Li_2S content. In another study, Hu et al.[148], observed that multilayer architecture can restrict dendrite growth by deflecting cracks either at the boundaries between layers with different elastic moduli or within the inner layer, where particle alignment creates favorable paths for crack redirection.

This thesis uses Li_6PS_5Cl as the model system in Chapter 3 and 4 due to its unique properties as discussed below.

- *Li_6PS_5Cl*

The Li-argyrodite family was introduced by Deiseroth's group in 2008[149] and has gained interest as a potential SE for ASSB due to its high ionic conductivity. Following their 2008 publication on Li_6PS_5X *(X=Cl, Br, I)*, significant efforts have been made to design and develop the argyrodite family with a focus on enhancing electrochemical performance and stability.[134,151]

In 2011, Rao et al.[151], reported a synthesis for argyrodite (Li_6PS_5X, X = Cl, Br, I) type solid electrolytes, prepared through high-energy mechanical milling and subsequent annealing steps. Depending on the required argyrodite stoichiometric amounts of crystalline Li_2S, LiX (X = Cl, Br, I) and P_2S_5 were used as the precursors. The powders were loaded in a 45 ml agate milling pot together with fifteen 10 mm diameter agate balls and milled for 20 hours. The resulted mixture was subsequently annealed at 550 °C for 5 hour. The powder was then pressed in 10 mm diameter disks and then heat treated. All steps of synthesis were carried out under an argon atmosphere to prevent contamination from moisture or oxygen. Researchers[152] have modified the synthesis to find the optimum milling time and for heat treatment, the mixed mixture can be sealed in a quartz tube instead of making a disk.

It shows ionic conductivities around 10^{-3} S cm^{-1} however, the process is long and tedious and due to their sticky nature, the precursors stick to the ball milling jar, causing compositional inhomogeneity.[154,155] To overcome these issues, wet ball milling is also used, where the same precursors are mixed in non-dissolving organic solvents like hexane, xylene, heptane and toluene. This method provides homogeneity and shorter duration of the production but this method is not promoted due to energy intensive post annealing step of evaporating the solvent used and also insufficient understanding of the complex chemistry occurring between the precursors and solvents.

As discussed by Hanghofer et al.[155], the crystal structure of argyrodite-type Li_6PS_5Cl is illustrated in Figure 1.5a. In an ideally ordered structure, some S^{2-} ions are in the centres of Li octahedra at the 4d sites, while others are situated at 4a sites, forming a face-centred cubic (FCC) lattice. Li-ions themselves occupy two main positions, 24g and 48h, as shown in Figure 1.5b, resulting in an octahedral arrangement that facilitates three distinct types of ion jumps. These are localised jumps between 48h - 24g - 48h', intracage jumps within a single cage between 48h - 48h", and intercage jumps $48h_1$- $48h_2$ connecting adjacent cages, which together create interconnected pathways for three-dimensional ion diffusion.

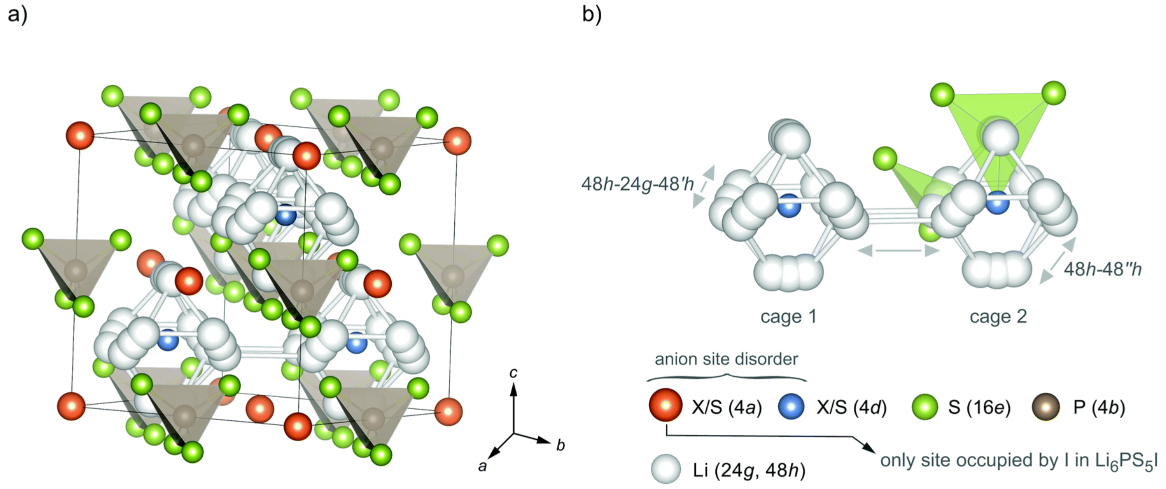

*Figure 1.5. Schematic showing a) crystal structure of L_6PS_5Cl. b) the arrangements of Li, S and P atoms within the Li_6PS_5Cl crystal structure. X refers to either Cl, Br and I. Reprinted with permission from Phys. Chem. Chem. Phys., 2019, **21**, 8489.*[155] *Copyright 2019 Royal Society of Chemistry.*

Due to the polycrystalline nature of solid electrolytes, ions migrate not only through the bulk, but also across grain boundaries (GB), which are defined as the interfaces between grains of different orientations. Depending on how they are structured and what impurities are present on them, it can either help or hinder the ion transport. When discussing ionic conductivities, effect of grain boundaries is important, as it is assumed that ionic conductivities decrease at the grain boundary due to distortions, due to degree of misorientations. Moreover, due to mismatch in ionic conductivities for bulk and grain boundaries, this can act as a site for Li metal dendrite propagation. In 2023, Kim et al.[156] conducted first-principles modeling in LLTO electrolytes and showed that Li nucleation tends to initiate in intergranular pore spaces or at grain boundaries acting as ionic bottlenecks. They demonstrated that even in the absence of external stress, pores adjacent to GBs allow the local μLi to overshoot sufficiently to make metallic Li nucleation thermodynamically favorable.

In sulphide solid electrolytes, Krauskopf et al.[157] showed that impact of grain boundaries is relatively minor in these mechanically soft materials. Similar behavior has been observed in other sulfide systems, for example in the argyrodite Li_6PS_5Br[158] and in $Li_{10}GeP_2S_1$[159], where the additional resistance from grain boundaries is reported to be small.[160] However, recent work on Li_6PS_5Cl by Buchberger et al.[161], demonstrates that microstructural features still influence measured conductivities: thick pellets measured by EIS showed higher activation energies and lower ionic conductivities compared to thin layers, due to additional resistance from grain boundaries and particle-particle contacts. This result confirms that, even though sulphides are mechanically softer and grain boundary resistance is usually smaller in sulphides compared to oxide solid electrolytes, grain boundaries, voids and interfacial contact still play a role in Li ions transport. Therefore, optimising the microstructure to reduce porosity and improve grain boundary conductivity is desirable.

1.2.2.2.2. Oxide solid electrolytes

Oxide based SEs tend to be less sensitive to moisture and air compared to sulphide SEs. They include garnets $Li_7La_3Zr_2O_{12}$ (LLZO and its dopants), LiPON, perovskites, anti-perovskites and NASICONS. Most of the oxide SEs have thermodynamic stability against Li metal[162,163] that hinders the growth of resistive SEI. Compared to sulphide SEs they show higher electrochemical and oxidation stability against Li metal that leads to reduced degradation.[12,164] Oxides exhibit good mechanical properties, including a high shear modulus, which theoretically aids in preventing the formation of lithium dendrites.[93,165] Garnets such as LLZO have gathered more attention than other oxides due to their high ionic conductivity and broad electrochemical stability window.[166] Although when compared to sulphides, they have lower ionic conductivities due to their large grain boundary resistance which restricts its ionic conductivity.[167,168] In a computational and simulation study in LLZO by Yu & Siegel et al.[169], it was found that while GB regions are enriched in Li and oxygen and show structural differences from the bulk, the extent to which Li-ion transport is hindered depends strongly on GB structure and temperature. At high temperatures, diffusion in GBs is only moderately slower than in bulk, but at room temperature, some GBs show orders-of-magnitude slower Li-ion diffusivity and significantly increased activation energies (~35% above bulk). These findings suggests that degraded ionic conductivity (or overpotential) in solid electrolytes can be traced back to GB structure, compaction, and processing history.

However, despite the advantages, oxides usually requires high sintering temperatures[163,170], limiting their application for practical purposes. To overcome these barriers, low temperature processing techniques need to be developed with interfacial modifications such as coatings for garnet SEs.[171,172] Figure 1.6 shows a comparison between sulphide, oxides and polymers on key performance indicators.

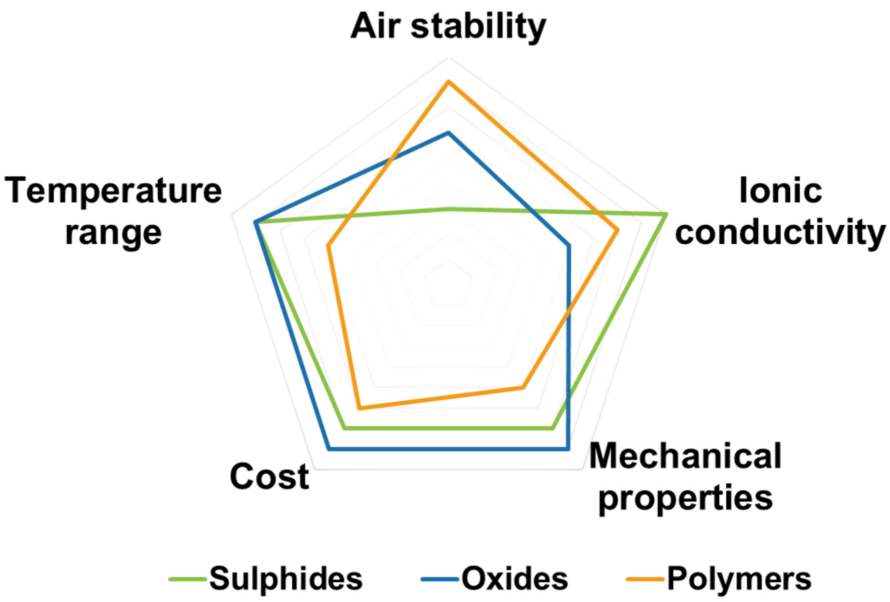

Figure 1.6. Schematic showing comparison in sulphides, oxides and polymers on key performance indicators. Adapted with permission from air-stable inorganic solid-state electrolytes for high energy density lithium batteries: Challenges, strategies, and prospects. InfoMat. 2022; 4(1):e12248.[173] *Copyright 2021 UESTC and John Wiley & Sons Australia, Ltd.*

- *Na-β"-Alumina*

As discussed in Section 1.2.1, sodium metal ASSBs are of interest for grid-scale storage.[174] Na-β"-Alumina (NBA) is a common Na ion conducting oxide solid electrolytes. It is a non-stoichiometric, hard polycrystalline ceramic with high ionic conductivity at room temperature, low electronic conductivity, and excellent stability against Na metal, which makes it an excellent candidate solid electrolyte.[94,111,112,114] It has a layered crystal structure with an essentially rigid framework containing channels which help in fast Na ion conduction as shown by structure in Figure 1.7a.

Ionic conduction happens *via* hopping from one site to another along these channels. The crystal consists of 'spinel' blocks linked by Al-O-Al bonds, which are separated by a loosely packed conduction plane with mobile Na ions in a cubic close-packed arrangement.

It has a rhombohedral symmetry with $R\bar{3}m$ space group, with three spinal blocks and adjacent conduction planes as shown in Figure 1.7a. They are stacked by spinel blocks consisting of [AlO_4] tetrahedral and [AlO_6] octahedral, oxygen ions in the adjacent spinel blocks are surrounded by mobile Na^+ ions to form conduction planes. More Na ions are present in Na-β''-Alumina in comparison to Na-β'-Alumina, enhancing its ionic conductivity and making it a preferred solid electrolyte, as shown in Figure 1.7b.[113,175] The bridging oxygen ion has weak electrostatic attraction to surrounding Na^+ ion, providing higher ionic conductivity of ~2 X 10^{-3} S cm^{-1}, at room temperature.[113,176,177] Na-β''-Alumina decomposes at temperatures higher than 1500°C into Al_2O_3 and leads to lower ionic conductivity, this was discussed by Bay et al.[178]

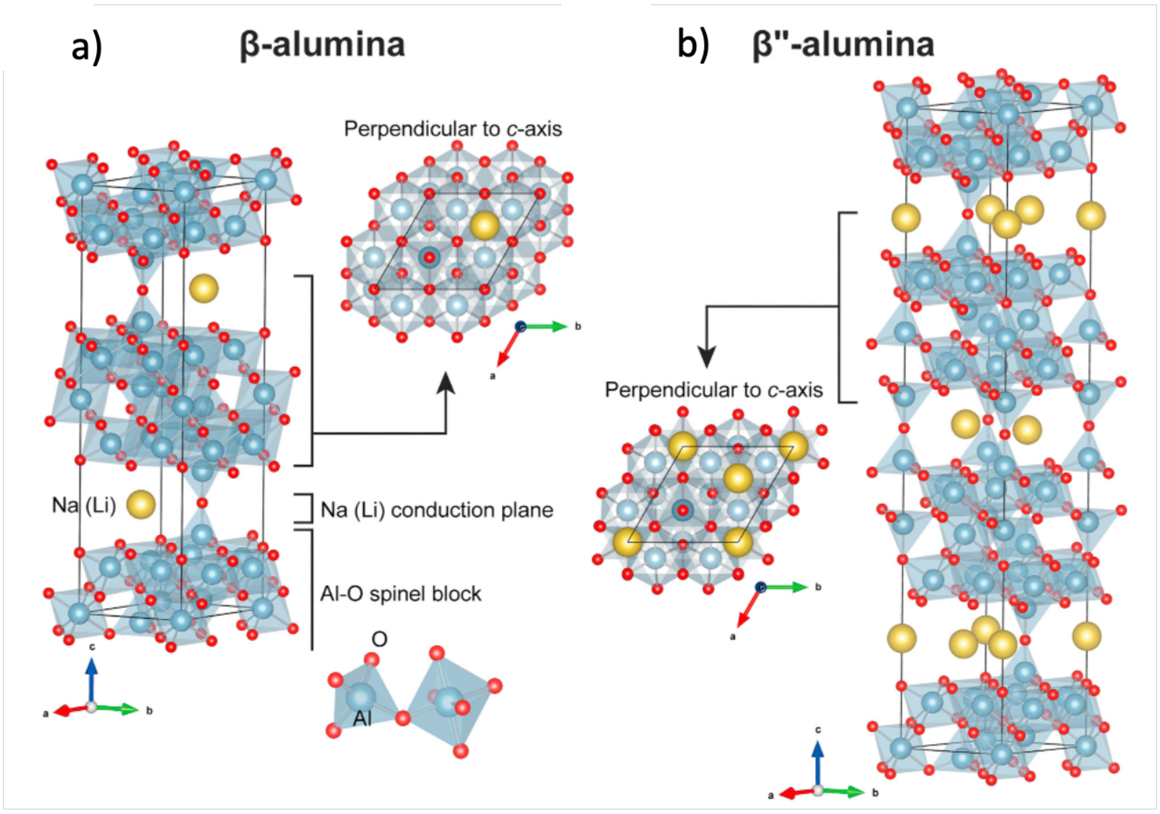

Figure 1.7. Figure showing the unit cells of a) Na-β-Alumina and b) Na-β''-Alumina. Alternating Al_2O_3 spinel block and Na_2O conduction plane is present, but they differ in stacking arrangement. Adapted and reprinted after permission from Chi et al.[175] *© 2016 Elsevier Ltd*

1.2.3 Challenges in ASSBs

Despite the tremendous interest in ASSBs with SEs, the chemically[15,64], physically[179,180], and electrochemically unstable SE/anode interface[14,62,123] has slowed the success of ASSBs.[145,165] Sometimes, due to the positive reduction potentials of the SE in comparison to the potential of lithium, the electrons from the anode are transferred to the LUMO of the SE.[15] This leads to the interphase formation which plays an important role in determining the cell stability and performance.

Interface stability between Li metal and ISEs is of utmost importance for an ASSB with satisfactory stability and fast kinetics.[15] The instabilities occur due to unstable SEI formation, side reactions[61,62,64,65], surface contamination[181–183], poor solid-solid contact, and dendrite formation[19,132,184] during charge/discharge. Therefore, these phenomena should be well investigated and understood to overcome them. In this section, challenges related to dendrites, stabilisation of interfaces and maintenance of good physical contact are discussed.

In an ASSB, there are two important interfaces, 1) SE and anode and 2) SE and cathode, and both come with their own set of challenges. This thesis focusses on the Anode/SE interface.

1.2.3.1 Insufficient solid-state contact

ASSB suffer from insufficient solid-solid contact at the electrode/electrolyte interface compared to liquid electrolytes as shown in Figure 1.8. Both ionic and electronic conducting pathways are required for redox reactions to occur across the cell and to the current collector.[185] Fu et al.[76], discuss that the poor interfacial contact leads to high interfacial resistance and inhomogeneous current distribution. This insufficient contact produces high interfacial resistance of 10^2 to 10^3 ohm cm^2, which lowers the performance of the cell. It also produces interfacial compatibility issues with either metallic anode or cathode.[186] To mitigate this effect, the group employed an Al interlayer between Li metal and LLZO garnet SE. It lowered the interfacial resistance from 950 to 75 ohm cm^2 at room temperature (20°C) and promotes uniform transport of both ions and electrons. There is substantial literature available for evidence of poor contact between garnets and Li metal.[76,180,187–192] However, due to the reactivity of sulphides, it is difficult to characterise the electrode/electrolyte interface, leading to limited reports.[189]

Another reason for insufficient solid-solid contact leading to high interfacial resistance is the presence of impurities as demonstrated by Cheng et al.[193], where Al-substituted LLZO pellets were prepared under controlled atmosphere and exposed to air. Using a combination of characterisation techniques, like SEM, XRD, Raman spectroscopy, XPS etc, it showed that exposure to air leads to the formation of a Li_2CO_3 layer on the LLZO surface. Bulk and surface-sensitive probes with different penetration depths were used to estimate both the distribution and thickness of this layer. This surface contamination is directly linked to the large interfacial resistances typically seen in LLZO/Li cells. Removing Li_2CO_3 by surface polishing was found to be highly effective, lowering the area specific resistance (ASR) at the LLZO/Li interface to 109 Ω cm^2. The presence of impurities results in inhomogeneous distribution of current during electrochemical cycling which leads Li metal to penetrate inside the electrolyte and short circuit the cell.[180,181,183,187–189] Due to inhomogeneous distribution of current, the current density in one particular area is increased, leading to dendrite formation and eventual cell failure. This phenomenon is often referred to as “current constriction”[180] and is discussed in detail in Section 1.3.2.3. Various ways to remove the contaminants from the surface of SE are discussed in Section 1.3.3.

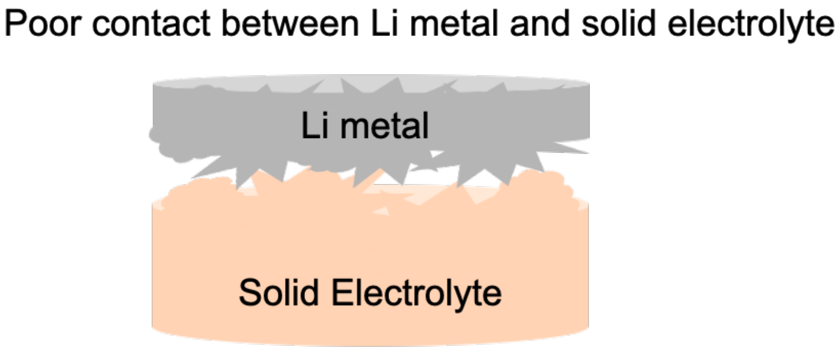

Figure 1.8. Schematic showing poor-contact between solid electrolyte and Li metal due to uneven surface.

1.2.3.2 Stabilisation of interfaces

The stabilisation of interfaces has proved to be a challenge. This is due to the formation of ionically resistive or electron-conducting decomposition products which inhibits the performance, even though Li presents better stability with solid electrolytes compared to liquid electrolytes.[123,194] Due to the narrow stability window of solid electrolytes it is difficult to achieve stable interfaces for both metal anode and cathode electrode as shown in Figure 1.9a.[60] For instance, sulphide SE demonstrates high ionic conductivity but have a narrow electrochemical stability window due to high-valence P and low-valence S atoms as shown in Figure 1.9b, making them incompatible with high-voltage cathodes and low-potential anodes[195,196]. These conditions cause sulphide decomposition, increased interfacial resistance, and hindered Li-ion transport.[141]

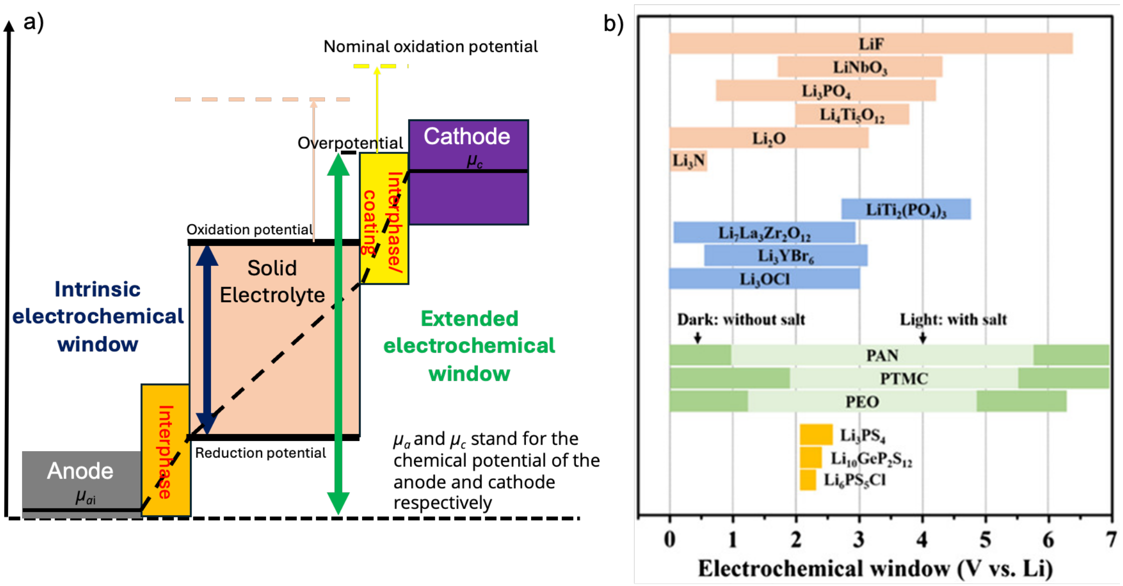

Figure 1.9. Schematic showing a) relation between the HUMO and LUMO band gap between anode and cathode material. Reproduced with permission from ACS Appl. Mater. Interfaces 2015, 7, 42, 23685-23693.[197] *2015 Copyright ACS publication; b) shows the electrochemical window of various solid electrolytes. Reprinted with permission from Electrochemical Compatibility of Solid-State Electrolytes with Cathodes and Anodes for All-Solid-State Lithium Batteries: A Review. Adv. Energy Sustainability Res., 2: 2000101.*[198] *Copyright 2021 Advanced Energy and Sustainability Research published by Wiley-VCH GmbH*

In 2015, Wenzel et al.[65] discuss three distinct types of interfaces that can form between a SE and a metal anode, as illustrated in Figure 1.10, i.e., a thermodynamically unstable interphase, a thermodynamically stable interphase and a mixed conducting interface (MCI). While selecting the SE for ASSB, this is a very important consideration.

For example, Chapter 3 and 4 of this thesis use Li_6PS_5Cl, which forms a self-passivating, thermodynamically unstable interphase and reacts with the metal anode to form an SEI. However, this thin SEI layer does not significantly inhibit ionic conductivity, despite being thermodynamically unstable. This is due to its negligible electronic conductivity which limits the SEI growth, making them viable for battery applications. This type of interphase is depicted in Figure 1.10a.

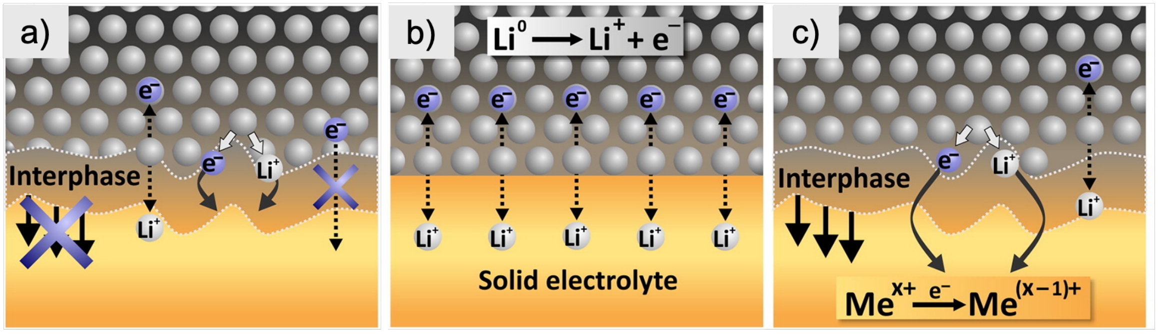

Figure 1.10. Schematic showing interfaces between lithium metal and a solid electrolyte; a) Thermodynamically unstable interface; b) Thermodynamically stable but non-reactive interface; c) reactive interface. Adapted and reprinted by permission from Wenzel et al.[65] Copyright © 2015 Elsevier B.V.

Chapter 5 uses Na-β''-alumina which forms a thermodynamically stable, non-reactive interface, where no significant interaction occurs between the metal anode and the SE, as depicted in Figure 1.10b. SE maintains a stable interface in contact with sodium metal. The third type involves the formation of a mixed conducting interface (MCI), characterised by a reactive interaction between the solid electrolyte and the metal anode, as shown in Figure 1.10c. In this scenario, the interface exhibits both ionic and electronic conductivity, leading to continuous reduction of the solid electrolyte. Consequently, a non-passivating, unstable SEI forms, resulting in a thick interfacial layer with high resistance. Solid electrolytes such as LAGP, LGPS, and LLTO typically form this type of interface.

Wenzel et al.[199] discuss interface growth rate of solid electrolytes in contact with Li metal i.e., the interfacial resistance growth with time is dependent on ionic and electronic conductivity of the interface compounds. In another study by Wenzel et al.[64], they estimated the thickness of SEI to be a few nm for the Li_6PS_5Cl anode interface using *in-situ* XPS. However, recent research by Narayanan et al.[62], investigate the Li-free ASSB Li_6PS_5Cl interface through *operando* XPS, estimating the SEI thickness to 100-200 nm at least. Another similar study was conducted by Otto et al.[61], where they used time-of-flight secondary ion mass spectroscopy (ToF-SIMS) and atomic force microscopy (AFM) to estimate the thickness of Li_6PS_5Cl interface to be around 250 ± 25 nm. This suggests there is an uncertainty of the real thickness of these interphases.

The major problem with studying these interphases in ASSBs is that they are buried deep in the cell, making it hard for researchers to characterise them without an appropriate technique. Also, due to more than one effect occurring at the same time, interfacial degradation can be accelerated by other sources of degradation. Development of *operando*, non-destructive techniques with high penetration depth would be useful for the study of these interfaces such as the ones conducted by Otto et al.[61] and Narayanan et al.[62] Without the proper understanding of these problems, it is difficult to make a stable working battery with good cycle life and high energy density.

1.2.3.3 Dendrites formation

In 1976, the first generation of Li-ion batteries failed due to the formation of fractal like lithium metal filaments, commonly known as dendrites. Selim and Bro et al.[200] reported a 15% loss of lithium in liquid electrolytes, accompanied by the formation of mossy lithium deposits. They proposed that this lithium loss is not solely due to chemical reactions but also involves physical loss. Bai et al.[88] revealed that dendrite formation happens in two stages in a Li-ion battery: first is the formation of mossy-dendrites, which grows from the roots, second is the fractal "dendritic" lithium, dendrites are observed to grow from tips and migrate to the opposite electrode. The whole process of this transition from mossy morphology to fractal dendrite morphology was demonstrated in 2016 for the first time by Bai et al.[88], with corresponding cell overpotential response explaining the dendrite formation in liquid electrolytes. They reveal that the transition is based on a reaction-limited to a diffusion-limited process and this has been widely accepted by the battery research community. The formation of fractal dendrites is attributed to limited diffusion, which leads to direct short circuiting and is more linked to mechanical effects.[201]

Classical dendrite growth in liquid electrolytes as proved by Bai et al.[88] is a factor of kinetic and diffusion processes. However, all ASSBs with Li metal negative electrodes suffer from short-circuit at high C rates during charge, which occurs due to thin Li filament or so called "dendrites" growth that penetrates the SE and directly connects the anode and cathode. Since SEs are mechanically stronger than LEs and separators used in liquid batteries, it is assumed that they will prevent dendrite formation better than their counterparts.

In 2005, Monroe and Newman[93] suggested a new dendrite propagation model to describe growth kinetics of dendrites and claimed that the shear modulus of the solid electrolyte should be twice as much as lithium to avoid dendrite formation.[93] However, that model is highly debatable,[147,192,202] because high ionic conductivity solid electrolytes have been researched widely with high Young's modulus[93], density and transference number close to one. However, Li metal still penetrated them at current densities lower than 0.5 mA cm^{-2}.[179] In 2019, Han et al.[19] demonstrated that it is easier for Li filaments to grow in LLZO and Li_2S-P_2S_5, than in liquid electrolytes. They tracked lithium evolution in three widely studies SEs: LiPON, LLZO and amorphous Li_3PS_4 using time-resolved operando neutron depth profiling. In LiPON, lithium distribution remained largely unchanged, whereas in both LLZO and Li_3PS_4, lithium deposited directly within the bulk of the electrolyte. These results point to the relatively high electronic conductivity of LLZO and Li_3PS_4 as the main driver of dendrite formation. Consequently, strategies to suppress dendrites should also focus on reducing electronic conductivity, rather than solely pushing for higher ionic conductivity in SEs. Moreover, in 2019, it was found that there exists a critical current density above which dendrites form and short circuit the battery which was demonstrated by Bruce and co-workers[184]. They showed that 0.2 mA cm^{-2} is the maximum current for avoiding voids and subsequent dendrite formation at 3 MPa stack pressure, increasing to 1 mA cm^{-2} at 7 MPa for a Li metal/Li_6PS_5Cl (argyrodite)/Li metal symmetric cell. This clearly shows that understanding the mechanism of dendrite formation and propagation is crucial for understanding the failure mechanism to enable Li metal batteries.

1.3 Li-free or anodeless solid-state battery

1.3.1 Overview

A new concept of SSB is being investigated in which the anode active material is removed completely as shown in Figure 1.11. During initial charging of this type of system, Li-ions are mobilised from cathode and electrodeposited on the anode side on the current collector as Li metal. During subsequent discharge, this electrodeposited Li metal is stripped from current collector as Li-ions and moves back to the cathode. It's worth noting that research into anode-less systems in LIBs has explored modifications to the current collector or engineering of the electrolyte.[1] A number of reviews[209, 210] and research[210] paper highlights this concept for ASSB. Ideally, because of the absence of excess Li metal present in the anode, the safety hazard present during storage and transportation is greatly reduced.[211] Moreover, due to the absence of excess Li, the gravimetric and volumetric energy density of the anodeless or “Li-free” batteries is increased compared to Li-ion battery, as after the first plating, the Li metal acts as an anode active material. It should potentially reduce the cost of production as only a thin current collector is used in place of anode active material compared to graphite or Li metal or any other anode material.[204]

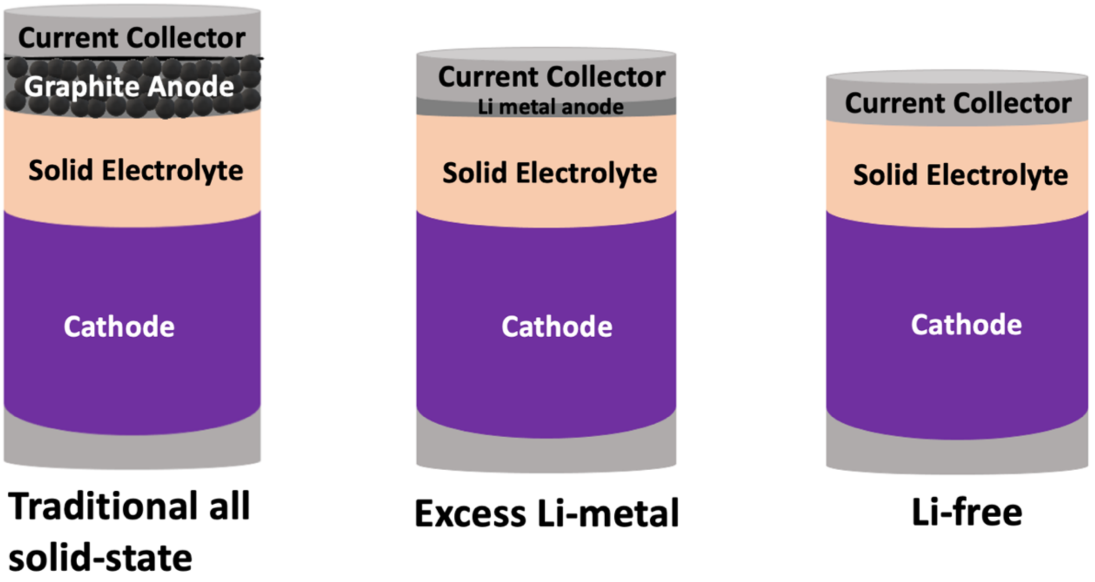

Figure 1.11. Schematic showing different components of traditional all-solid-state, excess Li metal and Li-free batteries.

As previously discussed, "Li-free" batteries, with no anode active material, offer higher energy density, safety and lower manufacturing cost compared to traditional Li-ion and SSB. Companies like Quantum Scape and Samsung SDI are trying to commercialise this concept. However, despite the advantages offered by Li-free ASSB, they experience restricted cycle life[210], poor CE[212], and uneven deposition of Li metal[213]. It is not caused by a single factor, but rather results from multiple interconnected factors discussed in Section 1.3.2, contributing to the irreversible consumption of Li metal and eventual battery failure.

In 2020, researchers from Samsung Advanced Institute of Technology[214] showed tremendous performance of silver-carbon composite anode in a Li-free pouch cell with 3.4 mA cm^{-2} current density, with high areal capacity (>6.8 mAh cm^{-2}) with a sulphide solid electrolyte. The cell showed high energy density of >900 Wh/L, a stable coulombic efficiency of over 99.8% and long cycle life of 1000 times at 60°C. However, the exact mechanism was left unexplored. Quantum scape in 2021 released results of their Li-free SSB design showcasing <800 cycles at 25°C with over 95% CE.[215,216]

Chapter 3 and 4 of the thesis focusses on improving the CE and cycle life of Li-free ASSBs on the anode side and attempts to overcome the challenges mentioned above.

1.3.2 Factors Influencing Coulombic Efficiency (CE) and cycle life

1.3.2.1 Solid Electrolyte Interphase (SEI)

As discussed in Section 1.2.3, anode and SE interface is an important factor when considering low CE. In the presence of graphite, a relatively stable SEI is formed but in the presence of a Li metal anode, during charge and discharge, volume changes occur which leads to mechanical strain on the SEI and the cell. Moreover, it leads to inhomogenous deposition of Li and formation of "dead" lithium. Due to the presence of this dead Li, more Li is consumed from cathode in the SEI formation and it compromises the gravimetric energy density of the cell.[217]

Furthermore, most solid electrolytes are sensitive to moisture and air.[218–221] This leads to the formation of surface contaminants such as oxides (Li_2O, CO_2), carbonates (Li_2CO_3, Na_2CO_3) and hydroxides (LiOH, NaOH) to name a few, which further leads to side reaction between Li metal and the SE, leading to an uneven local electric field. Due to the formation of these surface layers and an uneven local electric field, the interfacial resistance increases.[181] This also further reduces the wettability of the Li metal with the electrolyte.[183] In a recent study Wang et al.[222] investigated $Li_7La_3Zr_2O_{12}$ (LLZO) SE interface to understand the role of surface contamination and observed, that the impedance at the Li metal interface is not only caused by voids but also by ionically resistive contaminants on the surface. This also results in reduced conductivity and poor lithium wetting. Therefore, removing the surface contamination layer is important as it improves the wettability, reduces interfacial resistance, and helps with uneven current flux promoting homogenous local currents which helps enable higher critical currents.

Goodenough and co-workers[223] show that the interfacial resistance of LLZO can be reduced from 1210 Ω cm^2 to 28 Ω cm^2 at 25°C by treating LLZO with carbon at 700°C under an inert atmosphere, which helps to achieve high coulombic efficiencies and stable cycling. Sakamoto and co-workers[182,184,219] have done several studies to reduce the interfacial resistance of LLZO. They used heat treatment to enable homogeneous current density by removing the common surface contaminants such as hydroxides and carbonates. In one of the studies conducted by Sharafi et al.[183], a low interfacial resistance of 2 Ω cm^2 was demonstrated with heat treatment for LLZO by removing surface contaminants. Furthermore, the study discussed the interlinking relation of interfacial chemistry, wettability and electrochemical phenomenon, where it is discussed that in presence of surface impurities like Li_2CO_3 and LiOH, high resistance with poor wettability was observed as shown in Figure 1.12. Chapter 5 of this thesis focuses on surface treatment strategies for solid electrolytes.

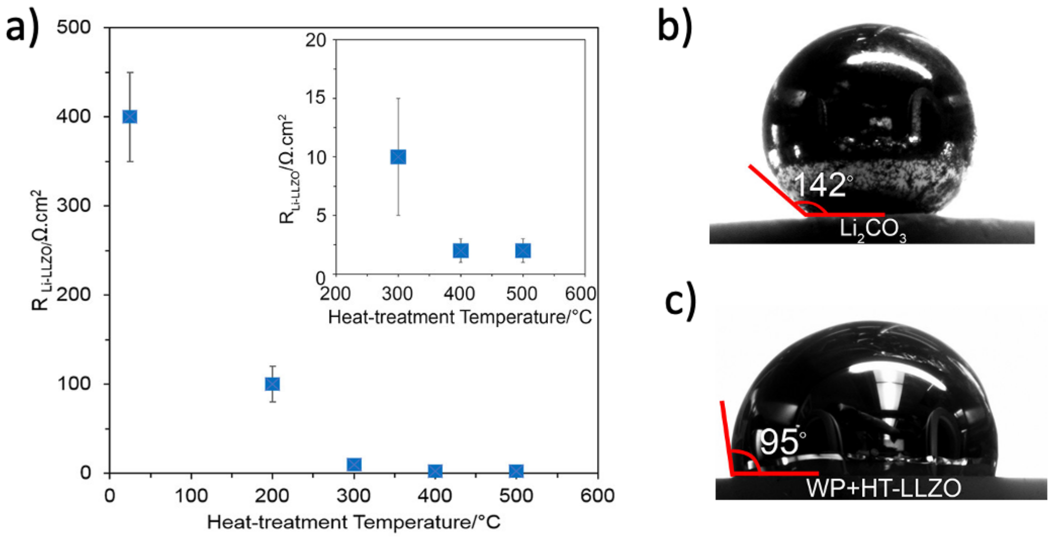

Figure 1.12. a) Graph showing LLZO interfacial resistance after heat-treatment at different temperatures; b) Image showing higher contact angle due to the presence of impurities; c) Image showing lower contact angle after heat-treatment due to reduction in impurities. Adapted with permission from Chem. Mater. 2017, 29, 18, 7961–7968.[183] *2017 ACS copyright.*

1.3.2.2 Morphology

Morphology of Li deposition is an important factor when considering cyclability in ASSBs and it depends on several factors such as solubility of Li and the interlayer material[224], temperature[225], diffusivity of the material[226] etc.

Kim et al.[227] investigated the role of Au, Ag and Si in electrodeposition of Li metal using operando microscopy. 100 nm thick metal interlayers were deposited on LLZO solid electrolyte in a Li-free setup. It was observed that these metals form an alloy with Li metal, but the growth kinetics are very different as shown in Figure 1.13. Li deposition was affected by the geometry of the LLZO surface, the pre-existing surface flaws acted as deposition sites as shown in Figure 1.13a. It formed island-shaped metal when low current 0.1 mA cm^2 was applied, where these island-shaped metal clusters kept on growing as filamentary Li metal. They also proposed how Li metal deposits using the Figure 1.13b, where it is shown that:

i) Local electric field is induced due to morphological flaws, which leads to Li concentrating at these sites,

ii) Li has preference to deposit at the defect sites in island-metals shape, than to deposit homogenously,

iii) As Li is further deposited, the island-shaped metal deposits keep on growing rather than homogenously depositing.

It was also found that Li diffusion in metal alloys plays an important role, where higher diffusion coefficient leads to more homogenous deposition of Li metal. It was found that solubility, nucleation kinetics, crystal structural, diffusivity and crystalline Li compatibility are important parameters that govern Li precipitation. A silver interlayer demonstrated enhanced stripping and deposition kinetics compared with gold and silicon interlayers.

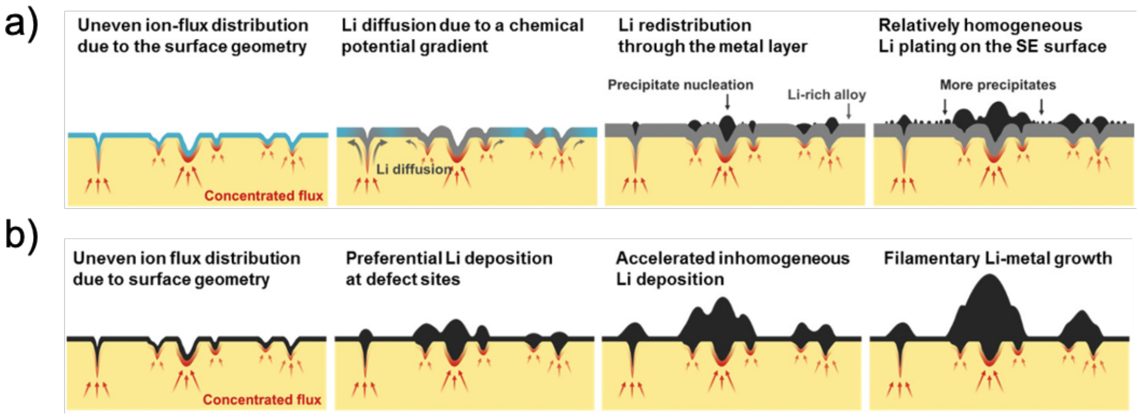

Figure 1.13. Schematic images showing a) role of metal interlayer in promoting homogenous Li plating on the SE surface and b) inhomogeneous lithium deposition due to surface flaws, leading to current constriction and inhomogeneous plating of Li-metal. Adapted with permission from Kim et al.[227]*, The Role of Interlayer Chemistry in Li-Metal Growth through a Garnet-Type Solid Electrolyte. Adv. Energy Mater. 2020, 10, 1903993. Copyright 2020 WILEY-VCH Verlag GmbH & Co. KGaA, Weinheim*

1.3.2.3 Uneven current density

Uneven current fluxes are electrical contact resistances that arise from limited contact between electrical conductors, leading to the concentration of current flow around small, discrete contact points. They are defined as "constriction resistances".[180,188] Eckhardt et al.[187] discuss how pores at the interface, reduce the electrochemically active surface area, causing the ionic current in the SE to become concentrated at the contact points, creating "bottlenecks." The phenomenon is referred as "current constriction" and has been well-documented in 1990's. According to the study, it typically occurs when there is a mismatch between the electrode and the electrolyte active area. Moreover, the role of geometric factors such as interface morphology as discussed above, is found to impact the "current constriction".

In 2019 Krauskopf et al.[180] investigated the use of $Li_7La_3Zr_2O_{12}$ (LLZO) as a model system due to its stability against Li metal and highlighted the role of constriction resistance in understanding interfacial behaviour. They demonstrated that the contact geometry, coupled with ionic transport within the solid electrolyte, is the primary factor influencing interfacial contributions at a clean, equilibrated interface. A significant finding of their work was that, under anodic operating conditions, the diffusion of lithium vacancies in the metal anode limits the rate capability due to contact loss. This contact loss is driven by vacancy accumulation and subsequent pore formation near the interface, which hampers performance. Krauskopf et al.[180] also emphasised the critical role of applying extremely high pressures up to 100 MPa in reducing interfacial resistance to nearly 0 Ω cm^2. By minimising interfacial resistance in this way, they were able to isolate the effects of contact geometry, confirming that the observed interfacial phenomena arise primarily from contact issues rather than intrinsic material properties. This insight underscores the importance of optimising contact conditions to enhance the performance of Li metal anodes. Moreover, the study around uneven current density of sulphide phase SE is limited.[189] In this thesis, instead of pores, isolated islands of Li metal are discussed in Chapter 3.

1.3.3 Current research trends and developments to tackle morphology instability

Recently, the morphological limitations of Li-free ASSB have been addressed by structural or surface modifications. In this section, the use of interlayers as a potential strategy to improve the morphological stability and increase the cycle performance is discussed.

Interlayers can be metallic or inorganic. Metallic interlayers form alloys when in contact with Li metal and Li metal forms alloys with several metals such as Si, Al, Bi, Zn, Sn, Ge, Ag, Mg, In, etc. all of which have been widely explored as anode active materials as discussed in a review by Obrovac et al.[84] They show higher volumetric and gravimetric energy density compared to graphite, as shown in Figure 1.14. Alloy materials look promising as alternative anode materials due to their high reversible capacity.[84,85]

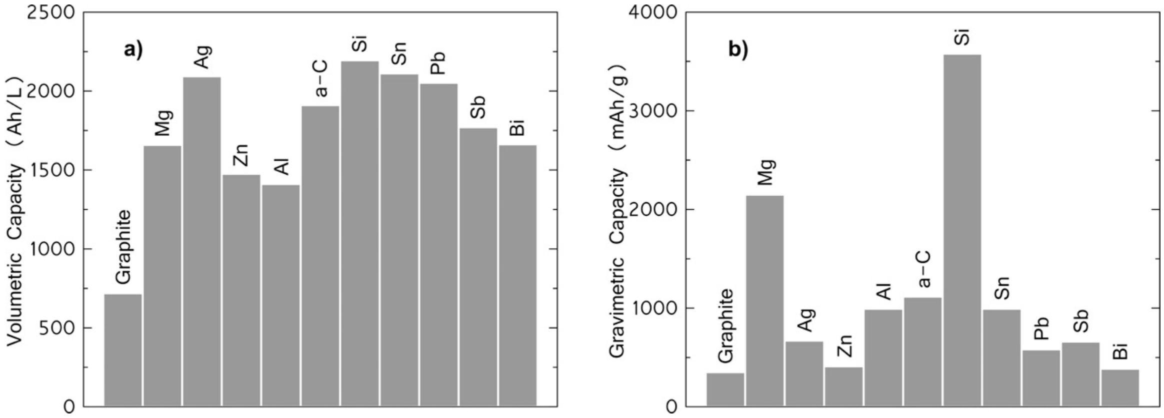

Figure 1.14. Graphs showing comparison between graphite and different metals in terms of a) Volumetric Capacity and b) Gravimetric Capacity. Reprinted with permission from Chem. Rev. 2014, 114, 23, 11444–11502.[84] Copyright © 2014 American Chemical Society.

Alloys help to increase the wettability of the metal anode with solid electrolyte.[76] Hence, it attempts to suppress the dendrite formation and helps to improve ionic conduction. Figure 1.15 shows how alloys help to increase the wettability.

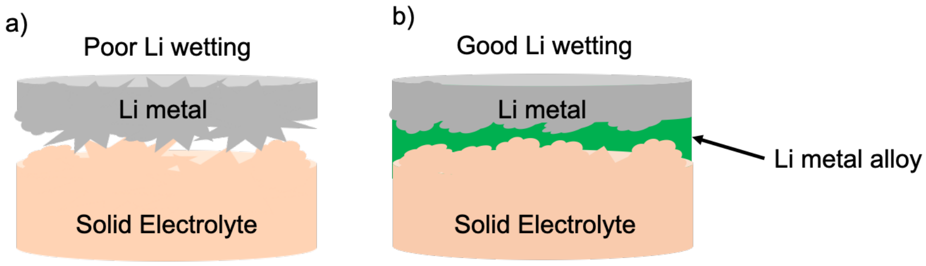

Figure 1.15. Schematic showing a) poor wetting behaviour of Li metal and insufficient contact between Li metal and solid electrolyte; b) schematic showing Li-metal alloys helps to provide better contact between the solid electrolyte and metallic anode by forming an interfacial layer which helps to increase wettability.

Moreover, metal alloys have been reported to lower the nucleation barrier especially for solid solution alloys such as Zn, Mg, Au and Ag, thus helping in modifying the current collector for stable, homogenous deposition of Li metal as discussed by Yan et al.[228] They investigated eleven metals as current collectors in liquid Li metal batteries to study their plating behaviour. It was observed that metals with 0 mV nucleation overpotential formed solid-solution alloys with metal as shown in Figure 1.16.

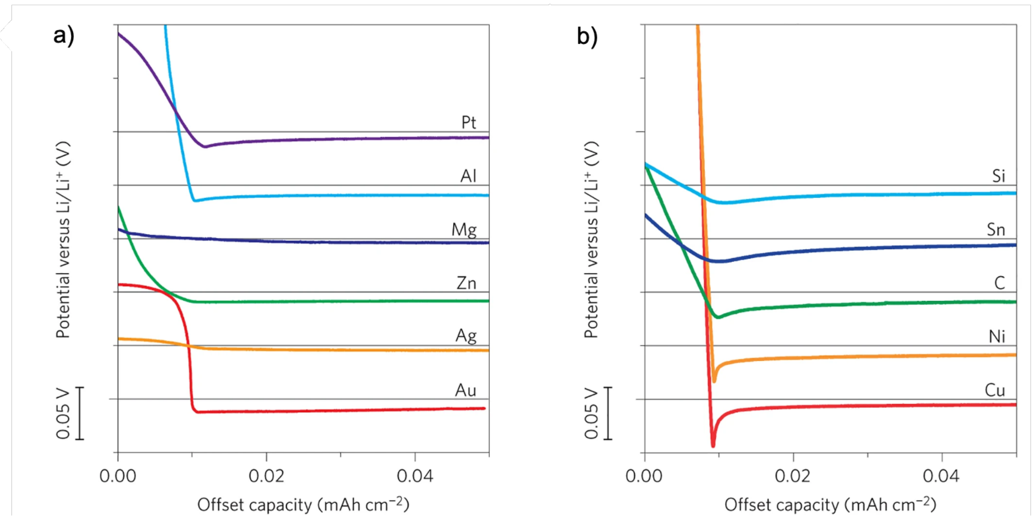

Figure 1.16.a and b) Potential vs capacity graph showing nucleation potential for 11 metals. a) shows Au, Ag, Zn, Mg, Al and Pt; b) Cu, Ni, C, Sn and Si. Adapted with permission from Yan et al. Nat Energy ***1****, 16010 (2016).*[228] *Copyright 2016 Springer Nature.*

Silver metal attracted a lot of attention recently when the researchers at Samsung Institute of Advanced Technologies[214] reported a high-performance Li-free ASSBs. They used a sulphide SE with Ag-C composite interlayer as anode in absence of excess Li, so called “anodeless” battery as shown in Figure 1.17.

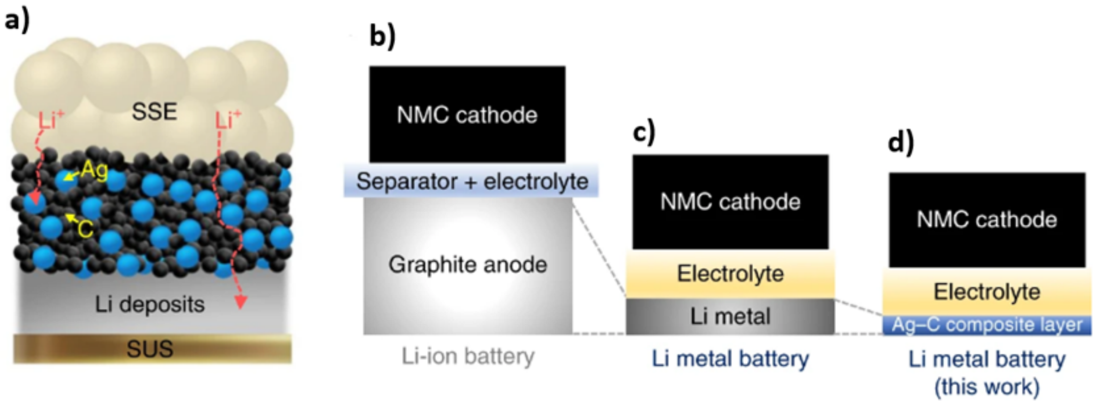

Figure 1.17. Schematic showing a) ASSB battery composed of stainless-steel foil as current collector, argyrodite as SE and Ag-C nanocomposite as anode material; traditional b) Li-ion battery; c) Li metal battery; d) Li-free ASSB that comprises Ag-C nanocomposite layer on SUS current collector for stable Li plating and stripping prepared in this work. Reprinted with permission from Lee et al, High-energy long-cycling all-solid-state lithium metal batteries enabled by silver–carbon composite anodes. Nat Energy **5**, *299–308 (2020).*[214] *Copyright 2020, under exclusive licence to Springer Nature Limited.*

They discussed the role of the Ag-C composite interlayer in effectively controlling Li deposition, which results in significantly extended electrochemical cyclability. NMC cathode was used to test full cell capabilities. A warm isostatic pressing technique was utilised to enhance the contact between the composite interlayer and sulphide SE, resulting in a prototype pouch cell demonstrating high energy density (>900 Wh l^{-1}) and sustained CE of over 99.8% over a long cycle life (1000 cycles).[214] They observed that Li plates at the stainless-steel current collector on charge i.e., between the composite layer and current collector, shown by SEM/EDX in Figure 1.18, rather than the solid electrolyte interface. The schematic in Figure 1.18, accompanied by corresponding SEM/EDX shows that silver nanoparticles move towards the current collector on repeated cycling. Using carbon has been proven to behave as a protective layer for Li deposition. However, in this cell it acts as separator and keeps the solid-state electrolyte and layer of Li metal separated from each other. This might help to increase the cycle life of the cell and avoids Li penetration. However, the mechanism behind the role of silver nanoparticles and the carbon interlayer was left unexplored, prompting the study in Chapter 4, to better understand this phenomenon.[a]

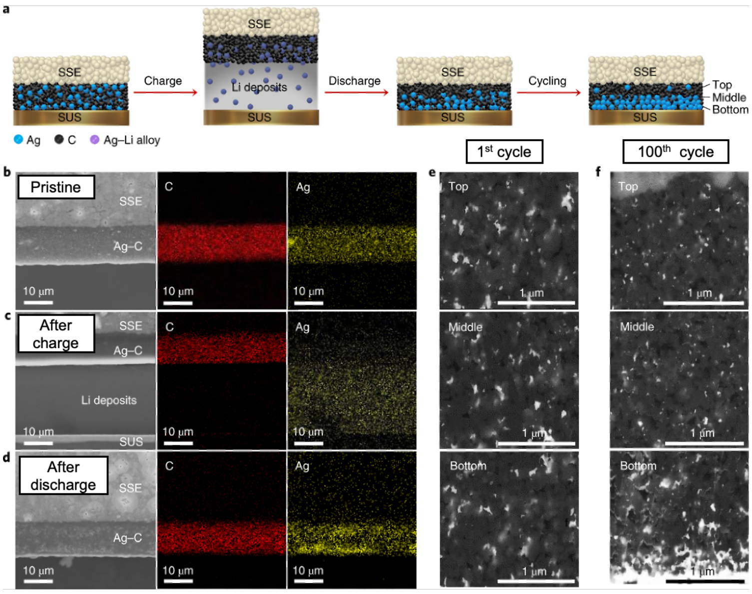

Figure 1.18. Schematic representing silver-carbon with sulphide SE: a) schematic representing Li plating-stripping process on the current collector in presence of Ag-C composite interlayer, b-d) Cross-section SEM with corresponding EDS images for the Ag-C composite interlayer, where b) is pristine, c) is after charging and d) is after discharging. e-f) Ag distributing in Ag-C composite interlayer after e) 1st cycle, after f) 100th cycle. Adapted and reprinted after permission from Lee et al, High-energy long-cycling all-solid-state lithium metal batteries enabled by silver–carbon composite anodes. Nat Energy ***5****, 299–308 (2020).*[214] *Copyright 2020, Springer Nature Limited.*

---

[a] The study in Chapter 4, began in collaboration with Dr Dominic Spencer Jolly in end of 2020, after the labs reopened after the first wave of COVID and some preliminary work on different carbon was investigated by him in his thesis[229], submitted in 2021. Some of the work performed in this Chapter is also reported in his thesis as is it forms the basics of the shared co-author ownership and is included here for completeness.

1.4 Summary and Aim of the work

All-solid-state batteries promise to increase the energy density compared to currently used Li-ion batteries with the help of a Li-free setup as discussed in this chapter. However, despite many advantages, Li-free ASSB's suffers from low CE, as there is no excess Li to compensate for Li loss due to SEI formation and inhomogeneous deposition of Li, which can lead to contact loss. Moreover, this inhomogeneous deposition of Li leads to mechanical stress accumulation which can initiate the formation of cracks in SE, leading to dendrite formation and eventual cell failure. To have a working all-solid-state Li-free battery, the interfacial chemistry, mechanisms of metal interlayer lithiation, role of low interfacial resistance as a response of Li plating and stripping must understood.

After discussing experimental techniques in Chapter 2, Chapter 3 explores the role of a silver metal interlayer in a Li-free setup with a sulphide SE. It discusses the interfacial reactivity of this metal interlayer with the sulphide solid electrolytes. It also demonstrates the role of silver in homogenous Li nucleation on charging/discharging and shows the full cell performance of these cells. Unfortunately, for most of the alloy anodes the main hinderance is poor wettability and stability of the anode with the electrolyte. Moreover, most of the alloy anodes suffer from volume expansion on lithiation as shown by previous studies.[84,85]

Subsequently, Chapter 4 investigates the structural changes happening in graphite-silver composite interlayers in a Li-free system and tracks the structural changes occurring through it using *operando* XRD. It also investigates the role of silver in the graphite-silver system by suppressing dendrite formation and promoting homogenous Li nucleation.

Finally, Chapter 5, provides a fundamental understanding of interfacial resistance using different surface treatments to make the surface of a SE contaminant free. Whilst the presence of impurities has been suggested to be the reason of high interfacial resistance in solid electrolytes, this work aims to utilise plasma cleaning and heat treatment as effective surface treatments for inorganic solid electrolytes. The chapter goes on to investigate the role of power, time and gas used. By characterising the surface treated SE through XPS and impedance microscopy, a qualitative theory is developed for the usage of plasma cleaning as a potential surface treatment technique.

2 Chapter 2: Experimental Techniques

2.1 Overview

The objective of this chapter is to present a comprehensive overview of the various experimental techniques employed in this thesis. It covers the underlying principles of these techniques and provides insights into the practical considerations involved when studying materials for solid-state batteries.

2.2 Sample Preparation

2.2.1 Cell Fabrication

There are three main cell form factors i.e., cylindrical, prismatic and pouch cells that are commercially used with each having its own advantages and disadvantages as shown in Figure 2.1.[230] They are usually produced through highly-automated processes to achieve high quality, precision and reproducibility.[231] Producing these cell form factors for research purposes at R&D scale in laboratories, poses a huge challenge, as the process needs to be flexible to understand the impact of various parameters. Hence, coin cells and pouch cells are usually employed for electrochemical measurements.[232]

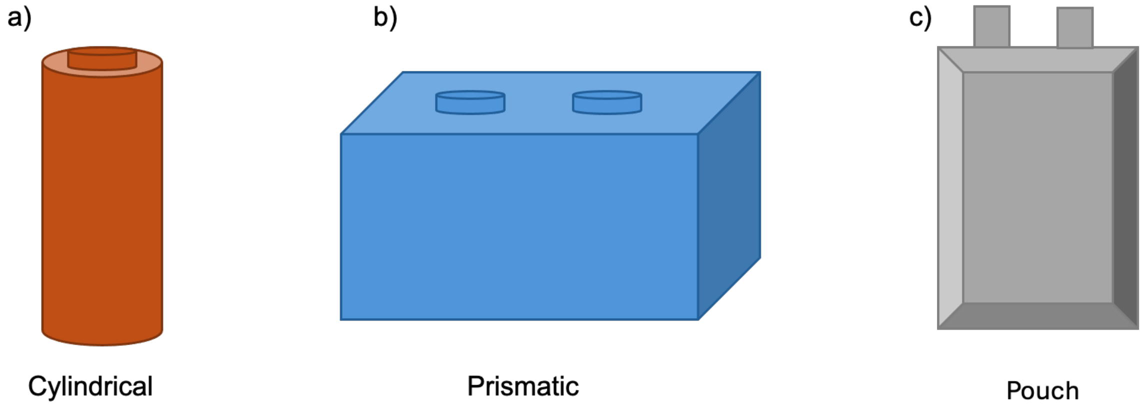

Figure 2.1. Schematic showing a) cylindrical, b) prismatic, c) pouch cell form factors.

In research laboratories, half-cells are usually employed, where Li metal is used as one electrode material and the material to be investigated is used as counter. This thesis uses coin-cells and pouch cells as half-cells as it is easy to characterise the material afterwards to understand structural and chemical change. However, due to the presence of excess Li in an electrode, half-cells can provide unreliable results for practical cells, as excess Li can hide issues caused by side reactions that consume the available lithium.[233] Therefore, this thesis also employs custom made polyether ether ketone (PEEK) full cell[b] as shown in Figure 2.2 in addition to asymmetric half-pouch cells. To prepare the full cells shown in Figure 2.2, all chemicals were thoroughly dried under vacuum and stored in an argon-filled glovebox, with oxygen and moisture levels maintained below 0.1 ppm. For the solid-state composite cathode, single-crystal $LiNi_{0.83}Mn_{0.06}Co_{0.11}O_2$ (MSE Supplies), ultra-fine Li_6PS_5Cl (MSE Supplies), and carbon nanofiber (CNF) (Merck) were combined in a mass ratio of 70:28:2 and manually mixed using a mortar and pestle. The assembled custom PEEK full cell consists of a PEEK tube cell as shown in Figure 2.2a with a 5 mm inner diameter, a conductive plunger is inserted on one side with a stainless-steel current collector and 30 mg of Li_6PS_5Cl is pressed with the help of 2nd conductive plunger and 400 MPa uniaxial pressure for 1 min. After that, the mixed composite cathode mixture (corresponding to an areal capacity of ~ 4 mAh cm^{-2}) is added to the pressed solid electrolyte. Followed by addition of another current collector or Li metal foil, depending on the experiment. The 2nd conductive plunger is then added on top of the current collector to make the circuit complete as shown in Figure 2.2a. This PEEK tube cell is then transferred to the cell housing as shown in Figure 2.2b, where a compression spring is added to apply asymmetric stack pressure, followed by screwing at the top, to allow

---

[b] This was designed by Dr Christopher Doerrer from Patrick Grant's group and used extensively in Peter Bruce's Group.

adjustment of pressure to 2 MPa and then assembled PEEK full was then connected to the Biologic instrument for cycling experiments. Coin cells are used in Chapter 4 in Section 4.3.1.5, to lithiate graphite, where dried graphite powder was loaded in a 2032-coin cell with electrolyte mixture, separator and Li metal counter electrode.

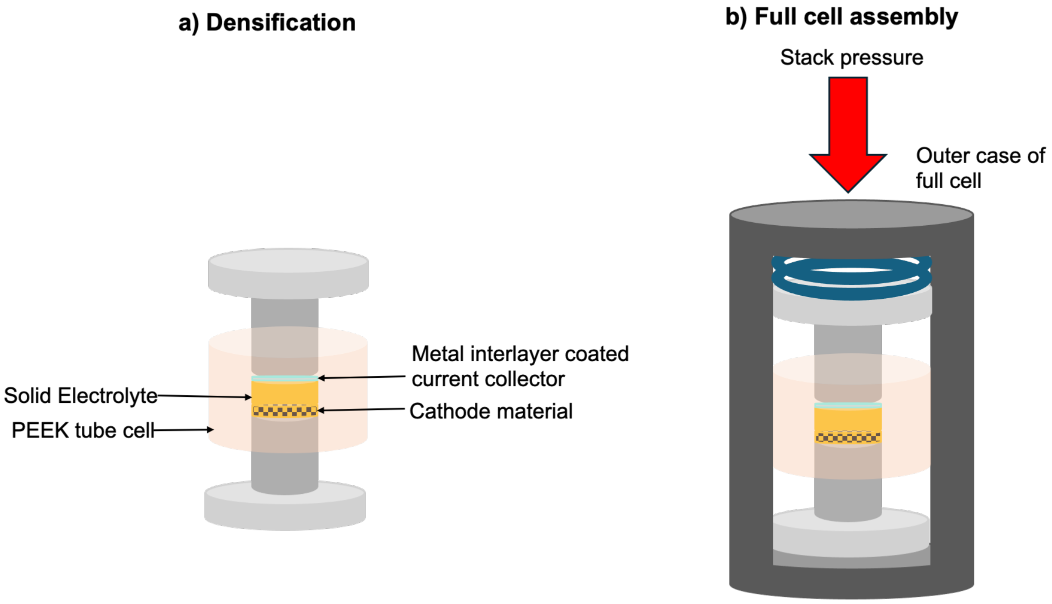

Figure 2.2. Schematic showing a) densification of solid electrolyte with metal interlayer coated current collector and cathode material in a PEEK tube cell, b) shows full assembly with springs on top to maintain pressure. Adapted with permission from ACS Appl Mater Interfaces. 2021 Jul 29;13(31):37809–37815.[234] *Copyright 2021 American Chemical Society under CC license.*

2.2.2 Physical Vapor Deposition (PVD)

Physical vapor deposition (PVD) is a type of vacuum deposition technique which is used to deposit thin films of composites, metals, ceramics, polymers, and glass *via* low pressure gas (or plasma). PVD is used for manufacturing items which require thin films of 1 nm to 10 µm thickness. Sputtering and evaporation are two methods of performing physical vapor deposition. [235,236]

In physical vapor deposition, atoms are transferred from a heated target called the sputter target to a substrate, i.e., the sample of interest, which is kept at a distance from the sputter target. It is a line-of-sight process that means that the substrate needs to be easily in view of the sputter target for direct deposition. The substrate is rotated to provide homogenous coatings as shown in Figure 2.3, film formation and growth happen atomically. Thermal energy is transmitted to the sputter target which evaporates or sublimes the atoms present in that sputter target by raising its temperature.[237–239]

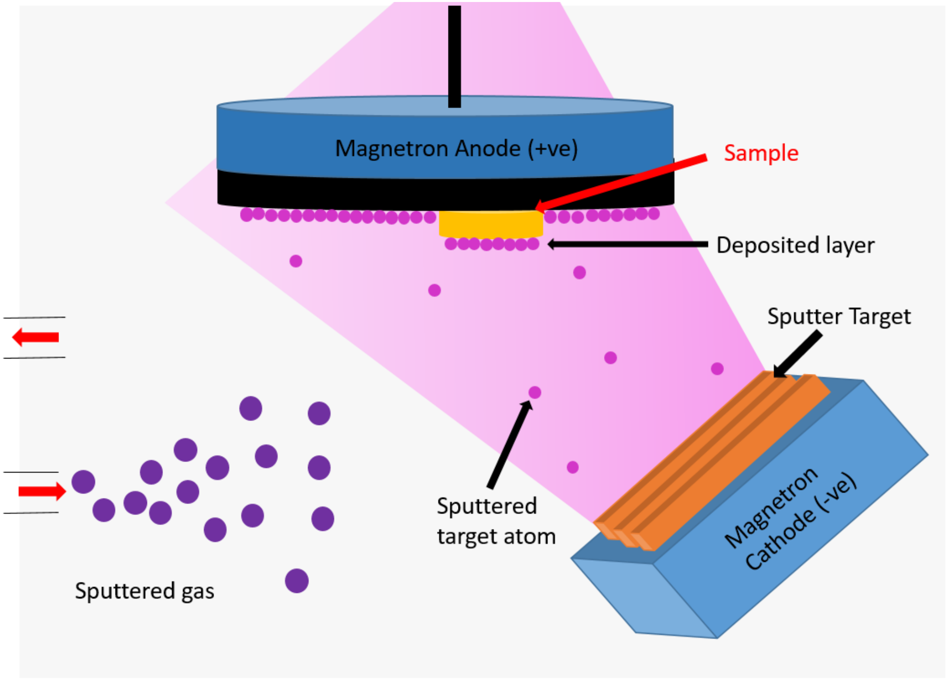

Figure 2.3. Schematic showing the working of the inside of a PVD chamber during sputtering.

Evaporation and sputtering are different processes. In sputtering, a high-energy electrical charge bombards the target, which results in the ejection of atoms or molecules. These ejected particles are then deposited onto a substrate. On the other hand, thermal evaporation involves heating the coating material in a high-vacuum environment until it reaches its melting point. This causes the material to vaporise, forming a stream that rises in the vacuum chamber and eventually condenses onto the substrate.[240]

Chapter 3 of this thesis uses PVD to deposit metal interlayers on the surface of SE and current collector through sputtering of a metal target. The PVD was optimised to obtain a homogenous film of the metal interlayers. It was operated in an argon atmosphere with an 80 Sccm flow rate with 45 seconds ignition time. The flow rate process was 10 Sccm with the valve in middle position for controlled flow of the gas.

2.2.3 Plasma Cleaning

Plasma cleaning is a technique to clean surfaces using low pressure plasma under a controlled vacuum. It removes impurities from the surface of materials by chemical reaction with ionised gases. This process is cost and energy efficient.[241]

In a plasma, the atoms of a gas are excited to higher energy states, where they are ionised. When these ions relax, they release a photon which emits a colour which is characteristic of the gas used. The argon plasma consists of ultra-violet (UV) light which is very effective in breaking down the organic impurities at the surface. The cleaning action is performed by the energetic ions produced from the plasma gas.[242] These species are broken down by the ignited plasma and are continuously pumped away from the chamber through a vacuum pump during the process as shown in Figure 2.4. These plasmas are created using high radiofrequency (RF) values and can be varied through the mixture, where RF 100 corresponds to 200 W power, RF 50 corresponds to 100 W and RF 10 corresponds to 50 W for the plasma cleaner used. High power can increase the temperature of the sample, therefore, if a sample is temperature sensitive it better to use low power.[243]

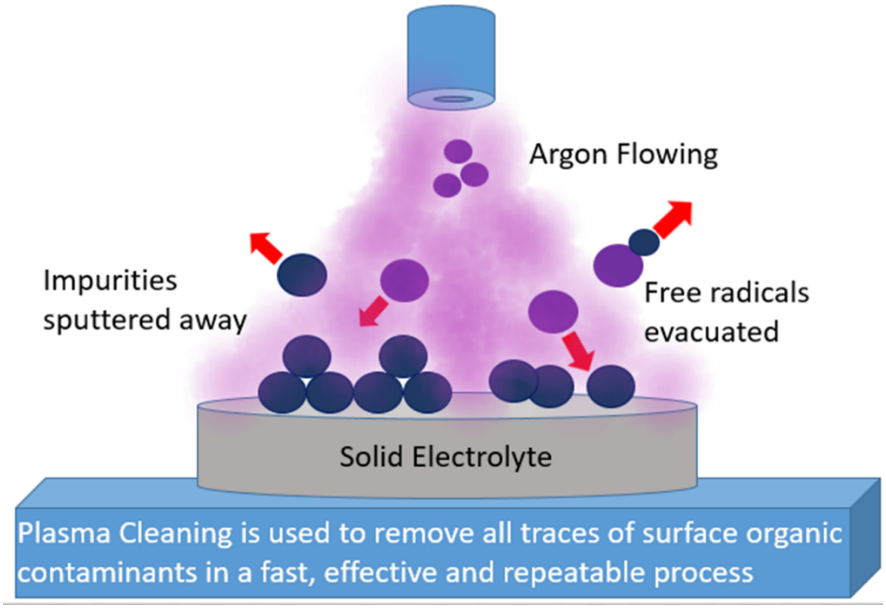

Figure 2.4. Schematic showing the working of plasma cleaner in the presence of argon gas. Visual adaption inspiration from[241,244,245]

The plasma cleaner can work with argon, oxygen, helium, and nitrogen. Mixtures of gases are also used to create plasmas[246]. Every gas has a different plasma colour, oxygen is very light blue, and nitrogen is bright red.[247] If the species to be cleaned consists of easily oxidised materials, then argon or helium plasma is used. The plasma activated ions and atoms act as a molecular sandblast, which can break down the organic contaminants. These contaminants are vaporised and evacuated from the chamber using a vacuum pump during the process, so no fragments remain on the surface, hence providing a clean surface. Any dry sample can be cleaned in a plasma cleaner.[241,242,244,245,248,249]

To check if the cleaning process is complete, contact angle measurement can be used.[183] A contact angle is usually higher for a sample containing impurities. X-ray Photoelectron Spectroscopy (XPS) can be used to measure the cleaning process of plasma cleaner.[181]

The main advantages of plasma cleaning are:

- Processes are easily controlled through power, process gas, pressure, and time.[247]
- It helps to provide an extremely clean surface.

- The gases used have low toxicity.
- The waste generated is in gaseous form. It can be liberated into the atmosphere. It is residual free removal.
- It is fast, effective, and repeatable process.
- It cleans even the smallest cracks and gaps.
- Very low process cost hence cost effective.
- Solvent free, hence can be used for cleaning of air-sensitive solid electrolytes .

In Chapter 5, plasma cleaning is utilised as a surface treatment technique for NBA SE as the model system, where NBA is exposed to air for 24 hour before the treatment. It is optimised for time, process gas and power. The treated samples are then assembled into half-cells.

2.3 Structural Characterisation

2.3.1 X-ray diffraction (XRD)

X-ray diffraction (XRD) is a non-destructive method for conducting structural analyses using X-rays. It determines the crystal structure, crystallinity level, crystallite size, atomic spacing and crystalline phases, along with their transitions and quantitative proportions. Additionally, it provides insights into the microstructure and quantitative analysis of chemical species.[250,251] In this thesis, *operando* XRD and *ex-situ XRD* are used to understand the structural changes occurring with graphite-silver interlayer in Chapter 4.

When a beam of X-ray is passed through a sample, the incident X-rays interact with the atomic planes of the sample and various phenomena occur, including diffraction, transmission, refraction, scattering and absorption according to Bragg's law.[250] Bragg's law states that when an X-ray of wavelength λ, which is comparable to atomic spacing, is reflected by the atoms of a crystalline sample, it goes through a constructive interference, where the incident and reflected waves are separated by the distance d between different layers of atoms.[252,253] Bragg's law can be written as:

$$n\lambda = 2d_{hkl}\sin\Theta$$

where n is an integer, also known as order of reflection, the wavelength of the incident X-ray is given by λ, d_{hkl} is the d-spacing which is the distance between two adjacent parallel (hkl) planes, i.e., Miller planes, and Θ is the incident angle of the X-ray for which a diffraction peak is observed as shown in Figure 2.5.

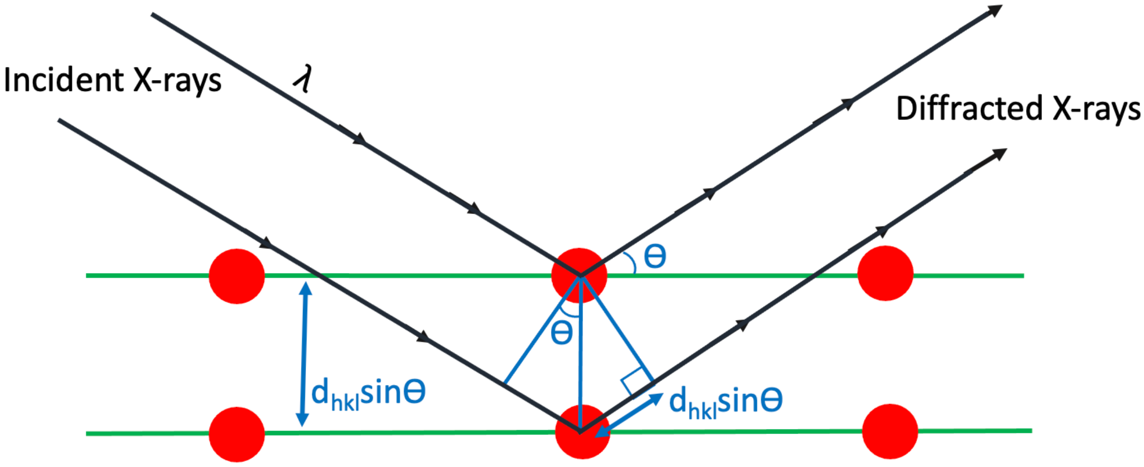

Figure 2.5. Schematic outlining the origin of Bragg's Law.

Visual adaption reference. [230,255–257]

Using Bragg's law and the peak positions, unit cell lattice parameters can be determined, which provide information on the crystal structure of that element. When an X-ray is passed through a disordered small mass of crystals through a filter, some wavelengths are absorbed due to the unique crystal structure and some are reflected, giving a unique diffraction pattern. Moreover, the distance from the center of the film is determined by the spacing between atomic planes in the crystal, with each significant set of planes in the crystal producing a corresponding line.[257] The peaks in the diffraction patterns give the atomic positions. They have different intensities, which depend on the identity and number of the atoms present. Additional details on X-ray diffraction experiments are available in standard textbooks[258,259]. Nowadays, the obtained unique pattern for an element can be matched with the reference database available online on Inorganic Crystal Structure Database (ICSD).

In this thesis, *operando* PXRD measurements were conducted using 3 kW Rigaku Smartlab diffractometer at room temperature, using a custom-built cell discussed in detail in Section 4.3.4 and lithiated graphite powders XRD data was collected using a Rigaku Miniflex diffractometer with low-background silicon sample holder. The data was collected with an X-ray beam of Cu Kα radiation (λ= 1.5418 Å), over a 2ϴ range of 10° to 90°, with a step size of 0.01°.

Refinement of the *operando* PXRD data was not carried out in this study, as the experimental setup was optimised for high time resolution rather than high angular resolution. The resulting patterns contained overlapping peaks from multiple phases and relatively weak Li signals, which made reliable Rietveld analysis impractical. Instead, phase evolution was tracked through qualitative peak shifts and the appearance/disappearance of reflections, which was sufficient to identify the key lithiated silver and graphite phases under operando conditions.

CrystalDiffract software (CrystalMaker Software Ltd) was utilised for analysing the data with guidance from Dr Robert House and Dr Dominic Spencer Jolly, using CIF files sourced from the Inorganic Crystal Structure Database (ICSD) for phase identification and peak assignment. Peak positions (2ϴ values) and relative intensities were matched with the reference ICSD standard references.

2.3.2 Scanning electron microscopy (SEM)

Scanning electron microscopy (SEM) is an important non-destructive characterisation technique to study the morphology of a sample and local elemental composition.[260] In this thesis, SEM is used extensively in all the chapters to study the surface and cross-sectional morphology of the SEs after plating and stripping. Air-sensitive transfer holder was used for all measurements, to avoid any exposure to air and samples were mounted in a glovebox on a Gatan stage using carbon adhesive tape. Top-down and cross-sectional imaging was conducted on Li_6PS_5Cl and NBA samples, with an accelerating voltage of 3-10 kV and a probe current of 200 pA.

SEM focuses a beam of electrons that interact with the sample to generate a topographical image. When the electron beam hits the sample, it produces secondary electrons, backscattered electrons (BSEs), and characteristic X-rays, which are detected by respective detectors and displayed on a computer screen.[261]

To ensure high-quality and accurate imaging, SEM operates within a vacuum chamber. This vacuum environment prevents any pre-existing molecules or atoms inside the microscope column from interacting with the electron beam, which could otherwise distort the resulting image. By eliminating these potential interferences, the vacuum helps maintain the precision and clarity of the images produced.[260]

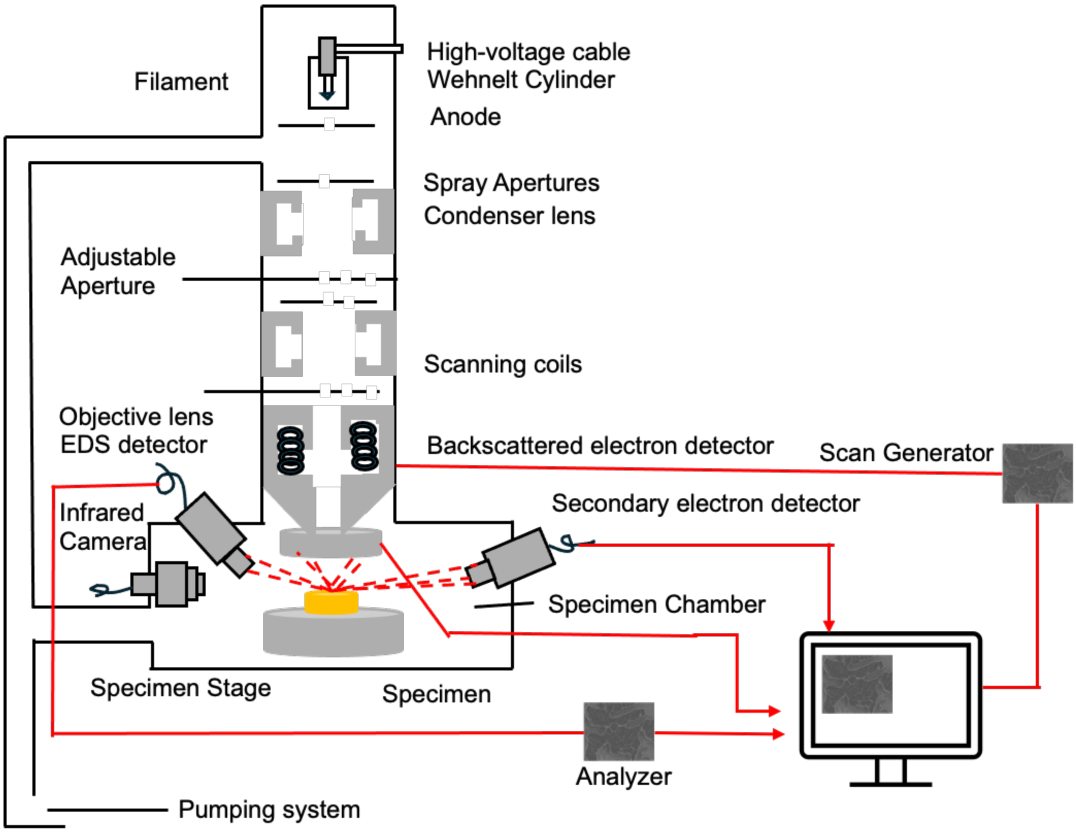

Figure 2.6. Schematic representing the working of scanning electron microscope. Adapted with permission from Ul-Hamid, A. (2023). Correction to: A Beginners' Guide to Scanning Electron Microscopy. Introduction[262]*. Copyright 2018 Springer Nature Switzerland AG.*

As shown in schematic of Figure 2.6, SEM instrument has an electron source at the top. The anode, positioned directly beneath the electron source, is a positively charged metal plate that pulls electrons downward, initiating the formation of the electron beam. The size and number of electrons in the beam are controlled by the condenser lens. Apertures also contribute to beam control, helping to regulate its size. Scanning coils then deflect the beam across the x and y axis, allowing it to scan the entire surface of the sample for accurate imaging. Before reaching the sample, the beam passes through the objective lens, the final lens in the system, which focuses it onto a precise spot on the sample. Once the electrons interact with the sample surface, two types of electrons can be produced to generate the image, back scattered electrons (BSE) and secondary electrons (SE) due to elastic and inelastic collisions, which are then detected by the detectors.[260,261]

To study the surface morphology, secondary electrons are more useful than BSE, as finer details of the surface can be captured. The incident secondary electrons are low energy, detection is only achieved for few nanometers of depth. Only the electrons that are reflected back to the detector, produces the image i.e., if there is an obstruction on the surface of sample, it will produce dark contrast on the image.[261] As this thesis studies the morphology, this type of detector is used to capture the images.

As shown in Figure 2.7, BSE come from deeper surface of the sample, so BSE detector is useful to study the compositional composition of a sample.[260] Moreover, sometimes these electrons gets trapped in the sample, giving rise to distorted images.[263] To mitigate this, low current of 200 pA and 10kV voltage is used.

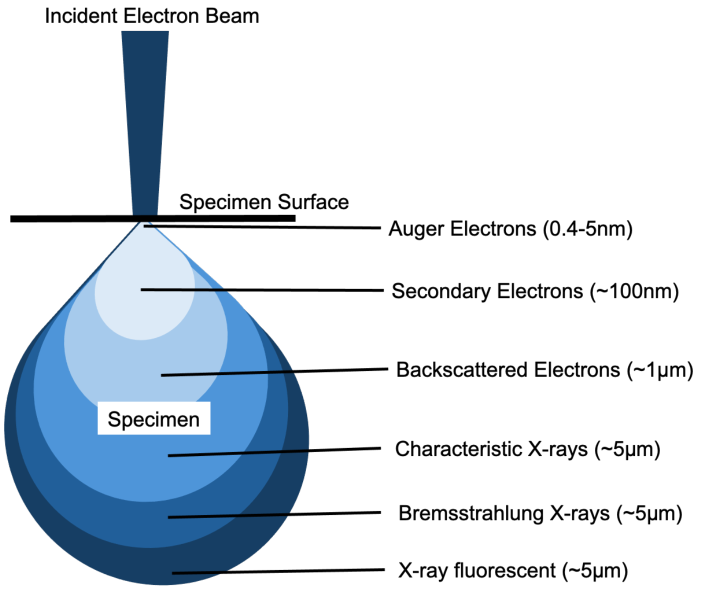

Figure 2.7. Schematic outlining the origin of secondary and backscattered electrons. Adapted with permission from Ul-Hamid, A. (2023). Contrast Formation in the SEM. In: A Beginners' Guide to Scanning Electron Microscopy. Springer, Cham.[263] *2018 Springer Nature Switzerland AG.*

SEM is an easy-to-use electron microscope, giving detailed information about the morphology of the sample. However, for cross-sectional imaging, it was difficult to prepare the sample, without disturbing the morphology. Hence plasma focused ion beam (PFIB) combined with EDX is employed in Chapter 3 and 4, to obtain morphological and chemical information after charging and discharging of metal interlayers.

2.3.3 Focused Ion Beam (FIB)

A FIB uses a focused beam of ions to mill a sample and combines the imaging technique of SEM to study buried interfaces. Since, Chapter 3 of this thesis studies the morphology after charging and discharging a Li-free ASSB with a sulphide SE, a technique to mill the interface, without disturbing it is desired. The sample is transferred to the Gatan stage holder with carbon adhesive tape in a glovebox to the FIB chamber, where Xe^+ as plasma source is used for PFIB to mill through the current collector and solid electrolyte to view the interface between the interlayer and the sulphide solid electrolyte.

As discussed by Yao[264], a direct stream of ionised atoms, usually Ga^+ are focussed on a position to mill the area. Due to higher mass of these ions, secondary electrons are expelled out of the surface, which are detected by the detector, using the same principle discussed in Section 2.3.2, to give an image on the computer screen. However, this can damage the sample, so to avoid it, FIB is usually employed with a SEM microscope, where the focussed beam of ions is used to mill the surface and the electrons from the SEM are used for non-destructive high resolution imaging as shown in Figure 2.8. Focussing on finer details. In this thesis, this technique is also combined with EDX, to obtain information on elemental composition. [264]

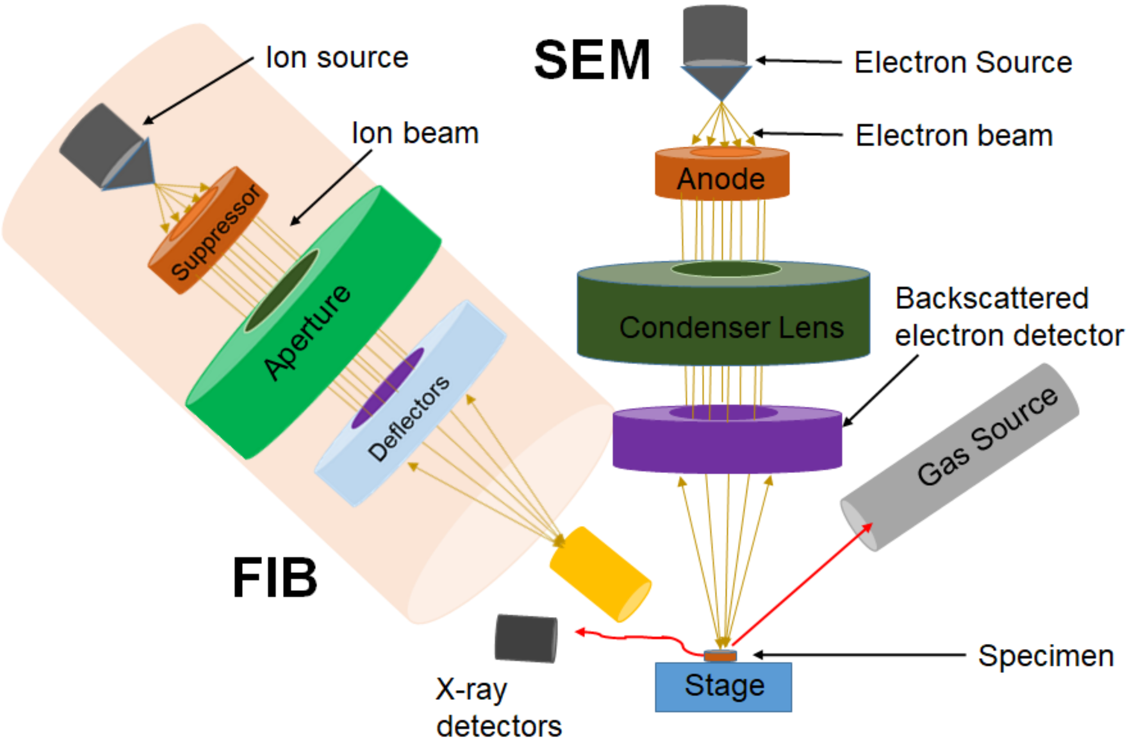

Figure 2.8. Schematic of PFIB-SEM setup. Visual adaption from[229,265–270].

Despite these advantages, sometimes due to ions being heavier in mass, the milling process is slow and time consuming. Moreover, ions collision can result in surface damage and redeposition.[271]

Due to the low melting point of lithium metal (180.5°C), it is prone to melting and Ga^+ ion implantation, resulting in chemical and morphological damage at room temperature. Inductively coupled plasmas, generated using gases such as nitrogen, oxygen, xenon, or argon can be used as an alternative option.[272] As during high beam currents, plasma generated through these gases are less prone to diverge in different directions, leading to less damage[273].[274] In thesis, Helios G4 PFIB CXe Dual Beam instrument (Thermo Scientific)[275], using Xe^+ as plasma source is used for PFIB. The instrument was operated by Dr Dominic Spencer Jolly.

2.4 Chemical characterisation

2.4.1 Energy dispersive X-ray (EDX)

EDX is a non-destructive surface analysis technique for the elemental analysis of a sample.[261] It helps to provide information on the chemical composition of the sample. It also identifies the concentration and distribution of elements.[276] It is commonly used in conjunction with some imaging characterisation technique. Here, it is used in combination with SEM and PFIB to analyse the material composition.

It works on the principle of Moseley's law i.e., X-rays are capable of ejecting the core (electrons not in the outermost shells) electrons from the atom, suggesting that there is a direct correlation between frequency of light and the atomic number of the atom.[277,278] When a ray of electrons is bombarded on a sample, the atoms from the inner shell of the orbitals are excited and ejected. This creates a vacancy in the orbital, which is then filled by an electron from outer shell, releasing energy in the form of photons as shown in Figure 2.9a, giving a characteristic wavelength as shown in Figure 2.9b, where the letters K, L, M etc refers to the orbitals of the atom[279]. This emitted wavelength is then detected by the detector, to help identify the element present by analysing the signal and is interpreted with the help of the software.[276] All elements have a characteristic wavelength, which acts like a fingerprint.[280]

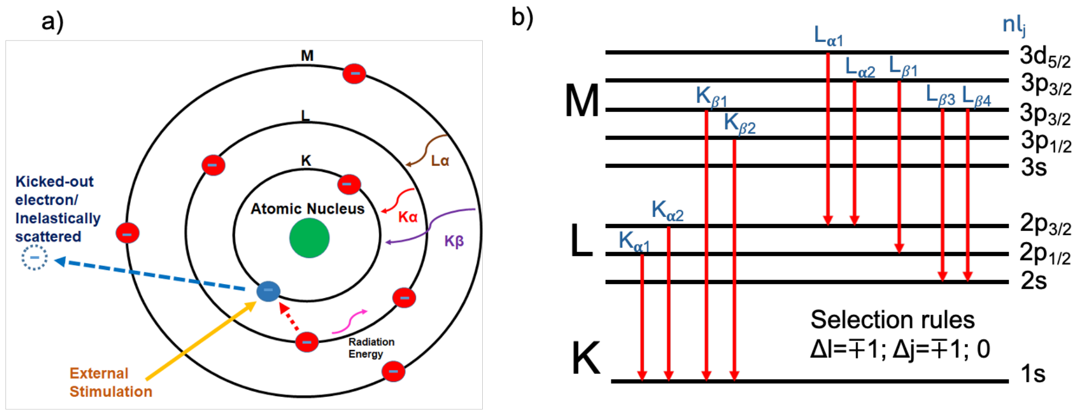

Figure 2.9. Schematic showing a) electrons being ejected from the core shells, creating a vacancy; figure adapted from[277]*, under the Creative Commons Attribution Share Alike 3.0 License; b) diagram depicting the energy transition happening at various orbitals, giving characteristics wavelength. Adapted from* [281].

The obtained chemical information can be represented through various techniques, such as elemental mapping and line scans, enabling visualisation of the elements within a sample. This approach allows X-rays to pinpoint and identify each element present.[276] Figure 2.10 shows different ways in which EDX data is obtained. Figure 2.10a is an electron image after charging a Li-free cell with zinc interlayer. Figure 2.10b shows X-ray map in a full frame of the sample, where the map shows spatial distribution of all elements in the sample as different colors, which helps to identify the elemental position in the map. Individual elemental maps of the elements such as teal for zinc, red for carbon and green for oxygen is displayed on the right. The colors can be changed according to the user in Aztec software. Moreover, Figure 2.10c shows X-ray spectrum for quantative data analysed through EDX detector, showing weight % of identified individual elements in the sample. Here, the data obtained through EDX is analysed by Aztec Software.

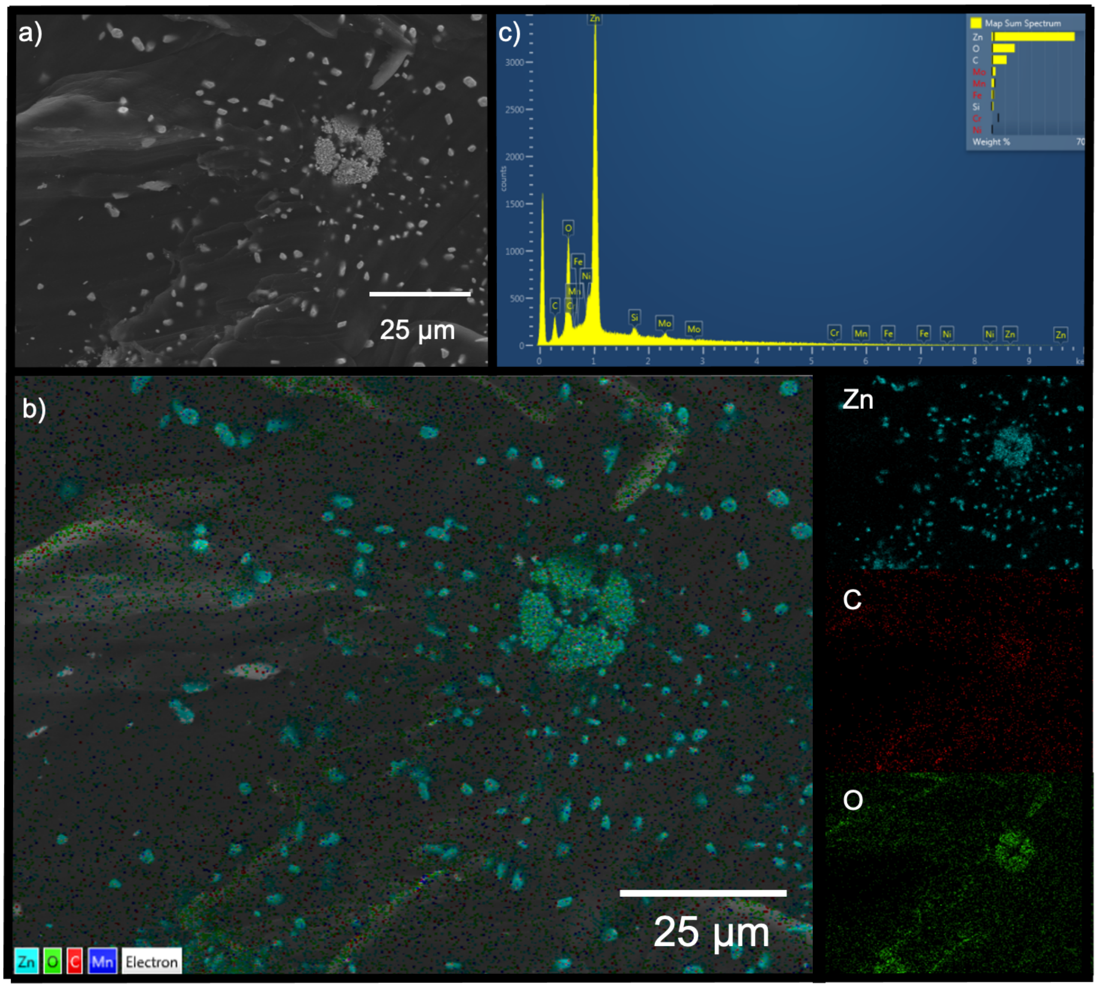

Figure 2.10. Data showing how EDX data is shown in Aztec software; a)electron image of the sample; b) elemental X-ray map of the sample with individual element map displayed on the right as Zn, C and O, where Zn refers to Zinc, C refers to carbon and O refers to Oxygen ; c) X-ray spectrum map for the sample.

2.4.2 X-ray Photoelectron Spectroscopy (XPS)

X-ray photoelectron spectroscopy (XPS) also known as electron spectroscopy for chemical analysis (ESCA), is an analytical, quantitative, non-destructive surface sensitive technique, which works on the principle of the photoelectric effect.[282] It can identify the chemical composition and electronic configuration of an element that exists on the surface of a material from organic to inorganic materials up to ~10 nm. Using the photoelectric effect principle, this technique studies the bonding environments of different chemical species.[283,284] All elements are detected by XPS except helium and hydrogen.[285]

When electromagnetic radiation of a known wavelength irradiates a sample, electrons are emitted from the atom and the kinetic energy (KE) of the emitted electron is measured. The photoelectron emitted is due to complete transfer of the X-ray energy to a core level electron.[286] The binding energy (BE), i.e., how tightly the electron is bound in the orbital, is calculated using the formula:

$$BE = hv\text{-}KE\text{-}\Phi_{spec}$$

Where BE is the binding energy, KE is the kinetic energy of the electron that is emitted, h is Planck's constant, v is frequency and Φ_{spec} is spectrometer work function, which is a constant value to a particular XPS. The reason Φ_{spec} is included is because BE is measured with respect to the sample fermi level. BE does not depend on the type of X-ray used, hence it won't vary according to different X-ray sources.[286]

An XPS instrument has a sample stage, analyser, X-ray source, and extraction lenses all placed in ultra-high vacuum (UHV). Figure 2.11 shows a schematic for all the main components of an XPS. There are two reasons why the XPS is placed in ultra-high vacuum. Firstly, while the emitted electrons travel to analyser, they should not be scattered off by air molecules and for this 10^{-5}-10^{-6} mbar pressure is required. Secondly, XPS is sensitive to every surface contaminant, and at atmospheric pressure every molecule which strikes the surface of the sample will stick to the surface, hence UHV reduces the surface contamination that occurs within the chamber.[286] The X-ray source is usually a heated tungsten or lanthanum hexaboride (LaB_6) filament that provides the electrons which are accelerated at high voltage anode.[286]

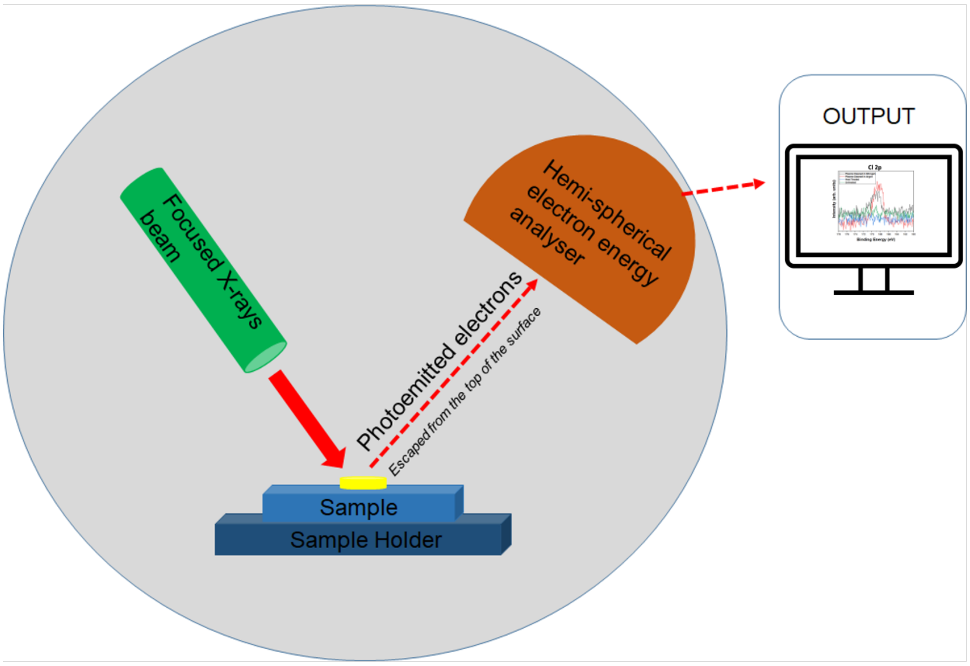

Figure 2.11. Schematic representing the working of X-ray photoelectron spectroscopy. Visual inspiration from copyright 2023 Wiley-VCH GmbH.[287]

XPS is a surface sensitive technique and not a bulk technique, it can only measure up to ~10 nm below the surface, so care must be taken while interpreting XPS results, as the surface maybe contaminated and hence not representative of the bulk. XPS unavoidably detects adventitious carbon almost every time. To avoid this problem, an ion beam is used in conjunction with XPS for depth profile analysis, which is useful for interfacial investigation in batteries.[286] In Chapter 3 of this thesis, XPS is used to analyse the interface formation in lithiated metal nanoparticles with a sulphide ceramic solid electrolyte using depth profiling. In Chapter 5 of this thesis, XPS is used for NBA solid electrolyte to understand the role of plasma cleaning technique to remove surface contaminants.

2.5 Electrochemical Testing

2.5.1 Electrochemical Impedance Spectroscopy (EIS)

Electrochemical impedance spectroscopy (EIS), is a powerful, non-destructive technique to measure the electrochemical properties of both bulk materials and the electrode/electrolyte interfaces in a SSB across a wide frequency range. It allows to isolate the bulk and interfacial contributions, making it an effective characterisation technique to investigate ionic conductivity and SEI formation over time in SE.[288] This technique is used extensively in Chapter 5 to understand the role of different surface treatments in decreasing the interfacial resistance due to surface impurities using non-blocking electrodes, symmetric NBA half-cells are assembled after exposing them to air and then treating with heat and plasma cleaner. The assembled half-cells are connected to Gamry 1010E potentiostat to conduct PEIS, where 10 points per decade were collected from 1 MHz to 1 Hz frequency range, using a 5 mV pertubation at 30°C.

In the case of an ideal resistor, the voltage of an electric circuit is directly proportional to the current, as given by Ohm's Law:

$$(V=IR)$$

However, in a setting with alternating current (AC) and a changing voltage, this relationship is more complex as the resistance might depend on the frequency and is potentially influenced by phase difference between the voltage and current. Therefore, the concept of "impedance" is introduced. Like the resistance, it describes the ability of a circuit to resist the flow of electrical current but takes into account the combined effects of resistance, inductance, and capacitance.[289]

To measure electrochemical impedance, an AC potential is applied to the system over a wide frequency range. This makes the charged species undergo dielectric polarisation, which gives a response when they are displaced from their equilibrium position to give an AC current signal response $I(t)$, assuming it to be a sinusoidal potential excitation. In a pseudo-linear or linear system, the AC current signal response can have different phase and amplitude but the same frequency.[289] The response varies according to the impedance elements such as the charge transfer resistance at interfaces, ion conduction in grain boundaries, bulk materials, surface films etc, which makes EIS as an appropriate technique to measure a system like battery with multiple interfaces. The current and voltage response can be described by[290]:

$$E_t = E_0 \, sin(\omega t)$$

$$I_t = I_0 \, sin(\omega t + \varphi)$$

where E_t denotes the voltage at time t, I_t denotes the current response at time t, φ is the phase shift and ω=2πf is the radians frequency of current and voltage expressed in radians/second (f denotes the frequency expressed in Hertz).[289]

The impedance Z of the system can be calculated, with an expression similar to Ohm's Law[289,291]:

$$Z = \frac{E_t}{I_t}$$

$$Z = \frac{E_0 \, sin(\omega t)}{I_0 \, sin(\omega t + \varphi)} = \frac{Z_0 \, sin(\omega t)}{sin(\omega t + \varphi)}$$

Using the Euler relationship, we can express the impedance as a complex function[289]:

$$e^{i\varphi} = \cos\varphi + i\sin\varphi$$

$$Z(\omega) = \frac{E}{I} = Z_0 e^{i\varphi} = Z_0(\cos\varphi + i\sin\varphi)$$

The impedance Z of the electrochemical cell can be represented using Nyquist plot as shown in Figure 2.12 in which the x-axis shows the real part $\cos\varphi$ and the y-axis shows the negative imaginary part $\sin\varphi$. This implies that for any value of Z, its magnitude |Z| is given by the distance to the origin and the phase φ is given by the angle to the x-axis.

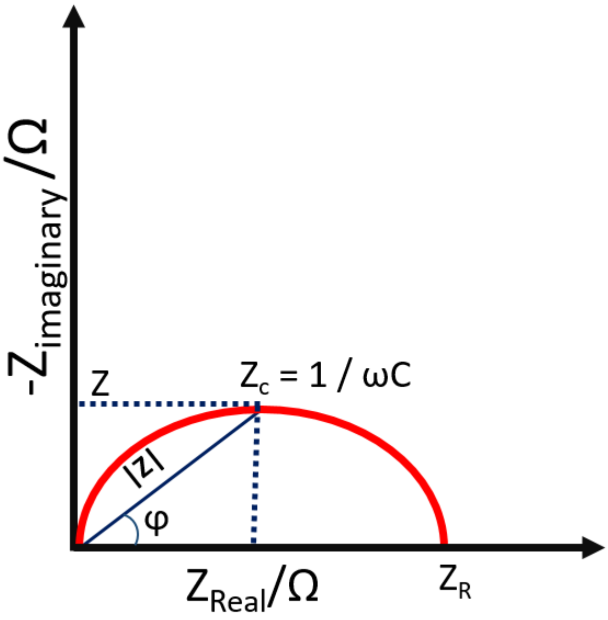

Figure 2.12. A representation of the Z in complex form shown by Nyquist plot.[289,292]

The impedance in SSB research is usually illustrated by the Nyquist plot as shown in Figure 2.12. However, Nyquist plots do not indicate the frequency associated with collecting the data.[289] A single semicircle on an electrochemical impedance plot typically represents one "time constant." However, these plots often display multiple semicircles, and in many cases, only a partial semicircle may be visible.[289] The obtained EIS data is usually fitted through an equivalent electric model, where the elements should have a physical basis in the system as described by Irvine et al.[293]

The obtained impedance spectra are strongly affected by the structural features of the electrochemical cell. Key factors such as the type of electrode, its configuration, and geometry all play a significant role in shaping these results.[15,288] In this study, 1-10 mV of AC frequency response is applied to obtained a pseudo-linear system. The measured impedance data were plotted, and equivalent Randles circuit models were constructed using ZView software (Scribner Associates Inc.).

2.5.2 Galvanostatic Cycling

Galvanostatic battery cycling, is an electrochemical cycling technique to measure the cell potential (V) while constant current (I) is applied, for a given time to assess the cycling performance of a battery. A programme with pre-defined upper and lower voltage cut offs, current and specific capacity is written by the user according to the experimental needs.

Specific capacity of the cell can be determined, as for a given time, constant current is passed, which when normalised to the active mass of the active material (m) of the electrode, gives the specific capacity (q)

$$q = \frac{I \cdot \Delta t}{m}$$

Data is represented as voltage *vs* capacity plot, as shown in Figure 2.13, where x-axis shows the capacity and y-axis shows the voltage of a Li-free all-solid-state cell full cell, assembled in the PEEK cell described in Section 2.2.1. The green lines shows good cycling performance, while the red shows cell failure, which is determined through the continuous voltage fluctuations in the dataset.

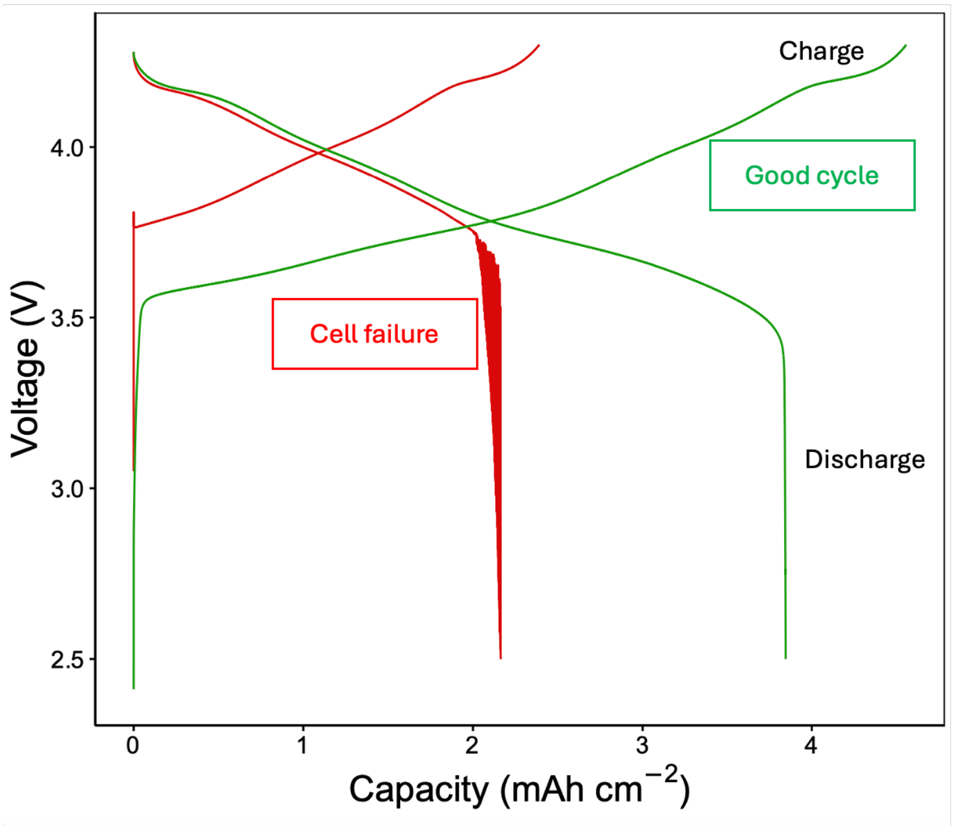

Figure 2.13. Graph representing voltage vs capacity for a Li-free all-solid-state battery, where green shows good cycling performance and red shows cell failure at certain point.

EIS is used in addition to galvanostatic cycling, after each charge and discharge, to determine the interfacial changes and to better understand the underlying processes by quantifying the cell degradation. To ensure EIS is measured accurately, open circuit voltage (OCV) is applied with a cell relaxation time of a few minutes before each EIS measurement.

In Chapters 3 and 4, half-cell and full cell setup has been extensively used to understand the CE and cycling performance. Differences in CE of different metal interlayers have also been studied using galvanostatic cycling, for comparison with symmetric Li/SE/Li and a Li-free battery. Biologic EC software is used to analyse the obtained data.

3 Chapter 3: Silver metal anode interlayers for Li-free all-solid-state batteries.

3.1 Overview

As discussed in Section 1.3, Li-free all-solid-state batteries also known as “anodeless” batteries, have several advantages but also suffer from low CE and cycle performance. This has been attributed to several factors such as inhomogeneous deposition of Li metal, undesirable SEI growth and mechanical stress, which leads to current constriction and dendrite growth. To overcome the challenges associated with Li-free ASSBs, metal interlayers offer a potential solution to achieve homogenous deposition of Li metal. This chapter investigates the cycling performance of a silver metal interlayer in a Li-free all-solid-state battery with a sulphide SE, which is studied using galvanostatic cycling, SEM-EDX, PFIB-SEM-EDX and XPS, to understand the role of the metal interlayer on charging and discharging. Moreover, the interfacial reactivity of the silver metal interlayer with a sulphide solid electrolyte is investigated thoroughly to understand its effect on coulombic efficiencies.

3.2 Introduction

All-solid-state batteries (ASSBs) have the potential to be a safer and more efficient alternative to traditional liquid electrolyte batteries.[208] They show a great promise as a next-generation energy storage technology capable of delivering higher energy density than traditional Li-ion batteries, because SSBs can support the use of Li metal anodes.[209,214,294,295]

However, their successful implementation faces significant challenges. The primary issue is the irreversible loss of active lithium and low coulombic efficiency (CE). Low CE is exacerbated by the inhomogeneous nucleation and growth of lithium. This irregular deposition increases the surface area and intensifies side reactions. Additionally, lithium can form dendrites or whiskers at high current densities, which risk perforating the solid electrolyte (SE) and causing short circuits.[294]

One approach to improve the performance of Li-free solid-state batteries is to use metal interlayers to enhance the interfacial properties between the electrodes and the solid electrolyte as discussed in Section 1.3.3. Specifically, it has been shown that metallic interlayers capable of alloying with lithium are highly effective.[1,213,214,227,296–300] They allow to enhance the wettability between the solid electrolyte and lithium, as well as lattice-lithium diffusion within the alloying matrix. This results in a more uniform distribution of Li-ion flux, even during high-rate stripping processes.[83,85,226] An ideal interlayer should possess these three key properties:

(1) establish close contact with both the SE and the Li metal,
(2) serve as a buffer layer to manage Li redistribution and reduce current inhomogeneity at the interface, and
(3) maintain its physical and chemical stability over extended cycling periods to guide Li deposition.[296]

A study by Lewis et al.[213], indicates that internal short circuits in batteries can be attributed to localised electrodeposition, which results from the non-uniform nature of the interface. Moreover, another study conducted by Sandoval et al.[296] from the same research group, investigates 100 nm thick Ag and Au interlayers in anode-free cells with a Li_6PS_5Cl solid electrolyte. The result suggests that alloy interlayers enhance Li nucleation density, promoting uniform Li growth and homogenous current flow, thereby improving CE. Additionally, plasma-focused ion beam (PFIB) analysis demonstrated that Ag and Au interlayers facilitate uniform Li metal alloy deposition during plating, stabilising the interface by mitigating uneven current distribution. Despite these advantages, limited cycle performance was observed, with Ag achieving approximately 30 cycles and Au around 15 cycles (average across four cells). The degradation mechanism was attributed to the formation of isolated agglomerated Li metal alloy islands during stripping, leading to contact loss and void formation, which may contribute to performance deterioration over extended cycling. Unknown to us, the above study was conducted concurrently to the investigation presented in this thesis and reached similar results.

As discussed in Section 1.2.3.2 of the introduction, not all interphases are equally resistive, and some interphase formation can even help Li^+ transport. As discussed by Wenzel et al.[64], Li metal and Li_6PS_5Cl form an unstable but self-passivating interphase. The SEI is formed, self-passivates, and does not continue to grow due to its negligible electronic conductivity.[180] Although an SEI is formed, the ionic conductivity of the SEI is not prohibitively poor, primarily because it is very thin.[15,61,180,301] Therefore, having a clear understanding of the interfacial reactions is crucial because it provides valuable insight into the interphase products and their impact on the stability and conductivity of a solid-state battery.[302,303]

The occurrence of side reactions at the interface of the Li metal and solid electrolyte in solid-state batteries not only leads to an increase in interfacial resistance which restricts the movement of Li-ions, but also causes consumption of the active Li metal. In a Li-free cell this is a problem as there in no excess of Li metal and therefore the Li lost to SEI formation leads to a degradation in cell capacity.

In this chapter, a silver metal interlayer with Li_6PS_5Cl in Li-free ASSB is investigated. Other metals such as aluminium and zinc were also investigated and discussed in

Appendix Figure A.1. For the simplicity, only silver was investigated in-depth and discussed here. These findings offer valuable new insights into the mechanics of Li-free interfacial layers, which should prove highly informative for the development of Li-free solid-state battery engineering.

3.3 Experimental Methods

This study uses metal interlayers deposited through Physical Vapor Deposition (PVD) on Li_6PS_5Cl disks and stainless-steel current collectors.

3.3.1 Preparation of Li_6PS_5Cl disks

Li_6PS_5Cl powder with an approximate particle size of 1-10 μm was procured from Ampcera with >99.9 purity. 30 mg of the powder was weighed and added to the 5 mm die-set from Specac. Uniaxial pressure of 400 MPa was applied in a press for 1 min, which yielded a 5 mm diameter Li_6PS_5Cl disk/pellet, showing an ionic conductivity of 0.2 mS cm^{-1}.[1,184] This is a standard lab protocol[147,263] to prepare these solid electrolyte pellets.

3.3.2 Preparation of metal interlayers on sulphide solid electrolyte for half-cell experiments

200 nm thick metal interlayers were sputtered onto prepared 5 mm diameter Li_6PS_5Cl disks using PVD in an argon atmosphere glovebox, where 10 Sccm gas (argon) flow is used as shown schematically in Figure 3.1. The area of the deposited metal layer was controlled by masking the surface of the Li_6PS_5Cl electrolyte with a polymer mask. The layer thickness during the sputtering deposition by PVD was carefully controlled by a crystal sensor.[c] Moreover, the experimental conditions were kept the same for all the respective sputtering.

---

[c] Trained on PVD instrument by Dr Stephen Turrell and Marco Siniscalchi.

The thickness and uniformity of the deposited metal interlayers was further checked by cross-sectional and top-down imaging using SEM.

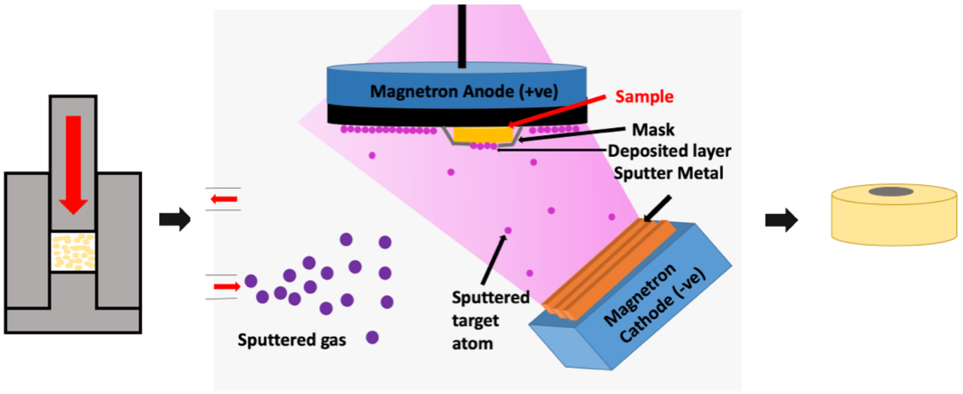

Uniaxial pressing of a Li_6PS_5Cl to form a disk

The prepared disk or stainless-steel current collector is mounted in a prepared mask and then mounted within the PVD chamber and sputter with silver metal

Li_6PS_5Cl/Ag thin-film disk for testing

Figure 3.1. Schematic of the sputtering of metal interlayer on sulphide solid electrolyte pellets using Physical Vapor Deposition.

3.3.2.1 Asymmetric half-cell construction

Two electrode cells were assembled by fixing a 5 mm diameter Li foil counter electrode, approximately 50 µm thick, to the opposite face of the Li_6PS_5Cl to the metal layer. The cells were then assembled into pouch cells with stainless steel current collectors and were sealed under a vacuum as shown in Figure 3.2. The cells were allowed to rest for a day and then removed from the glovebox for testing. This is a standard lab protocol[184,304] to prepare pouch cells. The pouch cells were immersed in oil bath at 60°C for 2 hours before taking any measurement to equilibrate the temperature.

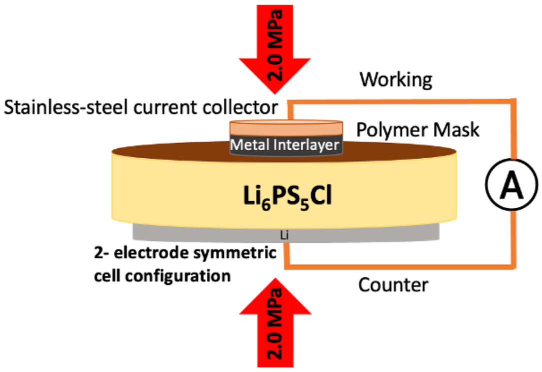

Figure 3.2. Schematic of an asymmetric two electrode half-cell using sulphide solid electrolyte with metal interlayer sputtered using PVD. Visual adaption from[229]*.*

3.3.3 Preparation of full cells

A 200 nm layer of metal was sputtered onto a sheet of stainless-steel current collector using PVD. The sputtering conditions used were the same as those described above for silver deposition onto the Li_6PS_5Cl electrolyte. As previously, the layer thickness and uniformity were checked using SEM/EDX. These coated stainless-steel current collectors were then punched into 4.5 mm discs using a puncher to have a uniform area. The morphology of the punched disks was not affected by punching.

To prepare full cells[d] as shown in Figure 2.2, all chemicals were dried under vacuum and stored in an Ar-filled glovebox (O_2 and H_2O levels < 0.1 ppm). For the solid-state composite cathode, single crystal $LiNi_{0.83}Mn_{0.06}Co_{0.11}O_2$ (MSE Supplies), ultra-fine Li_6PS_5Cl (MSE Supplies) and carbon nanofiber (CNF) (Merck) with a mass ratio of 70:28:2 was mixed using a pestle and mortar.

Solid-state cells were assembled in a custom-designed module with a PEEK mould and stainless-steel plungers as shown in Figure 2.2 in Chapter 2.[234] The inner diameter is 5 mm. A composite cathode mixture (corresponding to an areal capacity of ~ 4 mAh cm^{-2}), 30 mg

---

[d] Trained by Dr Hui Gao to assemble full cells, according to standard lab protocols.

of Li_6PS_5Cl and metal coated current collectors as anode were pressed at 400 MPa for 1 min. An external uniaxial stack pressure of 2 MPa was applied when cycling the solid-state cells. All work was carried out in an Ar-filled glovebox with O_2 and H_2O level below 0.1 ppm.

3.3.4 Structural and electro-chemical characterisation

The experimental conditions used were standard lab protocols in the research group and are described below, to keep the data comparable with other studies in the research group.[1,104,229]

3.3.4.1 Half-cell and full-cell testing

After the cells were prepared, Biologic VMP-3 potentiostat was used for Galvanostatic cycling with 2 MPa stack pressure, using sprung clips and 60°C temperature. More details about the technique can be found in Section 2.5.2.

3.3.4.2 SEM/EDX

The samples for morphology characterisation were disassembled in an argon filled glovebox and were mounted on Gatan stage using carbon adhesive tape. It was then transferred to the air-sensitive transfer holder for SEM analysis. A Merlin SEM (Zeiss) instrument equipped with secondary electron detector was used to analyse the morphology and deposition of Li on pristine and cycled cells using top-down imaging, with an accelerating voltage of 3-10 kV and a probe current of 200 pA. SEM was used in conjunction with energy dispersive X-ray spectroscopy (EDS), equipped with an X-Max 150 Silicon drift detector (Oxford Instruments) within the Zeiss Merlin instrument. Aztec software was used for data analysis.

3.3.4.3 PFIB

The FIB-SEM image collection was carried out in collaboration with Dr Dominic Spencer Jolly, using a Helios G4 PFIB CXe Dual Beam instrument (Thermo Scientific)[275]. The instrument was operated by him, sample preparation and analysis of data was conducted by me. Samples were transferred into the instrument from an argon filled glovebox using a Gatan iLoad transfer holder to avoid exposure to air. FIB was carried out in two steps; 1) a trench was milled in the sample using a Xe^+ beam with a 10 kV accelerating voltage and a 0.2 mA current for fast removal of material, and then 2) the cross-section of the trench was cleaned for imaging and characterisation using a lower beam current of 15 nA.[e]

3.3.4.4 XPS

X-ray photoemission spectroscopy (XPS) was used to analyse the interfacial chemical reactivity occurring at the surface of the solid electrolyte. These data were collected in collaboration with Dr Dominic Spencer Jolly, where the instrument was operated by him, sample preparation and analysis of data was conducted by me. A PHI Versaprobe III was used under ultrahigh vacuum conditions, with the main chamber maintained at pressures between ~10^{-7}-10^{-6} Pa. Focused, monochromatic Al Kα X-rays at 1486.6 eV were generated at a power of 25 W and an electron beam voltage of 15 kV. To avoid contamination and ambient exposure, samples were transferred from an argon filled glovebox into the XPS chamber using a custom vacuum transfer vessel. All measurements were conducted on three different spots for each sample to ensure measurements were representative, and depth profiling was performed by argon sputtering to probe the buried interphase. Charge compensation using argon ion gun and low charging electron was utilised to prevent sample charging. The acquired spectra were fitted using CasaXPS software, using a Shirley

---

[e] These parameters were used to minimise beam damage and were selected by Dr Dominic Spencer Jolly.

background and Lorentzian Asymmetric Lineshape (50). More details on parameters and constraints used can be found in Appendix Table A.1. In this study, all spectra were calibrated to adventitious carbon at 284.8 eV using the acquired carbon C 1s spectra.[62]

XPS was used to analyse the interfacial chemical reactivity occurring at the sulphide solid electrolyte/metal interface. To the best of our knowledge, at the time of this work, no study has investigated the role of chemical reactivity and SEI formation for these metal interlayers against a sulphide solid electrolyte in a Li-free ASSB.

3.4 Results and Discussion

Silver was selected as the model metal interlayers for this study to understand role of different parameters as discussed in Table 2[228] and was investigated in depth, as it shows a high solubility in Li, 0 mV nucleation overpotential barrier[228] and a high diffusion coefficient.[305,1,84,85,214,306] The Li diffusion coefficient values reported in Table 2, have broad range of values due to irregularities in studies conducted. This study aims to understand the relationship between these parameters.

Metal	**Capacity (mAh/g)**[84]	**% volumetric expansion upon lithiation**[84]	**Nucleation overpotential (mV)**[228]	**Li diffusion coefficient (cm^2/s)**[299]
Graphite	350	10	-	6.5×10^{-11} (307)
Aluminium	1411	90	5	10^{-9}–10^{-11} (308,309)
Silver	670	236	0	10^{-6}–10^{-10} (305)
Zinc	1476	98	0	10^{-8}–10^{-10}

Table 2. Different parameters for graphite, aluminium, silver and zinc metal.

Previous studies have shown that silver metal interlayers promote high cycling performance for Li-excess metal based SSBs using oxide solid electrolytes.[1,214,310–312]

However, this study investigates the role of a silver metal interlayer in a Li-free setup with a sulphide solid electrolyte during charge and discharge. Additionally, it studies the interfacial reactivity of the sulphide solid electrolyte with a lithiated metal to understand the sources of Li loss in a Li-free cell with a silver metal interlayer.

3.4.1 Full cell performance

Full cells were prepared to assess the performance, stability, capacity, and compatibility of Li-free cells with and without metal interlayers. They provide valuable data for understanding battery behaviour and addressing the challenges associated with Li-free ASSBs. Li-free full cells with and without metal interlayers were prepared as discussed in Section 3.3.3. Cells were charged at 0.05 mA cm^{-2}, at 60°C at 2 MPa to a 4.3 V cut-off voltage, followed by discharge at 0.05 mA cm^{-2} to a voltage of 2.4 V. This cycling was repeated for cells with and without the metal interlayer present until failure of the cell was observed to evaluate the performance. Figure 3.3a shows the number of cycles for Li-free and silver metal interlayer cells before cell failure. It can be observed from Figure 3.3a, that Li-free cells consistently showed failure after a low number of cycles of approximately 1 cycle, with range of values shown in purple. In presence of a silver metal interlayer, the cell can be cycled up to 97 times without failure as shown in Figure 3.3a, with the range of values shown in teal. A similar work for aluminium (Al) and zinc (Zn) is also provided in the Appendix Figure A.1.

Figure 3.3b shows the standard capacity *vs* cycle number plot for the best performing silver cell. As can be observed from Figure 3.3b, the capacity decreases drastically over several cycles for the cell. This can be due to several factors such as SEI formation, dead lithium etc and is discussed in detail in Section 3.4.4.

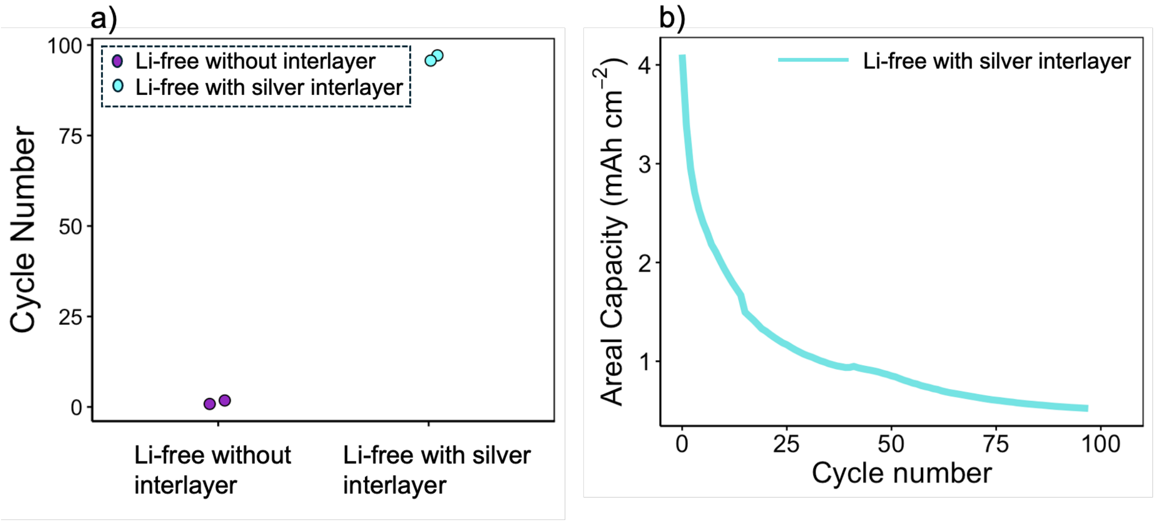

Figure 3.3 a) Bar graph showing comparative full cell cycling performance for Li-free without (purple) and with (teal) silver metal interlayer; b) Capacity vs cycle number graph showing decrease in capacity with cycling for Li-free cell with silver interlayer.

3.4.2 Electrochemical first charging profiles

Two asymmetric half-cells, with and without the silver interlayer, were charged at a low current density of 0.05 mA cm^{-2}, moving 4 mAh cm^{-2} capacity at 60°C under a stack pressure of 2 MPa. Both cells were left in an oil bath for 2 hours, prior to charging and showed an initial OCV of approximately 2.0 V *vs* Li^{+}/Li before lithiation. The voltage profiles, accompanied by schematics, are shown in Figure 3.4.

As shown in Figure 3.4a, in the case of the cell without the silver interlayer, at approximately 0.01 mAh cm^{-2}, the voltage plateaus drop below 0 V almost immediately due to lithium nucleation overpotential, which indicates Li plating on the current collector. Similar OCV trends have been observed by Wang et al.[313] The voltage profile of silver metal interlayer is shown in Figure 3.4b. It shows significant alloying overpotential as five plateaus. The first hump around 1.0 V (i) and 2nd hump at around 0.35 V (ii) is attributed to interfacial side reactions plateaus. At present, there is limited literature to support this hypothesis, as the reported literature available for sulphide solid electrolyte and silver metal charging shows voltage profile beginning from 1.0 V.[296,314] However, previous work indicates that Li_2S usually have a voltage plateau around 2.1 V[315], suggesting that the voltage plateau/hump observed around 1.0 V and 0.35 V may correspond to the formation of Ag_2S or AgCl interfacial species at the interface.

As the voltage decreases, three additional distinct voltage plateaus are observed. Similar behaviour was recently reported by Haslam et al.[316], for LLZO solid electrolyte and silver metal interlayer, where the voltage plateaus were attributed to the sequential formation of α, β and ϒ lithiated silver phases. It is further discussed that some recent computational work proposed that the plateaus below 0.10 V are more consistent with the coexistence of BCC and intermetallic γ phases of lithiated silver.[317] Lithium insertion into silver therefore proceeds stepwise, with LiAg typically forming at higher potentials and more lithium-rich phases such as Li_2Ag emerge at lower potentials, consistent with the trend of decreasing the chemical potential with increasing lithaiation.

Silver can exhibit multiple distinct phases upon lithiation and the sequence of Li-Ag phase formation has been systematically mapped by Huang et al.[318], where it is reported that as the Li content increases during charging, six single-phase regions appeared: Ag, LiAg, Li_9Ag_4, Li_4Ag, Li_9Ag, and Li, which correspond to the α, β, γ_3, γ_2, γ_1, and δ phases, respectively in Li-Ag phase diagram[319]. In the presented study, three voltage plateaus are observed (at 0.1 V (iii), 0.05 V (iv), 0.02 V (v), see magnified inset of Figure 3.4b), which may correspond to sequential transitions among Ag → LiAg → Li_9Ag_4/ Li_4Ag → Li_9Ag/ Li, i.e. from the β phase toward progressively more Li-rich γ and δ phases. These assignments are tentative, as the exact correspondence between voltage plateaus and individual Li-Ag phases can vary depending on current density, particle size, and interfacial effects. Nevertheless, the presence of distinct plateaus strongly supports stepwise alloying behaviour of Ag with Li, consistent with prior reports. The absence of certain transitions could arise from the relatively high charge rate, which may bypass slower phase transformations. Further studies will be required to unambiguously identify the exact phases formed during silver lithiation. The potential drops below 0 V at approximately 0.3 mAh cm^{-2}, suggesting Li deposition.[84,310]

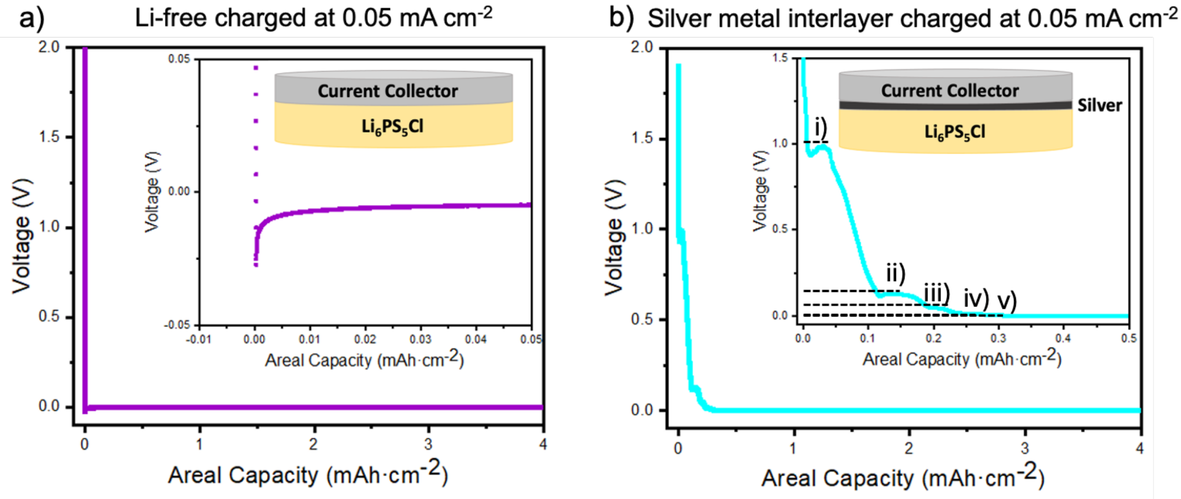

Figure 3.4. First charge voltage profiles of cell with sulphide solid electrolyte in a) Li-free asymmetric half-cell without silver metal interlayer and b) Li-free asymmetric half-cell with sputtered silver metal interlayer. Insets show zoomed in data and schematics of the anode-side of these cells. All cells were charged at 0.05 mA cm^{-2} moving 4.0 mAh cm^{-2} at 60°C under 2 MPa.

The profiles of the voltage curves are different with and without the silver metal interlayers as shown in the zoomed insets. This is because when the silver interlayer is present, lithium alloys with the silver on charge[310], whereas without silver interlayer, Li metal nucleates on the bare current collector[229, 297].

3.4.3 Morphology after charging

Li-free asymmetric half-cells with and without a silver interlayer were charged at 0.05 mA cm^{-2} at 60°C to 4 mAh cm^{-2}. The top-down SEM (Figure 3.5a) shows a pristine Li_6PS_5Cl solid electrolyte, which is indicated in the accompanied EDX by the presence of sulphur (yellow). In the case of the cell with no silver interlayer, after charging the cell, the SEM micrographs show an inhomogeneous web like thick layer of Li metal formed on the solid electrolyte, detected by the absence of sulphur signal[297] in the EDX (Figure 3.5b).

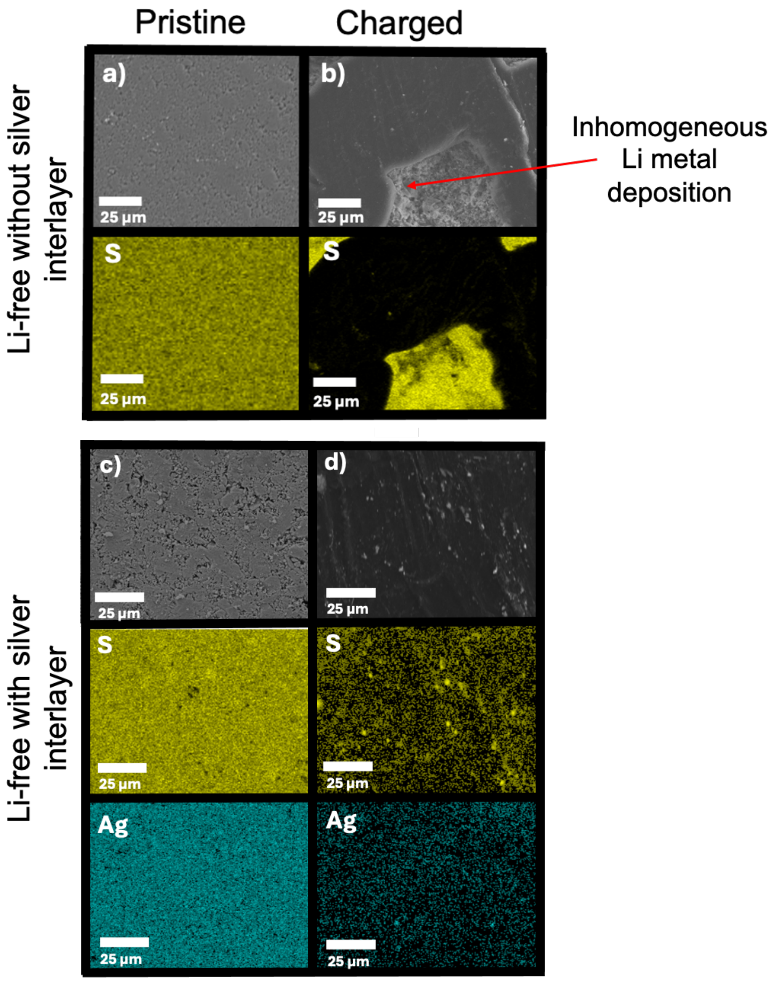

Figure 3.5. Evidence for improved homogeneity of Li deposition during charge at 0.05 mAcm^{-2} *for Li-free cells with silver metal interlayers using top view SEM images with EDX mapping. a) Pristine Li-free cell showing S signal in yellow due to the presence of sulphide solid electrolyte; b) after passing 4 mAhcm*$^{-2}$*; c) Pristine cell containing silver metal interlayer shown by Ag signal in teal; d) after passing 4 mAhcm*$^{-2}$*, Ag signal diminishes due to the formation of Li-Ag alloy.*

Li-free cells with a silver interlayer were charged under the same conditions as mentioned previously in Section 3.4.1. Figure 3.5c shows the pristine silver thin metal interlayer, deposited on top of Li_6PS_5Cl, which was identified through EDX. The silver signal is shown in teal. After charging, a layer of Li-Ag alloy forms as shown in Figure 3.5d, which was identified due to diffuse Ag (teal) signal in EDX. This layer formed is both homogenous and dense.

3.4.3.1 Morphology on the surface of solid electrolyte at different stages of charge

Li-free asymmetric half-cells with and without the silver interlayer were charged at 0.05 mA cm^{-2} at 60°C and arrested at different stages of charge: 0, 0.5, 2.0, 4.0 mAh cm^{-2}. After charging the cells to these capacities, they were disassembled, and the stainless-steel current collector was carefully removed prior to top-down SEM characterisation.

Figure 3.6 shows top-view SEMs for half-cells with no silver interlayer. In the pristine sample (Figure 3.6a), homogenous surface of sulphide SE is observed. As more charge is passed, more Li is observed on the surface of the SE in the form of flat globule-like structures, which grow to form a more complete but inhomogeneous layer (Figure 3.6b, c). After passing 4 mAh cm^{-2} capacity as shown in Figure 3.6d, Li metal forms a web like structure, suggesting inhomogeneous deposition of Li metal. Whilst top-down SEM imaging gives useful information on morphology of Li deposition, it must be considered that the careful removal of the stainless-steel current collector for sample preparation would cause some disturbance of the morphology, as discussed by Wang et al.[313]. Moreover, it should be noted that SEM contrast alone does not identify Li, due to its inability for chemical identification. However, the observed morphology is consistent with electrodeposited Li reported in the literature under similar condition.[320,321]. Furthermore, the assignment of this as Li metal is supported due to the experimental setup. Additional EDX and PFIB-SEM analysis is also conducted in further sections, which can confirm the presence of Li metal.

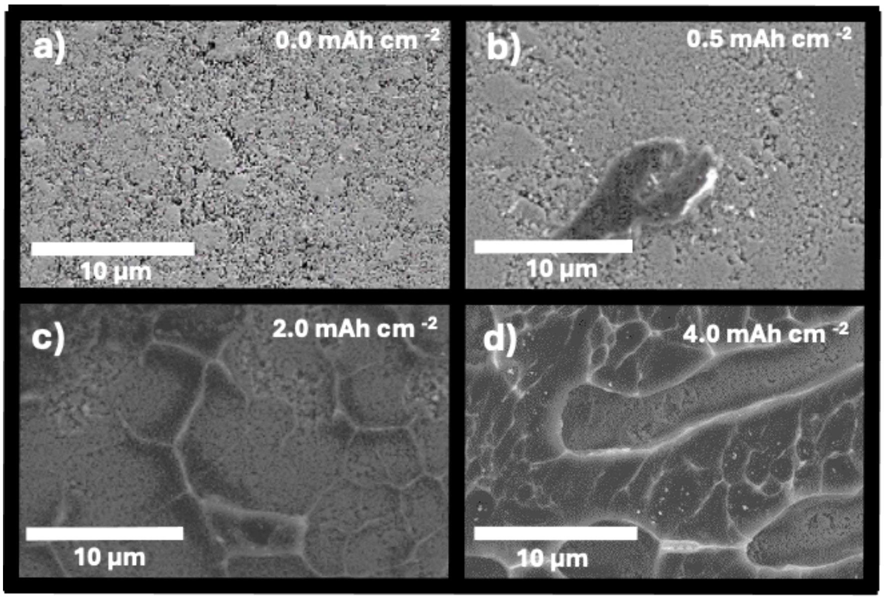

Figure 3.6. Top-view SEMs of Li-free asymmetric half-cells without metal interlayer. Each panel shows a separate SEM image at a different point in charge after a) 0.0 mAh cm^{-2}; b) 0.5 mAh cm^{-2}; c) 2.0 mAh cm^{-2} and d) 4.0 mAh cm^{-2} capacity of Li is passed.

For the samples with a silver metal interlayer, top-view SEM images are shown in Figure 3.7. For the sample before charging, it can be observed that the silver metal interlayer follows the highly porous surface morphology of the Li_6PS_5Cl electrolyte as shown in Figure 3.7a. At low capacities 0.5 mAh cm^{-2} (Figure 3.7b), small globules of Li-Ag are observed to form from the metal interlayer and the silver is no longer a homogenous film. After moving a greater capacity of 2 mAh cm^{-2} (Figure 3.7c) and 4 mAh cm^{-2} (Figure 3.7d), a dense homogenous layer of LiAg alloy is observed. This suggests that the silver metal interlayer promotes homogenous deposition of Li metal by forming Li-Ag alloy. Similar SEM analysis was conducted for zinc and aluminium metal interlayers as shown in Appendix Figure A.2 and Appendix Figure A.3. However, aluminium and zinc metal interlayers showed inhomogeneous deposition.

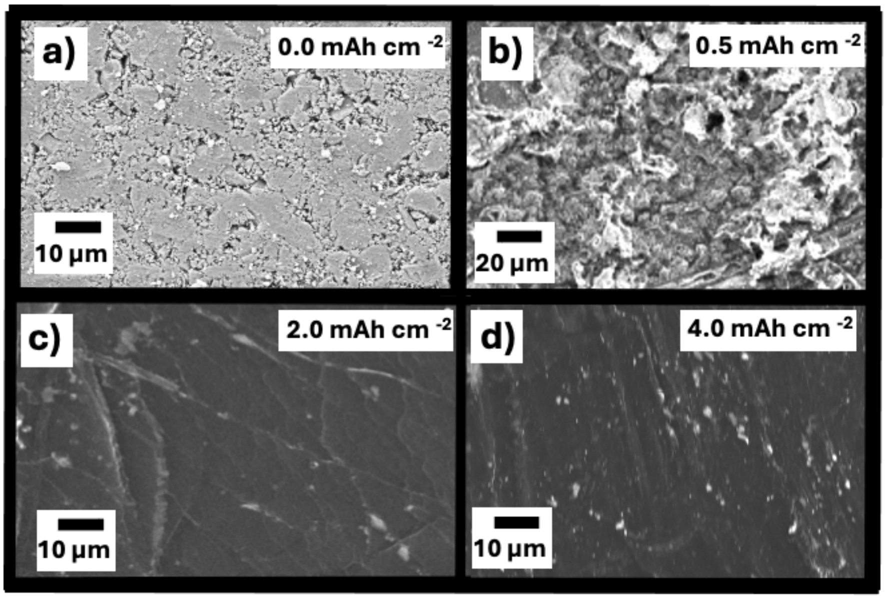

Figure 3.7. Top-view SEMs of half-cells with silver metal interlayer. Each panel shows a separate cell SEM arrested at a different point in charge after a) 0.0 mAh cm^{-2}; b) 0.5 mAh cm^{-2}; c) 2.0 mAh cm^{-2} and d) 4.0 mAh cm^{-2}.

3.4.3.2 Role of silver during charge

Comparing the morphology of the inhomogeneous Li layer in Figure 3.6 to the homogeneous morphology of Li-Ag alloy layer in Figure 3.7, there is a clear advantage to using silver metal interlayers. This is likely to be a contributing factor to the greater cycle life when silver metal interlayers are used, as observed in Figure 3.3a.

The inhomogeneous Li layer in Figure 3.6b,c and d exhibits uneven distribution and deposition of Li metal. This non-uniformity can lead to localised regions of high Li concentration, causing concentrated electric currents to develop during battery charging and discharging processes. The formation of concentrated electric currents can have detrimental effects on battery performance and longevity as discussed in Section 1.3.2.3. These currents can induce localised overcharging or over-discharging, resulting in uneven electrode reactions, electrolyte decomposition, and potential structural degradation.[322] Over numerous charge-discharge cycles, such non-uniformity and localised current concentrations can lead to cell deterioration and failure.

On the other hand, the deposited Li-Ag alloy layer in Figure 3.7d, appears uniform, indicating a more controlled and consistent deposition of lithium during battery operation. This uniformity is desirable as it promotes better electrochemical performance and stability[323,324].

The mechanism of silver movement during charging can be explained by several factors. First, as discussed in Section 3.4.2, during lithiation, silver goes through multiple phase transitions, suggesting the formation of Li-rich alloys. It provides energetically favourable nucleation sites that reduce the nucleation overpotential for Li (nucleation overpotential for silver is 0 mV)[228] and promote uniform deposition. Second, interfacial interactions between Ag and the sulphide solid electrolyte may influence local alloying kinetics, leading to gradients in Li-Ag formation across the contact area. Third, volume changes can occur during lithiation, which can push the silver interlayer, followed by dissolution of Li metal into the silver interlayer. Moreover, there are some clusters of silver in the image, which may reflect kinetically limited local alloying or incomplete redistribution at higher rates. Finally, electrochemical driving forces also play a role. Regions of higher current density during charging promote local lithiation, drawing Ag towards these areas where nucleation of Li-Ag alloys is most favourable. This can also lead inhomogeneous silver distribution, as seen in the Figure 3.4d but a uniform deposited layer. This suggests that the silver movement during charging is governed by i) rate of current, ii) kinetics of dissolution, iii) mechanical effects, and iv) electrochemical reactions.

In conclusion, the silver metal interlayers provide a more stable and controlled Li deposition process. They facilitate uniform distribution and diffusion of Li-ions within the anode by providing uniform nucleation and suppressing local current hotspots resulting in a homogenous Li-Ag alloy layer. Such redistribution is therefore key to understanding why Ag interlayers deliver improved electrochemical stability, cycle life and associated detrimental effects.

3.4.4 Low CE during full cell cycling

Full cells were prepared as discussed in Section 3.3.3. As shown in Figure 3.8, the average 1st cycle CE was found to be around 56% for cells with no silver interlayer (purple, average of 3 cells), whereas cells with a silver interlayer (teal) showed a CE of approximately 77% (average of 3 cells). For reference, cells with a Li metal anode (grey) showed the highest average 1st cycle CE of 84% (average of 3 cells). The black dot shows the range of values for respective samples.

Li-free batteries without interlayers might not be deemed to be suitable for achieving high-performance Li-free anode ASSBs due to low cycling performance and CE for Li-free cells. Moreover, Li-free ASSBs show a greater range of variability in CE % within the cells, this can be due to dead Li formation, which is discussed in detail in Section 3.4.4.3. The silver metal interlayer does enhance the uniformity of Li stored during charging, but they fail to address the critical drawback of low first coulombic efficiency compared to Li metal anode cells, which will be discussed in next section.

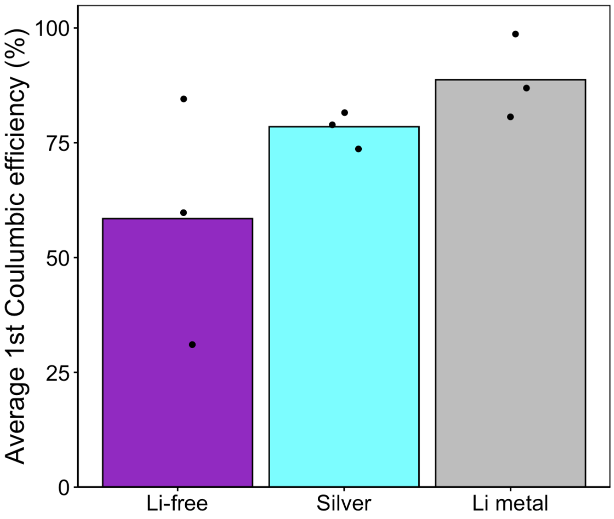

Figure 3.8. Coulombic efficiency compared for three different systems i.e., Li-free without metal interlayer (purple), Li-free with silver metal interlayer (teal) and Li metal (grey), in a full cell using composite NMC cathode. The bar height represents the average value, and the individual measurements are shown as black dots.

3.4.4.1 Low first CE

Full cells using silver coated stainless-steel current collectors and bare stainless-steel current collectors were charged at 0.05 mA cm^{-2} to 4.3 V and then discharged at 0.05 mA cm^{-2} under 2 MPa at 60°C. A full cell using a Li-excess anode was also cycled under the same conditions for reference. The first charge capacity of Li-free cell without a silver metal interlayer (purple) is highest at around 240 mAh g^{-1} as shown in Figure 3.9, followed by Li-excess metal anode cell (216 mAh g^{-1}) and then Li-free cell with silver metal interlayer (210 mAh g^{-1}).

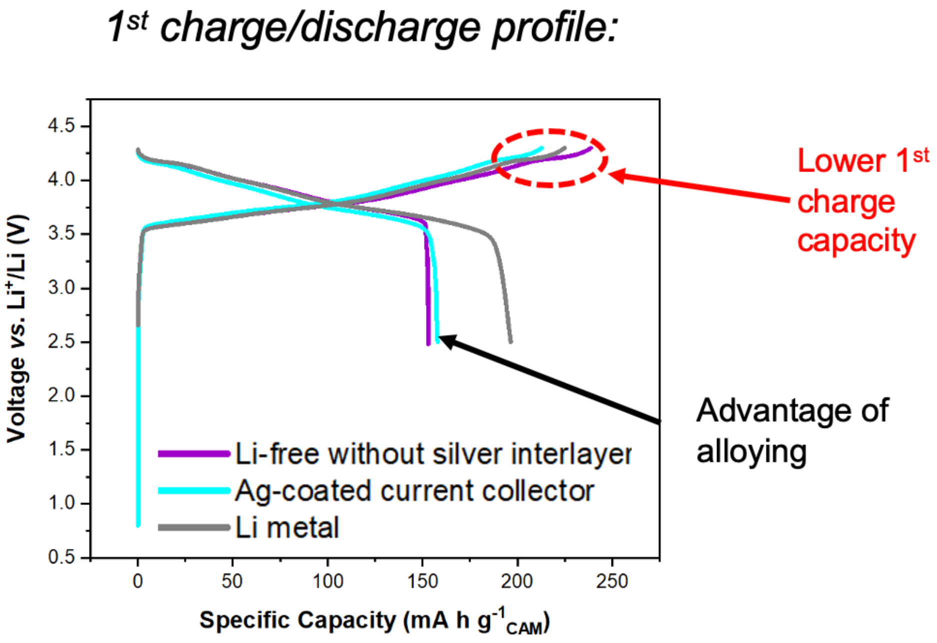

Lower 1st charge capacity

Advantage of alloying

Figure 3.9. Specific capacity compared for three different systems i.e., Li-free without silver metal interlayer (purple), Li-free with silver metal interlayer (teal) and Li metal (grey), in a full cell.

The 1st charge capacity trend might be due to the Li-free cells without the silver metal interlayer having thin SEI, which is expected due to pure lithium plating at the surface of the sulphide solid electrolyte for the first time during the first charge. As a result, the interphase between the Li metal and Li_6PS_5Cl has not yet fully formed, and so the interfacial resistance due to the interphase is minimised.

In a recent work, Sudarshan et al.[62] explored the thickness of the interfacial film in Li-free sulphide ASSBs by *operando* XPS and was found to be approximately 200 nm for a Li-free sulphide solid state battery.[62] Additionally, Otto et al.[61] uses TOF-SIMS to analyse the thickness of the interfacial film in a Li_6PS_5Cl system and was found to be 250 nm.[61] While in the case of a Li-excess metal anode cell, studies indicate the presence of a much thicker interfacial layer due to inherent contamination of the Li foils.[62, 326] This leads to the slightly lower average 1st charge capacity of the Li anode cell observed in Figure 3.9. The Li-free cell with silver metal interlayer anode cells showed the lowest 1st charge capacity as observed in Figure 3.9, which can be due to Li metal undergoing Li-Ag alloying and staying in that phase. It might also imply the presence of a thicker interfacial layer with a higher interfacial resistance.[326] This is explored further in subsequent sections.

The observed average 1st cycle CE can be attributed to different factors depending on the type of cell. In the case of cells with Li metal anode and silver-coated current collector, the presence of homogenous Li deposition during charging and Li stripping during discharge may attribute to the observed CE. However, in Li-free cells without the silver metal interlayer, a significant amount of Li could remain unused during discharge as “inactive” Li, resulting in a lower 1st average CE. Another interesting observation from Figure 3.9 is that in case of the silver metal interlayer, the 1st discharge capacity is still lower than Li-excess metal anode, it can be hypothesised that some of the Li metal is utilised in alloying process and might be left in the interlayer as Li-Ag alloy. This will also be explored further in the next Section 3.4.4.3.

3.4.4.2 Characterising the interphase composition

One possible explanation of the low 1st charge capacity and low average 1st CE is the chemical reactivity of Li_6PS_5Cl with the lithiated silver metal. This means that any capacity loss observed at 1st discharge is attributed to the interfacial film formation or some lithium leaving between the solid electrolyte and the current collector. To investigate this in detail, PFIB with SEM-EDX, and XPS analysis was carried out and is discussed in the subsequent sections.

3.4.4.2.1 FIB-SEM

PFIB was employed to cross-section the samples, accompanied with SEM-EDX imaging technique as shown in Figure 3.10 at different magnification on charged cells at

0.05 mA cm^{-2} to 4 mAh cm^{-2} with silver metal interlayers cells to investigate the structural and morphological evolution during cycling. The PFIB was conducted on charged cells after Li deposition and milling performed through 10 µm stainless-steel current collector, electrodeposited Li, and into the SE. The PFIB instrument was operated by Dr Dominic Spencer Jolly investigating samples prepared by me.

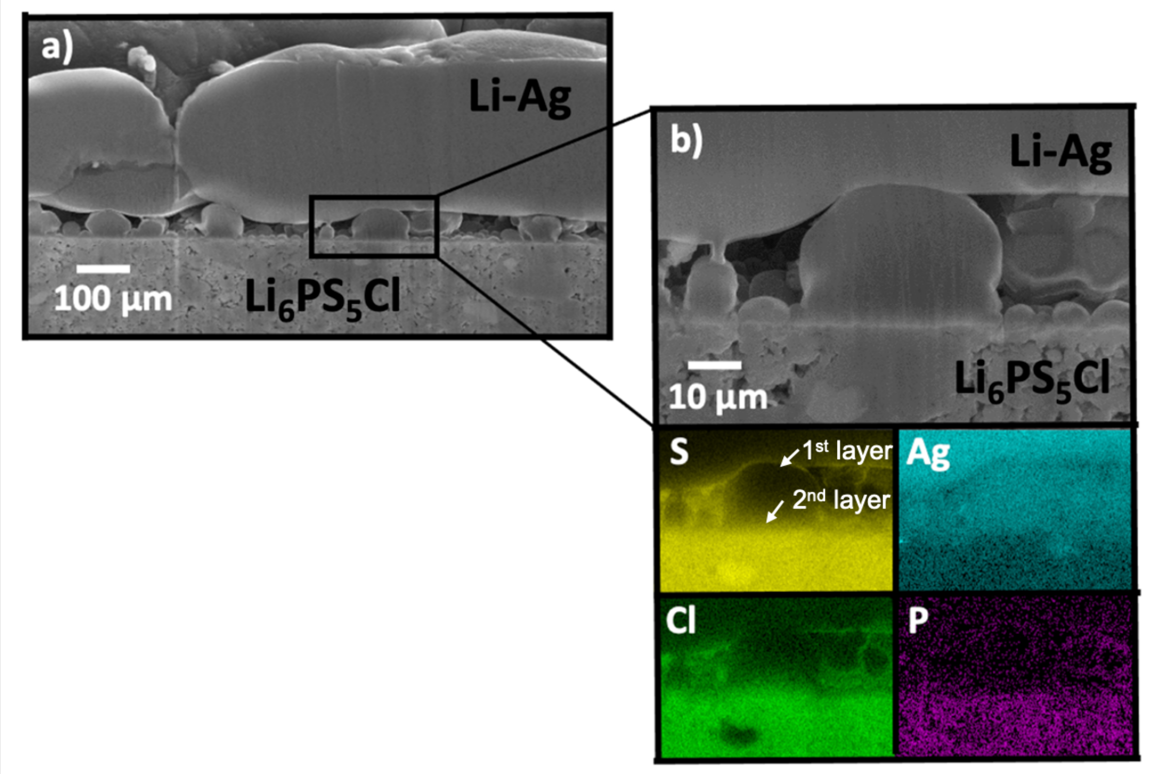

Figure 3.10. PFIB/SEM image showing reactivity of silver, a) cross-section SEM of a charged silver metal interlayer, b) zoomed in image with EDX spectra to observe the presence of S, Cl and P signal in Li-Ag alloy. This figure was produced from the images collected by Dr Dominic Spencer-Jolly.[f]

As can be seen from cross-sectional PFIB (Figure 3.10a), Li-Ag alloy deposits between the solid electrolyte and the stainless-steel current collector (the stainless-steel current collector is not visible in the Figure 3.10a, as it was not captured at this magnification). The magnified area shown in Figure 3.10b, followed by EDX mapping showing the presence

---

[f] The sample was prepared by me for PFIB-SEM-EDX, where the instrument was operated by Dr Dominic Spencer Jolly. The data was analysed by me.

of two-layer formation of Li-Ag alloy, confirmed by the presence of silver signal (teal in colour) throughout the deposited layer. From the S signal (yellow in colour) it can be observed that both the top of the first layer had sulphur signal and the bottom of the second deposited layer also had sulphur signal suggesting the formation of two interphases with sulphur content in that. Similarly for Cl spectra (shown in green). This EDX maps suggests the possibility of an interphase. Appendix A.4 shows line map for the quantification of the interphase products.

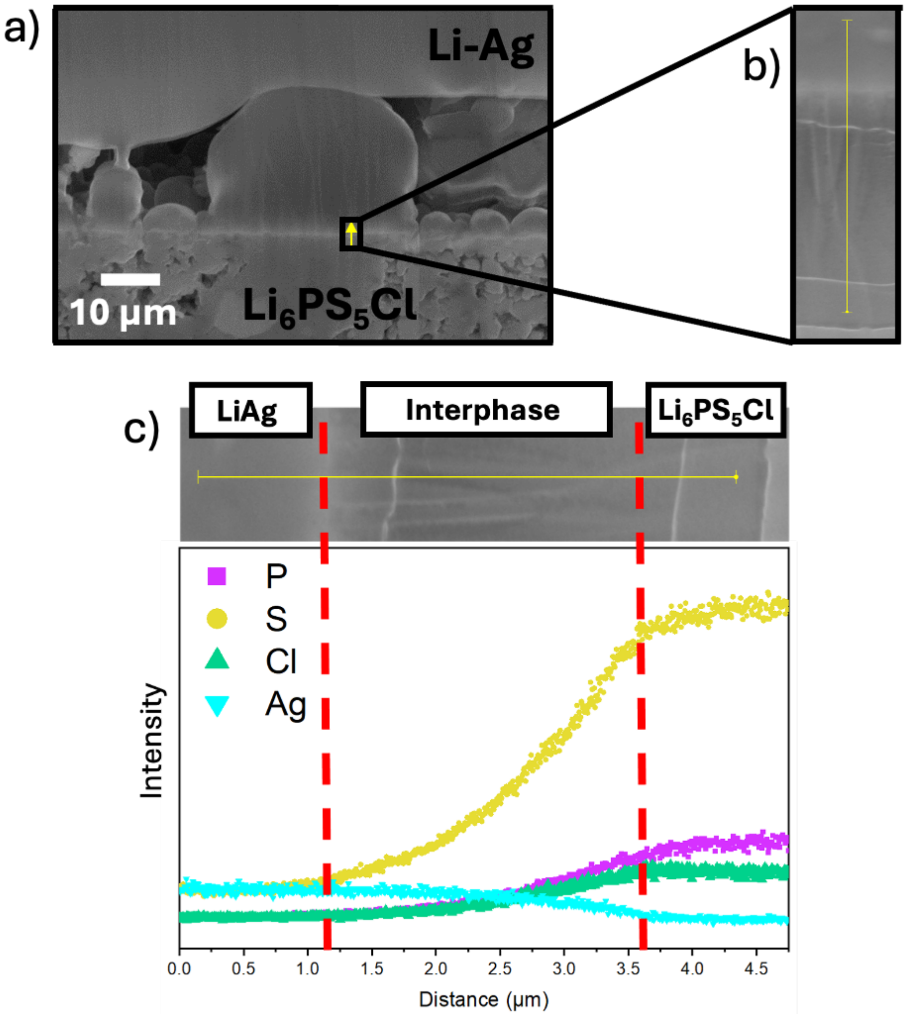

Figure 3.11. Interfacial reactivity of charged silver metal interlayer with sulphide solid electrolyte using line scan EDX, a) cross-sectional SEM, b) zoomed in SEM for the area where line scan EDX was performed, c) graph showing the thickness of interphase through EDX in the zoomed in region of image b. This figure was produced from the images collected by Dr Dominic Spencer-Jolly based on samples prepared by me.

Figure 3.11 shows an EDX line scan over a magnified region. Figure 3.11a is the magnified version of Figure 3.10 and Figure 3.11b is focusing on a smaller area at the interface, to understand the interphase at the SE interface. Moreover, Figure 3.11c shows the EDX mapping using line scan. As shown in Figure 3.11c, the sulphur, phosphorus, and chlorine signal increases after 3.5 µm, while the silver signal is absent after 3.5 µm. This implies that after ~3.75 µm, sulphide SE starts and in the region from 0 to ~3.75 µm silver is present in decreasing trend, suggesting the presence of Li-Ag alloy in the silver metal interlayer. However, in the region from ~1.25 µm to ~3.75 µm, there is presence of silver, sulphur, chlorine and phosphorus signal, which suggests that there might be an interface containing silver with sulphur. Another interesting observation from Figure 3.11c, also shows that the interphase might be around ~2 µm thick. This further confirms the possibility of an interfacial layer between the SE and the deposited Li-Ag alloy.

One key point to be aware of while making above observation is that there is a possibility of redeposition of Li, which can be the reason that two morphologies of deposited Li-Ag is observed, and the interphase might have formed again due to redeposition. Moreover, during the sputtering process with Xe^+ beam, the sputtered material may physically redeposit in the side trench i.e., in the area of analysis.[g] To further confirm this, XPS was conducted, which is discussed in the next section.

3.4.4.2.2 XPS

To further investigate the chemical composition of the interfacial film that is formed between the metal interlayer and solid electrolyte, XPS was carried out on a lithiated silver

---

[g] This point came from joint discussion with Dr Dominic Spencer Jolly.

interlayer. The XPS instrument was operated by Dr Dominic Spencer Jolly on samples prepared by me.

XPS samples were prepared by evaporating 200 nm of Li metal on the sputtered 200 nm silver interlayer on Li_6PS_5Cl and left overnight in vacuum at 60°C, to ensure that the experimental conditions were kept the same. Depth profiling was conducted and argon ion gun was used for charge compensation. CasaXPS software was used to analyse the acquired spectra. The spectra were calibrated to adventitious carbon at 284.8 eV using the acquired carbon C 1s spectra.[62] A survey scan of 0 to 1100 eV was collected. Shirley background was subtracted and the cross-section area was fixed to default values. Peaks were fitted using Lorentzian Asymmetric (LA(50)) lineshape, commonly used for metallic systems to capture asymmetric broadening. The full width at half maximum (FWHM) was constrained to be consistent across chemical similar species to avoid overfitting. Moreover, peak area ratios for Ag 3d spectra as doublets $3d^{5/2}$ and $3d^{3/2}$ were fixed as 2:3 ratio, consistent with the literature.[327] For S 2p spectra they are fitted as doublets $2p^{3/2}$ and $2p^{1/2}$, where peak area ratios were fixed as 1:2 ratio.[283] Reference spectra of pure Ag, Ag_2S and prepared LiAg were measured and fitted under identical conditions.

The measured data are presented in Figure 3.12(a-d) at the interfacial layer close to the solid electrolyte interface. Notably, two significant spectral features can be seen after fitting the Ag 3d spectra as doublets $3d^{5/2}$ and $3d^{3/2}$. The peak at 368 eV BE is determined to be LiAg, highlighted in blue and the orange peak at 369 eV BE is determined to be Ag_2S. Both features have been determined by measuring reference samples using the same XPS instrument as shown by Figures 3.12(e-f) and 3.12g. More information on the components and constraints used for fitting this data can be found in Appendix Table A.1.

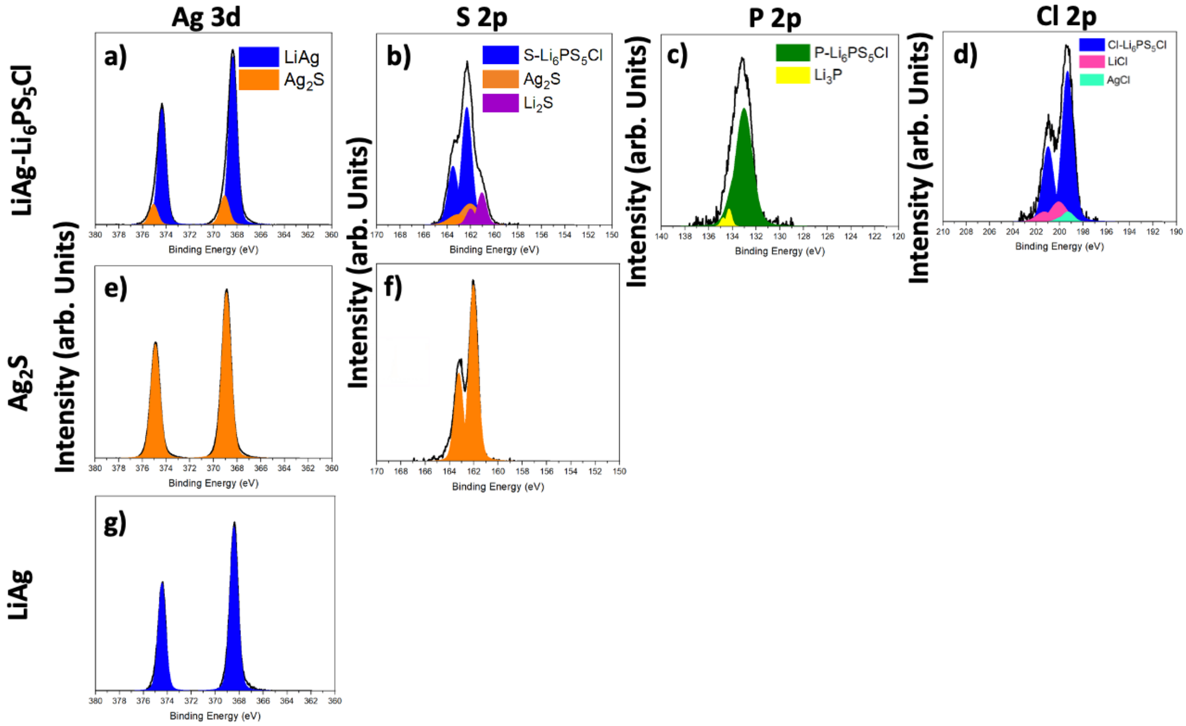

Figure 3.12. XPS analysis of reactivity of silver metal interlayer with sulphide solid electrolyte; a-d) charged silver metal interlayer in contact with sulphide solid electrolyte; e-f) reference Ag and S spectra for Ag_2S; g) reference Ag spectra for Li-Ag. The analysis was conducted by me based on the data collected by Dr Dominic Spencer-Jolly[h].

As can be seen from the S 2p spectra in Figure 3.12b, peaks arising from Li_2S and S - Li_6PS_5Cl, are well known[328]. They are fitted as doublets $2p^{3/2}$ and $2p^{1/2}$. The presence of a Ag_2S peaks in both the Ag 3d and S 2p spectra after the lithiation of metal interlayer are strong evidence of the presence of Ag_2S at the interface, formed by the reaction of Ag metal with Li_6PS_5Cl. Specifically, they are direct evidence of the creation of a new interfacial by-product. Further analysis reveals the possible presence of AgCl as a strong peak observed at the expected energy of 199 eV and 368 eV[329]. However, the BE for the AgCl and Li-Ag overlap so it is not possible to say definitely that AgCl is present.

---

[h] The sample was prepared by me for XPS, where the instrument was operated by Dr Dominic Spencer Jolly. The data was analysed by me. Was trained on CasaXPS by Dr Dominic Spencer Jolly and Dr Joshua Gibson.

3.4.4.3 Role of silver during discharge

Top-down SEM-EDX after discharge was collected to investigate the morphology of the stripped Li alloy on the solid electrolyte surface. Li-free asymmetric half-cells with and without a silver interlayer were charged and then discharged at 0.05 mA cm^{-2} at 60°C under 2 MPa. Figures 3.13a, b, d, and e SEM images are same to Figure 3.4, showing charging of Li-free ASSBs with and without silver metal interlayer. Figure 3.13c, shows the SEM morphology after discharge for a Li-free half-cell without metal interlayer. As can be observed from Figure 3.13c, in case of Li-free half cells without metal interlayer, Li metal is left behind on the surface of the SE, this is observed due to absence of sulphur signal in EDX (shown in yellow). This Li acts as "inactive" or dead Li, leading to loss of Li inventory and contact loss on subsequent cycles.

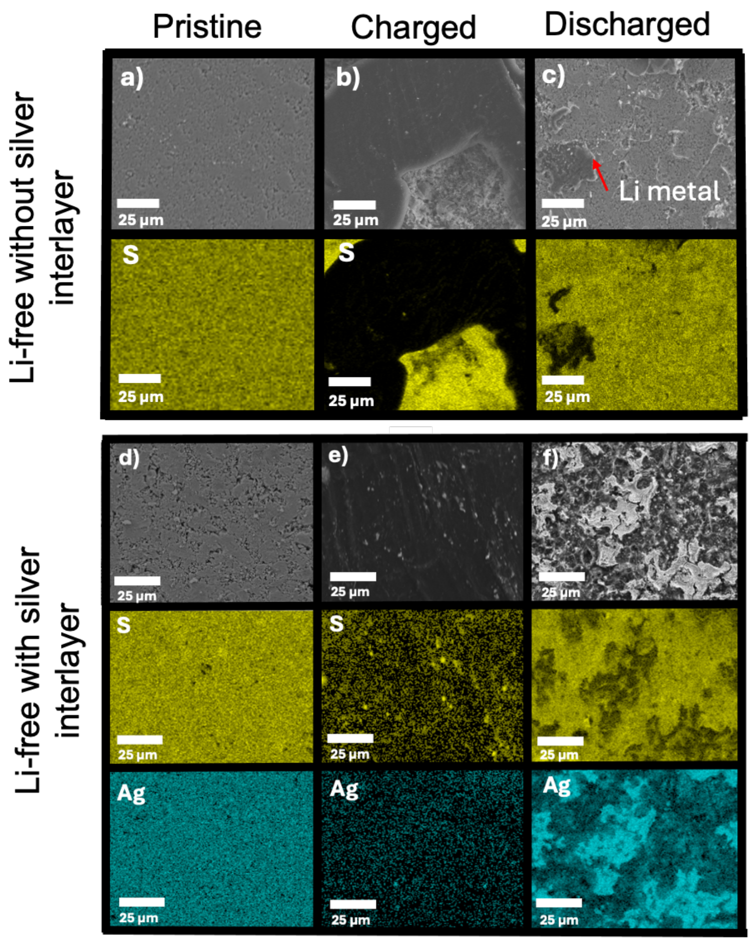

Figure 3.13. Top-view SEM/EDX colour maps of Li-free without and with silver metal interlayer after charge and discharge at 4 mAh cm^{-2} at 60°C at 0.05 mA cm^{-2} current density after the careful removal of stainless-steel current collector. (a) to (c) Li-free without metal interlayer and (d) to (f) Li-free with silver metal interlayer. (a) and (d) are pristine; (b) and (e) after charging; and (c) and (f) after discharge.

On the other hand, in the case of the silver metal interlayer, after discharge Li remains present as a Li-Ag alloy in a film, as can be seen from Figure 3.13f. The EDX after discharge shows regions of low and high intensity silver (teal), indicative of silver metal regions and some Li-Ag remaining in the interlayer. A similar SEM analysis was conducted for aluminium and zinc metal interlayers as shown in Appendix Figure A.5 and Appendix Figure A.6. However, aluminium and zinc metal interlayers showed inhomogeneous deposition.

Figure 3.14 shows the cross-sectional SEM images after PFIB of discharged Li-free asymmetric half-cells without and with a silver metal interlayer. It can be observed from Figure 3.14a that Li metal is present on the surface of the solid electrolyte in form of Li islands, globules and thin vertical pillars. While in case of the Li-free cell with silver metal interlayer, as can be visualised from Figure 3.14b, after discharge, the Li-Ag remains as a layer. Both the images have a 10 μm scale bar and Figure 3.14a is digitally zoomed using ImageJ software to make the data comparable. Raw image for Figure 3.14a can be found in Appendix Figure A.7.

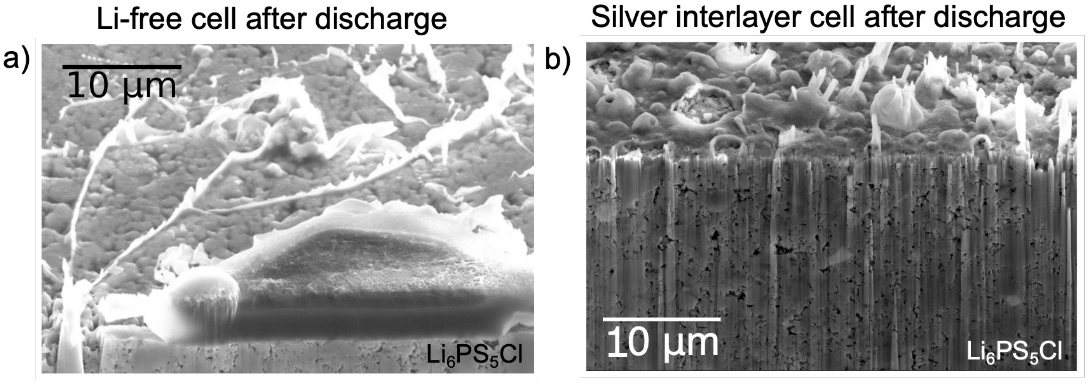

Figure 3.14. Cross-sectional PFIB/SEM image after discharge for a) Li-free cell without silver metal interlayer and b) Li-free cell with silver metal interlayer. This figure was produced by the images collected by Dr Dominic Spencer-Jolly[i]*. Figure a is digitally zoomed in to match the scale, using ImageJ software.*

A possible theory that might explain the Li loss during 1st discharge is that the Li metal remains as "dead" or inactive Li, more prominently in the case of Li-free cell without a silver metal interlayer compared to the silver metal interlayer. This "dead lithium" is disconnected from either the ionic or electronic circuit.[330,331] Moreover, the large volume change on discharge can also disconnect the circuit. However, in the presence of a silver metal interlayer, the Li is surrounded by silver, that helps to provide the electronic pathway,

---

[i] The sample preparation was conducted by me. Dr Dominic Spencer Jolly operated the PFIB instrument. Image analysis was conducted by me.

hence reducing the amount of “dead” inactive Li. In a recent review by Jiang et al.[332] the authors discussed the negative effects of dead lithium in a battery on cycle life and capacity retention. It also leads to current constriction, which again causes the low cell performance. Moreover, various ways to quantitively measure the dead lithium have been discussed in the review, which is beyond the scope of this study.

3.4.5 Role of silver as an interlayer during charge and discharge

Even though silver metal interlayer has some advantages, it is important to understand the chemical reactivity of these metal interlayers with the sulphide solid electrolyte. There are several possible reasons that can explain the improved interfacial contact when silver metal interlayers are present.

The presence of metal interlayers in Li-free ASSBs improves the consistency of lithium deposition by facilitating a more even distribution of lithium across the interfaces as seen in Figures 3.13 and 3.14. This effect can be understood in terms of surface energies[333], Gibbs energy[334,335], wettability[336] and the preference for epitaxial growth[333,337].

When considering the deposition of lithium on a substrate, its high surface tension and poor wettability often lead to clustering or island growth, rather than uniform deposition. High surface tension means that Li atoms minimise contact with the substrate, favouring compact islands rather than spreading, which ultimately results in non-uniform coverage and dendritic growth. This behaviour can be attributed to the large mismatch in surface energies of the materials involved, which makes epitaxial growth energetically unfavourable. Epitaxial growth[338] refers to the ideal scenario where the deposited material aligns and grows in a crystallographic manner with the underlying substrate, but this does not occur for Li.[330] The absence of such alignment means there is no preferred orientation during Li growth, further contributing to irregular deposition. Instead, lithium atoms tend to cluster together, forming compact islands or dendritic structures[339] rather than spreading out evenly across a surface[328], due to the high surface tension of lithium[340,340,341]. As a result when lithium is deposited on a substrate with a higher surface energy, it tends to form non-uniform structures with uneven coverage as observed in Figure 3.6, so it is important to have interlayers that can enhance the wetting behaviour of Li.[337,340]

In the context of alloy interlayers, the presence of an alloying metal, such as silver, can facilitate more even distribution of lithium.[337] The silver metal interlayer has a lower overpotential for nucleation[228], which allows for continuous formation of lithium nuclei at the interface. In addition, silver provides a surface with lower interfacial energy mismatch compared to direct Li deposition, thereby improving Li wetting and suppressing local current constriction. Li-Ag phases may also provide partial crystallographic compatibility with the electrolyte, which promotes more ordered deposition compared to bare Li. This results in a compact and uniform lithium layer of consistent thickness as observed in Figure 3.7.

The Gibbs free energy released during a reaction is a crucial factor that drives the wetting behaviour of liquid lithium.[335,336,342] As discussed by Wang et al.[335] a more negative Gibbs free energy corresponds to a stronger driving force, facilitating the spreading of Li and enhancing its wettability on a given surface[335], which enhances interfacial contact. The presence of Ag interlayers thus not only facilitates uniform deposition but also stabilises the interface thermodynamically.

Lastly, the silver interlayer during discharge helps to reduce the “dead” inactive Li by helping to provide electronic pathways to Li for further cycling. This helps the stripped

Li-Ag alloy to complete the electronic circuit for further cycling without causing a significant charge capacity loss in the next cycle.

Therefore, the presence of metal interlayers in Li-free ASSBs improves the consistency of lithium deposition by facilitating a more even distribution of lithium across the interface. The negative Gibbs free energy of the alloying promotes wetting of the substrate and provides a more favourable surface for lithium deposition, reducing the formation of non-uniform structures. This understanding of surface energies helps explain why lithium does not favour epitaxial growth or develop preferred orientations and how the presence of alloy interlayers can address this issue, leading to improved lithium deposition consistency in Li-free batteries. This is further complemented by the discussion in Section 3.2.3.2, where the mechanism of silver movement during charging is be explained by several factors.

3.4.6 Problems associated with metal interlayers

Asymmetric half cells with a silver metal interlayer were charged at 1 mA cm^{-2} at 60°C. As shown in Figure 3.15, the silver metal interlayer (shown by the Ag signal in teal) ruptures and this leads to inhomogeneous deposition of Li metal, observed as the absence of a S signal (in yellow) in the solid electrolyte. This leads to cell short failure.

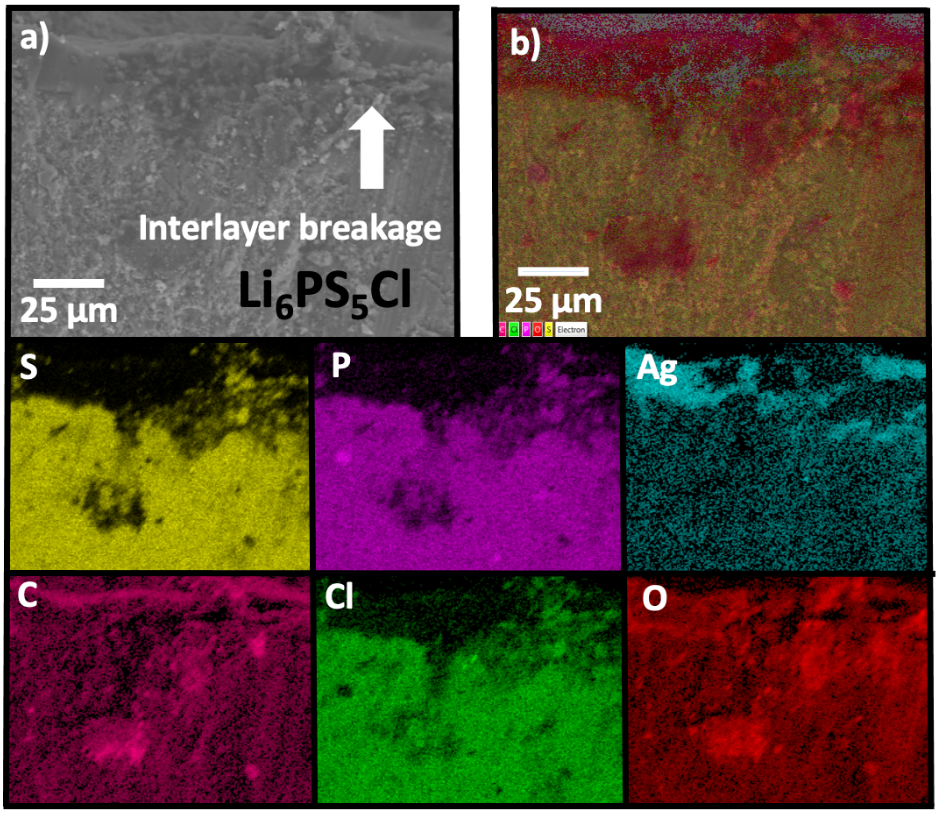

Figure 3.15. Cross-sectional SEM/EDX showing interlayer breakage of metal interlayers. a) SEM image of charged silver metal interlayer; b) corresponding electron image of the cross-sectional SEM image. Corresponding EDX images are also shown.

Electrochemical cycling results in mechanical stress on the electrode materials and these metal interlayers due to the reversible insertion and extraction of Li-ions, causing volumetric and structural changes.[192,334,343,344] The anode surface undergoes a continuous process of lithium metal deposition and removal.[334,343] In the study conducted by Li et al.[334], they lithiated Al, Zn, and Sn foils in liquid Li-ion battery and studied the effects of volume expansion and surface energies. They highlighted that the hardness of the metallic foils is crucial for balancing the strength of metal matrix and its lithiated phase. Maintaining comparable strength between different phases, would lead to a stable homogenous interface. As, in areas where there is unbalanced energy, inhomogeneous interface forms, which leads to current constriction and rupture of the alloy interlayer. Furthermore in another similar study conducted by Han et al.[343], they investigated silicon, tin and antimony with Li_6PS_5Cl SE and discussed that volume changes can lead to mechanical changes but engineering solutions can help to overcome the issues.

Lewis et al.[299] in a perspective paper discussed that alloy anodes undergo 50-300% volume expansion, depending on the metal used and leads to mechanical degradation. Moreover, in the review by Obravac et al.[84], it is showcased that silver undergoes 0-236% volume expansion depending on the phase, as volume expansion of metals upon lithiation is highly phase-dependent because each lithiated metal phase accommodates a different number of Li atoms per metal and then crystallises in a distinct structure.[345] This suggest that the Li-Ag alloy interlayer undergoes mechanical and electrochemical changes during charge and discharge above the critical current density, leading to the cell failure.

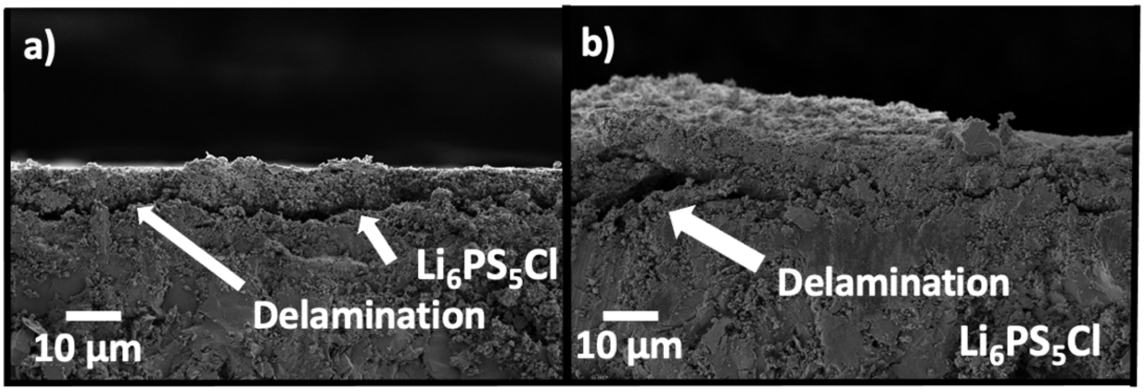

Figure 3.16. Cross-sectional image showing interlayer delamination a) shows delamination of interlayer from SE surface and b) shows delamination of SE with the interlayer.

Sometimes these metal interlayers delaminate from the surface of solid electrolyte as shown in Figure 3.16a. It is observed that the metal interlayers also sometimes delaminate the solid electrolyte with it as shown in Figure 3.16b. This can be due to volume expansion of the metal during the alloying process as discussed above. Alloying interlayers such as gold, silver, tin, germanium, and silicon, which have been widely reported, often undergo significant volume changes during alloying/dealloying processes.[85,86,335] The presence of alloy interlayers /structures can lead to the generation of stress and strain, as observed in previous studies through *in-situ* stress measurements.[300,344] Additionally, alloy anode materials exhibit mechanical properties that significantly change with their composition/phase, unlike lithium metal anodes, which have consistent mechanical properties.[334] Previous studies conducted on tin[346] and silicon[347] have demonstrated a notable decrease on both yield strength and Young's modulus as the materials transition from their pure form to the fully lithiated alloy state. Furthermore, the repeated deposition/stripping of lithium can cause the original morphology of the interlayer to deteriorate over time.

3.5 Conclusion

A Li-free solid-state battery was successfully developed by introducing a thin silver metal interlayer with a sulphide solid electrolyte. It was found to effectively facilitate homogenous lithium alloy deposition on the current collector. An important observation is the increase in 1st CE in presence of a silver interlayer compared to a Li-free battery without an interlayer. This is investigated and explained by the chemical reactivity of the silver metal interlayer with the sulphide solid electrolyte, which is confirmed by PFIB-SEM-EDX, and XPS experiments. Moreover, another possible mechanism for 1st CE loss on discharge is explained using SEM-EDX images, where it is observed that some dead Li is left behind after discharge in absence of silver metal interlayer.

Furthermore, different failure modes of metal interlayers were discussed. This study concludes that for a truly Li-free ASSB to operate, it would require a modified interface, which will help minimise the interfacial reactivity and promote homogenous plating/stripping of Li metal. This represents a significant advance in the research of Li-free ASSBs, and the findings of this study provide critical insights for ensuring a stable interface between the current collector and the sulphide-based electrolyte. While further studies on stripping performance and other metals are required, this study is expected to open new avenues for the development of Li-free ASSBs.

3.6 Future work

This study focussed on understanding the role of silver metal interlayers and the parameters that affect the cycling performance of a Li-free metal battery. It will be interesting to understand the rate dependency of charge and discharge and investigate different morphologies. Moreover, aluminium and zinc metal interlayers were investigated in Appendix Figure A.1 but more coherent study on other metals is needed to understand why silver behaves uniquely. It will be crucial to understand the importance of Li transport through the alloy and the diffusivity of Li in different Li-Ag alloy phases. Investigating the discharge morphology and dealloying behaviour might be an interesting avenue to consider understanding the role of these metal interlayers.

The evolving properties of alloys in ASSBs have significant implications due to their potential impact on mechanical behaviour, which can vary with the state of charge.[334,343] Such variations could potentially influence the structural and morphological evolution of the anode. To gain deeper insights, it is necessary to further explore the connections between mechanical properties and the evolution of alloy anodes in ASSBs.[334,343]

4 Chapter 4: Mechanistic understanding of graphite and graphite-silver anode interlayers for all-solid-state batteries

The work presented in this chapter was partly published collaboratively with Dr Spencer Jolly as co-shared 1st author as "Spencer-Jolly, Dominic, Varnika Agarwal**,** Christopher Doerrer, Bingkun Hu, Shengming Zhang, Dominic LR Melvin, Hui Gao et al. Structural changes in the silver-carbon composite anode interlayer of solid-state batteries. *Joule* 7, no. 3 (**2023**): 503-514".[1] *Parts of this chapter are based on my published research paper mentioned above and the figures are reprinted with permission.*

4.1 Overview

One of the major challenges for charging Li-free all-solid-state cells is low CE and cycle life as discussed in Section 1.3.2. Several strategies have been explored to understand and prevent them. Researchers and the previous chapter have reported that interlayers between the current collector and solid electrolyte can help mitigate some of the challenges associated with Li-free ASSBs. However, an in-depth understanding of how these interlayers help to mitigate the issue is still unexplored. In this chapter, a graphite-silver composite interlayer between a stainless-steel current collector and Li_6PS_5Cl, ceramic sulphide solid electrolyte is investigated using SEM/EDX, *operando* XRD, and electrochemical lithiation followed by full cell investigation. These methods help in understanding the structural changes happening in a composite interlayer at low and high current during charging and discharging with the critical current density determination for the composite. The role of silver nanoparticles in the composite interlayer is also discussed. Moreover, it studies the full cell performance of Li-free cells without Li located between the interlayer and the current collector, as well as ASSBs that utilise Li between the interlayer and current collector.

4.2 Introduction

As discussed in Section 1.2 and Section 1.3, improved safety and increased energy density can be obtained by Li-free all-solid-state batteries (ASSBs) with a Li metal anode and a ceramic solid electrolyte. However, the critical current densities for ASSBs are still low due to Li dendrite formation occurring even at low current densities, leading to short-circuiting and cell failure.[184,348] The problem of dendrite growth is one of the most prominent barriers to commercialisation of a working ASSB with a Li metal anode providing high gravimetric and volumetric energy densities.[105,165,202] The mechanism for dendrite propagation is still under investigation for ASSBs.

As discussed in Section 1.3.3, to overcome the problem of Li dendrite formation and propagation, thin metal layers or composite interlayers that have been deposited on the surface of the sulphide SE have been investigated in Chapter 3 of this thesis. On charging, these thin metal films, metals alloy with Li, rather than nucleating as Li metal. Commonly used thin films metals are Ag[227, 296, 351], Au[350,351], Al[76,352,353], Ge[354], Mg[355], Sb[79], Sn[356], Si[191,350] and Zn[357]. Most of these metal interlayer studies have been conducted with garnet oxide solid electrolyte. As discussed in Chapter 3, these thin metal films react with the sulphide SE to form a solid electrolyte interphase (SEI). Moreover, due to the formation of alloys from these thin metal films, they undergo large volume expansions, which lead to interlayer breakage and delamination as it puts strain on the interface with solid electrolyte.[84,299,343]

As discussed in Section 1.3.3, the mechanism behind the role of silver nanoparticles and the carbon interlayer in the study by Lee and co-workers at Samsung Advanced Technology[214] was left unexplored, prompting this study to better understand this phenomenon.[j] Recently Kim and co-workers[297] showed a Li metal battery with a LLZO solid electrolyte cycling at a current density of 2.5 mA cm^{-2} using carbon and graphite interlayers. They showed the preferred Li nucleation direction at different temperatures with carbon and graphite, with and without Li between the interlayer and current collector and state that the diffusivity of Li across the interlayer is very important for high critical currents. They also discuss the role of bare Li metal and conventional interlayer as shown in Figure 4.1.

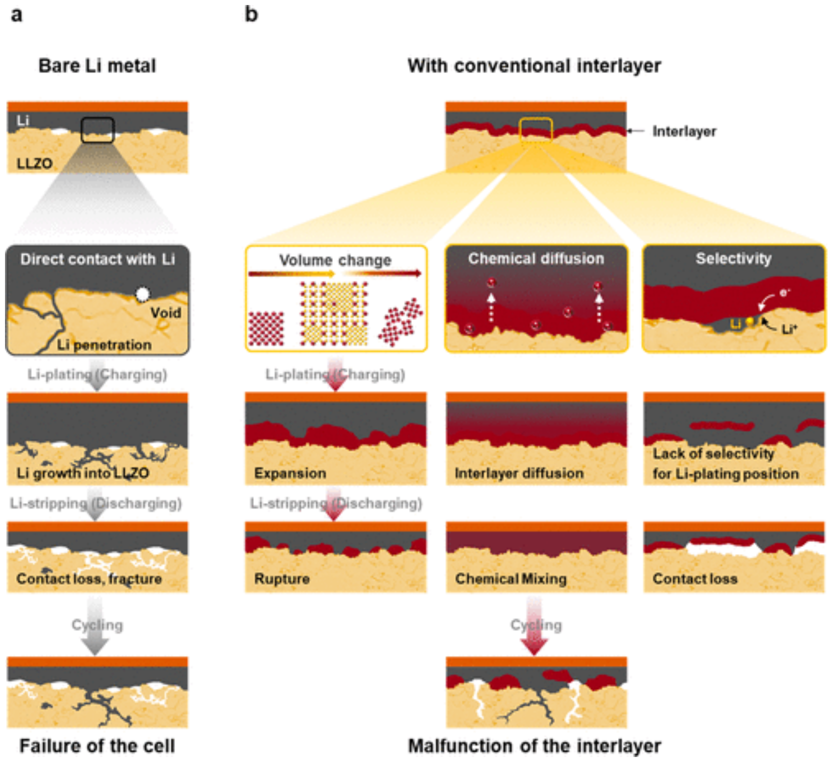

Figure 4.1. a) Schematic showing the challenges associated with all-solid-state battery with Li metal as an anode b) advantages and disadvantages of a conventional interlayer in an all-solid-state battery. Reprinted from Kim et al.[297] ACS Energy Lett. 2023, 8, 1, 9–20. Copyright © 2022 The Authors. Published by American Chemical Society. This publication is licensed under CC-BY 4.0 .

---

[j] This study began in collaboration with Dr Dominic Spencer Jolly in end of 2020, after the labs reopened after the first wave of COVID and some preliminary work on different carbon was investigated by him in his thesis[229], submitted in 2021. Some of the work performed in this Chapter is also reported in his thesis as is it forms the basics of the shared co-author ownership and is included here for completeness.

Hence, graphite and carbons can be used as composite anode protective layers as they can intercalate lithium with almost no or low reactivity with the sulphide SE and leads to low volume change, typically ~10-15%[340, 359–362].[1] Studying the composite anode interlayer system is an intriguing subject to explore.

In this study, *operando* powder X-ray diffraction (PXRD) was utilised to monitor the structural changes occurring in the graphite-silver composite layer. The choice of graphite was motivated by the need to track carbon's structural changes, as carbon possesses an amorphous structure that cannot be easily observed using XRD.

This chapter also provides a comparative analysis of the performance of the graphite-silver system with and without lithium in the interlayer.

4.3 Experimental Methods

4.3.1 Fabrication of interlayers and cells

This chapter uses two different types of anode interlayer: graphite only and graphite-silver.

4.3.1.1 Preparation of graphite and graphite-silver composite interlayers[k]

A custom technique was developed by our collaborator, Dr Christopher Doerrer[1,363] to spray deposit the graphite and graphite-silver composite interlayer on a thin stainless-steel current collector in an argon filled glovebox. The sprayed graphite was an intercalating graphite with 500 nm particle size (PI-KEM) and 60-80 nm silver nanoparticles (US Research). As optimised by Lee et al.[214], the PVdF was dissolved in a mixture of organic solvents (97% IPA, 3% NMP) and the suspended material (graphite or a mixture of graphite-silver) was

---

[k] This methodology for cell assembly was formulated after discussions with Dr Dominic Spencer Jolly in end of 2020 and reported in his thesis[229] and in the joint paper in Joule[1]. The materials with the specified properties and dimensions were identified and procured by me. The collaboration with Dr Christopher Doerrer was led by Dr Dominic Spencer Jolly, to obtain the spray printed interlayers, where Dr Christopher Doerrer decided the parameters and methodology for spray printing.

prepared by stirring for 10 minute using a magnetic stirrer, followed by 5 minute of sonication to disperse the particles homogenously. The PVdF solution was prepared by suspending silver nanoparticles and graphite particles in a ratio of 1:3 by weight. This resulted in an Ag:Graphite:PVdF ratio that was consistent with their findings[214]. The prepared suspension was then passed through a spray-nozzle and spray deposited on a stainless-steel current collector. This spray-coated stainless-steel substrate was vacuum heated to 110°C during the deposition to evaporate the carrier solvent almost instantaneously. This process yields a sheet of composite interlayer composed of just graphite and graphite-silver composite containing PVdF.[1]

4.3.1.2 Preparation of sulphide solid electrolyte using the prepared graphite and graphite-silver composite interlayers[1]

The prepared composite interlayer on a stainless-steel current collector were cut into 4.0 mm diameter circular disks using a hollow punch to control the area. The 4.0 mm disks were then vacuum dried at 70°C for at least 2 hours to evaporate any remaining solvent. The dried disks were then uniaxially pressed against Li_6PS_5Cl in an argon filled glovebox. These circular composite interlayers were first loaded into the bottom of a 5 mm stainless-steel die-set with the coated composite interlayer facing up. 30 mg of Li_6PS_5Cl (AMPCERA) with 1-10 μm approximate particle size (>99.9 purity) was weighed and added to the die-set. A pressure of 400 MPa was applied uniaxially in a press for 1 min, yielding a 5 mm diameter Li_6PS_5Cl disk/pellet with composite interlayer laminated on one side as shown in Figure 4.2 with 5 μm thickness.[1,229] The Li_6PS_5Cl prepared disks were not heat treated due to the presence of PVdF in the composite interlayer. Researchers at

---

[1] This methodology for cell assembly was formulated after discussions with Dr Dominic Spencer Jolly in end of 2020 and reported in his thesis[229] and in the joint paper in Joule[1].

Samsung Advanced Technical Institute[214] also left their Li_6PS_5Cl unheated. As the polymer can degrade at high temperatures, leading to unwanted side reactions.

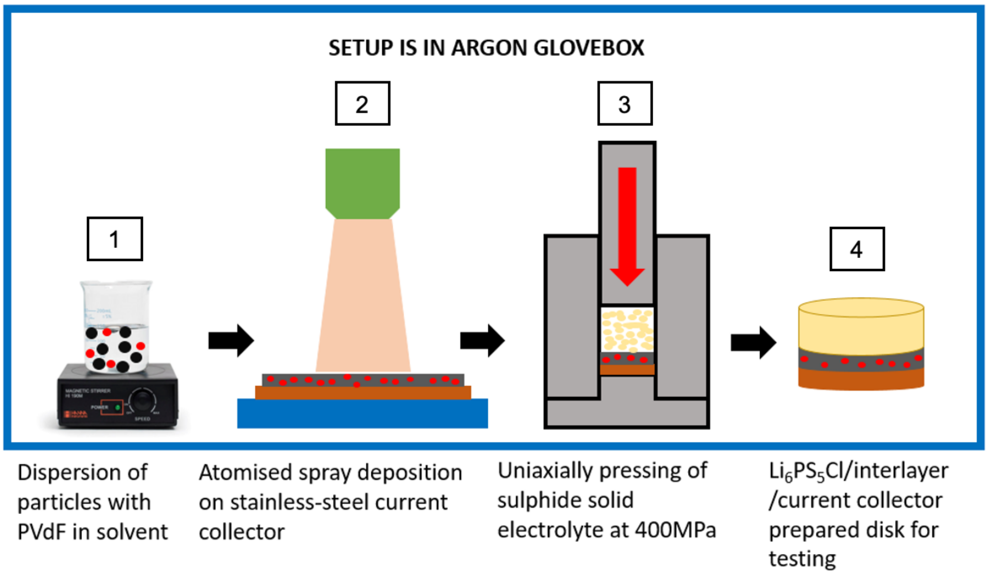

Figure 4.2. Schematic of 1) composite interlayer preparation by creating a suspension of the mixture, 2) Spraying the prepared mixture suspension on the stainless-steel current collector, 3) Circular disks of these interlayers were cut and loaded in stainless-steel die-set with Li_6PS_5Cl powder uniaxially pressed at 400 MPa to, 4) make 5 mm diameter pellets. Visual adaptation[229].

4.3.1.3 Morphology of prepared interlayer

To determine the uniformity of the sprayed layer in Section 4.3.1.1, SEM analysis was conducted on the composite layer before and after uniaxial pressing as shown in Figure 4.3. The sprayed layer is quite porous as can be seen in Figure 4.3a before the uniaxial pressing and becomes dense after the pressing on the sulphide SE, as shown in Figure 4.3b. Moreover, while most of the silver nanoparticles were homogenously distributed in the sprayed graphite interlayer, some silver nanoparticles agglomerated, giving some undesirable silver rich region in the graphite-silver interlayer. Similar work and results were also observed in SEM conducted by Dr Dominic Spencer Jolly[229] on the prepared interlayers.

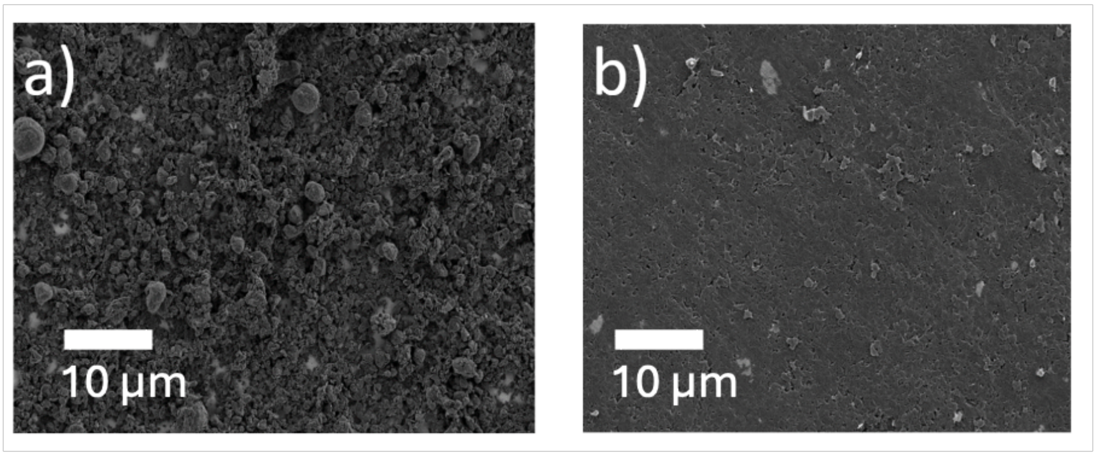

Figure 4.3. a) SEM micrograph showing the graphite only containing interlayer as quite porous. b) SEM micrograph showing the graphite only containing interlayer where the porosity reduced greatly after uniaxial pressing at 400 MPa. Figure 4.3b was collected by Dr Dominic Spencer Jolly.

4.3.1.4 Preparation of asymmetric half-cell[m]

Two-electrode cells were assembled using 4 mm diameter lithium foil disks, approximately 50 µm thick, as counter electrodes. The prepared Li_6PS_5Cl disk, with a 4 mm composite interlayer on one side and lithium foil on the other, was then sealed in vacuum-packed pouch cell with stainless-steel current collector. They were allowed to rest for a day before being removed from the glovebox for testing.

4.3.1.5 Preparation of LiC_x samples

Coin cells for lithiation of graphite were prepared to study the chemical reactivity of lithiated graphite with silver nanoparticles. They were prepared by loading dried graphite (~23-25 mg) powder as the working electrode. Electrodes were assembled into 2032-coin cells with electrolyte (Lithium hexafluorophosphate solution in ethylene carbonate and dimethyl carbonate, 1.0 M $LiPF_6$ in EC/DMC-50/50 (v/v), battery grade, Sigma Aldrich) soaked Whatman glass fibre separators and Li metal counter electrode. Electrochemical

---

[m] This is a standard methodology to prepare two electrode pouch cells in our research group.[1,137,184,304]

lithiation[n] was performed in coin cells using a Maccor Series 4000 potentiostat at the rate of 10 mA g^{-1} while moving a capacity of 372.2 mAh g^{-1}, 186.1 mAh g^{-1}, 124.0 mAh g^{-1}, 93.0 mAh g^{-1} for LiC_6, LiC_{12}, LiC_{18} and LiC_{24} respectively at 30°C. The cells were disassembled, the electrode was removed, washed with dry dimethyl carbonate (anhydrous, Sigma Aldrich), and dried in vacuum for 30 min. The dried lithiated graphite powder was then taken for PXRD in nitrogen atmosphere.

After the XRD, the lithiated graphite powder was mixed with silver nanoparticles in 6:1 ratio by weight, and then ground for 20 min in a mortar and pestle for complete reactivity. 5 mm pellets were made using a Specac stainless-steel die-set to increases the contact area for reactivity and then the pellet was left in vacuum at 60°C overnight to keep the conditions same as the cell. The pellet was ground and PXRD pattern was collected. The assembling/disassembling of coin cell and electrodes was prepared in glovebox in an inert atmosphere (H_2O<0.1 ppm, O_2<0.1 ppm).

4.3.1.6 Preparation of Full Cell

All chemicals were dried under vacuum and stored in an Ar-filled glovebox. For the solid-state composite cathode, single crystal $LiNi_{0.83}Mn_{0.06}Co_{0.11}O_2$ (MSE Supplies), ultra-fine Li_6PS_5Cl (MSE Supplies) and carbon nanofiber (CNF) (Merck) with a mass ratio of 70:28:2 was mixed by pestle and mortar.[o] Solid-state cells were assembled in a custom-designed module with a PEEK mould and stainless-steel plungers[234] as shown in Figure 2.2[p]. The inner diameter is 5 mm. A series of layers comprising the composite cathode mixture (corresponding to an areal capacity of ~4 mAh cm^{-2}), 30 mg of Li_6PS_5Cl and a

---

[n] I was trained on making coin-cells by Dr Robert House and the conditions used for experiment were discussed with him.

[o] I was trained on full cell fabrication by Dr Hui Gao.

[p] The custom PEEK full cell was designed by Dr Christopher Doerrer.

metal coated current collector were pressed at 400 MPa for 1 min. An external stack pressure of 2 MPa was used when making measurements on the solid-state cells.[q] All work was carried out in an Ar-filled glovebox with O_2 and H_2O level below 0.1 ppm. Galvanostatic cycling was carried out at 60 °C using a VMP3 potentiostat (Biologic).

4.3.2 Electrochemical Testing

High-rate cycling data at 2.0, 2.5, and 4.0 mA cm^{-2} was primarily collected at 60°C, except where mentioned. The experimental conditions were decided after conducting single plating charging experiments on half-cells. Due to limitations in the XRD equipment, low rate cycling at 30 μA cm^{-2} was performed at room temperature using Gamry 1010E potentiostat. To reduce the effects of void formation at the interface with the counter electrode during high-rate cycling, a 5 mm diameter lithium foil counter electrode was used[184,364].[1]

For single charge and galvanostatic cycling experiments, a Biologic VMP-3 potentiostat was used. 2 MPa stack pressure was applied to prepared pouch cells using sprung clips. The pouch cells were immersed in oil bath for 2 hours before taking any measurement to equilibrate the temperature[r] and full cells were kept in heating chamber at 60°C for 2 hours prior to taking any measurements.

Electrochemical lithiation was performed in coin cell using a Maccor Series 4000 potentiostat at 30°C.

---

[q] This is a standard methodology to prepare full cells in our research group.[1]

[r] This is a standard methodology to test pouch cells in our research group. However, the experimental protocols were kept similar to Dr Dominic Spencer Jolly[229] work to keep the results comparable.

4.3.3 Chemical Characterisation

To analyse top-down and cross-sectional views of pristine and cycled half-cells, SEM and EDX techniques were utilised. The cells were first disassembled within an argon-filled glovebox, and the stainless-steel current collector was carefully removed. After cross-sectioning the sample using scalpel, the samples were mounted onto a Gatan stage using carbon adhesive tape. To maintain the samples' inert environment, the stage was sealed in an air-tight transfer holder for transport from the glovebox to the Merlin SEM (Zeiss) system, ensuring no air exposure during transfer.

For SEM imaging, a backscattered electron detector was used, operating at an accelerating voltage of 3 kV with a probe current of 200 pA. For EDX analysis, a higher voltage of 10 kV was employed to acquire data. The EDX measurements were conducted using an X-Max 150 silicon drift detector (Oxford Instruments), integrated with the Zeiss Merlin system. Data collection and analysis were completed using the Aztec software.

4.3.4 Structural Characterisation

The *operando* PXRD measurements was performed in 3 kW Rigaku Smartlab diffractometer at room temperature, using a custom-built air-tight cell (Rigaku)[s], which featured an aluminium-coated beryllium (Be) window. To prevent any reaction between the Be window and Li metal during cycling, a 1 μm thick copper current collector (Goodfellow) was used. This copper collector was pressed against the composite interlayer, with a conical spring applied to maintain consistent stack pressure throughout the experiment.[1] The setup can be visualised using the schematic shown in Figure 4.4.

---

[s] The custom setup was designed based on discussions with Dr Robert House. The materials with the specified properties and dimensions were identified and procured by me, Dr Dominic Spencer Jolly and Dr Robert House.

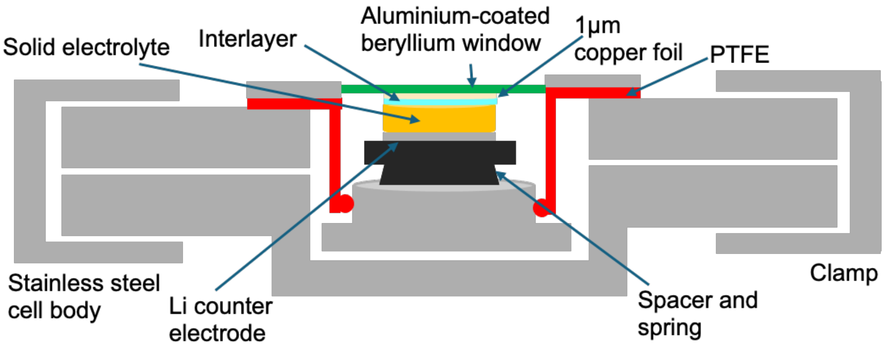

Figure 4.4. Schematic showing cell set-up for the operando PXRD. Redrawn from Spencer-Jolly & Agarwal et al.[1]

Moreover, to analyse the lithiated graphite powders, the data was collected using a Rigaku Miniflex diffractometer. All the samples were measured on low-background silicon sample holders. The collected diffraction data were analysed using Crystal Diffract.[t]

4.3.5 *Operando* XCT

For high rate cycling at 60°C, a synchrotron X-ray source was used to achieve high resolution. Cells used for *operando* XCT characterisation were assembled into a customised tube-cell in an argon filled glovebox. The customised tube-cell was designed by Dr Ziyang Ning[304] and it is used to maintained air-tightness and stack pressure control.

The tube-cell was mounted into a levelled stage on I12 (JEEP) at the Diamond Light Source to avoid any shadowing from the current collecting pin on imaging. I12 (JEEP) beam source can do imaging and collect diffraction. The cell was kept in a transparent cage in which heat can be supplied to maintain a temperature of 60°C during cycling. The cell was charged using a Gamry Interface 1010E, connected with custom built cell. The PXRD was carried out in transmission.[1u]

---

[t] Standard methodology in our research group. Was trained on the software by Dr Robert House.

[u] The experiment was setup with help from Dr Oxana V. Magdysyuk and the data was collected with help from Dr Dominic Spencer Jolly, Dr Bingkun Hu and Shengming Zhang. Initial sample preparation was done by me.

Throughout the cell cycling process, tomograms were captured at regular intervals, and an additional set of tomograms was obtained before and after charge/discharge to capture the static state of the cell. The projections were then reconstructed as volume rendered image using a specialised algorithm developed specifically for the beamline. Imaging data was processed by Dr Bingkun Hu to obtain the volume rendered image. The data was collected by Dr Dominic Spencer Jolly, Varnika Agarwal, Dr Bingkun Hu and Shengming Zhang at I12 (JEEP) at the Diamond Light Source, with help from Oxana V. Magdysyuk (beamline scientist)

4.4 Results and Discussion

4.4.1 Critical Current Densities of graphite and graphite-silver composite interlayers

Asymmetric half-cells were prepared according to the procedure outlined in Section 4.3.1.4. to determine the critical current densities of the graphite-silver composite interlayers. Charging was conducted on various cells with a capacity of 2 mAh cm^{-2}, at current densities of 1.5, 2.0, and 2.5 mA cm^{-2}. The thickness of the composite interlayers remained the same, as discussed in Section 4.3.1.4, as that thickness performed better in the work conducted by Dr Dominic Spencer Jolly[229]. Figure 4.5 illustrates that the critical current density for both the graphite-only and graphite-silver composite interlayers is 2.0 mA cm^{-2}, which is identical for both. Graphite-silver interlayer failed at a current density of 2.5 mA cm^{-2} as shown in Figure 4.5a, with inset showing dendrite growth. The short circuiting of the cell due to dendrite growth is determined by sudden variations in the voltage pattern as shown by various studies[1,184,213,304,365].

The observation that the presence of silver does not lead to a significant increase in critical current densities raises the question of the role of silver in the system. This prompts further scientific inquiry to investigate the underlying mechanisms and potential benefits of incorporating silver into the system, beyond simply increasing critical current densities.[1] Additionally, subsequent sections of this thesis will delve into the structural changes that occur above and below critical densities.

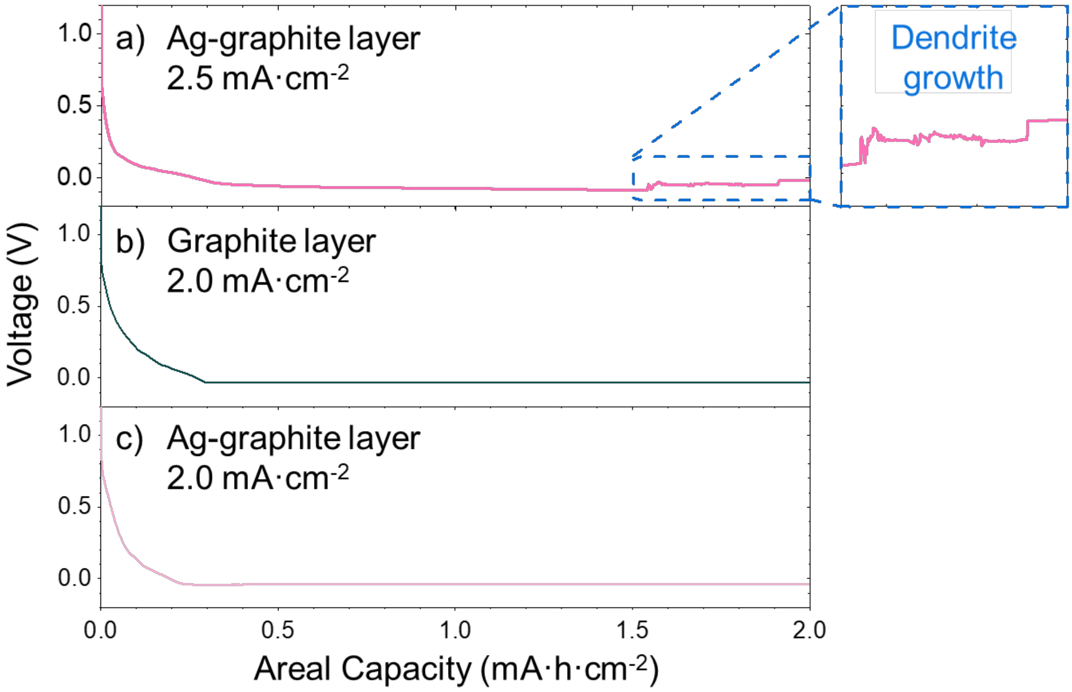

Figure 4.5. Charge at different current densities for graphite only and graphite-silver composite interlayer after moving 2.0 mAh cm^{-2} capacity at 60°C. a) Voltage profile of graphite-silver composite interlayer at 2.5 mA cm^{-2} charge, showing failure due to voltage fluctuations due to the presence of dendritic growth (magnified region); b) Graphite only interlayer showing dendrite-free charging at 2.0 mA cm^{-2}; c) Graphite-silver composite interlayer showing dendrite-free charging at 2.0 mA cm^{-2}. Reprinted with permission from Spencer-Jolly & Agarwal et al.[1]

4.4.2 Charging graphite-silver interlayer at low rate using *operando* XRD

3 kW Rigaku Diffractometer was used to investigate structural changes happening in the graphite-silver anode interlayer using a low rate charging of 30 µA cm^{-2} at room temperature. A 2D detector was used to achieve a high time resolution and to minimise the time taken to collect the full PXRD pattern.[1] High rates will be discussed in a later section of this chapter.

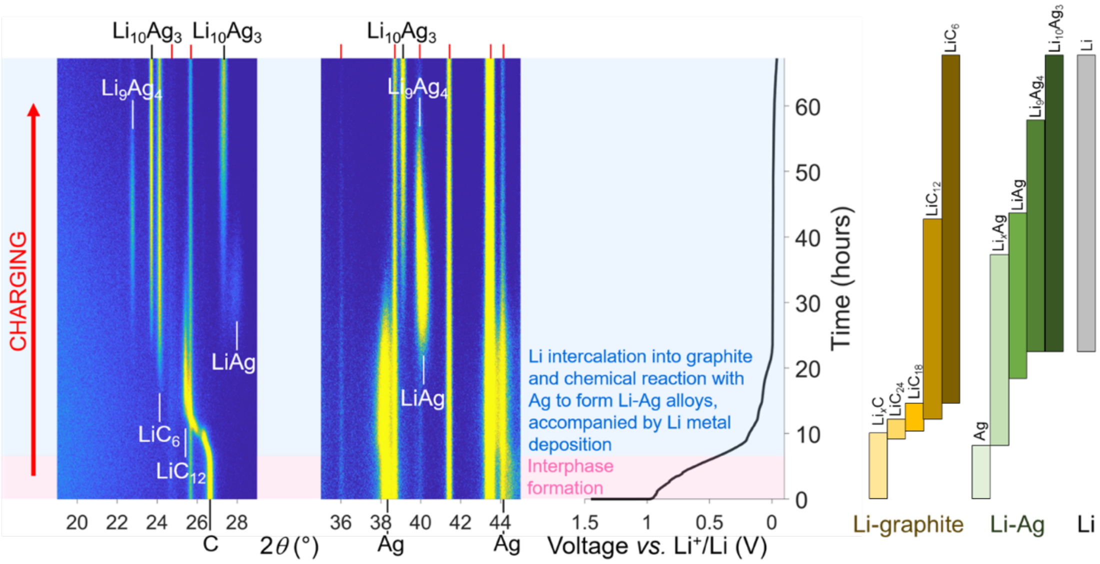

Figure 4.6. A graphite-silver composite layer operando PXRD patterns, analysing the anode side of the cell with low rate charging of 30 µA cm^{-2}. Regions of PXRD where peak occurs is shown by left and centre panels, displayed as a colour map with yellow, which indicates intensity. Corresponding charging profile vs. a Li^+/Li counter electrode is shown on right panel. Red marks indicate the diffraction peaks for Li_6PS_5Cl and cell body. Interphase formation is depicted by pink region, graphite intercalation by blue and green region indicates chemical reaction with silver and silver alloying dominating respectively. Visual keys are represented on right side of the figure demonstration phase changes in graphite (gold), silver (green) and lithium (grey). This figure was produced in collaboration with Dr Dominic Spencer-Jolly and the data was collected with help from Dr Robert House[v]. Reprinted with permission from Spencer-Jolly & Agarwal et al.[1]

The charging voltage profile and *operando* PXRD of a graphite-silver nanoparticle composite interlayer are shown in Figure 4.6. The behaviour of charge will be discussed in two regions; interphase formation (pink), interlayer lithiation dominated by graphite intercalation, interlayer lithiation dominated by silver alloying and Li metal formation (teal).

---

[v] The cell preparation was conducted by me. The XRD instrument was operated by Dr Robert House, with cell program from me. Heat map of the XRD data was prepared by Dr Robert House. Data was analysed jointly with Dr Dominic Spencer Jolly and Prof Peter Bruce. Figure arrangement was with inputs from Dr Dominic Spencer Jolly.

At the beginning of charge at low current, there is no initial intercalation as can be observed by no change in diffraction patterns in PXRD and the capacity begins to pass at approximately 0.95 V *vs* Li^+/Li and falls gradually to 0.4 V over a period of 8 hours. This observation is in accord with the slow formation of an interphase at the interface between the interlayer and Li_6PS_5Cl, due to the reduction of sulphide solid electrolyte at low voltage, as shown in literature for sulphide solid electrolytes in contact with graphite-only anodes.[123,366]

The blue region of the load curve indicates intercalation of graphite as it shares several key characteristics with the load curve of graphite alone.[367–369] Initially, the cell potential continues to fall, and the first shifts are observed in PXRD. A very slight shift in 2θ of the principal reflection for C_6 to lower angle indicates lithiation of C_6 to form a solid solution of Li in C_6 (eg, the 003 peak at 26.6°). Simultaneous to this observation, there are also shifts in the two main silver reflections at 38.3 and 44.1° to lower 2θ, due to the formation of solid solution of Li in silver (Li_xAg). It is a key observation that these silver peaks are not simply broadening but are keeping approximately the same peak width at half maximum, i.e., not forming a mixture of pure silver and Li-doped silver, but are uniformly forming Li-doped Ag, giving a uniform shift in 2θ. Such uniform peak shifts are therefore a crystallographic fingerprint of a continuous structural evolution, where lithium is evenly accommodated across the silver lattice. This is significant, as silver only occupies 5.7 % of the volume in the composite mixture. Due to such low quantity of silver in the interlayer, very little silver is in direct contact with the sulphide solid electrolyte and lithium present is not expected to alloy with the silver directly electrochemically to a significant extent. Therefore, for silver to lithiate as shown by PXRD patterns, it must be due to a chemical reaction between lithiated graphite and the silver nanoparticles. Additionally, the load curve exhibits a pattern similar to that of graphite, but with an extended capacity. This can only be explained by a chemical reaction between lithiated graphite and silver nanoparticles present in the interlayer, as discussed in more detail in the next section.

Lithiation of the graphite and chemical reaction between the lithiated graphite and silver to form Li-doped silver continues until the first graphite phase change, which can be observed as a plateau at 200 mV. This phase change is from the solid solution of Li in C_6 to LiC_{24}. The fall in cell potential that accompanies LiC_{24} formation provides a thermodynamic driving force for further doping of Li-doped silver by chemical reaction, although the lithiated graphite phase is not yet at a low enough potential that a new Li-Ag alloy (LiAg) can be formed. Further evidence that silver can be lithiated by chemical reactivity with LiC_{24} is discussed in next section. On further charging, the voltage of the load curve drops to form a plateau at 105 mV and peaks appear at 25.5° 2θ, which indicate the formation of LiC_{12}. The silver peaks continue to shift, suggesting continuous chemical reactivity of lithiated graphite with silver. On further charging, the fully lithiated LiC_6 phase appears in the PXRD pattern, at which point the Li_xAg solution forms LiAg intermetallic alloy.

The sequence of phase formation in the PXRD can be explained with the help of chemical potentials of lithium (μLi) and electrochemical reactions discussed in detail in Section 3.4.2. This suggests that Li-ions first insert in regions of higher chemical potential, forming LiC_6/LiC_{12}, as literature suggests that lithiation of graphite is at higher V. As discussed in Section 3.2.3.2, alloying of silver goes through three/four plateaus at lower voltage depending on the rate of lithiation, which is dependent on current, temperature and pressure of the cell. Therefore, once the chemical potential is low, the reaction is thermodynamically driven to different phases of Li-Ag alloy.

On further charging, LiAg changes to Li_9Ag_4 and then finally to $Li_{10}Ag_3$ with the phases co-existing simultaneously over a broad range of the charging load curve, rather than passing successively through more Li-rich phases. This suggests that the chemical reactivity between LiC_6 and the Li-Ag phases might not be wholly uniform throughout the interlayer.[370]

As the amount of charge passed increases, the diffraction peak for LiAg gradually diminishes in intensity, followed by Li_9Ag_4, while the peaks for $Li_{10}Ag_3$ increase in intensity. This phenomenon indicates that due to the chemical reactivity between LiC_6 and LiAg phases, LiC_6 continues to lithiate the silver toward the more Li-rich alloy phases. Upon close examination of PXRD patterns, the peak for Li metal was detected at 36.4° as shown in Figure 4.7a, though analysing Li through PXRD can be challenging due to its poor scattering. SEM/EDX imaging was carried out after charging to reach the final voltage plateau, as shown in Figure 4.7b, to confirm the presence of Li metal. Silver signals were visualised through the teal colour on the EDX maps, while the absence of silver signals and the presence of carbon suggested the formation of Li metal deposition with little to no silver metal present.

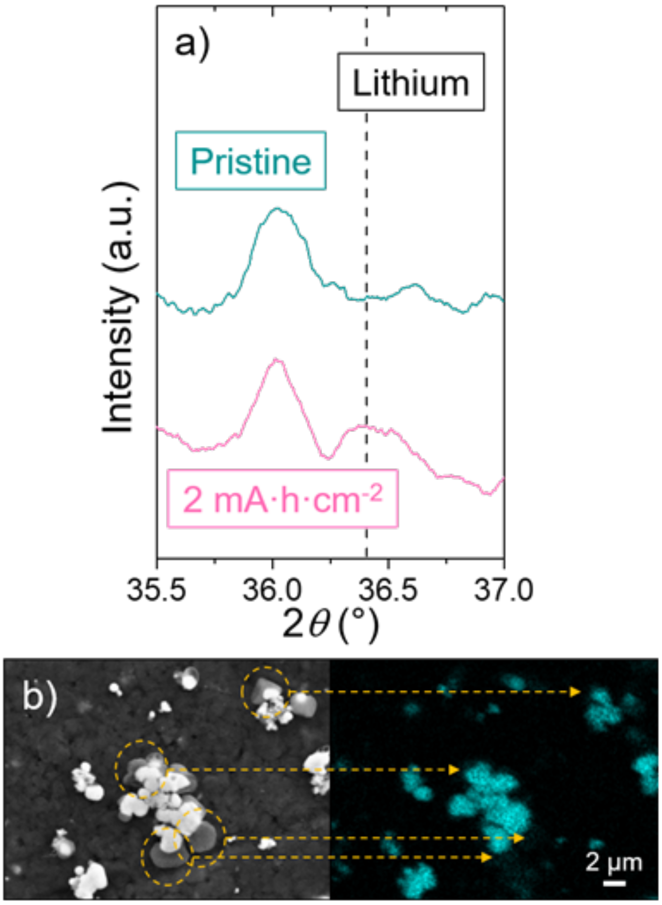

Figure 4.7. Li deposition evidence during low rate charge. a) Absence of Li peak in the pristine cell (teal), and after passing 2 mAh cm^{-2} *capacity, Li peak can be observed in PXRD (pink); b) Top view images with SEM/EDX map of Ag signal of the graphite-silver layer after the careful removal of stainless-steel current collector. SEM image after charging is shown on left and right shows the corresponding EDX map of Ag signal (teal). Regions with poor or negligible Ag signals are observed with darker in colour deposits as marked by yellow arrows. The SEM/EDX (b) image is collected by Dr Dominic Spencer-Jolly. Reprinted with permission from Spencer-Jolly & Agarwal et al.*[1]

4.4.2.1 Chemical reactivity between lithiated graphite and silver nanoparticles

Lithiated graphite with compositions LiC_6, LiC_{12}, LiC_{18} and LiC_{24} were prepared in coin cells using liquid electrolyte as discussed in Section 4.3.1.5 and PXRD measured using a Rigaku Miniflex in a nitrogen filled glovebox. This lithium intercalated graphite with different phases were mixed with silver nanoparticles in 6:1 weight ratio using a mortar pestle and pressed into 5 mm disks. They were left overnight at 60°C for the reaction to happen under the same conditions as the cell and then powdered by grinding using a pestle and mortar, PXRD patterns were collected as shown in Figure 4.8.

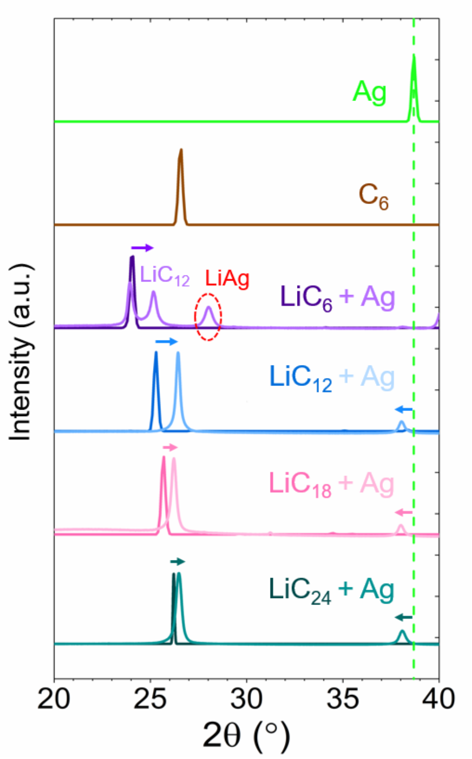

Figure 4.8. Chemical reactions between lithiated graphite phases and silver nanoparticles shown by powder X-ray diffraction patterns. The lithiated graphite phases before reaction with silver; LiC_{24} *(dark teal),* LiC_{18} *(dark pink),* LiC_{12} *(dark blue), and* LiC_6 *(dark purple) is indicated by darker colours. Lighter colours show the result of mixing lithiated graphite phases with silver nanoparticles;* LiC_{24}*+ Ag (light teal),* LiC_{18}*+ Ag (light pink),* LiC_{12}*+ Ag (light blue), and* LiC_6*+ Ag (light purple). Reprinted with permission from Spencer-Jolly & Agarwal et al.*[1]

In each case, LiC_{24}, LiC_{18} and LiC_{12}, the lithiated graphite and silver nanoparticles continue to chemically react as observed by the shift in LiC_x diffraction peak to higher angles denoting lower lithium content accompanied by Li-doping of Ag.

LiC_6 reacts with silver to form the LiAg phase while continuously delithiating. To ensure the reaction could proceed completely to the LiAg phase, the LiC_x:Ag ratio was chosen to provide an excess of lithium. This excess ensures that LiC_6 can fully convert to LiAg. Among the different LiC_x phases, only LiC_6 has a high enough chemical potential or low enough voltage-to drive the formation of LiAg. This behaviour matches the voltage profiles of graphite and silver observed in electrochemical cells using liquid electrolytes.[310] The results here are consistent with these profiles, confirming that only fully lithiated LiC_6 has a voltage low enough to react with silver and form LiAg.[1,367,369]

4.4.3 Discharging graphite-silver interlayer at low rate using *operando* XRD

The structural changes as tracked by *operando* PXRD on discharge at low rate of a graphite-silver composite interlayer is shown by Figure 4.9. On charge, chemical reaction drives the lithiation of silver by the electrochemical lithiation of graphite, which is different than the discharging process. However, if the rate of charge exceeds the rate of chemical reaction, Li metal can also be plated out on the current collector and so the rate of the chemical reaction is not wholly rate-limiting. However, during discharge, graphite is electrochemically delithiated, driving chemical delithiation of Li and Li-Ag alloy to re-lithiate the graphite. Moreover, if the rate of delithiation of the graphite interlayer exceeds the rate of the chemical reaction, graphite will continue to delithiate, leading to high potentials, resulting in low cell efficiency. This difference appears to lead to some unique phase behaviour on discharge.

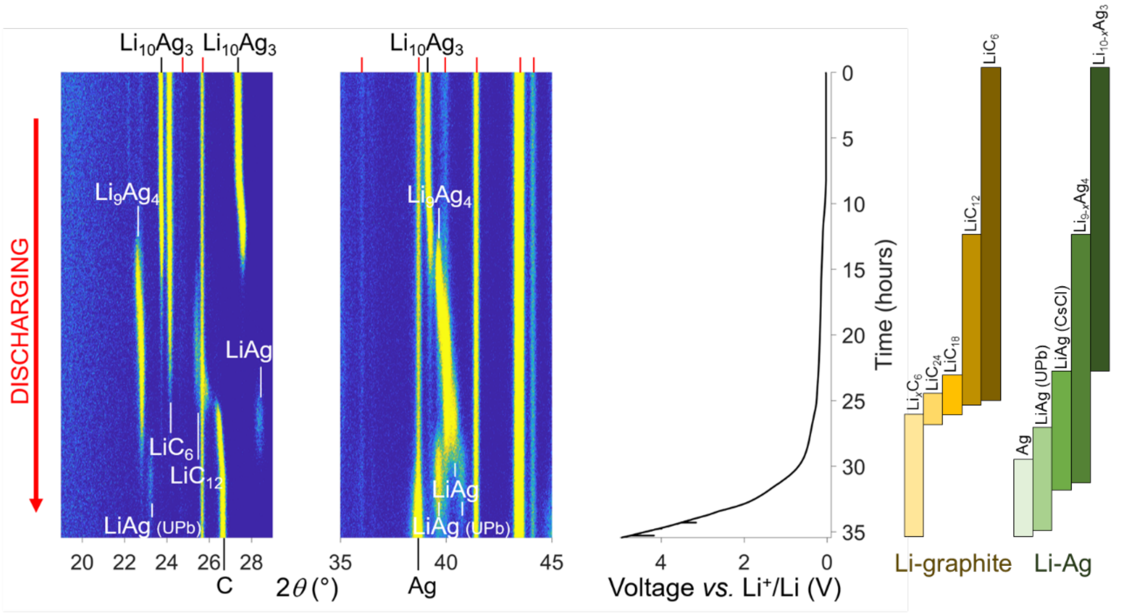

Figure 4.9. Discharge operando PXRD patterns for a graphite-silver composite layer at the anode side of the cell with sulphide SE and stainless-steel current collector. Discharged at low rate of 30 µA cm^{-2}. Regions of PXRD where peak occurs is shown by left and centre panels, displayed as a colour map with yellow, which indicates intensity. Corresponding charging profile vs. a Li^{+}/Li counter electrode is shown by right panel. Red marks indicate the diffraction peaks for Li_6PS_5Cl and cell body. Visual keys are represented on right side of the figure demonstration phase changes in graphite (gold), silver (green) and lithium (grey). This figure was produced in collaboration with Dr Dominic Spencer Jolly and data was collected with help from Dr Robert House.[w] *Reprinted with permission from Spencer-Jolly & Agarwal et al.*[1]

During the discharge process, minimal changes are observed in the diffraction patterns for both LiC_6 and $Li_{10}Ag_3$ phases over the first 8 hours. After this period, however, the diffraction peaks associated with $Li_{10}Ag_3$ start shifting to higher 2θ values, approximately 27.4° and 39.1°. This shift suggests a volume contraction, which can be attributed to lithium deficiency in the phase, forming $Li_{10-x}Ag_3$. Importantly, these peak shifts occur without any significant changes in the LiC_6 peaks, indicating that lithium is being electrochemically

---

[w] The cell preparation was conducted by me. The XRD instrument was operated by Dr Robert House, with cell program from me. Data was analysed jointly with Dr Dominic Spencer Jolly and Prof Peter Bruce. Figure was produced jointly with inputs from Dr Dominic Spencer Jolly on visualisation.

extracted from the LiC_6 phase and reacting with $Li_{10}Ag_3$, causing the delithiation of the $Li_{10}Ag_3$ phase while LiC_6 remains unchanged.[1]

As the discharge progresses further, the peaks of $Li_{10-x}Ag_3$ continue shifting, leading to the formation of Li_9Ag_4, with characteristic peaks at 22.6° and 39.7°. Simultaneously, the LiC_6 phase transforms into LiC_{12} as lithium is progressively deintercalated from the graphite. At this stage, the chemical potential of the Li-Ag alloy phase drops significantly compared to the lithiated graphite, driving further delithiation. This results in the appearance of the LiAg phase.[1]

With continued discharge, lithium is completely removed from LiC_{12}. At the same time, LiAg continues to alloy further. Both Li_9Ag_4 and CsCl-structured LiAg peak intensities decrease concurrently, leading to the appearance of new peaks not observed during the charging process. This new peak corresponds to the formation of a new phase, UPb-structured LiAg, with peaks at 23.1°, 39.7° and 40.8°.[319] This UPb structure of LiAg is known to be more stable than CsCl structured LiAg in Li-deficient LiAg, hence promoting its formation and explaining why it only appears on discharge.[1,319]

As the discharge reaches towards completion, only peaks corresponding to graphite and silver are observed, as they fully delithiate, returning to their pristine states, accompanied by an increase in cell potential. It is important to note that there is severe capacity loss over this first cycle. Most of this capacity loss can be explained by the interphase formation between the composite interlayer and sulphide solid electrolyte, which leads to Li inventory loss. However, there might be other reasons for Li losses during this first cycle which are unaccounted for.[1]

4.4.4 Charging the graphite-silver interlayer at high rate with *operando* XRD and XCT

The experiment was performed at 60°C at high charging rates using the setup discussed in Section 4.3.3.2.2.[214] It is useful to understand the structural changes happening in Li-Ag alloys through *operando* XRD and *operando* XCT, at more realistic rates of 2.0 mA cm^{-2} and 4.0 mA cm^{-2} as shown in Figure 4.10.

As discussed in Section 4.4.3 and 4.4.4, at low rates, charge proceeds through electrochemical lithiation of graphite and then chemically reacting with silver nanoparticles to lithiate them. When charging at 2.0 mA cm^{-2} (shown in Figure 4.10a), the graphite phases are less elongated in capacity compared to the lower rate PXRD patterns discussed in Section 4.4.3. This suggests that the rate of intercalation of graphite with Li^{+} is significantly higher than the rate of chemical reaction of Li with silver, and therefore less capacity is used in silver alloying in the early stages of charge. On further charging, LiC_6 is formed. Once LiC_6 is formed, the silver peak decreases in intensity to zero and is replaced by the peak indicative of LiAg. At higher capacities, this then goes on to be replaced by increasingly Li-rich Li-Ag phases, such as $Li_{10}Ag_3$. No peak indicative of Li_9Ag_4 at 39.8° (slightly lower 2θ than the 40° LiAg peak, with which it overlaps) was observed at high rates of 2.0 mA cm^{-2}, however this is due to the peak of cell body overlapping at that angle. After the graphite has been fully lithiated to LiC_6, a weak Li metal peak is also observed at 36° and it gets more intense as more charge is passed. This is further supported by volume rendered image produced by Dr Bingkun Hu from *operando* XCT shown in Figure 4.10c, where XCT is performed at the top of charge. This shows a greyscale-segmented region of the interface where the LiC_6 layer (green) is still present in a uniform layer, suggesting that it is still acting as an effective barrier to dendrite growth, with all Li metal and LiAg alloy phases (purple) nucleating at the current collector interface.

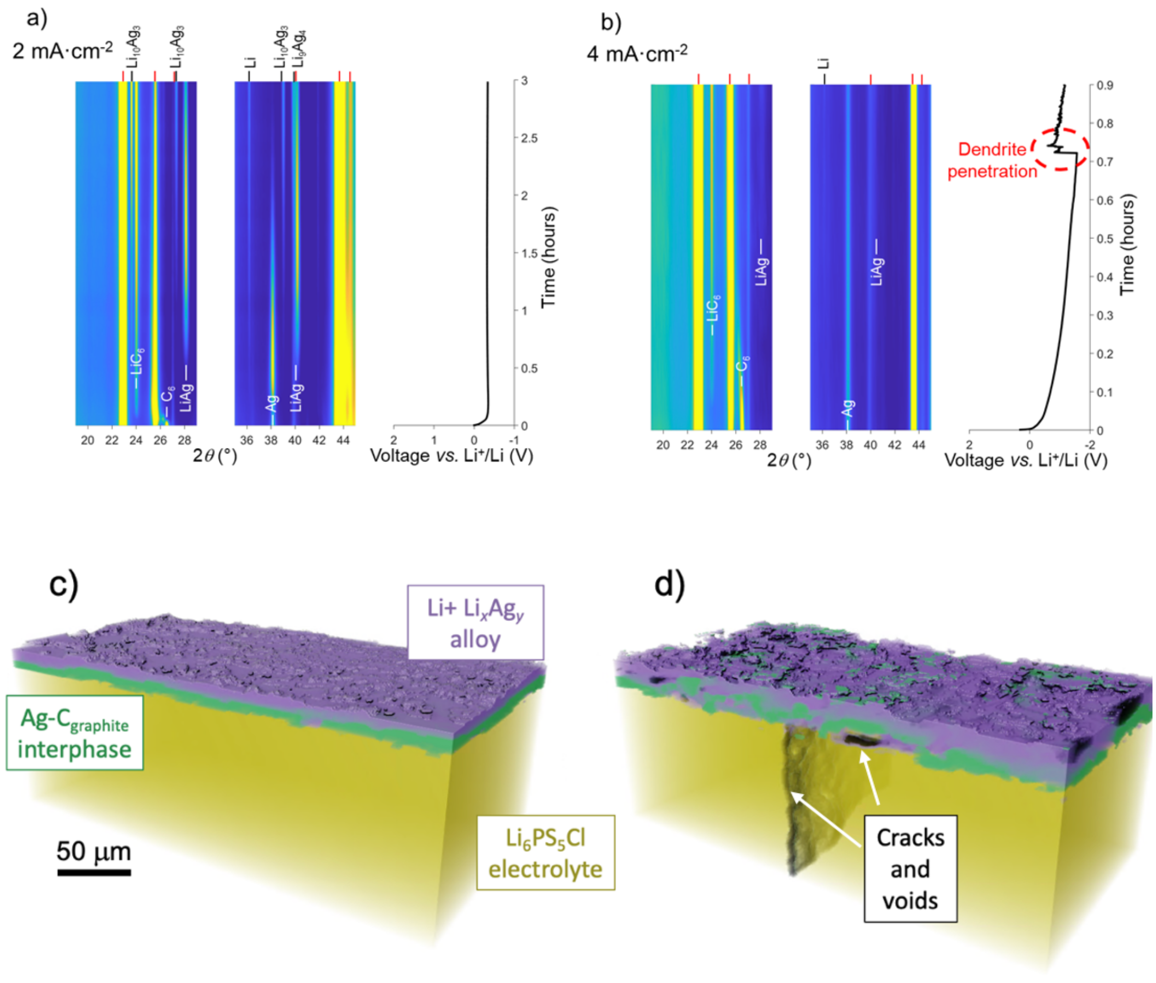

Figure 4.10. High rates operando PXRD patterns for a graphite-silver composite layer at the anode side of the cell with sulphide SE and stainless-steel current collector at 60°C. a) charging at 2.0 mA cm^{-2} and b) charging at 4.0 mA cm^{-2}. a and b) Regions of PXRD where peak occurs is shown by left and centre panels, displayed as a colour map with yellow, which indicates intensity. Corresponding charging profile vs. a Li^{+}/Li counter electrode is shown by right panel. Red marks indicate the diffraction peaks for Li_6PS_5Cl and cell body. Short-circuit at 4.0 mA cm^{-2} is shown by sudden variation in cell potential; c) shows a volume rendered image of portion of the interface after charging at 2.0 mA cm^{-2} and d) at 4.0 mA cm^{-2}. This figure was produced in collaboration with Dr Dominic Spencer-Jolly and data was collected with help from Shengming Zhang and Dr Bingkun Hu. Dr Bingkun Hu processed the data for c and d.

At charging rates exceeding the critical current density (e.g., 4.0 mA cm^{-2} in this instance and shown by Figure 4.10b), the presence of LiC$_x$, where x>6, is observed for a greater duration compared to charging at 2.0 mA cm^{-2}, wherein the appearance of the LiC_6 peak becomes visible at a later stage. This indicates that the rate of transport of Li^+ ions to the anode is greater than the rate at which Li^+ ions can intercalate into graphite due to the higher current densities used. This is further shown by the presence of the Li metal peak in the PXRD. At this rate, the LiAg peak is visible, although pristine Ag peaks persists through the charging, indicating that due to higher rate above the critical current density, rapid lithiation of graphite is hindered due to slow kinetics of lithiation relative to the charge rate. Therefore, there is insufficient time for the effective reaction between silver and lithiated graphite to occur. Ultimately, the cell short circuits as can been seen in load curve in Figure 4.10b, suggesting Li metal, and subsequently dendrites, form at the interface between the solid electrolyte and composite interlayer as shown by Figure 4.11. This is further visible in volume rendered image at the top of charge. It can be observed that after charging at 4.0 mA cm^{-2}, the interlayer containing LiC_6 gets severely fractured due to lithium nucleation and Li-Ag alloy formation at the solid electrolyte interface, at the current collector interface, and possibly even within the interlayer. Li metal nucleation at the solid electrolyte interface leads to dendrite growth into the solid electrolyte, which can be observed as transverse cracking in Figure 4.10d. When charging at rates above the critical current density, the lithiated graphite interlayer is not able to act as a physical barrier to dendrite growth, as the intercalation of Li into graphite is slow than the rate of charging, leading to short circuiting of the cell. The transport of Li^+ through the graphite to the current collector interface (determined by the diffusivity of Li^+ in LiC_x), rather than the rate of chemical reactivity with the Ag/Ag-alloy, becomes rate limiting[371].

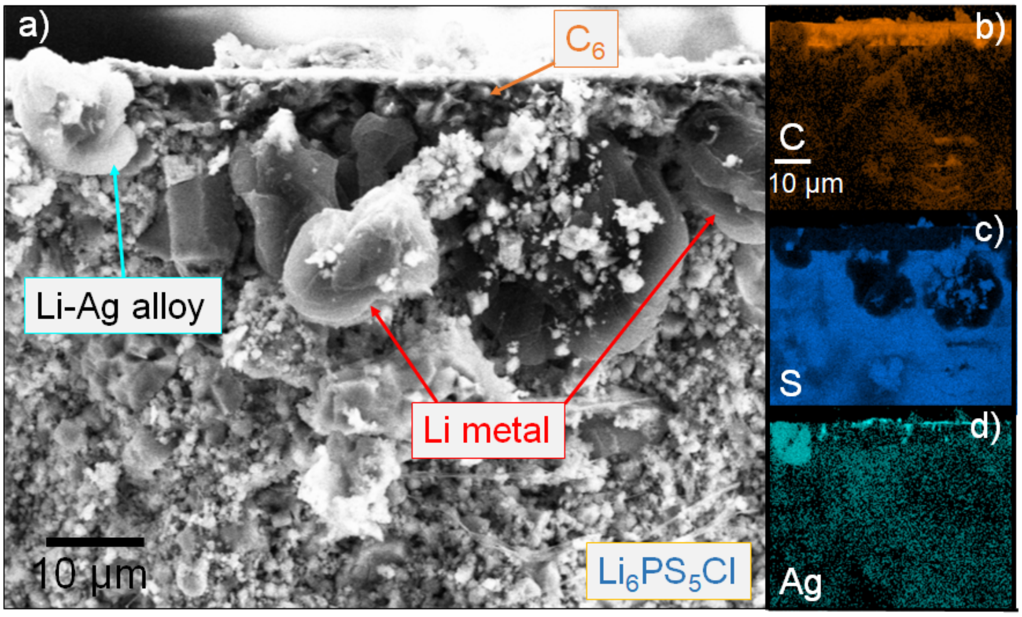

Figure 4.11. Graphite-silver composite interlayer cell failure at 4.0 mA cm^{-2} *after moving 6 mAh cm*$^{-2}$ *capacity at 60°C shown by cross-sectional SEM/EDX image, a) SEM image showing Li metal deposition and Li-Ag alloying at the wrong interface i.e. the solid electrolyte and the composite interlayer; b) C signal shown by EDX, helping to identify the position of the composite interlayer; c) S signal shown by EDX, helping the identify the* Li_6PS_5Cl *position; and d) Ag signal shown by EDX, which helps to identify Li-Ag alloying and silver nanoparticle- rich areas. Adapted from Spencer-Jolly & Agarwal et al.*[1]

So how could the composite interlayer be modified to increase its charge rate performance? Failure is clearly induced by the transport limitations of Li^+ in the graphite, so modifications that improve this should increase the maximum stable charge rate. Use of a carbon other than graphite, which has a greater Li^+ diffusivity across its full lithiation range will enable this, as might increasing the operating temperature of the cell and decreasing the thickness of the composite layer. Less critically, modifications could also be made to encourage Li-Ag alloying over Li metal precipitation. Use of smaller particle size of silver would increase the surface area of contact for reaction, and once again higher operating temperatures are expected to improve the reaction kinetics.

4.4.5 The role of silver nanoparticles in composite interlayers

The use of composite interlayers in the Li-free cells is motivated by their ability to suppress dendrites and promote higher charging rates.[214,362,372,373] However, the results from this study indicate that in the case of the graphite-silver composite interlayer, dendrites are suppressed at low rates (< 2.5 mA cm^{-2}) because at these currents the rate of intercalation of Li in graphite is faster than the rate of Li nucleation at the solid electrolyte interface, enabling Li plating and Li-Ag alloy formation at the interface with the current collector. No evidence was found of direct electrochemical alloying of silver at the interface with the solid electrolyte, as shown in Figure 4.12. This is likely due to the low quantity of silver present in the composite interlayer. This again prompts the question of the role of silver nanoparticles in the composite interlayer as discussed in Section 4.4.4, it doesn't help in higher critical current density, and then what does it do?

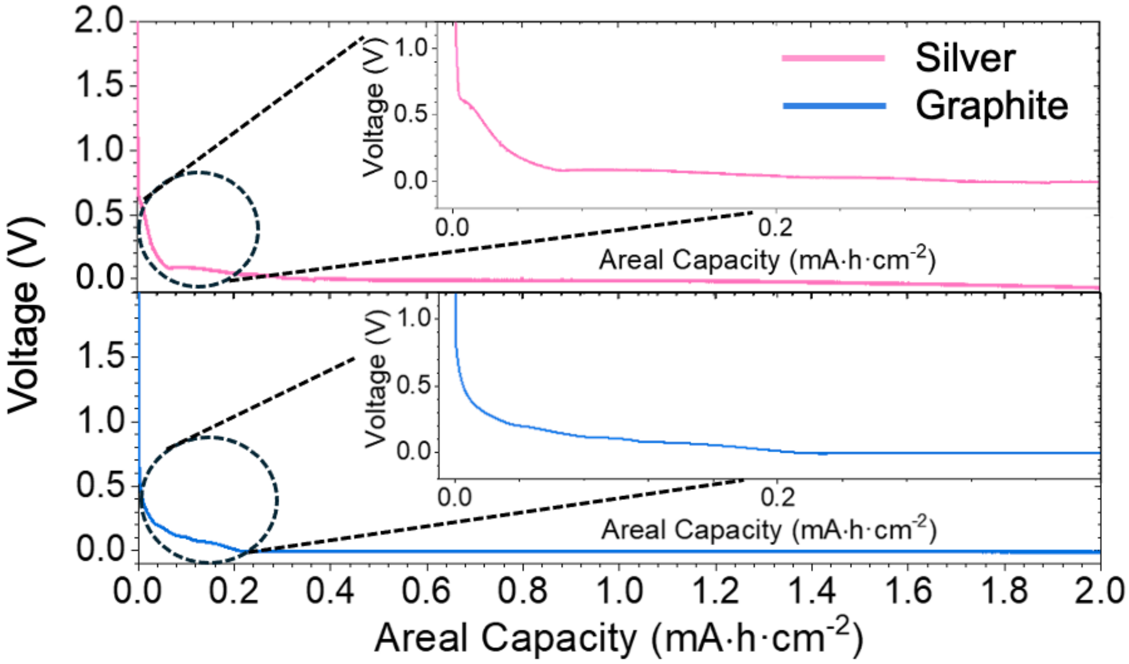

Figure 4.12. Voltage profiles of silver only and graphite only interlayers when charging at a current density of 30 μA cm^{-2}. Silver only is shown on top as pink and graphite only interlayer charging profile is shown as blue in bottom.

SEM study conducted by Dr Dominic Spencer Jolly[229] in Figure 4.13, raises another interesting question, why does Li nucleate at the current collector interface rather than solid electrolyte interface for rates below critical current densities i.e. ≤ 2.0 mA cm^{-2} as shown in Figure 4.13a and 4.13b. Dr Dominic Spencer Jolly also observed the same phenomenon for just the graphite interlayer with no silver nanoparticles. At current densities below 2.5 mA cm^{-2}, for the graphite only interlayer, it was observed that Li lithiates graphite into LiC_6 and deposits on the current collector as shown by Figure 4.13c. What is the role of silver then, if it's not promoting Li deposition at the current collector interface at higher rates of charge? Some studies[1,215,230,297] have stated that Li metal deposits at the current collector interface rather than the solid electrolyte due to the relative nucleation overpotentials at the different sites, with lower surface energies and potentially greater free space favouring the current collector interface as discussed in Chapter 3, Section 3.4.5.

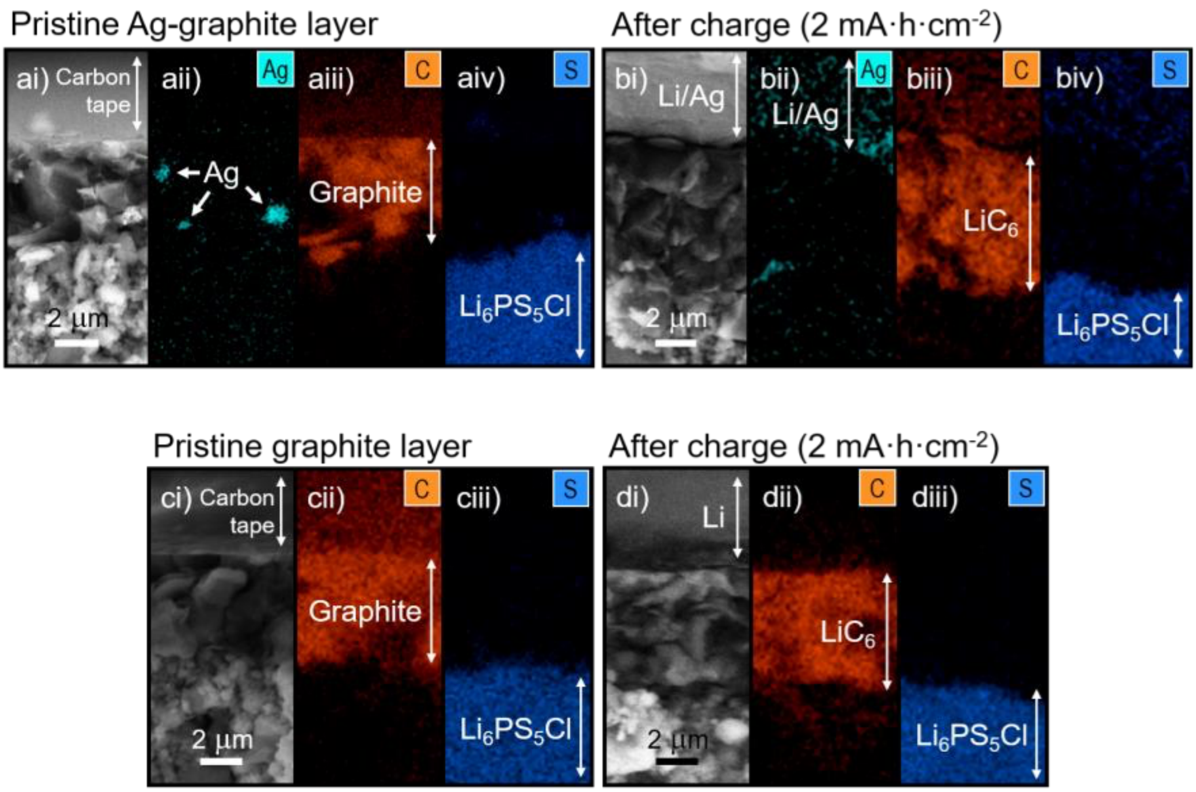

Figure 4.13. A graphite only and a graphite-silver interlayer cross-sectional SEM/EDX images with Li_6PS_5Cl solid electrolyte. a) pristine graphite-silver composite interlayer with Li_6PS_5Cl; b) after charging the graphite-silver interlayer to 2.0 mA h cm^{-2}; c) pristine graphite only interlayer with Li_6PS_5Cl; d) after charging the graphite only interlayer to 2.0 mA h cm^{-2}. EDX maps showing orange for carbon, blue for sulphur and teal for silver. After charging, in case of graphite-silver composite interlayer a silver rich layer can be observed to plate between the composite interlayer and stainless-steel current collector. In case of graphite only interlayer, Li metal can be seen to deposit between the graphite only interlayer and stainless-steel current collector as can be confirmed by no EDX signal (Li metal). Reprinted with permission from Spencer-Jolly & Agarwal et al.[1] The image was collected by Dr Dominic Spencer Jolly and data is published in his thesis.

Figure 4.14 compares cells with just graphite only interlayer and graphite-silver composite interlayer to explore the role of silver on first charge and discharge. This has been explored by a series of SEM and associated EDX images collected on the surface of the composite interlayer, which was in contact with the stainless-steel current collector. For each cell, after careful removal of the stainless-steel current collector, the surface of the interlayer was examined for pristine, after charging at 2.0 mA cm^{-2} and after fully discharging the cell, with 2.0 mAh cm^{-2} capacity passed on charge. After charging, the graphite only interlayer, Figure 4.14b, shows highly inhomogeneous deposition of Li metal above the graphite layer. The honeycomb-like web structure is most prominent at the interface, although other lithium morphologies such as flake-like growths were also observed as shown in Figure 4.14b. On subsequent discharging of the cell, some Li metal persists at the top the graphite interlayer as shown in Figure 4.14c. (Li is not detected by the EDX, so the regions where carbon signal is not detected is assumed to be low atomic number Li metal). This inhomogeneous stripping of Li metal is most likely due the rate of delithiation of graphite under the discharge current load exceeding the rate at which Li metal could react with the delithiating graphite.

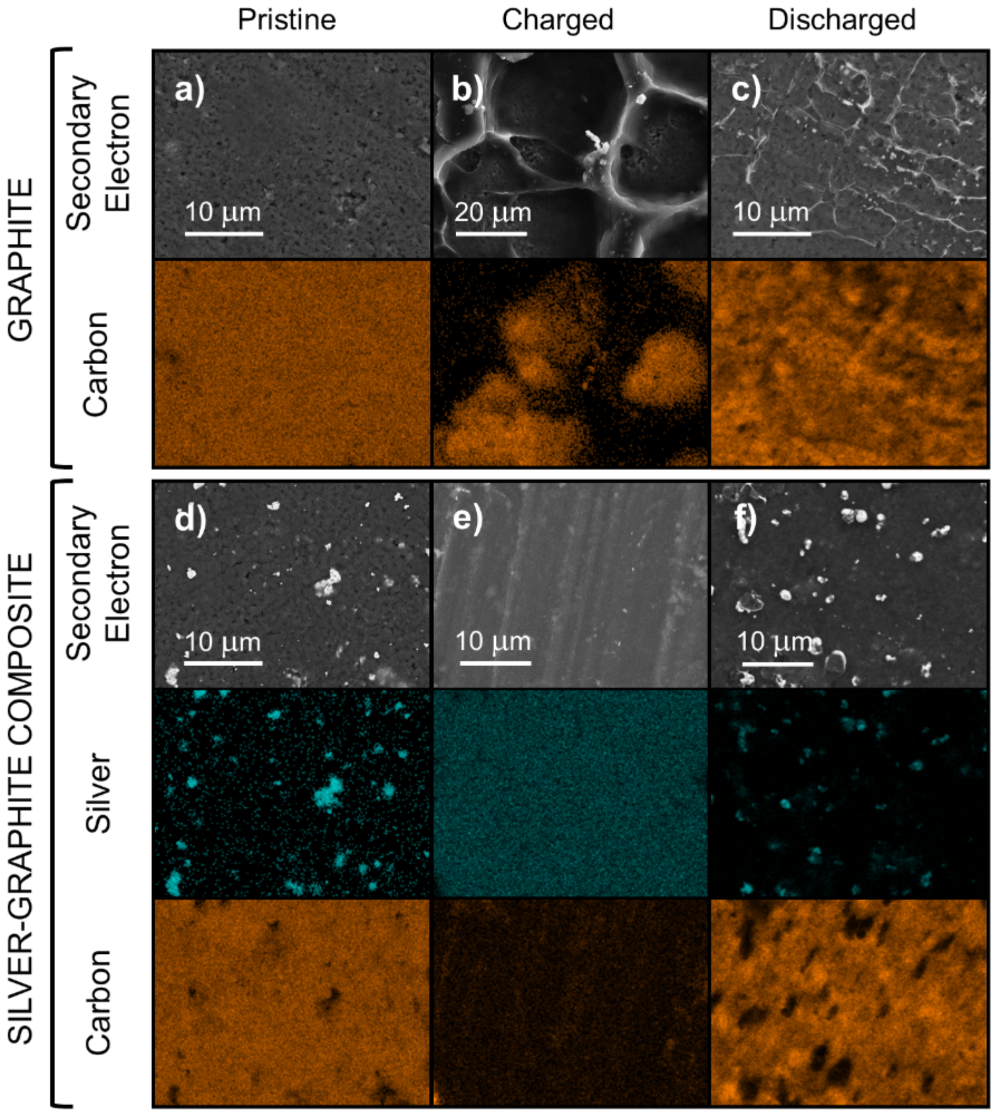

Figure 4.14. Graphite only and graphite-silver composite interlayer SEM/EDX colour maps of surfaces after charge and discharge at 2 mAh cm^{-2} at 60°C at 0.1 mA cm^{-2} current density after the careful removal of stainless-steel current collector. (a) to (c) graphite only and (d) to (f) graphite-silver composite interlayer. (a) and (d) are pristine; (b) and (e) after charging; and (c) and (f) after discharge. Reprinted with permission from Spencer-Jolly & Agarwal et al.[1] This data was collected in collaboration with Dr Dominic Spencer Jolly.[x]

A contrasting deposition morphology was obtained in the presence of the graphite-silver interlayer as can been seen through Figure 4.14e, which shows uniform deposition of Li-Ag alloy and Li metal. The uniformly deposited nucleation is a mixture of Li-Ag alloys

---

[x] Figure 4.18a and b was collected by Dr Dominic Spencer Jolly and the image visualisation was adapted from his thesis and published in co-shared research paper. Other images were collected by me.

and Li metal as seen by EDX. On subsequent discharging, much of the Li-Ag alloy returns to the graphite interlayer. It should be noted that as lithium signal cannot be directly detected through EDX mappings, regions in the carbon EDX, which are devoid of carbon signals (the black regions) are greater in area than the regions that are occupied by silver signal, suggesting that there may be some Li-Ag alloy and Li metal remaining after discharge, as shown in Figure 4.14f. This remaining Li-Ag and Li metal would explain some of the capacity loss experienced over the first cycle of the cell, which is discussed in next section. All these SEM/EDX images imply that the main role of silver in the composite interlayer is promoting homogenous morphology of Li nucleation and formed Li-Ag alloy on charge, and homogenous return of Li metal and Li-Ag alloy on discharge.

4.4.6 Full cell performance of graphite-silver composite interlayers

Full cells were assembled, either using a graphite-silver interlayer, or a graphite only interlayer, as discussed in Section 4.3.1.6. For the solid-state composite cathode, single crystal $LiNi_{0.83}Mn_{0.06}Co_{0.11}O_2$ (MSE Supplies), ultra-fine Li_6PS_5Cl (MSE Supplies) and carbon nanofiber (CNF) (Merck) with a mass ratio of 70:28:2. It was mixed by pestle and mortar. Full cells were investigated at 60°C to keep the study comparative with previous sections. All full cells were charged at 0.5 mA cm^{-2} and discharged at 0.1 mA cm^{-2}, unless stated otherwise. The experiments discussed here were performed at 2 MPa stack pressure.

4.5 mm diameter disks of circular interlayer on stainless steel current collector were punched and dried in vacuum for 2 hours before being used in a full cell. As can be seen from Figure 4.15a, the coulombic efficiency of graphite was lower than the coulombic efficiency for graphite-silver composite interlayer. It was also observed that the graphite only interlayer full cell short circuits after approximately 5-7 cycles at 0.5 mA cm^{-2}, while the graphite-silver composite interlayer full cells were observed to cycle for up to

100 cycles at 0.5 mA cm^{-2}. In this only 20 cycles are shown, to keep the graph easy to read. Moreover, the best cell data was selected from a sample size of 5 cells for graphite-silver composite interlayer, but only one operational cell for graphite was obtained due to high failure rate as shown in Figure 4.15. Furthermore, as observed in Figure 4.15b, the discharge capacity for the graphite only interlayer decreases over cycling to a much greater extent than the graphite-silver composite interlayer. This longer cycling with better coulombic efficiency and discharge capacity over longer cycles for graphite-silver composite interlayer is due to the role of silver discussed in above section. Since silver helps in homogenous stripping of lithium and Li-Ag alloy, it helps to provide better full cell performance. Nevertheless, although the graphite-silver composite interlayer performs better than the graphite only interlayer, it still does not show the performance required from practical batteries.

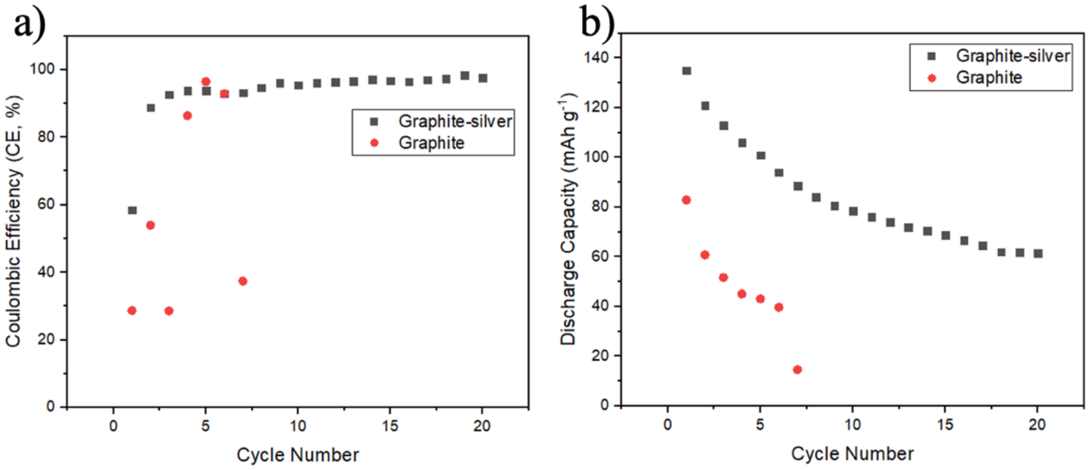

Figure 4.15. Coulombic efficiency using full cell compared for cells with graphite only layer and for cells with graphite-silver composite interlayer at 0.5 mAcm^{-2}, 2 MPa and 60°C; b) Discharge capacity using full cell compared for cells with graphite only layer and for cells with graphite-silver composite interlayer.

4.4.7 Strategies to improve full cell performance of graphite-silver composite interlayer cells

As discussed in Section 4.4.6, despite demonstrating an extended cycle life, improved coulombic efficiency, and higher discharge capacities through the homogenous nucleation of Li metal, the performance of full cells utilising the graphite-silver composite interlayer in purely a "Li-free" or "anodeless" batteries was not commercially viable. These results suggest that while the incorporation of silver in the composite interlayer has benefits, further optimisation is necessary to achieve the desired commercial battery performance standards. Therefore, methods to improve the cycling performance were investigated for full cells.

Full cells were assembled using graphite-silver and graphite only interlayers as discussed in Section 4.3.1.6. A 50 µm thick Li foil (5 mm diameter) is put behind these interlayers i.e., between the interlayer and stainless-steel current collector, to investigate the role of these interlayers in an all-solid-state battery. As can be seen from Figure 4.16, when Li is put between composite interlayer and current collector these interlayers, such that the cells are no longer “Li-free”, the coulombic efficiency increases markedly. Another key observation is that it is almost as same as the graphite-silver composite interlayer. Similarly, the discharge capacity for the cell with the graphite only interlayer with Li foil behind as shown in Figure 4.16b increased to 180 mAh g^{-1} for first cycle compared to 80 mAh g^{-1} for only graphite interlayer without Li foil in Figure 4.15b.

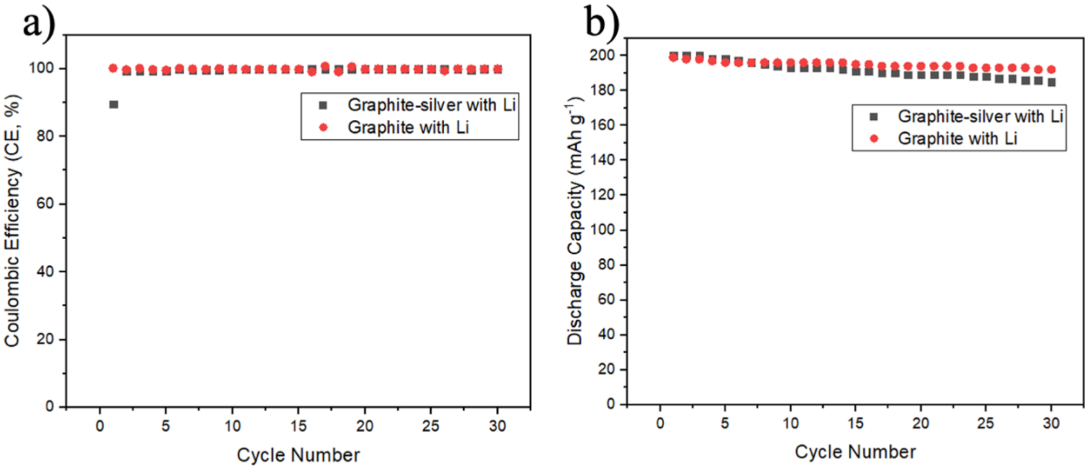

Figure 4.16. Comparing the coulombic efficiency of a full cell with a graphite-only layer and lithium between composite interlayer and current collector, to that of a full cell with a graphite-silver composite interlayer and lithium between composite interlayer and current collector at 0.5 mA cm^{-2}, 2 MPa and 60℃.; b) Discharge capacity using full cell compared for cells with graphite only layer and Li between composite interlayer and current collector and for cells with graphite-silver composite interlayer and Li foil between composite interlayer and current collector.

Figure 4.17 shows comparison using bar graph for CE % and discharge capacity for four different cells and an interesting point to note in Figure 4.17, is that the CE% and discharge capacity for just graphite with Li (shown in red bar) behind is higher than graphite-silver with Li behind (shown in purple). When there is no Li present, silver plays a key role in homogenous deposition but in presence of Li foil behind the interlayer, the role of silver becomes obsolete as there is already a homogenous film of Li present behind the interlayer, which promotes better stripping capabilities. Indeed, it may even have a negative impact by exacerbating the volume change of the anode.[214]

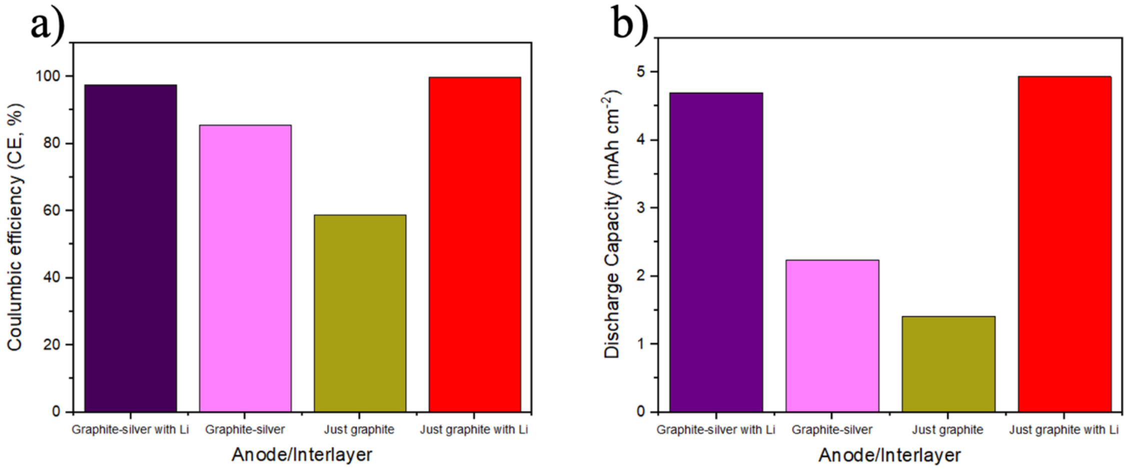

Figure 4.17. a) Coulombic efficiency compared for four different systems in a full cell at 0.5 mA cm^{-2}*, 2 MPa and 60ºC; b) Discharge capacity compared for four different anode interlayers in a full cell.*

One proposed mechanism is that, in the presence of Li, the graphite remains as lithiated graphite i.e., LiC_6 phase all the time during charge and discharge, so the Li coming from cathode is never used for intercalating the graphite and hence the interlayer just acts as a protective barrier to dendrite suppression, promoting higher cycling performance. To further prove this point, more experimental work is needed, which is beyond the scope of this thesis.

4.5 Conclusions

In this investigation, both graphite and graphite-silver composite interlayers effectively promote high charging rates and protect the solid electrolyte from Li dendrite growth. Mechanistic understanding of structural changes happening in composite interlayers is discussed.

The study demonstrated that graphite-silver composite interlayers function through lithium intercalation into graphite during charging and deintercalation during discharge. Chemical reaction of silver with LiC_x was investigated. Chemical potential of Li in LiC_x and Li_xAg

determines the changes in composite as demonstrated by *operando* XRD. When the lithium chemical potential in graphite increases on Li intercalation, chemical reaction with silver occurs and Li_xAg alloys when they are formed and as the Li chemical potential decreases on discharge, Li_xAg alloys are delithiated. Li-Ag goes through different phases of LiAg, Li_9Ag_4 (CsCl and UPb structure) and $Li_{10}Ag_3$ as observed by *operando* XRD. At all rates, Li metal is deposited on top of the interlayer. Li dendrites are found to penetrate at rates above critical current density i.e. 2.5 mA cm^{-2}. It was observed that silver nanoparticles helps in homogenous deposition of Li metal and alloy between the composite interlayer and current collector and on discharge, it helps in homogenous stripping, while in the case of just graphite only interlayer, inhomogeneous deposition of Li was observed. This was further proved by full cell performance, where the interlayer with silver performed more cycles with higher coulombic efficiencies and discharge capacities than graphite only interlayer.[205]

This study has helped to understand the structural changes happening in composite interlayers, which is a topic of interest after the researchers at Samsung Advanced Institute of Technology[214] reported a composite interlayer showing good performance.

4.6 Future work

4.6.1 Investigating the role of Li behind these interlayers

As discussed in Section 4.4.7, putting Li foil behind these interlayers, helps to improve the cell performance many folds. So, these interlayers should also be investigated for all-solid-state batteries rather than just for Li-free ASSBs. It is important to understand the mechanism and structural changes of these composite interlayers in presence of Li metal, to make a well-informed analysis on the role of graphite-silver composite interlayer.

4.6.2 Exploring different carbons and metal nanoparticles

In this investigation, the structural changes happening in just graphite and graphite-silver composite interlayers are discussed. It will be interesting to investigate different types of carbon, such as hard carbon, soft carbon, graphene, carbon nanotubes etc, having different properties such as diffusivity, size and then study their full cell performance. It will also be important to examine factors such as volume expansion and the diffusivity of Li^+ through these carbon materials, as the transport of Li^+ varies depending on the type of carbon used.[359,362,371,374] This work is being explored by Lechen Yang in our research group for her DPhil study.

The selection of graphite as the material for this study was based on its well-documented usage in prior research. This made it an ideal material to investigate the mechanism of the graphite-silver composite system for interlayers. By utilising a familiar material, it was easier to understand and interpret the results of the study, providing valuable insights into the behaviour of the system. As it was found in Section 4.4.7, the impact of silver in the presence of lithium is not significant, thus, it is imperative to explore various types of carbon and metal nanoparticles in a similar configuration for various conditions, including current densities, pressure, thickness, and temperature. This is essential to gain a comprehensive understanding of the system's behaviour and performance. It is recommended to conduct further investigations to assess the effects of these parameters on the system's efficiency and effectiveness. Such studies could contribute significantly to the development of more efficient and reliable energy storage systems. Therefore, it is crucial to explore different types of carbon for various conditions to obtain a thorough understanding of the system's behaviour and performance.

Moreover, as different metals have different properties, it will be interesting to investigate the role of them in these interlayers. Metal nanoparticles such as aluminium, zinc, magnesium, gold and stainless steel with varying properties, sizes and nucleation potential would be interesting to explore.

4.6.3 Other areas to investigate

Discharge mechanism for graphite-silver composite interlayer was discussed in this chapter at low rates. However, it will be interesting to explore this further at high rates and for different carbons to determine whether the mechanism changes or it remains same. Morphology study during discharge can give useful insights into the CE% and discharge capacity mechanism. Moreover, it can also help to understand the poor cycling performance in absence of silver nanoparticles. However, due to limitations on *operando* investigation of full cell study, it might prove to be a challenging task.

5 Chapter 5: Surface treatment of Na-β”-Alumina solid electrolyte by plasma cleaning

5.1 Overview

All-solid-state batteries with alkali metal anodes can achieve high current densities but one of the major challenges for ASSBs is the need for non-contaminated surfaces to obtain low interfacial resistance. In this chapter, plasma cleaning is demonstrated to be a potential surface treatment technique to remove impurities from the surface of Na-β”-Alumina (NBA) after the solid electrolyte (SE) has been exposed to air for 24 hours. NBA was selected as the model SE for this investigation due to its high ionic conductivity and excellent stability against sodium metal anode. Here, different conditions were investigated to optimise the plasma treatment. Finally, SEM and XPS were used to understand the effect of plasma cleaning on the morphology and surface chemistry on this SE, and how these relate to the interfacial resistance against a Na anode.

5.2 Introduction

The NBA possesses environmentally friendly properties and is composed of abundant elements. It exhibits notable characteristics such as high ionic conductivity, mechanical strength, and low electronic conductivity with exceptional electrochemical stability.[111,114] Wenzel et al.[63] demonstrated that NBA remains stable when exposed to sodium. Additionally, disk-shaped NBA is increasingly utilised in solid-state batteries for mid-to low-temperature applications.[375]

In the past, research literature has highlighted the detrimental effects of water vapor on the performance of NBAs, particularly during the 1970s and 1980s.[221, 378] These effects increase weight and reduce ionic conductivity.[94] Surface layers were observed to develop, along with alterations in the position and intensity of reflections in diffractograms and resulted in increased resistance in the radial direction for tubular samples and annulets stored in laboratory air. Fertig et al.[221] studied the effect of humidity on Li stabilised NBA in three different environments and found that the ionic conductivity gradually decreases up to two orders of magnitude due to layers developed during storage. It is believed that water initially gets trapped in the ceramic's micropores, followed by a slower ion exchange process where H_3O^+ replaces Na^+, leading to the increase in resistivity of NBA by more than an order of magnitude.[377]

The interaction between the SE and its adjacent electrodes is crucial as insufficient contact at the interface can result in the formation of dendrites and short circuits at high currents.[104,181,378] Going beyond the critical current density (CCD) as defined by Bruce and co-workers in Section 1.2.3.3. leads to the failure of the electrolyte and ultimately results in cell malfunction.[184] Bay et al.[181] showed that the maximum plating current density is related to the interfacial resistance between the SE and the metal electrode. Decreasing the resistance leads to increase in CCD.

SEs lack of sufficient chemical stability can lead to degradation of interfaces, causing an increase in resistance and overpotential.[63,64] Therefore, it is necessary to engineer the interfaces of the negative and positive electrodes. Even if the electrolyte has high macroscopic conductivity, it may exhibit high impedances if it is not compatible with the electrodes.[64] A good interface between SE and the electrodes leads to fast ion transport, maximum contact area and chemical stability throughout cycling.[379] Hence, the effectiveness of ASSBs is no longer limited by the ability of the SE to conduct ions, but rather by the lack of sufficient contact between the rigid SE and its adjacent electrodes.[353] To achieve optimal performance in these cells, it is crucial to ensure good contact between the SE and electrodes, along with the mechanical and structural stability. This requires modifications to SEs and a better understanding of their interfacial stability for novel cell systems.[15,123,380]

Surface treatments and modifications are particularly important for cell systems operating at room temperature, where maintaining sodium wetting is challenging.[336,342] Reasonable sodium wetting, which refers to intimate contact between the sodium negative electrode and NBA, leads to low polarisation, improved electrochemical cell performance and longer cycle life.[381,382] Fortunately, NBA shows excellent stability against sodium metal, so any side reactions happening are due to the presence of contaminants on the surface of NBA resulting in interfacial film formation.[63,382] Therefore, it is important to investigate surface treatment techniques to minimise the effect of water uptake due to exposure to air.

Plasma cleaning is often considered more interesting than heat treatment as a surface treatment technique due to several advantages it offers such as enhanced surface activation, selective cleaning, and lower thermal impact compared to heat treatment. As heat treatment can induce thermal stress, dimensional changes, and potential damage to sensitive components.[244] In contrast, plasma cleaning operates at lower temperatures, minimising the thermal impact on the material. Additionally, it is a chemical-free process, versatile and has a short processing time.[242,248] These factors contribute to increased interest as a surface treatment technique in various industries and applications.[243,383]

A Na|NBA|Na symmetric cell was chosen as a model system because the Na|NBA|Na interface is thoroughly characterised, with extensive literature evidence showing no chemical reactions between the electrode and electrolyte.[63] This stability ensures that any changes in impedance can be attributed to surface contamination rather than chemical interactions between Na and NBA.[63,178] Finally, NBA's inert nature compared to sulphides, makes it an ideal model for studying plasma cleaning as a surface treatment.

5.3 Experimental Methods

5.3.1 Cell Fabrication

5.3.1.1 Preparation of NBA solid electrolytes disks for plasma cleaning

Commercially manufactured disks of NBA were purchased from Ionotec Ltd, with 10 mm diameter and 0.7 mm thickness.[229,378] The disks were stored in an Ar filled glovebox (O_2 and H_2O <0.1 ppm).

The purchased NBA disks were successively polished using SiC paper with increasingly finer grits, starting with 800, followed by 1200, 2500, and finishing with 4000. These disks were then vacuum dried overnight at 60°C and then heat treated in a platinum crucible at 900°C for 10 hours in a furnace, stored in argon-filled glovebox. This method was adapted from Dr Dominic Spencer Jolly[229] and Bay et al.[181] These disks were then exposed to air for 24 hours by leaving them in an open vial before further surface treatments, to test the effectiveness of plasma cleaning at removing contaminants from air-exposed samples.

5.3.1.2 Two-Electrode half-cells

2-electrode cells were used for testing; the configuration is shown in Figure 5.1. For a Na|NBA|Na cell, Na metal was cut from an ingot stored in argon filled glovebox (O_2 and H_20 <0.1 ppm) and the surface film on sodium metal containing contaminants was removed by scrapping to expose a shiny surface. A thin film of Na metal (approximately 100 µm thick) was cut and pressed on an NBA disk which had been masked by a 5 mm polypropylene mask to control the surface area of contact. Na metal was pressed on both sides of the Na-β"-Alumina disk to make a symmetric cell. This disk was then inserted between copper current collectors in a mylar-coated aluminium pouch cell body and sealed under vacuum. The cells were removed from the glovebox and potentiostatic electrochemical impedance spectroscopy (PEIS) measurements were taken under a 7 MPa stack-pressure. This experimental method is similar to Dr Dominic Spencer-Jolly.[229,378]

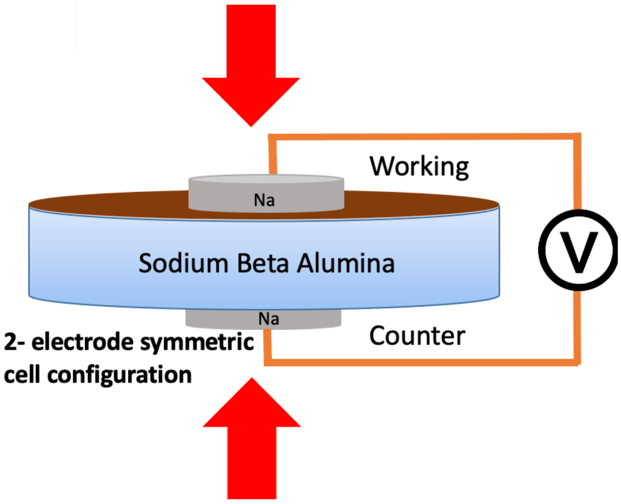

Figure 5.1. Schematic showing the 2-electrode cell configuration used in this chapter using a 5 mm mask shown in brown to control the surface area of sodium metal in contact with solid electrolyte.

5.3.2 Electrochemical Testing of 2-electrode cells

A Gamry 1010E potentiostat was used to conduct PEIS, where 10 points per decade were collected from 1 MHz to 1 Hz frequency range, using a 5 mV perturbation. All measurements were done on 2-electrode symmetric sodium cells at 30°C. ZView software was used for analysing and fitting the data.[y]

5.3.3 Plasma Cleaner

A custom designed Diener plasma cleaner[z] was used to carry out the surface treatment. This instrument was kept in an argon-filled glovebox to enable loading and unloading under an inert atmosphere. The instrument is connected to different gas sources, which can be

---

[y] These are standard experiment conditions used in our research group to keep the data comparable between different studies.[229,378]

[z] The plasma cleaner was customised by previous research group members.

changed. Different optimisation conditions were used. The total power of the plasma cleaner is 200 W. Throughout the chapter, RF 10, 50 and 100 corresponds to 20 W, 100 W and 200 W power, unless stated otherwise.

5.3.4 Heat Treatment

The samples were heat treated in a furnace kept in argon atmosphere at 900°C for 10 hours, with heating and cooling rates of 5ºC/min.

5.3.5 Impedance *vs* time

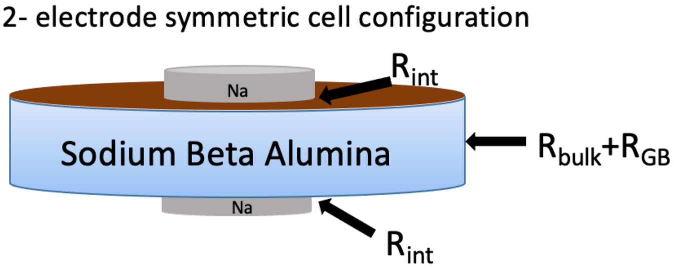

Figure 5.2. Schematic showing the origin of the bulk, grain boundary and interfacial resistances in a symmetric NBA cell.

To study the impact of heat treatment and plasma cleaning on the interfacial resistance (R_{int}) between the NBA disk and sodium metal as shown in Figure 5.2. PEIS measurements were conducted for untreated, heat treated and plasma cleaned pellets. NBA disks were used in the assembly of symmetric half-cell as described in Section 5.3.1.2 and PEIS *vs* time was collected every 1 hour for 96 hours to analyse the reactivity of the surface contaminants with the sodium metal over time.

5.3.6 Wettability test

The Na metal was melted in a stainless-steel crucible and dropped on the surface of the NBA disk. Both were kept on top of a hot plate, with a temperature around 150°C, to keep the temperature of both the stainless-steel crucible and NBA disk above the melting point of Na metal. The native layers present on the surface of the Na metal were scraped off to expose a shiny surface. This ensured that the Na metal deposited on the surface of NBA disks was devoid of any impurities present on its surface. This was adapted from a similar method discussed by Sharafi et al.[183] for testing wettability of Li metal on LLZO, after surface treatment. Images were captured using a high-resolution camera (Grasshopper GRAS-50S5M-C) with a Fujinon HF75SA-1 lens, kept in a glovebox and analysed using Fiji ImageJ software. All the experiments were performed in an argon atmosphere glovebox.

5.3.7 Characterisation

5.3.7.1 SEM

SEM was performed on untreated and treated samples to track the morphological changes. The cells were disassembled in an argon filled glovebox. The samples were then mounted on Gatan stage using carbon adhesive tape. The stage containing the plate with mounted samples was then sealed in an air-tight transfer holder, which was used to transfer the samples to Merlin SEM (Zeiss) from the glovebox without exposure to air. Secondary electron imaging was carried with an accelerating voltage of 10 kV and a probe current of 200 pA.

5.3.7.2 XPS

X-ray photoemission spectroscopy (XPS) was used to analyse the interfacial chemical reactivity occurring at the surface of solid electrolyte. The experiment was conducted by

Dr Joshua Gibson[aa] from Department of Materials, Oxford using a PHI Versaprobe III under ultrahigh vacuum conditions, with the main chamber maintained at pressures between ~10^{-7}-10^{-6} Pa. Focused, monochromatic Al Kα X-rays at 1486.6 eV were generated at a power of 25 W and an electron beam voltage of 15 kV. To avoid contamination and exposure to air, samples were transferred from an argon filled glovebox into the XPS chamber using a custom vacuum transfer vessel. All measurements were conducted on three different spots in the diameter of 10 mm of each sample. Charge compensation using argon ion gun and low charging electron was utilised to prevent sample charging. The acquired spectra were fitted using CasaXPS software, after application of a Shirley background and Lorentzian Asymmetric Lineshape(50). More details on parameters and constraints used can be found in Appendix Table A.2. In this study, all spectra were calibrated to adventitious carbon at 284.8 eV using acquired carbon C 1s spectra.[63] All experiments were performed under these conditions unless stated otherwise.

5.4 Results and Discussions

5.4.1 Surface treatment of NBA Disks

Contaminants such as carbonates and hydroxides are commonly found on the surfaces of materials such as oxide ceramics, and these can hinder the adhesion of other materials during subsequent processing.[183,221] As investigated in prior studies for oxides SE's, contaminants impact the mechanical, electrochemical and safety performance of ASSB.[181,384,385] Recently, open-air plasma treatment was employed to remove Li_2CO_3 surface contaminants from a LLZTO SE and the study also explored the effect of different

---

[aa] The prepared sample was provided to Dr Joshua Gibson to run the instrument and the collected data was processed by me using CasaXPS.

process parameters through XPS.[182] However, this technique has never been employed to remove the surface contaminants for a sodium based SE.

During the plasma cleaning process, ions, radicals, and high-energy UV radiation work together to break down the carbonates and hydroxides. Meanwhile, gas radicals are formed and attach themselves to the free ends of the broken molecules, creating new by-products. These by-products are then removed from the chamber using a vacuum. This cleaning method is suitable for almost all materials, and purified dry air or gases such as argon, nitrogen, oxygen or a mixture of these can be used.[241,249,386]

As highlighted in the review by Hueso et al.[112] numerous studies on sodium based batteries have been conducted using molten sodium as the anode, which requires the use of high temperatures, resulting in low interfacial resistances. Consequently, surface treatment of these NBA is not required at high temperatures. However, the interfacial resistance of NBA with solid Na metal is found to be quite high at room temperature as discussed in later sections.[181] So, to achieve high critical current densities and long cycling, it is essential to optimise the NBA surface to achieve an interface with minimal resistance.[63,181,378] To achieve this, plasma cleaning is explored as a potential alternative to energy intensive heat treatment.

5.4.2 Comparative study of different surface treatment techniques

5.4.2.1 Using PEIS

The surface of an untreated NBA sample was compared to samples prepared using heat treatment and plasma cleaning by measuring the interfacial resistance 24 hours after cell assembly. Figure 5.3 represents the comparison of different surface treatments with (a-c) showing equivalent circuits, d) corresponding Nyquist plots and e) bulk+grain boundary and interfacial resistance. The PEIS spectra in Figure 5.3d show semi-circular contributions which are representative of bulk, grain and interface resistance. All three PEIS were modelled as a resister (R) with a constant phase element (CPE) in parallel, using different R/CPE circuits due to the different contributions that are fittable in the data. As described by Irvine, Sinclair and West[293] each contribution was assigned as a physical process that is occurring within the cell from the calculated characteristic capacitances.

Representative Nyquist plots of cells containing SEs prepared with the different surface treatment techniques are shown in Figure 5.3d. As can be seen from Figure 5.3d, the optimised plasma cleaned NBA pellet (black) showed the lowest impedance value of 4 Ω cm^2 (the optimisation of plasma cleaner conditions is discussed later) compared to heat treated (160 Ω cm^2, red) and untreated (3200 Ω cm^2, blue). One key observation to note is that the three equivalent circuits could not be fitted with the same circuit model. This is discussed in detail later.

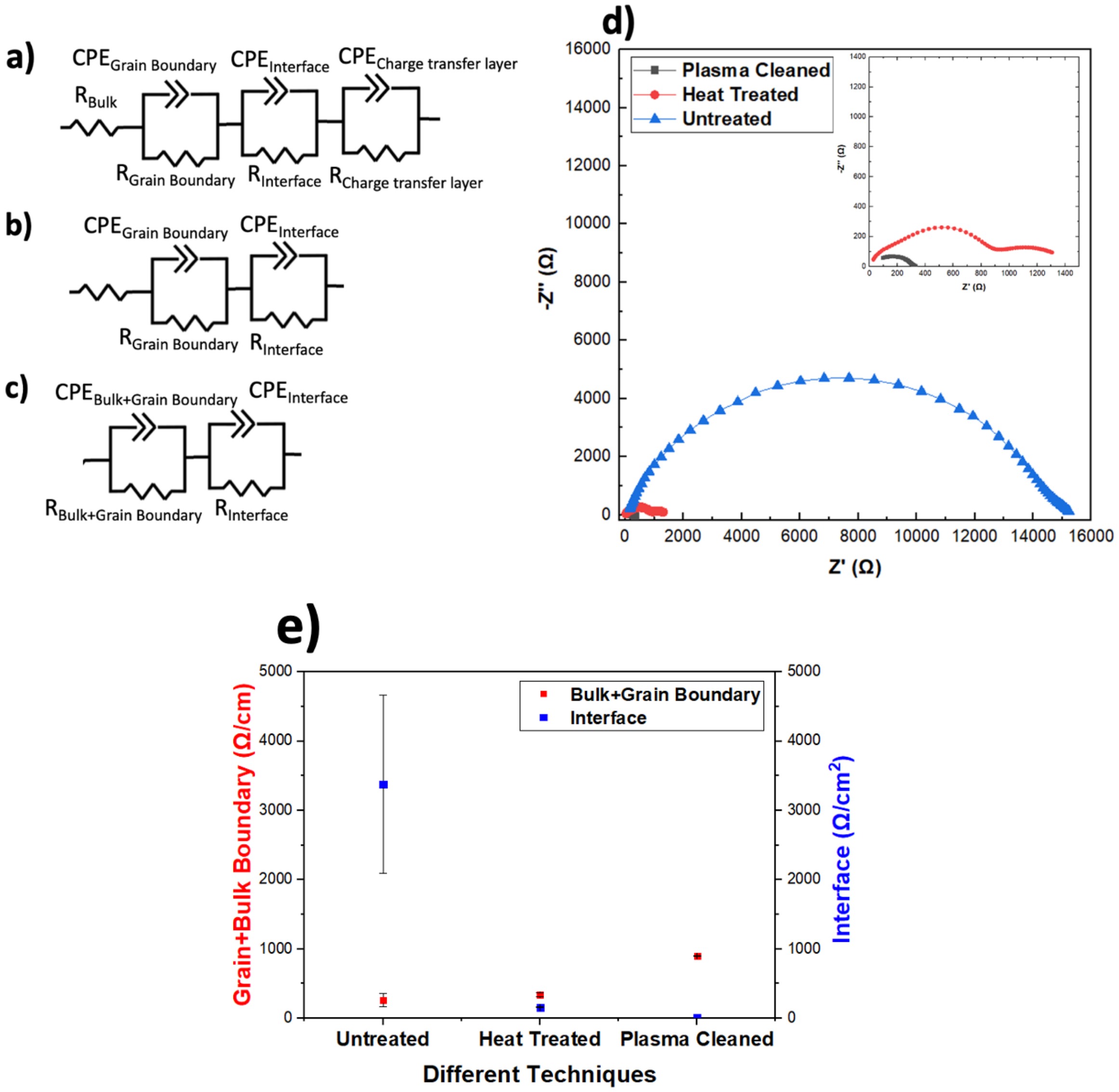

Figure 5.3. Comparison of different surface treatment techniques with an untreated sample. a-c) Schematics representing the equivalent circuit models for untreated, heat treated and plasma cleaned; d) Representative Nyquist plots of respective samples; e) Bulk + grain boundary and interfacial resistance of respective samples.

The untreated disk shows the highest interfacial resistance of 3200 Ω cm^2, where the PEIS spectrum is fitted with three parallel R/CPE circuits in series together with an additional resistor, which accounts for bulk resistance. The first parallel R/CPE circuit represents grain boundary, and the other two R/CPE circuits correspond to interfacial resistance, possibly distinct layers of interfacial impurities as shown in Figure 5.3a.

Sodium beta alumina is known for its chemical and electrochemical stability against sodium metal.[63,111] However, when exposed to water or water vapor, it tends to occlude water molecules and allow the diffusion of hydronium ions into its crystal lattice.[220,221] This occlusion process is rapid and can occur within a few hours, resulting in the formation of a surface layer of several micrometres. This process leads to ion exchange in the conducting plane, which can take several days to complete. β”-Alumina is particularly susceptible to water intake compared to β-Alumina, leading to a significant increase in the SE’s resistivity.[220,221,377] This explains the observation of two interfacial layers for untreated sample and need for a different equivalent circuit to fit the data in Figure 5.3a. To mitigate these effects, it is recommended that researchers should minimise the exposure time of NBA to moisture and consider a treatment step before using them.

The heat-treated sample at 900°C for 10 hours shows an interfacial resistance of 160 Ω cm^2 as shown by Figure 5.3d. The conditions were optimised by Bay et al.[181] in which they showed interfacial resistance of NBA at different heat treatment temperatures and time. The interfacial resistance obtained in this study using similar optimisation conditions is higher than that obtained by Bay et al.[181] This can be due to different pristine state of the sample used, the untreated sample used in this study was exposed to air for a day, while the sample used by Bay et al.[181] in the study was never exposed to air. Spencer Jolly et al.[378] showed that exposure of NBA to air at room temperature increases the resistivity considerably. Bay et al.[181] showed that decreasing the interfacial resistance increased the critical current density of NBA to 12 mA cm^{-2}. The PEIS spectrum for the heat-treated sample was fitted using two parallel R/CPE circuits in series together with an additional resistor, which accounts for bulk resistance as shown in Figure 5.3b. This is the same fitting model used by Bay et al.[181] Due to heat treatment, the impurities present on the surface of the NBA are removed, which helps to decrease the interfacial resistance leading to a different equivalent circuit compared to untreated sample. XPS is used in further sections to explore the surface chemistry due to heat treatment.

The plasma cleaned sample, after optimising the different cleaning parameters (discussed in later sections), shows the lowest interfacial resistance of 4 Ω cm^2, here the PEIS spectra for plasma cleaned sample was fitted using two parallel R/CPE circuits in series together as shown in Figure 5.3c. As the bulk and grain boundary were considered in one semicircle. Because interfacial resistance was too low, it was difficult to separate the bulk and grain boundary resistance. The bulk+grain and interfacial resistance is plotted in Figure 5.3e. A significant decrease in interfacial resistance was obtained after optimising the plasma cleaning conditions. This suggests the use of plasma cleaning as a potential surface treatment technique as it is an energy efficient technique compared to the alternative of subjecting the material to a 10-hour heat treatment at 900°C used by Bay et al.[181] Additionally, plasma cleaning offers the advantage of reducing interfacial resistance as shown in this study, making it a desirable option for enhancing surface properties.

5.4.2.2 Using XPS

To explore the chemical composition of the surface of NBA, XPS was conducted on untreated, heat treated, and plasma cleaned NBA disks and fitted using CasaXPS software.[bb] These data are presented in Figure 5.4, showing spectra of C 1s, O 1s, Al 2p, and Na 2s core levels. Oxidised carbon contamination (C-O/O-C=O) is observed at higher binding energy in all the samples, at 284.8 eV. A high amount of Na_2CO_3 contamination is found in the untreated sample (Figure 5.4a) and the amount of Na_2CO_3 decreases for heat

---

[bb] Details on the parameters used for fitting the data, can be obtained in Appendix Table A.2.

treated and optimised plasma cleaned sample, suggesting the removal of Na_2CO_3 surface contamination. The Na_2CO_3 binding energy value used is reported in the literature.[181,183]

The peak of O 1s spectra is very broad and cannot be fitted as a single component for any of the samples. The broadening of the peaks can be attributed to the formation of the interfacial contaminants present on the surface of the SE.[181] However, the width of the peak decreases slightly for the surface treated samples implying a reduced concentration of the interfacial species. Using the values present in literature[181], the peak at 530.7 eV, shown in blue in Figure is 5.4c fitted as Al-O peak from the NBA structure and hydroxyl, Al-OH at 532.2 eV present as a surface contaminant corresponding to orange in Figure 5.4c. Moreover, C-O/O-C=O and Na_2CO_3 peaks are observed at corresponding binding energies with the intensity decreasing in surface treated samples compared to untreated sample. Moreover, there is an unfitted additional small peak at higher binding energy in all the O 1s spectra, which is attributed to auger peak.[387] Due to the complexity involved in fitting the peak, it is not fitted as it is beyond the area of interest in this study.

Al 2p spectra are also shown in Figure 5.4c, the Al 2p doublet ($2p^{3/2}$ and $2p^{1/2}$) can be assigned to Al-O and Al-OH. Na 2s spectra were also fitted, which shows the treatment decreases the Na_2CO_3 contamination, which is consistent with the results from spectra C 1s and O 1s.[181]

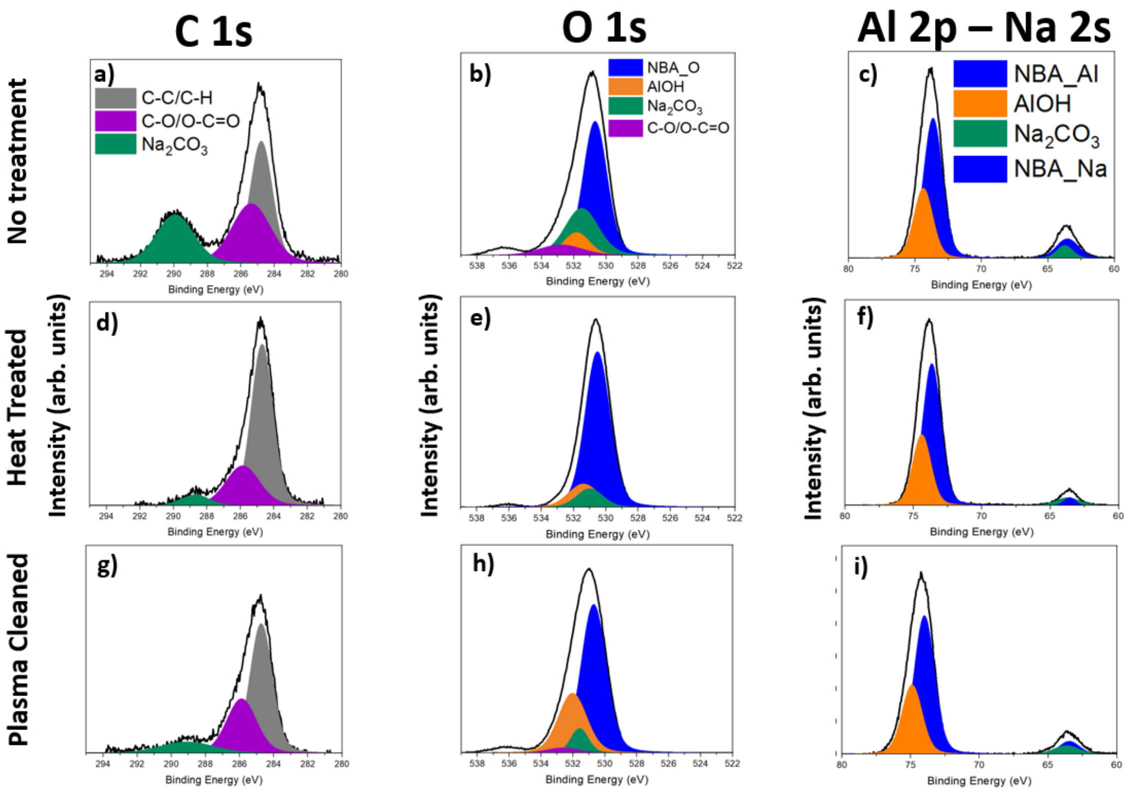

Figure 5.4. XPS analysis of Na-β"-Alumina surfaces when untreated, after heat treatment and after plasma cleaning. XPS spectra of C 1s, O 1s, Al 2p-Na 2s core levels spectra of Na-β"-Alumina; a-c) before any treatment; d-f) after heat treatment; g-i) after plasma cleaning. Data was collected by Dr Joshua Gibson.[cc]

The XPS results discussed above confirmed that plasma cleaning and heat treatment, both reduce the amount of hydroxyl groups and carboxyl contaminants significantly on the surface of Na-β"-Alumina. This is in correlation with PEIS data discussed in Section 5.4.2.1, which shows that interfacial resistance decreases to 160 Ω cm^{-2} for heat treated and this for 4 Ω cm^{-2} plasma cleaned NBA samples.

5.4.3 Optimisation of plasma cleaning conditions

As can be seen by Figure 5.3d, plasma cleaning helps in removing the surface contaminants and giving low interfacial resistance values. To maximise the transport kinetics, the plasma

---

[cc] The data was collected with help from Dr Joshua Gibson, where I prepared and transferred the sample and Dr Gibson operated the XPS instrument.

cleaning conditions were optimised, such as the effect of gas, RF power and time as these parameters can affect the removal of contaminants.[247] All the measurements were performed on fresh and identical electrolyte disks. As discussed by Sahal et al.[182], all these parameters affect the extent of removal of surface impurities for LLZTO. However, they did not study the effect of power in plasma cleaning.

5.4.3.1 Using different plasma gases

NBA disks prepared as described in Section 5.4.1.2 were taken from argon filled glovebox and exposed to air for 24 hours and then plasma cleaned in different plasma gases: oxygen, nitrogen and argon, for 15 min at 100 RF to study the effect of different plasma gases. These plasma cleaned pellets were then assembled into symmetric half cells. Figure 5.5 shows the PEIS after 24 hours of air exposed and then plasma treated NBA with three different plasma gases. As can be observed from Figure 5.5, the interfacial resistance for NBA prepared using the oxygen plasma is relatively high, while the nitrogen and argon plasma give lower interfacial resistances.

This is because argon and nitrogen plasma are typically considered to be inert or non-reactive in terms of oxidation or reduction reactions.[388] However, under certain conditions, nitrogen plasma can react with oxygen to form reactive nitrogen species, such as nitrogen oxides (NO_x) as discussed in the review by Talebizadeh et al.[389] These reactive species can have oxidising properties, but the extent of oxidation depends on the specific plasma conditions and the presence of other reactive species. Whereas oxygen plasma is typically considered to be oxidising in nature. Most of the work on this is done for pulsed power technology.[389,390]

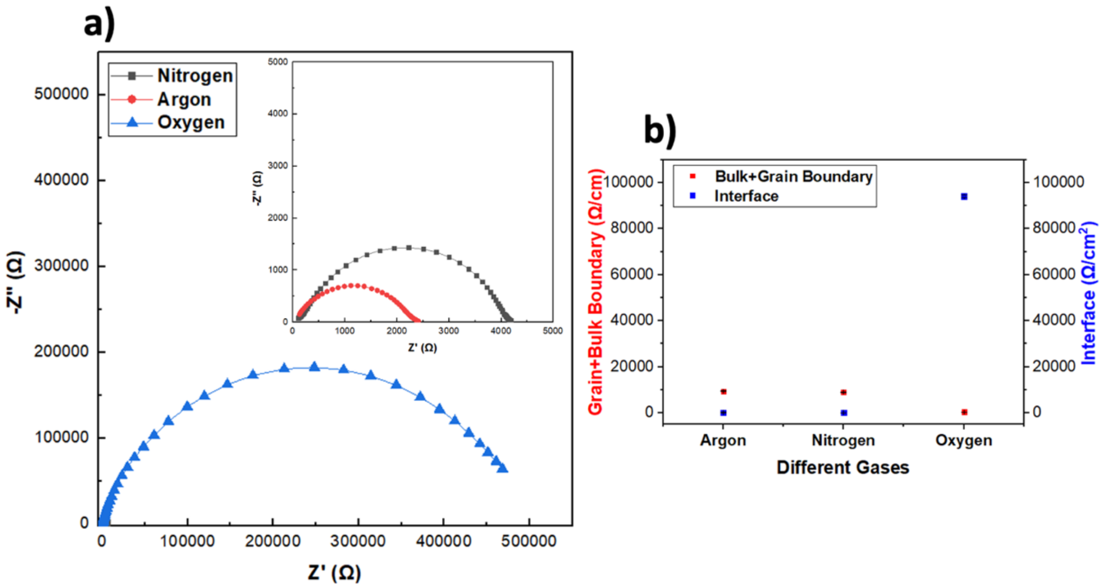

Figure 5.5. a) Representative Nyquist plots for different gases used in plasma cleaning; b) bulk+grain boundary and interfacial resistances for different plasma gases.

Oxygen plasma is generated by subjecting oxygen gas to high-energy electrical discharges, which leads to the dissociation of oxygen molecules (O_2) and the formation of highly reactive oxygen species, such as atomic oxygen (O) and oxygen radicals (O*). These reactive species readily react with other materials or compounds present in the plasma environment.[391]

It is important to note that the oxidising or reducing properties of a plasma can be influenced by various factors, such as plasma parameters, gas composition, power settings, and substrate materials.[182] In some cases, under specific conditions, oxygen plasma may exhibit some reducing behaviour.[392] However, in general, oxygen plasma is predominantly considered to be oxidising due to the highly reactive oxygen species it generates.[393]

The study conducted by Sahal et al.[182] showed that N_2 and O_2 both performed similar for removal of Li_2CO_3 in LLZTO SE through open-air plasma treatment. This suggests that the choice of gas is also SE dependent and confirms the previous argument that the properties of N_2 and O_2 gases vary according to different situations.

To further investigate the effect of the nitrogen, argon and oxygen plasma gasses for cleaning, XPS was performed on treated NBA disk as shown in Figure 5.6, showing spectra of C 1s, O 1s, Al 2p, and Na 2s core levels.

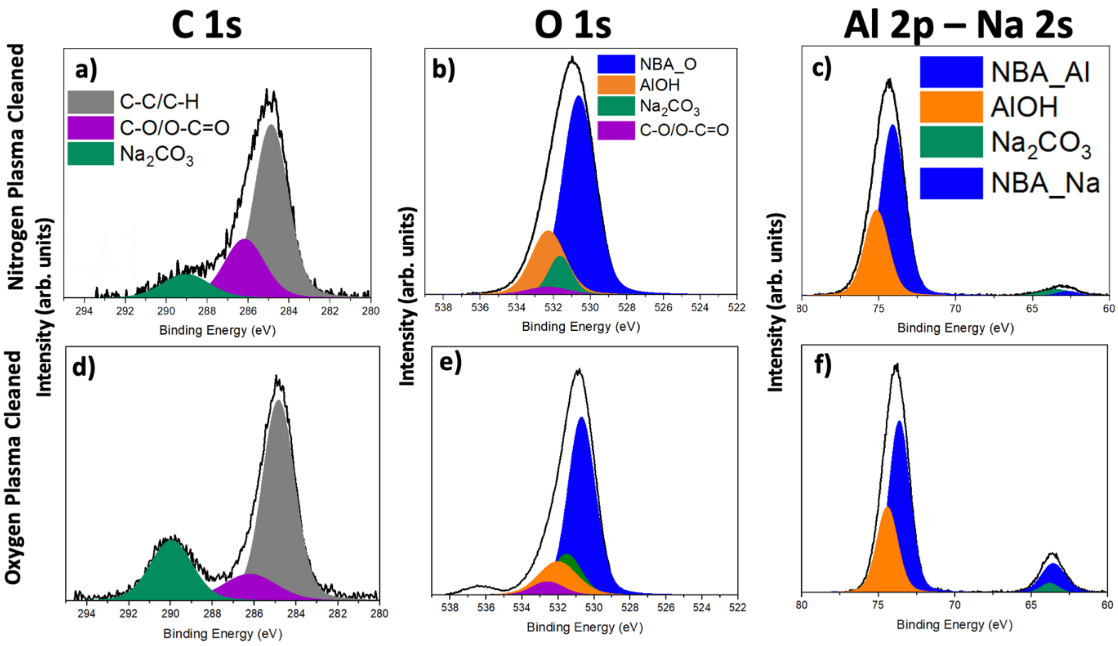

Figure 5.6. XPS analysis of Na-β"-Alumina surfaces after plasma cleaning with nitrogen and argon. XPS spectra of C 1s, O 1s, Al 2p-Na 2s core levels spectra of Na-β"-Alumina ; a-c) with nitrogen plasma; d-f) with oxygen plasma. This figure was produced by the data collected by Dr Joshua Gibson.

The C 1s spectra for nitrogen and argon is very similar as shown in Figure 5.6(a-c) for nitrogen and Figure 5.4(g-h) for argon, The Na_2CO_3 (green) peak at and C-O/O-C=O (purple) at in case of nitrogen and Na_2CO_3 peak at and C-O/O-C=O at in case of argon are reduced in intensity compared to untreated NBA sample, suggesting that both the gases remove the Na_2CO_3 surface contamination to similar extent as shown in Figure 5.4a and Figure 5.6a. However, in case of oxygen gas shown in Figure 5.6d, the Na_2CO_3 peak at and C-O/O-C=O is not reduced to similar extent.

The peak of O 1s spectra is very wide and cannot be fitted as a single component for nitrogen and oxygen gas, suggesting the presence of other species like what was observed in argon plasma treated sample shown in Figure 5.4h. Using the values present in literature[181], the peak was fitted at 530.7 eV, blue in colour in Figure 5.6c as Al-O peak from the NBA structure and hydroxyl, Al-OH at 532.2 eV present as a surface contaminant corresponding to orange in Figure 5.6c. Moreover, C-O/O-C=O and Na_2CO_3 peaks are observed at corresponding binding energy with the intensity of Na_2CO_3 decreasing in nitrogen and argon samples, while in case of oxygen, the intensity of the corresponding peaks remains almost unchanged compared to untreated samples, with a slight shift in the peaks.

Al 2p spectra are also shown in Figure 5.6c and f, it is split into the expected Al 2p doublet ($2p^{3/2}$ and $2p^{1/2}$) with different binding energies into Al-O and Al-OH. Both peaks are at the same binding energy and intensity for nitrogen, oxygen and argon plasma treated samples. Na 2s spectra was also fitted, which shows that argon and nitrogen gas decreases the Na_2CO_3 surface contaminant, which is consistent with the results from spectra C 1s and O 1s, while in case of oxygen, it remains almost unchanged.

The XPS results discussed above confirm that nitrogen and argon atmosphere plasma cleaning both reduce the amount of surface impurities of hydroxyl groups and carbon contaminants significantly on the surface of NBA resulting in low interfacial impedance. Since, most of the battery research is conducted in argon atmosphere gloveboxes in this research, argon system was used for further optimisation.

Figure 5.7 shows the F 1s and Cl 2p spectra, where grey represents plasma cleaned in nitrogen, red represents, plasma cleaned in argon, blue represents heat treated and green represents untreated. In case of F 1s spectra, the peaks of plasma cleaned for NBA samples increased in intensity compared to heat treated and untreated samples. Similarly, in the case of Cl 2p spectra, the peaks at 168 eV are increased in intensity for argon and nitrogen plasma cleaned samples. This suggests an interesting observation in the argon and nitrogen plasma cleaned surfaces, that after plasma cleaning, the F and S surface contaminants increase compared to heat treated and untreated samples. The gloveboxes used in this research are also used for handling sulphide solid electrolytes. A possible explanation is that plasma cleaning activates the surface of the NBA, so the tendency of the cleaned NBA to react with small traces of S and F present in the glovebox increases.

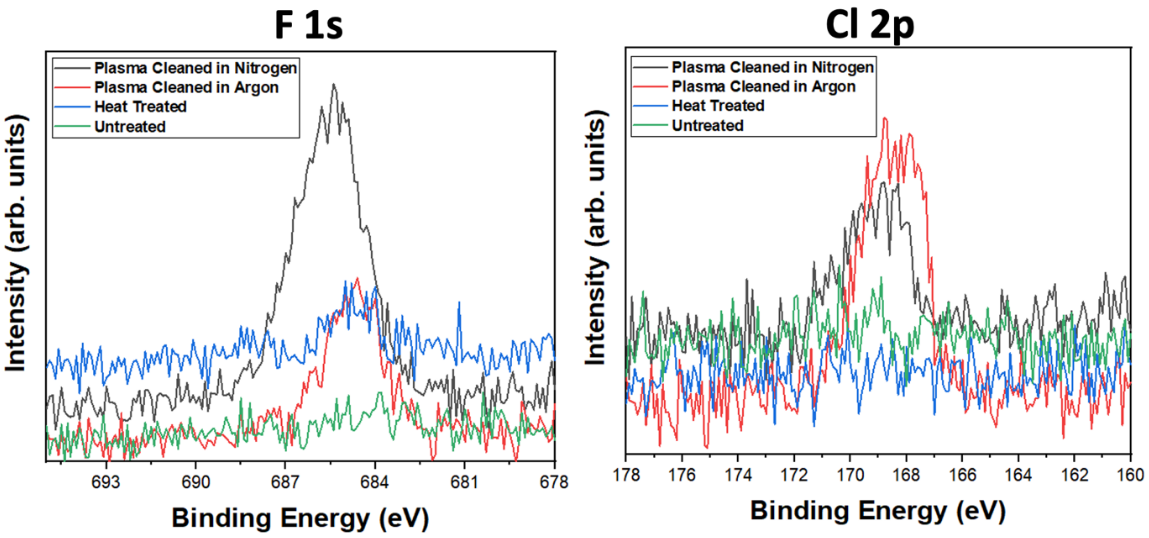

Figure 5.7. XPS analysis of Na-β"-Alumina surfaces after plasma cleaning with nitrogen and argon. XPS spectra of F 1s, Cl 2p core levels spectra of Na-β"-Alumina. This figure was produced from the data collected by Dr Joshua Gibson.

5.4.3.2 Using different power

NBA disks were prepared by as described in Section 5.4.1.2. They were taken from an argon filled glovebox and exposed to air for 24 hours and then plasma cleaned for 15 min at different power settings in nitrogen and argon atmosphere to study the effect of plasma power. Plasma cleaned pellets were then assembled into symmetric half cells. Figure 5.8a shows Nyquist plots of PEIS for cleaning at different powers. NBA pellets cleaned with 200 W power showed the lowest interfacial resistance for both the nitrogen and argon atmosphere and the trend showed that higher power cleans the surface better than lower power. This could be due to high radio frequency (RF) removing the surface contaminants better as the energy at which ions are striking the solid electrolyte surface increases.

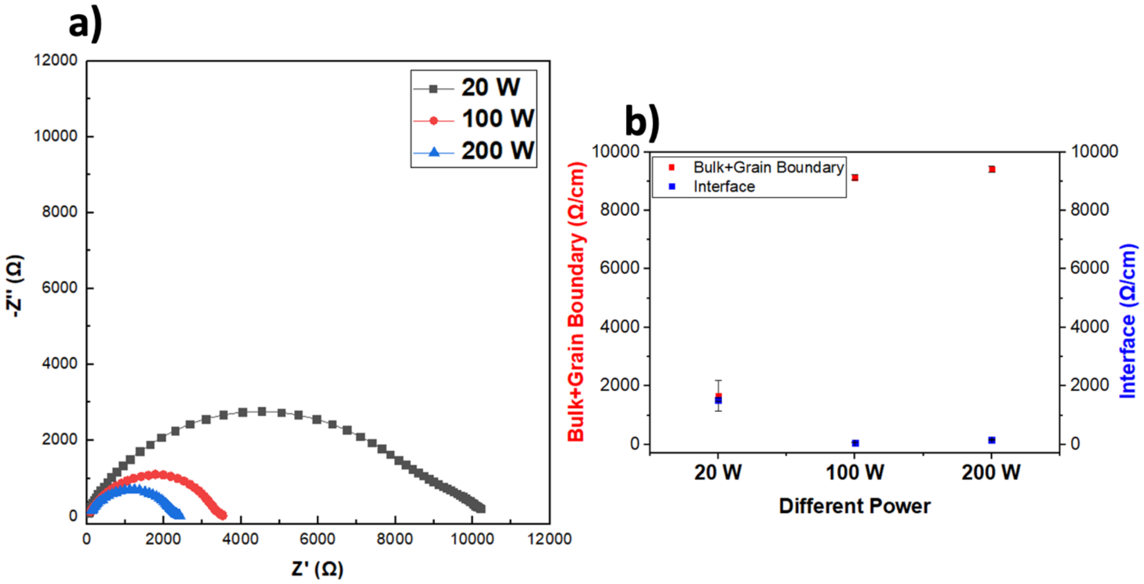

Figure 5.8. a) Representative Nyquist plot for different powers used in plasma cleaning in argon atmosphere; b) bulk+grain boundary and interfacial resistance for different powers.

XPS analysis in Figure 5.9 for different powers confirm that at 20 W power, the surface impurities persist while at 200 W power, the Na_2CO_3 signal decreases drastically as can be observed from C 1s, O 1s and Al 2p-Na 2s spectra shown in Figure 5.9(g-i). As the power increases, the intensity of Na_2CO_3 in C 1s, O 1s and Na 2s spectra decreases.

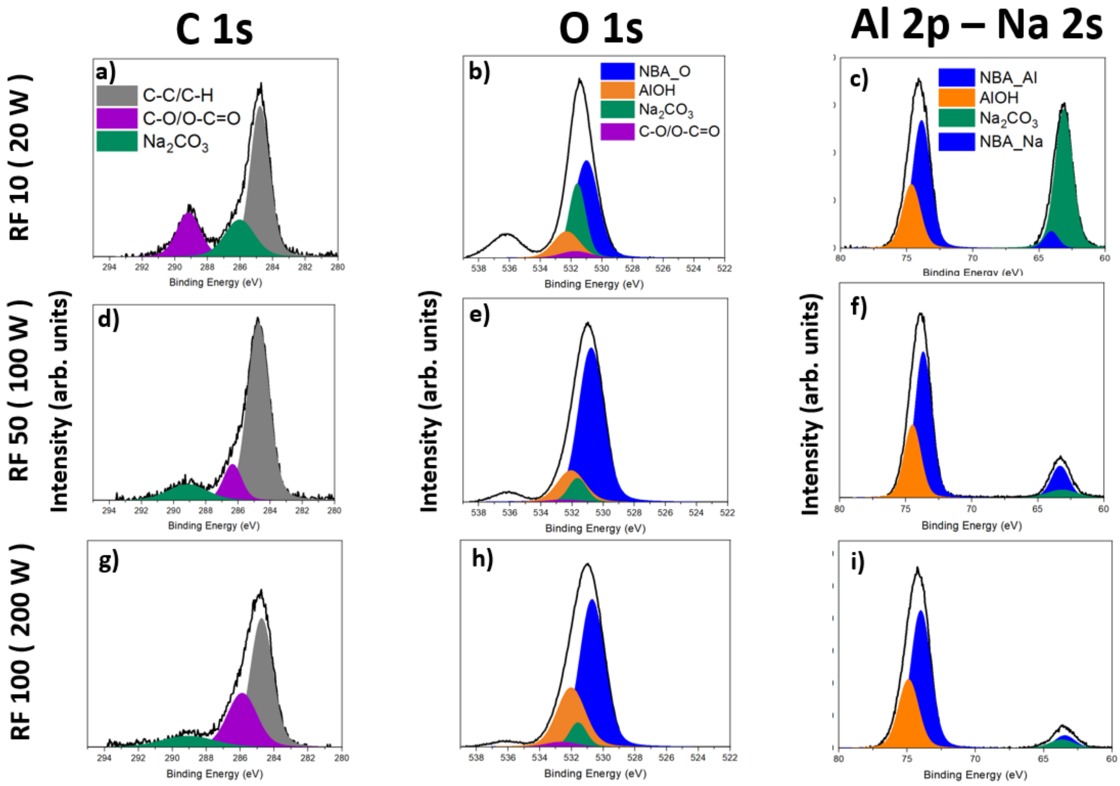

Figure 5.9. XPS analysis of Na-β"-Alumina surfaces plasma cleaning at different power denoted by RF. XPS spectra of C 1s, O 1s, Al 2p-Na 2s core levels spectra of Na-β"-Alumina ; a-c) at RF 10 (20 W); d-f) at RF 50 (100 W) ; g-i) at RF 100 (200 W) in argon. This figure was produced from the data collected by Dr Joshua Gibson.

5.4.3.3 Plasma cleaning for different time periods

NBA disks were prepared as described in Section 5.4.1.2. They were taken from an argon filled glovebox and exposed to air for 24 hours and then plasma cleaned for different time periods of 5 min, 15 min, 30 min and 60 min at 200 W in argon as 200 W power was determined to be the best conditions from previous section. Plasma cleaned pellets were then assembled into symmetric half cells. As shown in Figure 5.10a, NBA disks cleaned for 30 min (shown in blue) showed the lowest interfacial resistance of 4 Ω cm^{-2} compared to 1322 Ω cm^{-2} for 5 min, 81 Ω cm^{-2} for 15 min and 72 Ω cm^{-2} for 60 min. This suggests that 30 min of plasma cleaning at 200 W in argon atmosphere are the optimum conditions for removing the contaminants from the surface of the solid electrolyte pellet without destroying the morphology of the solid electrolyte surface.

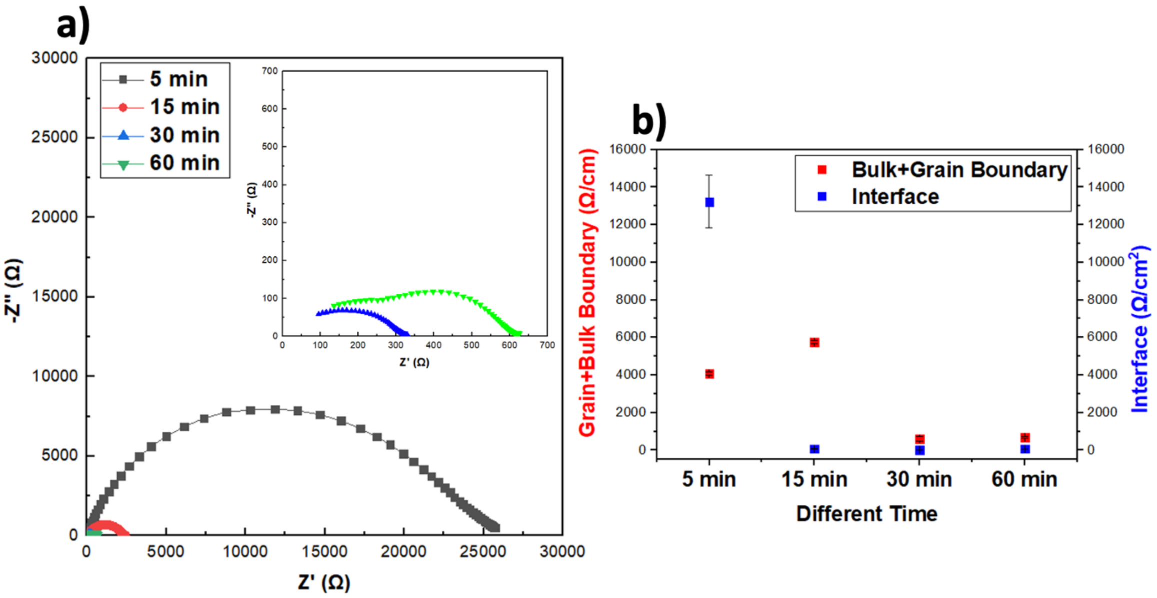

Figure 5.10. a) Representative Nyquist plot showing different plasma cleaning times at 200 W; b) bulk+grain boundary and interfacial resistance for different plasma cleaning times.

5.4.4 Morphology

The morphological changes due to the duration of the ions striking the surface of the SE were analysed using SEM. Figure 5.11 shows surface SEM images with corresponding images for untreated (Figure 5.11a), plasma cleaned for 30 min (Figure 5.11b) and plasma cleaned for 2-hour (Figure 5.11c) NBA samples in argon at 200 W. Through surface top-down SEM image analysis, it was observed that the untreated NBA surface is uneven with some debris (Figure 5.11a), while the NBA sample after 30 min of plasma cleaning shows a smooth homogenous morphology and the sample does not change colour in the image (Figure 5.11b). For the NBA sample, plasma cleaned for 2 hours (Figure 5.11c), the NBA sample changes colour from white to dirty yellow with fine lines all over the surface. The SEM image analysis depicts that the surface becomes rougher. It is suggested that the duration of plasma ions striking the surface of the NBA samples plays an important role, as the corresponding PEIS data suggests that if the time is lower than 30 min, the duration is not long enough to remove of all the contaminants present on the surface, while if the duration is too long, it damages the surface of the NBA sample, and then the interfacial resistance increases.[247] Apart from this study, there is limited literature for the effect of treatment time for the study of removal of Na_2CO_3 contaminants in NBA. Recently, Sahal et al.[182] showed that all the studied treatment times were effective for removal of Li_2CO_3 for LLZTO, however 20 min and 40 min showed significant reduction of Li_2CO_3 through XPS characterisation.

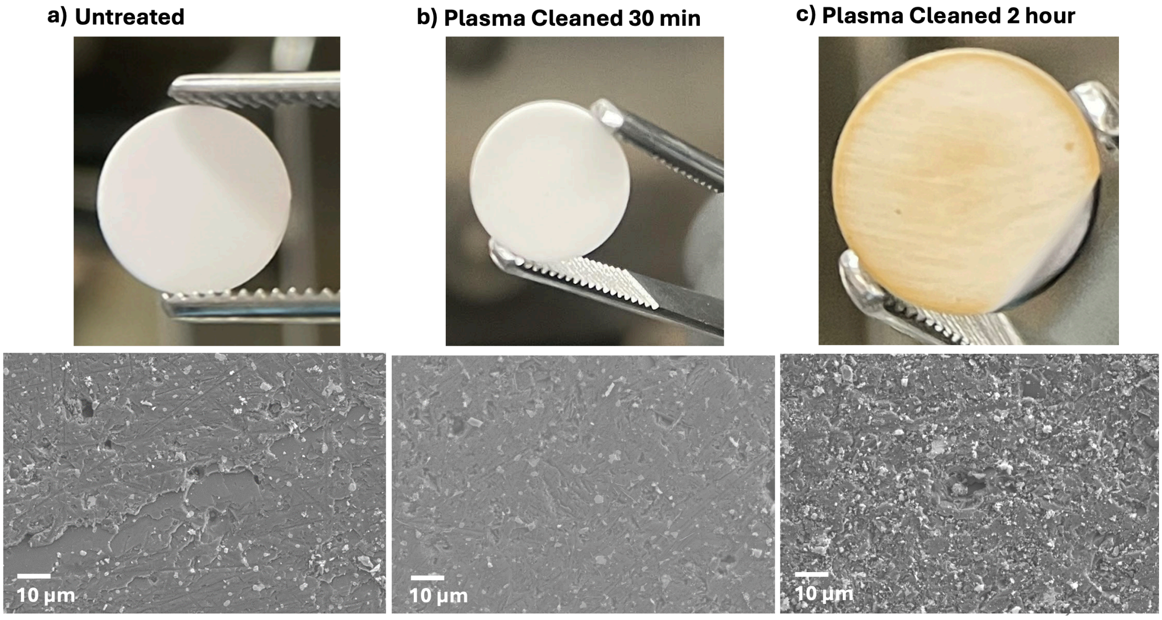

Figure 5.11. Photographs and SEM images showing morphology after plasma cleaning for different time periods; a) an untreated sample; b) NBA sample plasma cleaned for 30 min; c) NBA sample plasma cleaned sample for 2 hours.

5.4.5 Wettability

To study the effect of surface treatment techniques, wettability of the NBA disk was characterised using melted Na metal on untreated, heat treated, and plasma cleaned (30 min, 200 W power, 0.20 mbar pressure in argon) NBA disks. The wettability of a SE by metallic sodium (Na) is believed to affect the interfacial resistance in SSBs as discussed in the review by Tang et al.[394] As shown in the Figure 5.12a, the untreated NBA disk exhibited the highest contact angle of 122.5°. High contact angle suggests a non-wetting behaviour which is exhibited due to weak interfacial adhesion.[183] The heat treated and plasma cleaned samples demonstrated lower contact angles with molten Na compared to the untreated sample. They showed similar contact angles of 112.6° as shown in Figure 5.12b and c. According to the impedance and XPS analysis, it is hypothesised that this reduction in contact angle is due to the removal of surface impurities. As the surface has reduced carbonates and hydroxides, it more closely resembles bulk NBA, which interacts more strongly with Na metal.[181] Recently, researchers have demonstrated that spontaneous formation of Li_2CO_3 layers occurs on the surface of LLZO in humid air, leading to significant increases in interfacial impedance. Additionally, a recent investigation compared the wettability of LLZO to that of Li_2CO_3 and revealed that the wettability of LLZO can be substantially enhanced by eliminating Li_2CO_3 contamination from its surface.[183] This study indicate that the interaction between Li metal and LLZO is not solely determined by the morphology of the LLZO surface characteristics but is also strongly influenced by the extent of contamination present on the LLZO surface. It is assumed that NBA could also be affected by similar phenomenon.

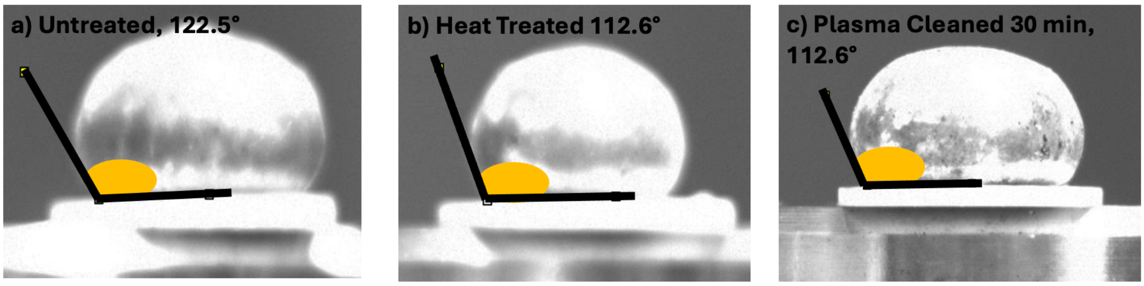

Figure 5.12. Contact angle measurements of molten Na metal on a) untreated; b) Heat treated; c) plasma cleaned NBA.

5.4.6 Problems with Plasma Cleaning

Plasma cleaning can be used as a potential surface treatment technique for NBA as it is more energy efficient than heat treatment at 900ºC for 10 hours.[181] It helps to remove the contaminants on the surface of NBA by removal of unwanted carboxyl and hydroxyl group as confirmed by XPS. Moreover, it helps to improve the wettability of the Na metal with NBA. However, plasma cleaning comes with its own set of challenges as discussed:

5.4.6.1 Making the surface more reactive

Plasma cleaning makes the surface of the NBA sensitive. As discussed in Section 5.4.3.1, after the surface of NBA is plasma cleaned in both argon and nitrogen gas, the F and S content increases for the plasma cleaned sample. This is due the F and S present in the glovebox from the usage of sulphides which react with the cleaned NBA surface. In the untreated sample, due to the presence of a thick contamination layer, the presence of tiny trace of impurities such as F and S does not make any difference.

5.4.6.2 Aging study

To study the effects of surface reactivity in more detail, an aging study of the plasma cleaned NBA surface was performed. As shown in Figure 5.13, two identical plasma cleaned NBA samples were prepared.

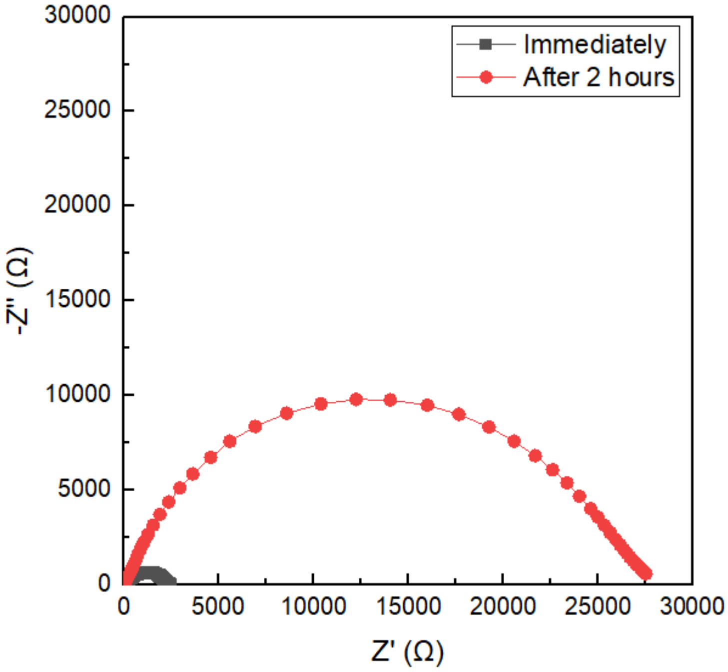

Figure 5.13. PEIS obtained for an optimised plasma cleaned NBA disks for sample assembled immediately after plasma cleaning (grey) and assembled after 2 hours storage in glovebox (red).

Just after the treatment, a two-electrode symmetric cell was prepared for the sample shown in gray colour in the Figure 5.13. For the sample shown in red colour, the plasma cleaned NBA sample was left in the glovebox for 2 hours and after that a two-electrode symmetric cell was assembled and tested in same conditions. Sample left in glovebox for 2 hours (red) shows high impedance compared sample just prepared after plasma cleaning (grey). This implies that when solid electrolyte is left in glovebox for long duration after plasma cleaning treatment, it reacts with the impurities present and increases the interfacial resistance.

Due to this reason, all the study conducted throughout the chapter was performed on immediately plasma cleaned NBA samples. To avoid, any errors due to the reaction of the plasma cleaned sample with the glovebox atmosphere.

5.5 Conclusions

The chapter describes a comprehensive optimisation of plasma cleaning as a potential surface treatment technique, where NBA is used as a model SE system. In this study, interfacial resistance was decreased to 4 Ω cm^{-2} from 3200 Ω cm^{-2} for NBA disk exposed to air for 24 hours. It was further confirmed by XPS analysis that the carbonate surface contaminants decreased after surface treatment. This resulted in increased wettability of the sodium metal on the NBA surface. The best conditions for the model system were determined to be, 30 min, 200 W power, 0.20 mbar pressure in argon.

Low cost and environment friendly methods are required to address poor wetting at the interface between the negative electrode and the electrolyte, such as coatings[115], heat treatment[181] or plasma cleaning[182]. This study demonstrates that by using plasma cleaning, the contact angle for Na metal can be decreased, implying better wetting behaviour. A higher CCD allows for faster charging and discharging, resulting in higher power densities. At room temperature, sodium-based cell systems have a CCD one magnitude higher (12 mA cm^{-2}) than lithium-based systems under identical measurement conditions as demonstrated by Bay et al.[181]

6 Chapter 6: Conclusions and Outlook

All-solid-state batteries hold a strong promise to provide high energy density and higher safety compared to traditional Li-ion batteries by enabling the use of Li metal as the anode active material. However, as discussed in Chapter 1, they are still several years away from mass production due to challenges associated with poor cycling performance and low CE of ASSBs. The results discussed in **Chapter 3** and **Chapter 4** have been directed towards gaining a deeper understanding in a Li-free all-solid-state cell, studying the position of Li deposition, effect of silver nanoparticles and a silver metal interlayer with a sulphide solid electrolyte.

Chapter 3 investigated silver metal interlayers in an all-solid-state Li-free cell with a sulphide solid electrolyte to understand the role of metal interlayer. Full cell cycling performance reveals that a silver metal interlayer can cycle upto 100 cycles compared to 2 cycles for Li-free cell. Homogenous deposition of Li metal at the current collector interface in presence of silver metal interlayer was observed. Moreover, a loss in coulombic efficiency is attributed to interfacial reactivity of lithiated silver with a sulphide solid electrolyte. The results confirm and support the hypothesis that homogenous deposition of Li metal in presence of silver metal interlayer helps in high cycling performance. XPS and PFIB analysis show the formation of an approximately 2 μm thick interfacial layer. The PFIB after discharge shows the presence of dead Li in Li-free case compared to a homogenous layer for silver metal interlayer. This dead Li leads to contact loss, inhibiting further cycling.

Chapter 4 investigated the underlying mechanisms of a graphite-silver composite interlayer. It concluded that graphite and graphite-silver composite interlayers effectively protect the solid electrolyte from Li dendrite growth, enabling high charging rates. The structural changes discussed reveal that graphite-silver composites operate through lithium intercalation into graphite during charging and deintercalation during discharging. The findings indicated that the charging process involves electrochemical lithiation of the graphite, followed by a chemical reaction between the lithiated graphite and silver, resulting in the formation of Li-Ag alloy. *Operando* XRD also revealed that phase formation during discharging leads to Li deficient phases (CsCl and UPb structure). Critical current determination showed that at rates above 2.5 $mAcm^{-2}$, dendrite penetration occurs for graphite and graphite-silver composite interlayer. Just as for the silver metal interlayer in Chapter 3, the role of silver nanoparticles in the graphite-silver composite interlayer is anticipated in homogenous deposition of Li metal on the current collector interface during charge and discharge.[1]

Li-free all-solid-state batteries offer tremendous benefits, but it suffers from low critical current density, cycle life and coulombic efficiency. The results discussed in Chapter 3 and Chapter 4, helps to further enhance the understanding of these batteries. In addition to gaining a better understanding of the structural changes happening in graphite-silver composite interlayer during charge and discharge, this thesis explores the role of silver nanoparticles and silver metal interlayer with sulphide solid electrolyte. Chapter 3 also address the critical issue of low coulombic efficiency and cycle life. Although these silver containing interlayers have demonstrated success in achieving high cycling performance, their practical applications remain uncertain due to expensive silver, low critical current density and challenging operating conditions. Hence, additional investigations are necessary in this field to identify the role of different carbons with different sizes and properties, role of diffusion coefficient of carbons and nanoparticles in ASSBs. Furthermore, metals cheaper than silver should also be investigated to understand the charge and discharge behaviour on the deposited Li morphology without imposing excessively challenging operating conditions. It will be interesting to understand the structural changes in different carbons and metal nanoparticles like aluminium, zinc, magnesium, bismuth, indium etc. This work is further explored by Lechen Yang in my research group.

As discussed in Section 1.2.1 and Section 5.2, NBA has exceptional stability against sodium metal anode and possess high ionic conductivity. **Chapter 5**, thoroughly optimised plasma cleaning as a potential surface treatment technique with a significant reduction in interfacial resistance for NBA disks exposed to air for 24 hours. This technique can be utilised for other SE's to increase the critical current densities. XPS analysis confirmed a decrease in surface contaminants particularly carbonates after the surface treatment. The study also showcased reduction in Na contact angle, indicating improved wetting behaviour. It is a cost-effective and eco-friendly process compared to heat treatment at 900ºC for 10 hours. This surface treatment technique can be applied to a wide variety of solid electrolytes to remove the unwanted contaminants from the surface. Additional work on mixture of gases would be quite interesting with in-depth study on how it affects the surface chemistry of the SE's.

7 References

(1) Spencer-Jolly, D.; Agarwal, V.; Doerrer, C.; Hu, B.; Zhang, S.; Melvin, D. L. R.; Gao, H.; Gao, X.; Adamson, P.; Magdysyuk, O. V.; Grant, P. S.; House, R. A.; Bruce, P. G. Structural Changes in the Silver-Carbon Composite Anode Interlayer of Solid-State Batteries. *Joule* **2023**, *7* (3), 503–514.

(2) Zhai, L.; Lee, J.-E. Investigating Vulnerability, Adaptation, and Resilience: A Comprehensive Review within the Context of Climate Change. *Atmosphere* **2024**, *15* (4), 474. https://doi.org/10.3390/atmos15040474.

(3) *Consequences of climate change - European Commission*. https://climate.ec.europa.eu/climate-change/consequences-climate-change_en (accessed 2024-11-17).

(4) Walker, A.; Webb, D.; Hutton, G.; Jozepa, I.; Stewart, I.; Tyers, R.; Hinson, S. *Electric vehicles and infrastructure*. House of commons. https://commonslibrary.parliament.uk/research-briefings/cbp-7480/ (accessed 2024-08-25).

(5) *8 States Now Plan to Ban Gas-Powered Car Sales*. Money. https://money.com/states-banning-gas-powered-cars/ (accessed 2024-09-07).

(6) *2035 Diesel and Petrol Car Ban: Everything You Need to Know*. Pod Point. https://pod-point.com/guides/2035-diesel-and-petrol-car-ban-in-the-uk-everything-you-need-to-know (accessed 2024-09-07).

(7) Packroff, J. *Car industry warns EU leaders against reversing 2035 combustion engine ban*. www.euractiv.com. https://www.euractiv.com/section/electricity/news/car-industry-warns-eu-leaders-against-reversing-2035-combustion-engine-ban/ (accessed 2024-09-07).

(8) *Are electric vehicles definitely better for the climate than gas-powered cars? | MIT Climate Portal*. https://climate.mit.edu/ask-mit/are-electric-vehicles-definitely-better-climate-gas-powered-cars (accessed 2024-09-07).

(9) *CATL Unveils Shenxing PLUS, Enabling 1,000-km Range and 4C Superfast Charging*. https://www.catl.com/en/news/6239.html (accessed 2024-09-07).

(10)Nishi, Y. Lithium Ion Secondary Batteries; Past 10 Years and the Future. *J. Power Sources* **2001**, *100* (1), 101–106. https://doi.org/10.1016/S0378-7753(01)00887-4.

(11) Frith, J. T.; Lacey, M. J.; Ulissi, U. A Non-Academic Perspective on the Future of Lithium-Based Batteries. *Nat. Commun.* **2023**, *14* (1), 420. https://doi.org/10.1038/s41467-023-35933-2.

(12) Goodenough, J. B.; Park, K.-S. The Li-Ion Rechargeable Battery: A Perspective. *J. Am. Chem. Soc.* **2013**, *135* (4), 1167–1176. https://doi.org/10.1021/ja3091438.

(13) Liu, Y.; Zhou, G.; Liu, K.; Cui, Y. Design of Complex Nanomaterials for Energy Storage: Past Success and Future Opportunity. *Acc. Chem. Res.* **2017**, *50* (12), 2895–2905. https://doi.org/10.1021/acs.accounts.7b00450.

(14) Wu, H.; Jia, H.; Wang, C.; Zhang, J.-G.; Xu, W. Recent Progress in Understanding Solid Electrolyte Interphase on Lithium Metal Anodes. *Adv. Energy Mater.* **2021**, *11* (5), 2003092. https://doi.org/10.1002/aenm.202003092.

(15) Krauskopf, T.; Richter, F. H.; Zeier, W. G.; Janek, J. Physicochemical Concepts of the Lithium Metal Anode in Solid-State Batteries. *Chem. Rev.* **2020**, *120* (15), 7745–7794. https://doi.org/10.1021/acs.chemrev.0c00431.

(16) Whittingham, M. S. History, Evolution, and Future Status of Energy Storage. *Proc. IEEE* **2012**, *100* (Special Centennial Issue), 1518–1534.

(17) Deng, D. Li-Ion Batteries: Basics, Progress, and Challenges. *Energy Sci. Eng.* **2015**, *3* (5), 385–418. https://doi.org/10.1002/ese3.95.

(18) Eshetu, G. G.; Elia, G. A.; Armand, M.; Forsyth, M.; Komaba, S.; Rojo, T.; Passerini, S. Electrolytes and Interphases in Sodium-Based Rechargeable Batteries: Recent Advances and Perspectives. *Adv. Energy Mater.* **2020**, *10* (20), 2000093. https://doi.org/10.1002/aenm.202000093.

(19) Han, F.; Westover, A. S.; Yue, J.; Fan, X.; Wang, F.; Chi, M.; Leonard, D. N.; Dudney, N. J.; Wang, H.; Wang, C. High Electronic Conductivity as the Origin of Lithium Dendrite Formation within Solid Electrolytes. *Nat Energy* **2019**, *4*, 187.

(20) *BU-106: Advantages of Primary Batteries*. Battery University. https://batteryuniversity.com/article/bu-106-advantages-of-primary-batteries (accessed 2024-09-07).

(21) *Watch Batteries | Energizer & Duracell Available*. https://www.batterystation.co.uk/batteries-by-use/watch-batteries.html?srsltid=AfmBOorpIBxVT4Pjwt5f5bai4hGsrsbD7mP3rwGPPoX8Y0WOAsuxCRp3 (accessed 2025-01-02).

(22) *BU-103: Global Battery Markets*. Battery University. https://batteryuniversity.com/article/bu-103-global-battery-markets (accessed 2024-09-07).

(23) Burheim, O. S. Chapter 7 - Secondary Batteries. In *Engineering Energy Storage*; Burheim, O. S., Ed.; Academic Press, **2017**; pp 111–145. https://doi.org/10.1016/B978-0-12-814100-7.00007-9.

(24) Kurzweil, P. Gaston Planté and His Invention of the Lead–Acid Battery—The Genesis of the First Practical Rechargeable Battery. *J. Power Sources* **2010**, *195* (14), 4424–4434. https://doi.org/10.1016/j.jpowsour.2009.12.126.

(25) Nzereogu, P. U.; Omah, A. D.; Ezema, F. I.; Iwuoha, E. I.; Nwanya, A. C. Anode Materials for Lithium-Ion Batteries: A Review. *Appl. Surf. Sci. Adv.* **2022**, *9*, 100233. https://doi.org/10.1016/j.apsadv.2022.100233.

(26) *Keywords to understanding Sony Energy Devices ｜Sony Energy Devices Corporation*. https://web.archive.org/web/20160304224245/http://www.sonyenergy-devices.co.jp/en/keyword/ (accessed 2024-09-07).

(27) *Battery production set to pass 1 TWh in 2023*. Benchmark Source. https://source.benchmarkminerals.com/article/battery-production-set-to-pass-1-twh-in-2023 (accessed 2024-09-07).

(28) *CATL, BYD Reveal Battery with 600km Range, 10-Minute Charge*. Mexico Business. https://mexicobusiness.news/automotive/news/catl-byd-reveal-battery-600km-range-10-minute-charge (accessed 2024-09-07).

(29) Tarascon, J. M.; Armand, M. Issues and Challenges Facing Rechargeable Lithium Batteries. In *Materials for Sustainable Energy: A Collection of Peer-Reviewed Research and Review Articles from Nature Publishing Group*; World Scientific Publishing Co., **2010**; pp 171–179. https://doi.org/10.1142/9789814317665_0024.

(30) Whittingham, M. S. Electrical Energy Storage and Intercalation Chemistry | Science. **1976**, *192*, 1126–1127. https://doi.org/10.1126/science.192.4244.1126.

(31) Mizushima, K.; Jones, P. C.; Wiseman, P. J.; Goodenough, J. B. LixCoO2 ($0<x\leqslant1$): A New Cathode Material for Batteries of High Energy Density. *Solid State Ion.* **1981**, *3–4*, 171–174. https://doi.org/10.1016/0167-2738(81)90077-1.

(32) Thackeray, M. M.; David, W. I. F.; Bruce, P. G.; Goodenough, J. B. Lithium Insertion into Manganese Spinels. *Mater. Res. Bull.* **1983**, *18* (4), 461–472. https://doi.org/10.1016/0025-5408(83)90138-1.

(33) Deng, D.; Gyu Kim, M.; Yang Lee, J.; Cho, J. Green Energy Storage Materials: Nanostructured TiO 2 and Sn-Based Anodes for Lithium-Ion Batteries. *Energy Environ. Sci.* **2009**, *2* (8), 818–837. https://doi.org/10.1039/B823474D.

(34) *Nissan Leaf - an overview | ScienceDirect Topics*. https://www.sciencedirect.com/topics/engineering/nissan-leaf (accessed 2024-09-07).

(35) Lemon, S.; Miller, A. Lectric Vehicles in New Zealand: Technologically Challenged; **2013**.

(36) *China Already Makes as Many Batteries as the Entire World Wants*. BloombergNEF. https://about.bnef.com/blog/china-already-makes-as-many-batteries-as-the-entire-world-wants/ (accessed 2024-10-24).

(37) Abdel-Ghany, A.; Hashem, A. M.; Mauger, A.; Julien, C. M. Lithium-Rich Cobalt-Free Manganese-Based Layered Cathode Materials for Li-Ion Batteries: Suppressing the Voltage Fading. *Energies* **2020**, *13* (13), 3487. https://doi.org/10.3390/en13133487.

(38) Li, X.; Qiao, Y.; Guo, S.; Xu, Z.; Zhu, H.; Zhang, X.; Yuan, Y.; He, P.; Ishida, M.; Zhou, H. Direct Visualization of the Reversible O2−/O− Redox Process in Li-Rich Cathode Materials. *Adv. Mater.* **2018**, *30* (14), 1705197. https://doi.org/10.1002/adma.201705197.

(39) Liang, Y.; Zhao, C.-Z.; Yuan, H.; Chen, Y.; Zhang, W.; Huang, J.-Q.; Yu, D.; Liu, Y.; Titirici, M.-M.; Chueh, Y.-L.; Yu, H.; Zhang, Q. A Review of Rechargeable Batteries for Portable Electronic Devices. *InfoMat* **2019**, *1* (1), 6–32. https://doi.org/10.1002/inf2.12000.

(40) Zhang, H.; Yang, Y.; Ren, D.; Wang, L.; He, X. Graphite as Anode Materials: Fundamental Mechanism, Recent Progress and Advances. *Energy Storage Mater.* **2021**, *36*, 147–170. https://doi.org/10.1016/j.ensm.2020.12.027.

(41) Padhi, A. K.; Nanjundaswamy, K. S.; Goodenough, J. B. Phospho-olivines as Positive-Electrode Materials for Rechargeable Lithium Batteries. *J. Electrochem. Soc.* **1997**, *144* (4), 1188. https://doi.org/10.1149/1.1837571.

(42) Purwanto, A.; Yudha, C. S.; Ubaidillah, U.; Widiyandari, H.; Ogi, T.; Haerudin, H. NCA Cathode Material: Synthesis Methods and Performance Enhancement Efforts. *Mater. Res. Express* **2018**, *5* (12), 122001. https://doi.org/10.1088/2053-1591/aae167.

(43) Liu, Z.; Yu, A.; Lee, J. Y. Synthesis and Characterization of LiNi1−x−yCoxMnyO2 as the Cathode Materials of Secondary Lithium Batteries. *J. Power Sources* **1999**, *81–82*, 416–419. https://doi.org/10.1016/S0378-7753(99)00221-9.

(44) Blomgren, G. E. The Development and Future of Lithium Ion Batteries. *J. Electrochem. Soc.* **2017**, *164* (1), A5019–A5025. https://doi.org/10.1149/2.0251701jes.

(45) Li, Q.; Chen, J.; Fan, L.; Kong, X.; Lu, Y. Progress in Electrolytes for Rechargeable Li-Based Batteries and Beyond. *Green Energy Environ.* **2016**, *1* (1), 18–42. https://doi.org/10.1016/j.gee.2016.04.006.

(46) Liu, C.; Neale, Z. G.; Cao, G. Understanding Electrochemical Potentials of Cathode Materials in Rechargeable Batteries. *Mater. Today* **2016**, *19* (2), 109–123. https://doi.org/10.1016/j.mattod.2015.10.009.

(47) Maisch, M. *Japanese scientists develop high energy density, cobalt-free lithium-ion battery*. pv magazine International. https://www.pv-magazine.com/2023/12/06/japanese-scientists-develop-high-energy-density-cobalt-free-lithium-ion-battery/ (accessed 2024-09-07).

(48) Mohammadi, F.; Saif, M. A Comprehensive Overview of Electric Vehicle Batteries Market. *E-Prime - Adv. Electr. Eng. Electron. Energy* **2023**, *3*, 100127. https://doi.org/10.1016/j.prime.2023.100127.

(49) Sun, P.; Bisschop, R.; Niu, H.; Huang, X. A Review of Battery Fires in Electric Vehicles. *Fire Technol.* **2020**, *56* (4), 1361–1410. https://doi.org/10.1007/s10694-019-00944-3.

(50) Aalund, R.; Diao, W.; Kong, L.; Pecht, M. Understanding the Non-Collision Related Battery Safety Risks in Electric Vehicles a Case Study in Electric Vehicle Recalls and the LG Chem Battery. *IEEE Access* **2021**, *9*, 89527–89532. https://doi.org/10.1109/ACCESS.2021.3090304.

(51) Fang, C.; Wang, X.; Meng, Y. S. Key Issues Hindering a Practical Lithium-Metal Anode. *Trends in Chemistry*, **2019**, *1*, 152–158. https://doi.org/10.1016/j.trechm.2019.02.015.

(52) Davies, C. *The real lessons South Korea should learn from an EV fire*. https://www.ft.com/content/5e7519ce-60ec-4a2e-8fbf-8b3fabb397a2 (accessed 2024-09-07).

(53) Moynihan, T. Samsung Finally Reveals Why the Note 7 Kept Exploding. *Wired*. https://www.wired.com/2017/01/why-the-samsung-galaxy-note-7-kept-exploding/ (accessed 2024-09-07).

(54) Samsung Recalls Note 7 Flagship over Explosive Batteries. *BBC News*. September 2, 2016. https://www.bbc.com/news/business-37253742 (accessed 2024-09-07).

(55) Chen, Y.; Kang, Y.; Zhao, Y.; Wang, L.; Liu, J.; Li, Y.; Liang, Z.; He, X.; Li, X.; Tavajohi, N.; Li, B. A Review of Lithium-Ion Battery Safety Concerns: The Issues, Strategies, and Testing Standards. *J. Energy Chem.* **2021**, *59*, 83–99. https://doi.org/10.1016/j.jechem.2020.10.017.

(56) Yikai, J. Safety Issues and Mechanisms of Lithium-Ion Battery Cell Upon Mechanical Abusive Loading: A Review. **2019**. https://doi.org/10.1016/j.ensm.2019.06.036.

(57) Tobishima, S. I.; Yamaki, J. I. A Consideration of Lithium Cell Safety. *J. Power Sources* **1999**, *81–82*, 882–886. https://doi.org/10.1016/S0378-7753(98)00240-7.

(58) Pistoia, G.; Liaw, B. *Behaviour of Lithium-Ion Batteries in Electric Vehicles: Battery Health, Performance, Safety, and Cost*; Springer, **2018**.

(59) An, S. J.; Li, J.; Daniel, C.; Mohanty, D.; Nagpure, S.; Wood, D. L. The State of Understanding of the Lithium-Ion-Battery Graphite Solid Electrolyte Interphase (SEI) and Its Relationship to Formation Cycling. *Carbon* **2016**, *105*, 52–76. https://doi.org/10.1016/j.carbon.2016.04.008.

(60) Goodenough, J. B.; Kim, Y. Challenges for Rechargeable Li Batteries. *Chemistry of Materials*, **2010**, *22*, 587–603. https://doi.org/10.1021/cm901452z.

(61) Otto, S. K.; Riegger, L. M.; Fuchs, T.; Kayser, S.; Schweitzer, P.; Burkhardt, S.; Henss, A.; Janek, J. In Situ Investigation of Lithium Metal–Solid Electrolyte Anode Interfaces with ToF-SIMS. *Adv. Mater. Interfaces* **2022**, *9* (13), 2102387. https://doi.org/10.1002/ADMI.202102387.

(62) Narayanan, S.; Ulissi, U.; Gibson, J. S.; Chart, Y. A.; Weatherup, R. S.; Pasta, M. Effect of Current Density on the Solid Electrolyte Interphase Formation at the lithium|Li6PS5Cl Interface. *Nat. Commun. 2022 131* **2022**, *13* (1), 1–9. https://doi.org/10.1038/s41467-022-34855-9.

(63) Wenzel, S.; Leichtweiss, T.; Weber, D. A.; Sann, J.; Zeier, W. G.; Janek, J. Interfacial Reactivity Benchmarking of the Sodium Ion Conductors Na3PS4 and Sodium β-Alumina for Protected Sodium Metal Anodes and Sodium All-Solid-State Batteries. *ACS Appl. Mater. Interfaces* **2016**, *8* (41), 28216–28224. https://doi.org/10.1021/acsami.6b10119.

(64) Wenzel, S.; Sedlmaier, S. J.; Dietrich, C.; Zeier, W. G.; Janek, J. Interfacial Reactivity and Interphase Growth of Argyrodite Solid Electrolytes at Lithium Metal Electrodes. *Solid State Ion.* **2018**, *318* (July 2017), 102–112. https://doi.org/10.1016/j.ssi.2017.07.005.

(65) Wenzel, S.; Leichtweiss, T.; Krüger, D.; Sann, J.; Janek, J. Interphase Formation on Lithium Solid Electrolytes - An in Situ Approach to Study Interfacial Reactions by Photoelectron Spectroscopy. *Solid State Ion.* **2015**, *278*, 98–105. https://doi.org/10.1016/J.SSI.2015.06.001.

(66) Maleki, H.; Deng, G.; Anani, A.; Howard, J. Thermal Stability Studies of Li-Ion Cells and Components. *J. Electrochem. Soc.* **1999**, *146* (9), 3224. https://doi.org/10.1149/1.1392458.

(67) Edge, J. S.; O'Kane, S.; Prosser, R.; Kirkaldy, N. D.; Patel, A. N.; Hales, A.; Ghosh, A.; Ai, W.; Chen, J.; Yang, J.; Li, S.; Pang, M. C.; Bravo Diaz, L.; Tomaszewska, A.; Marzook, M. W.; Radhakrishnan, K. N.; Wang, H.; Patel, Y.; Wu, B.; Offer, G. J. Lithium Ion Battery Degradation: What You Need to Know. *Phys. Chem. Chem. Phys.* **2021**, *23* (14), 8200–8221. https://doi.org/10.1039/d1cp00359c.

(68) Sato, K.; Noguchi, M.; Demachi, A.; Oki, N.; Endo, M. A Mechanism of Lithium Storage in Disordered Carbons. *Science* **1994**, *264* (5158), 556–558. https://doi.org/10.1126/science.264.5158.556.

(69) Mishra, A. K.; Monika; Patial, B. S. A Review on Recent Advances in Anode Materials in Lithium Ion Batteries. *Mater. Today Electron.* **2024**, *7*, 100089. https://doi.org/10.1016/j.mtelec.2024.100089.

(70) Jyoti, J.; Singh, B. P.; Tripathi, S. K. Recent Advancements in Development of Different Cathode Materials for Rechargeable Lithium Ion Batteries. *J. Energy Storage* **2021**, *43*, 103112. https://doi.org/10.1016/j.est.2021.103112.

(71) Zuo, X.; Zhu, J.; Müller-Buschbaum, P.; Cheng, Y. J. Silicon Based Lithium-Ion Battery Anodes: A Chronicle Perspective Review. *Nano Energy*, **2017**, *31*, 113–143. https://doi.org/10.1016/j.nanoen.2016.11.013.

(72) Ferraresi, G.; El Kazzi, M.; Czornomaz, L.; Tsai, C. L.; Uhlenbruck, S.; Villevieille, C. Electrochemical Performance of All-Solid-State Li-Ion Batteries Based on Garnet Electrolyte Using Silicon as a Model Electrode. *ACS Energy Lett.* **2018**. https://doi.org/10.1021/acsenergylett.8b00264.

(73) Jia, H.; Li, X.; Song, J.; Zhang, X.; Luo, L.; He, Y.; Li, B.; Cai, Y.; Hu, S.; Xiao, X.; Wang, C.; Rosso, K. M.; Yi, R.; Patel, R.; Zhang, J.-G. Hierarchical Porous Silicon Structures with Extraordinary Mechanical Strength as High-Performance Lithium-Ion Battery Anodes. *Nat. Commun.* **2020**, *11* (1), 1474. https://doi.org/10.1038/s41467-020-15217-9.

(74) Tan, D. H. S.; Chen, Y.-T.; Yang, H.; Bao, W.; Sreenarayanan, B.; Doux, J.-M.; Li, W.; Lu, B.; Ham, S.-Y.; Sayahpour, B.; Scharf, J.; Wu, E. A.; Deysher, G.; Han, H. E.; Hah, J.; Jeong, H.; Lee, J. B.; Chen, Z.; Meng, Y. S. Carbon-Free High-Loading Silicon Anodes Enabled by Sulfide Solid Electrolytes. **2021**, *373* (6562), 1494–1499. https://doi.org/10.1126/science.abg7217.

(75) Graetz, J.; Ahn, C. C.; Yazami, R.; Fultz, B. Nanocrystalline and Thin Film Germanium Electrodes with High Lithium Capacity and High Rate Capabilities. *J. Electrochem. Soc.* **2004**, *151* (5), A698. https://doi.org/10.1149/1.1697412.

(76) Fu, K. K.; Gong, Y.; Liu, B.; Zhu, Y.; Xu, S.; Yao, Y.; Luo, W.; Wang, C.; Lacey, S. D.; Dai, J. Toward Garnet Electrolyte–Based Li Metal Batteries: An Ultrathin, Highly Effective, Artificial Solid-State Electrolyte/Metallic Li Interface. *Sci. Adv.* **2017**, *3*, e1601659. https://doi.org/10.1126/sciadv.1601659.

(77) Zhong, H.; Sang, L.; Ding, F.; Song, J.; Mai, Y. Conformation of Lithium-Aluminium Alloy Interphase-Layer on Lithium Metal Anode Used for Solid State Batteries. *Electrochimica Acta* **2018**, *277*, 268–275. https://doi.org/10.1016/j.electacta.2018.04.191.

(78) Huang, B.; Pan, Z.; Su, X.; An, L. Tin-Based Materials as Versatile Anodes for Alkali (Earth)-Ion Batteries. *Journal of Power Sources*, **2018,** *395*, 41–59. https://doi.org/10.1016/j.jpowsour.2018.05.063.

(79) Dubey, R.; Sastre, J.; Cancellieri, C.; Okur, F.; Forster, A.; Pompizii, L.; Priebe, A.; Romanyuk, Y. E.; Jeurgens, L. P. H.; Kovalenko, M. V.; Kravchyk, K. V. Building a Better Li-Garnet Solid Electrolyte/Metallic Li Interface with Antimony. *Adv. Energy Mater.* **2021**, *11* (39). https://doi.org/10.1002/AENM.202102086.

(80) Hu, F.; Li, Y.; Wei, Y.; Yang, J.; Hu, P.; Rao, Z.; Chen, X.; Yuan, L.; Li, Z. Construct an Ultrathin Bismuth Buffer for Stable Solid-State Lithium Metal Batteries. *ACS Appl Mater Interfaces* **2020**, *12*. https://doi.org/10.1021/acsami.9b21717.

(81) Nagao, M.; Hayashi, A.; Tatsumisago, M. Bulk-Type Lithium Metal Secondary Battery with Indium Thin Layer at Interface between Li Electrode and Li2S-P2S5 Solid Electrolyte. *Electrochemistry* **2012**, *80*, 734.

(82) Luo, S.; Wang, Z.; Li, X.; Liu, X.; Wang, H.; Ma, W.; Zhang, L.; Zhu, L.; Zhang, X. Growth of Lithium-Indium Dendrites in All-Solid-State Lithium-Based Batteries with Sulfide Electrolytes. *Nat. Commun.* **2021**, *12* (1). https://doi.org/10.1038/s41467-021-27311-7.

(83) Sun, B.; Lang, J.; Liu, K.; Hussain, N.; Fang, M.; Wu, H. Promoting a Highly Stable Lithium Metal Anode by Superficial Alloying with an Ultrathin Indium Sheet. *Chem Commun* **2019**, *55*, 1592–1595. https://doi.org/10.1039/c8cc08934e.

(84) Obrovac, M. N.; Chevrier, V. L. Alloy Negative Electrodes for Li-Ion Batteries. *Chemical Reviews*, **2014**, *114*, 11444–11502. https://doi.org/10.1021/cr500207g.

(85) Obrovac, M. N.; Christensen, L.; Le, D. B.; Dahn, J. R. Alloy Design for Lithium-Ion Battery Anodes. *J. Electrochem. Soc.* **2007**, *154* (9), A849. https://doi.org/10.1149/1.2752985.

(86) Xu, W.; Wang, J.; Ding, F.; Chen, X.; Nasybulin, E.; Zhang, Y.; Zhang, J.-G. Lithium Metal Anodes for Rechargeable Batteries. *Energy Environ. Sci.* **2014**, *7* (2), 513–537. https://doi.org/10.1039/C3EE40795K.

(87) Zheng, J.; Engelhard, M. H.; Mei, D.; Jiao, S.; Polzin, B. J.; Zhang, J.-G.; Xu, W. Electrolyte Additive Enabled Fast Charging and Stable Cycling Lithium Metal Batteries. *Nat. Energy* **2017**, *2* (3), 1–8. https://doi.org/10.1038/nenergy.2017.12.

(88) Bai, P.; Li, J.; Brushett, F. R.; Bazant, M. Z. Transition of Lithium Growth Mechanisms in Liquid Electrolytes. *Energy Environ. Sci.* **2016**, *9* (10), 3221–3229. https://doi.org/10.1039/C6EE01674J.

(89) Yang, L.; Hagh, N. M.; Roy, J.; Macciomei, E.; Klein, J. R.; Janakiraman, U.; Fortier, M. E. Review-Challenges and Opportunities in Lithium Metal Battery Technology. *J. Electrochem. Soc.* **2024**, *171* (6), 060504. https://doi.org/10.1149/1945-7111/ad4ff2.

(90) Aurbach, D.; Zinigrad, E.; Teller, H.; Dan, P. Factors Which Limit the Cycle Life of Rechargeable Lithium (Metal) Batteries. *J. Electrochem. Soc.* **2000**, *147* (4), 1274. https://doi.org/10.1149/1.1393349.

(91) Louli, A. J.; Coon, M.; Genovese, M.; deGooyer, J.; Eldesoky, A.; Dahn, J. R. Optimizing Cycling Conditions for Anode-Free Lithium Metal Cells. *J. Electrochem. Soc.* **2021**, *168* (2), 020515. https://doi.org/10.1149/1945-7111/abe089.

(92) Zhong, Y.; Xiaoyu Yang; Ruiqi Guo; Liqing Zhai; Xinran Wang; Feng Wu; Chuan Wu; Ying Bai. Protecting Lithium Metal Anodes in Solid-State Batteries. *Electrochem. Energy Rev.* **2024**, *7* (30). https://doi.org/10.1007/s41918-024-00230-z.

(93) Monroe, C.; Newman, J. The Impact of Elastic Deformation on Deposition Kinetics at Lithium/Polymer Interfaces. *J Electrochem Soc* **2005**, *152*, A396.

(94) Engstrom, H.; Bates, J. B.; Brundage, W. E.; Wang, J. C. Ionic Conductivity of Sodium Beta″-Alumina. *Solid State Ion.* **1981**, *2* (4), 265–276. https://doi.org/10.1016/0167-2738(81)90027-8.

(95) Liu, Z.; Fu, W.; Payzant, E. A.; Yu, X.; Wu, Z.; Dudney, N. J.; Kiggans, J.; Hong, K.; Rondinone, A. J.; Liang, C. Anomalous High Ionic Conductivity of Nanoporous β-Li 3PS4. *J. Am. Chem. Soc.* **2013**, *135* (3), 975–978. https://doi.org/10.1021/ja3110895.

(96) Janek, J.; Zeier, W. G. A Solid Future for Battery Development. *Nat. Energy 2016 19* **2016**, *1* (9), 1–4. https://doi.org/10.1038/nenergy.2016.141.

(97) *Automobile Solid State Battery SHE 360C.* https://www.solidstatelion.com/en/product_page/291.html (accessed 2024-09-07).

(98) Li, Z.; Yu, R.; Weng, S.; Zhang, Q.; Wang, X.; Guo, X. Tailoring Polymer Electrolyte Ionic Conductivity for Production of Low- Temperature Operating Quasi-All-Solid-State Lithium Metal Batteries. *Nat. Commun.* **2023**, *14* (1), 482. https://doi.org/10.1038/s41467-023-35857-x.

(99) Huo, H.; Janek, J. Solid-State Batteries: From 'All-Solid' to 'Almost-Solid.' *Natl. Sci. Rev.* **2023**, *10* (6), nwad098. https://doi.org/10.1093/nsr/nwad098.

(100) *SAIC to supply IM Motors EVs with solid-state batteries*. electrive.com. https://www.electrive.com/2024/05/28/saic-to-supply-im-motors-evs-with-solid-state-batteries/ (accessed 2024-09-07).

(101) Andrews, M. *Nio's semi-solid state 150 kWh battery launch June 1*. CarNewsChina.com. https://carnewschina.com/2024/04/29/nios-semi-solid-state-150-kwh-battery-launch-june-1/ (accessed 2024-09-07).

(102) *China's 'battery king' dismisses solid-state EV commercialisation as years away*. https://www.ft.com/content/7a8207d9-b2e0-4969-a10a-2c41e8639fb7 (accessed 2024-09-07).

(103) Hatzell, K. B.; Chen, X. C.; Cobb, C.; Dasgupta, N. P.; Dixit, M. B.; Marbella, L. E.; McDowell, M. T.; Mukherjee, P.; Verma, A.; Viswanathan, V. Challenges in Lithium Metal Anodes for Solid State Batteries. *ACS Energy Lett* **2020**, *5*, 922.

(104) Kasemchainan, J.; Bruce, P. G. All-Solid-State Batteries and Their Remaining Challenges A Potential Route towards Safer, Higher Performing Batteries. *Technol Rev* **2018**, *62* (2), 177–180. https://doi.org/10.1595/205651318X696747.

(105) Albertus, P.; Anandan, V.; Ban, C.; Balsara, N.; Belharouak, I.; Buettner-Garrett, J.; Chen, Z.; Daniel, C.; Doeff, M.; Dudney, N. J.; Dunn, B.; Harris, S. J.; Herle, S.; Herbert, E.; Kalnaus, S.; Libera, J. A.; Lu, D.; Martin, S.; McCloskey, B. D.; McDowell, M. T.; Meng, Y. S.; Nanda, J.; Sakamoto, J.; Self, E. C.; Tepavcevic, S.; Wachsman, E.; Wang, C.; Westover, A. S.; Xiao, J.; Yersak, T. Challenges for and Pathways toward Li-Metal-Based All-Solid-State Batteries. *ACS Energy Lett.* **2021**, *6* (4), 1399–1404. https://pubs.acs.org/doi/full/10.1021/acsenergylett.1c00445.

(106) *ProLogium opens first factory for series production of solid-state cells*. electrive.com. https://www.electrive.com/2024/01/24/prologium-opens-first-factory-for-series-production-of-solid-state-cells/ (accessed 2024-09-07).

(107) *Samsung SDI begins construction of the solid-state battery pilot line*. Best Magazine. https://www.bestmag.co.uk/samsung-sdi-begins-construction-of-the-solid-state-battery-pilot-line/ (accessed 2024-09-08).

(108) *USA: Factorial Energy opens solid-state battery development and production site*. electrive.com. https://www.electrive.com/2023/10/24/usa-factorial-energy-opens-solid-state-battery-development-and-production-site/ (accessed 2024-09-08).

(109) *Samsung SDI to start mass production of solid-state batteries in 2027*. electrive.com. https://www.electrive.com/2024/03/05/samsung-sdi-to-start-mass-production-of-solid-state-batteries-in-2027/ (accessed 2024-09-07).

(110) *ProLogium Announces €5.2b Gigafactory in Dunkirk France and Greets French President Emmanuel Macron*. ProLogium Technology Co., Ltd. https://prologium.com/prologium-announces-e5-2b-gigafactory-in-dunkirk-france-and-greets-french-president-emmanuel-macron/ (accessed 2024-09-08).

(111) Fertig, M. P.; Skadell, K.; Schulz, M.; Dirksen, C.; Adelhelm, P.; Stelter, M. From High- to Low-Temperature: The Revival of Sodium-Beta Alumina for Sodium Solid-State Batteries. *Batter. Supercaps* **2022**, *5* (1), e202100131–e202100131. https://doi.org/10.1002/BATT.202100131.

(112) Hueso, K. B.; Armand, M.; Rojo, T. High Temperature Sodium Batteries: Status, Challenges and Future Trends. *Energy Environ. Sci.* **2013**, *6* (3), 734–749. https://doi.org/10.1039/C3EE24086J.

(113) Zhao, C.; Liu, L.; Qi, X.; Lu, Y.; Wu, F.; Zhao, J.; Yu, Y.; Hu, Y. S.; Chen, L. Solid-State Sodium Batteries. *Adv. Energy Mater.* **2018**, *8* (17), 1703012. https://doi.org/10.1002/AENM.201703012.

(114) Lu, X.; Xia, G.; Lemmon, J. P.; Yang, Z. Advanced Materials for Sodium- Beta Alumina Batteries: Status, Challenges and Perspectives. *J. Power Sources* **2010**, *195* (9), 2431–2442. https://doi.org/10.1016/j.jpowsour.2009.11.120.

(115) Zhou, W.; Li, Y.; Xin, S.; Goodenough, J. B. Rechargeable Sodium All-Solid-State Battery. *ACS Cent. Sci.* **2017**, *3* (1), 52–57. https://doi.org/10.1021/acscentsci.6b00321.

(116) Ellis, B. L.; Nazar, L. F. Sodium and Sodium-Ion Energy Storage Batteries. *Curr. Opin. Solid State Mater. Sci.* **2012**, *16* (4), 168–177. https://doi.org/10.1016/J.COSSMS.2012.04.002.

(117) Yang, H.-L.; Zhang, B.-W.; Konstantinov, K.; Wang, Y.-X.; Liu, H.-K.; Dou, S.-X. Progress and Challenges for All-Solid-State Sodium Batteries. *Adv. Energy Sustain. Res.* **2021**, *2* (2), 2000057. https://doi.org/10.1002/aesr.202000057.

(118) Xiang, L.; Li, X.; Xiao, J.; Zhu, L.; Zhan, X. Interface Issues and Challenges for NASICON-Based Solid-State Sodium-Metal Batteries. *Adv. Powder Mater.* **2024**, *3* (3), 100181. https://doi.org/10.1016/j.apmate.2024.100181.

(119) Wolfenstine, J.; Allen, J. L.; Sakamoto, J.; Siegel, D. J.; Choe, H. Mechanical Behavior of Li-Ion-Conducting Crystalline Oxide-Based Solid Electrolytes: A Brief Review. *Ionics* **2018**, *24*, 1271.

(120) Su, Y.; Ye, L.; Fitzhugh, W.; Wang, Y.; Gil-González, E.; Kim, I.; Li, X. A More Stable Lithium Anode by Mechanical Constriction for Solid State Batteries. *Energy Environ. Sci.* **2020**, *13* (3), 908–916. https://doi.org/10.1039/C9EE04007B.

(121) Ulvestad, A. A Brief Review of Current Lithium Ion Battery Technology and Potential Solid State Battery Technologies. **2018**. https://doi.org/arXiv%2520preprint%2520arXiv:1803.04317.

(122) Taylor, N. J.; Stangeland-Molo, S.; Haslam, C. G.; Sharafi, A.; Thompson, T.; Wang, M.; Garcia-Mendez, R.; Sakamoto, J. Demonstration of High Current Densities and Extended Cycling in the Garnet Li7La3Zr2O12 Solid Electrolyte. *J Power Sources* **2018**, *396*, 314.

(123) Banerjee, A.; Wang, X.; Fang, C.; Wu, E. A.; Meng, Y. S. Interfaces and Interphases in All-Solid-State Batteries with Inorganic Solid Electrolytes. *Chem. Rev.* **2020**, *120* (14), 6878–6933. https://pubs.acs.org/doi/full/10.1021/acs.chemrev.0c00101.

(124) Han, J.; Vu, A.; Kim, J. J.; Gim, J.; Croy, J. R.; Lee, T. H.; Lee, E. Room-Temperature Fabrication of Garnet-Type Solid-Electrolyte: Optimizing Particle Size for High Ionic Conductivity. *Chem. Eng. J.* **2024**, *481*, 148645. https://doi.org/10.1016/j.cej.2024.148645.

(125) Chen, L.; Li, W.; Fan, L.-Z.; Nan, C.-W.; Zhang, Q. Intercalated Electrolyte with High Transference Number for Dendrite-Free Solid-State Lithium Batteries. *Adv. Funct. Mater.* **2019**, *29* (28), 1901047. https://doi.org/10.1002/adfm.201901047.

(126) Maurya, D. K.; Dhanusuraman, R.; Guo, Z.; Angaiah, S. Composite Polymer Electrolytes: Progress, Challenges, and Future Outlook for Sodium-Ion Batteries. *Adv. Compos. Hybrid Mater.* **2022**, *5* (4), 2651–2674. https://doi.org/10.1007/s42114-021-00412-z.

(127) Lu, Y.; Tikekar, M.; Mohanty, R.; Hendrickson, K.; Ma, L.; Archer, L. A. Stable Cycling of Lithium Metal Batteries Using High Transference Number Electrolytes. *Adv. Energy Mater.* **2015**, *5* (9), 1402073. https://doi.org/10.1002/aenm.201402073.

(128) Yang, S.; Shao, C.; Xiao, X.; Fang, D.; Li, N.; Zhao, E.; Wang, C.; Chen, L.; Li, N.; Li, J.; Su, Y.; Jin, H. Revealing Stable Organic Cathode/Solid Electrolyte Interface to Promote All-Solid-State Sodium Batteries Using Organic Cathodes. *Energy Storage Mater.* **2024**, *73*, 103857. https://doi.org/10.1016/j.ensm.2024.103857.

(129) Eriksson, T.; Mace, A.; Manabe, Y.; Yoshizawa-Fujita, M.; Inokuma, Y.; Brandell, D.; Mindemark, J. Polyketones as Host Materials for Solid Polymer Electrolytes. *J. Electrochem. Soc.* **2020**, *167* (7), 070537. https://doi.org/10.1149/1945-7111/ab7981.

(130) Liu, Y.; Xu, B.; Zhang, W.; Li, L.; Lin, Y.; Nan, C. Composition Modulation and Structure Design of Inorganic-in-Polymer Composite Solid Electrolytes for Advanced Lithium Batteries. *Small* **2020**, *16* (15), 1902813. https://doi.org/10.1002/smll.201902813.

(131) Teo, L. P.; Buraidah, M. H.; Arof, A. K. Development on Solid Polymer Electrolytes for Electrochemical Devices. *Molecules* **2021**, *26* (21), 6499. https://doi.org/10.3390/molecules26216499.

(132) Cao, D.; Sun, X.; Li, Q.; Natan, A.; Xiang, P.; Zhu, H. Lithium Dendrite in All-Solid-State Batteries: Growth Mechanisms, Suppression Strategies, and Characterizations. *Matter* **2020**, *3*, 57.

(133) Adeli, P.; Bazak, J. D.; Park, K. H.; Kochetkov, I.; Huq, A.; Goward, G. R.; Nazar, L. F. Boosting Solid-State Diffusivity and Conductivity in Lithium Superionic Argyrodites by Halide Substitution. *Angew. Chem. - Int. Ed.* **2019**, *58* (26), 8681–8686. https://doi.org/10.1002/anie.201814222.

(134) Yang, H.; Wu, N. Ionic Conductivity and Ion Transport Mechanisms of Solid-State Lithium-Ion Battery Electrolytes: A Review. *Energy Sci. Eng.* **2022**, *10* (5), 1643–1671. https://doi.org/10.1002/ESE3.1163.

(135) Krauskopf, T.; Dippel, R.; Hartmann, H.; Peppler, K.; Mogwitz, B.; Richter, F. H.; Zeier, W. G.; Janek, J. Lithium-Metal Growth Kinetics on LLZO Garnet-Type Solid Electrolytes. *Joule* **2019**, *3* (8), 2030–2049.

(136) Guo, Y.; Wu, S.; He, Y.-B.; Kang, F.; Chen, L.; Li, H.; Yang, Q.-H. Solid-State Lithium Batteries: Safety and Prospects. *eScience* **2022**, *2* (2), 138–163. https://doi.org/10.1016/j.esci.2022.02.008.

(137) Jolly, D. S.; Melvin, D. L. R.; Stephens, I. D. R.; Brugge, R. H.; Pu, S. D.; Bu, J.; Ning, Z.; Hartley, G. O.; Adamson, P.; Grant, P. S.; Aguadero, A.; Bruce, P. G. Interfaces between Ceramic and Polymer Electrolytes: A Comparison of Oxide and Sulfide Solid Electrolytes for Hybrid Solid-State Batteries. *Inorganics* **2022**, *10* (5), 60. https://doi.org/10.3390/INORGANICS10050060/S1.

(138) Kraft, M. A.; Ohno, S.; Zinkevich, T.; Koerver, R.; Culver, S. P.; Fuchs, T.; Senyshyn, A.; Indris, S.; Morgan, B. J.; Zeier, W. G. Inducing High Ionic Conductivity in the Lithium Superionic Argyrodites Li6+xP1–xGexS5I for All-Solid-State Batteries. *J. Am. Chem. Soc.* **2018**, *140* (47), 16330–16339. https://doi.org/10.1021/jacs.8b10282.

(139) Faizal, A.; Song, J. H.; Mercy, T. D.; Kim, D. K.; Kamala Bharathi, K. Improved Ionic Conductivity and Li7P3S11 Solid Electrolyte Based All-Solid State Batteries for Practical Applications. *J. Mater. Sci. Mater. Electron.* **2024**, *35* (11), 749. https://doi.org/10.1007/s10854-024-12513-8.

(140) Zhang, Z.; Zhang, L.; Liu, Y.; Yan, X.; Xu, B.; Wang, L. One-Step Solution Process toward Formation of Li6PS5Cl Argyrodite Solid Electrolyte for All-Solid-State Lithium-Ion Batteries. *J. Alloys Compd.* **2020**, *812*, 152103. https://doi.org/10.1016/j.jallcom.2019.152103.

(141) Hu, J.; Yang, S.; Pei, Y.; Wang, X.; Liao, Y.; Li, S.; Yue, A.; Huang, J.-Q.; Yuan, H. Perspective on Powder Technology for All-Solid-State Batteries: How to Pair Sulfide Electrolyte with High-Voltage Cathode. *Particuology* **2024**, *86*, 55–66. https://doi.org/10.1016/j.partic.2023.04.005.

(142) Wu, L.; Wang, Y.; Guo, X.; Ding, P.; Lin, Z.; Yu, H. Interface Science in Polymer-Based Composite Solid Electrolytes in Lithium Metal Batteries. *SusMat* **2022**, *2* (3), 264–292. https://doi.org/10.1002/sus2.67.

(143) Wu, D.; Chen, L.; Li, H.; Wu, F. Recent Progress of Solid-State Lithium Batteries in China. *Appl. Phys. Lett.* **2022**, *121* (12), 120502. https://doi.org/10.1063/5.0117248.

(144) Wang, S.; Fang, R.; Li, Y.; Liu, Y.; Xin, C.; Richter, F. H.; Nan, C.-W. Interfacial Challenges for All-Solid-State Batteries Based on Sulfide Solid Electrolytes. *J. Materiomics* **2021**, *7* (2), 209–218. https://doi.org/10.1016/j.jmat.2020.09.003.

(145) Huang, W. Z.; Zhao, C. Z.; Wu, P.; Yuan, H.; Feng, W. E.; Liu, Z. Y.; Lu, Y.; Sun, S.; Fu, Z. H.; Hu, J. K.; Yang, S. J.; Huang, J. Q.; Zhang, Q. Anode-Free Solid-State Lithium Batteries: A Review. *Adv. Energy Mater.* **2022**, *12* (26), 2201044. https://doi.org/10.1002/AENM.202201044.

(146) Deng, Z.; Wang, Z.; Chu, I.-H.; Luo, J.; Ong, S. P. Elastic Properties of Alkali Superionic Conductor Electrolytes from First Principles Calculations. *J Electrochem Soc* **2016**, *163*, A67.

(147) Sakuda, A.; Akitoshi Hayashi; Yorinobu Takigawa; Kenji Higashi; Masahiro Tatsumisago. Evaluation of Elastic Modulus of Li2S–P2S5 Glassy Solid Electrolyte by Ultrasonic Sound Velocity Measurement and Compression Test. *J. Ceram. Soc. Jpn.* **2013**, *121* (1419), 946–949.

(148) Hu, B.; Zhang, S.; Ning, Z.; Spencer-Jolly, D.; Melvin, D. L. R.; Gao, X.; Perera, J.; Pu, S. D.; Rees, G. J.; Wang, L.; Yang, L.; Gao, H.; Marathe, S.; Burca, G.; Marrow, T. J.; Bruce, P. G. Deflecting Lithium Dendritic Cracks in Multi-Layered Solid Electrolytes. *Joule* **2024**, *8* (9), 2623–2638. https://doi.org/10.1016/j.joule.2024.06.024.

(149) Deiseroth, H.-J.; Kong, S.-T.; Eckert, H.; Vannahme, J.; Reiner, C.; Zaiß, T.; Schlosser, M. Li6PS5X: A Class of Crystalline Li-Rich Solids with an Unusually High Li+ Mobility. *Angew Chem Int Ed* **2008**, *47*, 755.

(150) Park, J.-S.; Jo, C.-H.; Myung, S.-T. Comprehensive Understanding on Lithium Argyrodite Electrolytes for Stable and Safe All-Solid-State Lithium Batteries. *Energy Storage Mater.* **2023**, *61*, 102869. https://doi.org/10.1016/j.ensm.2023.102869.

(151) Rao, R. P.; Adams, S. Studies of Lithium Argyrodite Solid Electrolytes for All-Solid-State Batteries. *Phys. Status Solidi Appl. Mater. Sci.* **2011**, *208* (8), 1804–1807. https://doi.org/10.1002/pssa.201001117.

(152) Yu, C.; van Eijck, L.; Ganapathy, S.; Wagemaker, M. Synthesis, Structure and Electrochemical Performance of the Argyrodite Li_6PS_5Cl Solid Electrolyte for Li-Ion Solid State Batteries. *Electrochimica Acta* **2016**, *215*, 93–99. https://doi.org/10.1016/j.electacta.2016.08.081.

(153) Yu, C.; Zhao, F.; Luo, J.; Zhang, L.; Sun, X. Recent Development of Lithium Argyrodite Solid-State Electrolytes for Solid-State Batteries: Synthesis, Structure, Stability and Dynamics. *Nano Energy* **2021**, *83*. https://doi.org/10.1016/J.NANOEN.2021.105858.

(154) Wang, Z.; Jiang, Y.; Wu, J.; Jiang, Y.; Huang, S.; Zhao, B.; Chen, Z.; Zhang, J. Reaction Mechanism of Li2S-P2S5 System in Acetonitrile Based on Wet Chemical Synthesis of Li7P3S11 Solid Electrolyte. *Chem. Eng. J.* **2020**, *393* (November 2019), 124706. https://doi.org/10.1016/j.cej.2020.124706.

(155) Hanghofer, I.; Brinek, M.; Eisbacher, S. L.; Bitschnau, B.; Volck, M.; Hennige, V.; Hanzu, I.; Rettenwander, D.; Wilkening, H. M. R. Substitutional Disorder: Structure and Ion Dynamics of the Argyrodites Li6PS5Cl, Li6PS5Br and Li6PS5I. *Phys. Chem. Chem. Phys.* **2019**, *21* (16), 8489–8507. https://doi.org/10.1039/C9CP00664H.

(156) Kim, H.; Conlin, P.; Bergschneider, M.; Chung, H.; Kim, S. Y.; Cha, S. W.; Cho, M.; Cho, K. First Principles Study on Li Metallic Phase Nucleation at Grain Boundaries in a Lithium Lanthanum Titanium Oxide (LLTO) Solid Electrolyte. *J. Mater. Chem. A* **2023**, *11* (6), 2889–2898. https://doi.org/10.1039/D2TA07950J.

(157) Krauskopf, T.; Culver, S. P.; Zeier, W. G. Local Tetragonal Structure of the Cubic Superionic Conductor Na3PS4. *Inorg. Chem.* **2018**, *57* (8), 4739–4744. https://doi.org/10.1021/acs.inorgchem.8b00458.

(158) Yu, C.; Ganapathy, S.; Eck, E. R. H. van; Eijck, L. van; Basak, S.; Liu, Y.; Zhang, L.; Zandbergen, H. W.; Wagemaker, M. Revealing the Relation between the Structure, Li-Ion Conductivity and Solid-State Battery Performance of the Argyrodite Li6PS5Br Solid Electrolyte. *J. Mater. Chem. A* **2017**, *5* (40), 21178–21188. https://doi.org/10.1039/C7TA05031C.

(159) Sun, Y.; Suzuki, K.; Hori, S.; Hirayama, M.; Kanno, R. Superionic Conductors: Li10+δ[SnySi1−y]1+δP2−δS12 with a Li10GeP2S12-Type Structure in the Li3PS4–Li4SnS4–Li4SiS4 Quasi-Ternary System. *Chem. Mater.* **2017**, *29* (14), 5858–5864. https://doi.org/10.1021/acs.chemmater.7b00886.

(160) Dawson, J. A.; Canepa, P.; Clarke, M. J.; Famprikis, T.; Ghosh, D.; Islam, M. S. Toward Understanding the Different Influences of Grain Boundaries on Ion Transport in Sulfide and Oxide Solid Electrolytes. *Chem. Mater.* **2019**, *31* (14), 5296–5304. https://doi.org/10.1021/acs.chemmater.9b01794.

(161) Buchberger, D. A.; Garbacz, P.; Słupczyński, K.; Brzezicki, A.; Boczar, M.; Czerwiński, A. Lithium Transport Studies on Chloride-Doped Argyrodites as Electrolytes for Solid-State Batteries. *ACS Appl. Mater. Interfaces* **2023**, *15* (46), 53417–53428. https://doi.org/10.1021/acsami.3c10857.

(162) Rettenwander, D.; Wagner, R.; Reyer, A.; Bonta, M.; Cheng, L.; Doeff, M. M.; Limbeck, A.; Wilkening, M.; Amthauer, G. Interface Instability of Fe-Stabilized Li7La3Zr2O12 versus Li Metal. *J Phys Chem C* **2018**, *122*, 3780.

(163) Kotobuki, M.; Munakata, H.; Kanamura, K.; Sato, Y.; Yoshida, T. Compatibility of Li7La3Zr2O12 Solid Electrolyte to All-Solid-State Battery Using Li Metal Anode. *J. Electrochem. Soc.* **2010**, *157* (10), A1076. https://doi.org/10.1149/1.3474232.

(164) Xu, X.; Wen, Z.; Wu, J.; Yang, X. Preparation and Electrical Properties of NASICON-Type Structured Li1.4Al0.4Ti1.6(PO4)3 Glass-Ceramics by the Citric Acid-Assisted Sol-Gel Method. *Solid State Ion.* **2007**, *178* (1–2), 29–34. https://doi.org/10.1016/j.ssi.2006.11.009.

(165) Machín, A.; Morant, C.; Márquez, F. Advancements and Challenges in Solid-State Battery Technology: An In-Depth Review of Solid Electrolytes and Anode Innovations. *Batteries* **2024**, *10* (1), 29. https://doi.org/10.3390/batteries10010029.

(166) Thangadurai, V.; Weppner, W. Li6ALa2Ta2O12 (A = Sr, Ba): Novel Garnet-Like Oxides for Fast Lithium Ion Conduction. *Adv. Funct. Mater.* **2005**, *15* (1), 107–112. https://doi.org/10.1002/adfm.200400044.

(167) Wang, C.; Fu, K.; Kammampata, S. P.; McOwen, D. W.; Samson, A. J.; Zhang, L.; Hitz, G. T.; Nolan, A. M.; Wachsman, E. D.; Mo, Y. Garnet-Type Solid-State Electrolytes: Materials, Interfaces, and Batteries. *Chem Rev* **2020**, *120*, 4257.

(168) Ma, C.; Chen, K.; Liang, C.; Nan, C. W.; Ishikawa, R.; More, K.; Chi, M. Atomic-Scale Origin of the Large Grain-Boundary Resistance in Perovskite Li-Ion-Conducting Solid Electrolytes. *Energy Environ. Sci.* **2014**, *7* (5), 1638–1642. https://doi.org/10.1039/c4ee00382a.

(169) Yu, S.; Siegel, D. J. Grain Boundary Contributions to Li-Ion Transport in the Solid Electrolyte Li7La3Zr2O12 (LLZO). *Chem Mater* **2017**, *29*, 9639.

(170) Xia, W.; Xu, B.; Duan, H.; Guo, Y.; Kang, H.; Li, H.; Liu, H. Ionic Conductivity and Air Stability of Al-Doped Li 7 La 3 Zr 2 O 12 Sintered in Alumina and Pt Crucibles. **2016**. https://doi.org/10.1021/acsami.5b12186.

(171) He, L.; Sun, Q.; Chen, C.; An, J.; Oh, S.; Sun, J.; Li, M.; Tu, W.; Zhou, H.; Zeng, K.; Lu, L. Failure Mechanism and Interface Engineering for NASICON-Structured All-Solid-State Lithium Metal Batteries. **2019**. https://doi.org/10.1021/acsami.9b05516.

(172) Sun, Y.; Guan, P.; Liu, Y.; Xu, H.; Li, S.; Chu, D. Recent Progress in Lithium Lanthanum Titanate Electrolyte towards All Solid-State Lithium Ion Secondary Battery. *Crit. Rev. Solid State Mater. Sci.* **2019**, *44* (4), 265–282. https://doi.org/10.1080/10408436.2018.1485551.

(173) Chen, X.; Guan, Z.; Chu, F.; Xue, Z.; Wu, F.; Yu, Y. Air-Stable Inorganic Solid-State Electrolytes for High Energy Density Lithium Batteries: Challenges, Strategies, and Prospects. *InfoMat* **2022**, *4* (1), e12248. https://doi.org/10.1002/inf2.12248.

(174) Hirsh, H. S.; Li, Y.; Tan, D. H. S.; Zhang, M.; Zhao, E.; Meng, Y. S. Sodium-Ion Batteries Paving the Way for Grid Energy Storage. *Adv. Energy Mater.* **2020**, *10* (32), 2001274. https://doi.org/10.1002/aenm.202001274.

(175) Chi, C.; Katsui, H.; Goto, T. Effect of Li Addition on the Formation of Na-β/B″-Alumina Film by Laser Chemical Vapor Deposition. *Ceram. Int.* **2017**, *43* (1), 1278–1283. https://doi.org/10.1016/j.ceramint.2016.10.077.

(176) Dunn, B.; Schwarz, B. B.; Thomas, J. O.; Morgan, P. E. D. Preparation and Structure of Li-Stabilized Na(+) Beta' Alumina Single Crystals. *Calif. Univ* **1988**, *Los Angeles Report 16*.

(177) de Kroon, A. P.; Guenter W, S.; Fritz Aldinger. Direct Synthesis of Binary K-.Beta.- and K-.Beta.''-Alumina. 1. Phase Relations and Influence of Precursor Chemistry. *Chem. Mater.* **1995**, *7, no. 5*, 878–887.

(178) Bay, M.-C.; Heinz, M. V. F.; Linte, C.; German, A.; Blugan, G.; Battaglia, C.; Vogt, U. F. Impact of Sintering Conditions and Zirconia Addition on Flexural Strength and Ion Conductivity of Na-β"-Alumina Ceramics. *Mater. Today Commun.* **2020**, *23*, 101118. https://doi.org/10.1016/j.mtcomm.2020.101118.

(179) Kazyak, E.; Garcia-Mendez, R.; LePage, W. S.; Sharafi, A.; Davis, A. L.; Sanchez, A. J.; Chen, K.-H.; Haslam, C.; Sakamoto, J.; Dasgupta, N. P. Li Penetration in Ceramic Solid Electrolytes: *Operando* Microscopy Analysis of Morphology, Propagation, and Reversibility. *Matter* **2020**, *2* (4), 1025–1048. https://doi.org/10.1016/j.matt.2020.02.008.

(180) Krauskopf, T.; Hartmann, H.; Zeier, W. G.; Janek, J. Toward a Fundamental Understanding of the Lithium Metal Anode in Solid-State Batteries - An Electrochemo-Mechanical Study on the Garnet-Type Solid Electrolyte Li 6.25 Al 0.25

La 3 Zr 2 O 12. *ACS Appl. Mater. Interfaces* **2019**, *11* (15), 14463–14477. https://pubs.acs.org/doi/full/10.1021/acsami.9b02537.

(181) Bay, M.; Wang, M.; Grissa, R.; Heinz, M. V. F.; Sakamoto, J.; Battaglia, C. Sodium Plating from Na-β″-Alumina Ceramics at Room Temperature, Paving the Way for Fast-Charging All-Solid-State Batteries. *Adv. Energy Mater.* **2020**, *10* (3), 1902899. https://doi.org/10.1002/aenm.201902899.

(182) Sahal, M.; Guo, J.; Chan, C. K.; Rolston, N. Surface Reduction of Li2CO3 on LLZTO Solid-State Electrolyte via Scalable Open-Air Plasma Treatment. *Batteries* **2024**, *10* (7), 249. https://doi.org/10.3390/batteries10070249.

(183) Sharafi, A.; Kazyak, E.; Davis, A. L.; Yu, S.; Thompson, T.; Siegel, D. J.; Dasgupta, N. P.; Sakamoto, J. Surface Chemistry Mechanism of Ultra-Low Interfacial Resistance in the Solid-State Electrolyte $Li_7La_3Zr_2O_{12}$. *Chem. Mater.* **2017**, *29* (18), 7961–7968. https://doi.org/10.1021/acs.chemmater.7b03002.

(184) Kasemchainan, J.; Zekoll, S.; Spencer, D. J.; Ning, Z.; Hartley, G. O.; Marrow, J.; Bruce, P. G. Critical Stripping Current Leads to Dendrite Formation on Plating in Lithium Anode Solid Electrolyte Cells. *Nat Mater* **2019**, *18*, 1105.

(185) Wang, J.-C.; Zhao, L.-L.; Zhang, N.; Wang, P.-F.; Yi, T.-F. Interfacial Stability between Sulfide Solid Electrolytes and Lithium Anodes: Challenges, Strategies and Perspectives. *Nano Energy* **2024**, *123*, 109361. https://doi.org/10.1016/j.nanoen.2024.109361.

(186) Xu, R. C.; Xia, X. H.; Zhang, S. Z.; Xie, D.; Wang, X. L.; Tu, J. P. Interfacial Challenges and Progress for Inorganic All-Solid-State Lithium Batteries. *Electrochimica Acta*. Elsevier Ltd September 10, **2018**, pp 177–187. https://doi.org/10.1016/j.electacta.2018.07.191.

(187) Eckhardt, J. K.; Klar, P. J.; Janek, J.; Heiliger, C. Interplay of Dynamic Constriction and Interface Morphology between Reversible Metal Anode and Solid Electrolyte in Solid State Batteries. *ACS Appl. Mater. Interfaces* **2022**, *14* (31), 35545–35554.

(188) *Electrical Contacts: Principles and Applications, Second Edition*, 2nd ed.; Slade, P. G., Ed.; CRC Press: Boca Raton, **2017**. https://doi.org/10.1201/b15640.

(189) Singh, D. K.; Henss, A.; Mogwitz, B.; Sann, J.; Richter, F. H.; Janek, J. Li6PS5Cl Microstructure and Influence on Dendrite Growth in Solid-State Batteries with Lithium Metal Anode. **2022**. https://doi.org/10.1016/j.xcrp.2022.101043.

(190) Wang, C.; Gong, Y.; Liu, B.; Fu, K.; Yao, Y.; Hitz, E.; Li, Y.; Dai, J.; Xu, S.; Luo, W.; Wachsman, E. D.; Hu, L. Conformal, Nanoscale ZnO Surface Modification of Garnet-Based Solid-State Electrolyte for Lithium Metal Anodes. *Nano letters*, **2017**, *17*, 565–571. https://doi.org/10.1021/acs.nanolett.6b04695.

(191) Luo, W.; Gong, Y.; Zhu, Y.; Fu, K. K.; Dai, J.; Lacey, S. D.; Wang, C.; Liu, B.; Han, X.; Mo, Y. Transition from Superlithiophobicity to Superlithiophilicity of Garnet Solid-State Electrolyte. *J Am Chem Soc* **2016**, *138*, 12258.

(192) Han, X.; Gong, Y.; Fu, K. K.; He, X.; Hitz, G. T.; Dai, J.; Pearse, A.; Liu, B.; Wang, H.; Rubloff, G. Negating Interfacial Impedance in Garnet-Based Solid-State Li Metal Batteries. *Nat Mater* **2017**, *16*, 572.

(193) Cheng, L.; Crumlin, E. J.; Chen, W.; Qiao, R.; Hou, H.; Lux, S. F.; Zorba, V.; Russo, R.; Kostecki, R.; Liu, Z.; Persson, K.; Yang, W.; Cabana, J.; Richardson, T.; Chen, G.; Doeff, M. The Origin of High Electrolyte–Electrode Interfacial Resistances in Lithium Cells Containing Garnet Type Solid Electrolytes. *Phys. Chem. Chem. Phys.* **2014**, *16* (34), 18294–18300.

(194) Santhanagopalan, D.; Qian, D.; McGilvray, T.; Wang, Z.; Wang, F.; Camino, F.; Graetz, J.; Dudney, N.; Meng, Y. S. Interface Limited Lithium Transport in Solid-

State Batteries. *J. Phys. Chem. Lett.* **2014**, *5* (2), 298–303. https://doi.org/10.1021/jz402467x.

(195) Cheng, X.; He Liu; Hong Yuan; Hong-Jie Peng; Cheng Tang; Jia-Qi Huang; Qiang Zhang. A Perspective on Sustainable Energy Materials for Lithium Batteries. *SusMat 1* **2021**, *1* (1), 38–50.

(196) *Protecting lithium metal anodes in lithium–sulfur batteries: A review | Energy Material Advances*. https://spj.science.org/doi/full/10.34133/energymatadv.0010 (accessed 2024-10-27).

(197) Zhu, Y.; He, X.; Mo, Y. Origin of Outstanding Stability in the Lithium Solid Electrolyte Materials: Insights from Thermodynamic Analyses Based on First-Principles Calculations. *ACS Appl Mater Interfaces* **2015**, *7*, 23685.

(198) Chen, X.; Jian Xie; Xinbing Zhao; Tiejun Zhu. Electrochemical Compatibility of Solid-State Electrolytes with Cathodes and Anodes for All-Solid-State Lithium Batteries: A Review. *Adv. Energy Sustain. Res. - Wiley Online Libr.* **2021**, *2* (5), p.2000101.

(199) Wenzel, S.; Randau, S.; Leichtweiß, T.; Weber, D. A.; Sann, J.; Zeier, W. G.; Janek, J. Direct Observation of the Interfacial Instability of the Fast Ionic Conductor Li10GeP2S12 at the Lithium Metal Anode. *Chem. Mater.* **2016**, *28* (7), 2400–2407. https://doi.org/10.1021/acs.chemmater.6b00610.

(200) Selim, R.; Bro, P. Some Observations on Rechargeable Lithium Electrodes in a Propylene Carbonate Electrolyte. *J. Electrochem. Soc.* **1974**, *121* (11), 1457. https://doi.org/10.1149/1.2401708.

(201) Kazyak, E.; Regina Garcia-Mendez; William S. LePage; Asma Sharafi; Andrew L. Davis; Adrian J. Sanchez; Kuan-Hung Chen; Catherine Haslam; Jeff Sakamoto; Neil P. Dasgupta. Li Penetration in Ceramic Solid Electrolytes: Operando Microscopy Analysis of Morphology, Propagation, and Reversibility. *Matter* **2020**, *2* (4), 1025–1048.

(202) Kerman, K.; Luntz, A.; Viswanathan, V.; Chiang, Y.-M.; Chen, Z. Review—Practical Challenges Hindering the Development of Solid State Li Ion Batteries. *J. Electrochem. Soc.* **2017**, *164* (7), A1731–A1744.

(203) Louli, A. J.; Eldesoky, A.; Weber, R.; Genovese, M.; Coon, M.; DeGooyer, J.; Deng, Z.; White, R. T.; Lee, J.; Rodgers, T.; Petibon, R.; Hy, S.; Cheng, S. J. H.; Dahn, J. R. Diagnosing and Correcting Anode-Free Cell Failure via Electrolyte and Morphological Analysis. *Nat. Energy 2020 59* **2020**, *5* (9), 693–702. https://doi.org/10.1038/s41560-020-0668-8.

(204) Qian, J.; Adams, B. D.; Zheng, J.; Xu, W.; Henderson, W. A.; Wang, J.; Bowden, M. E.; Xu, S.; Hu, J.; Zhang, J.-G. Anode-Free Rechargeable Lithium Metal Batteries. *Adv Funct Mater* **2016**, *26*, 7094.

(205) Weber, R.; Genovese, M.; Louli, A. J.; Hames, S.; Martin, C.; Hill, I. G.; Dahn, J. R. Long Cycle Life and Dendrite-Free Lithium Morphology in Anode-Free Lithium Pouch Cells Enabled by a Dual-Salt Liquid Electrolyte. *Nat. Energy 2019 48* **2019**, *4* (8), 683–689. https://doi.org/10.1038/s41560-019-0428-9.

(206) Tian, Y.; An, Y.; Wei, C.; Jiang, H.; Xiong, S.; Feng, J.; Qian, Y. Recently Advances and Perspectives of Anode-Free Rechargeable Batteries. *Nano Energy* **2020**, *78*, 105344. https://doi.org/10.1016/j.nanoen.2020.105344.

(207) Neudecker, B. J.; Dudney, N. J.; Bates, J. B. “Lithium-Free” Thin-Film Battery with In Situ Plated Li Anode. *J. Electrochem. Soc.* **2000**, *147* (2), 517. https://doi.org/10.1149/1.1393226.

(208) Lee, N.; Oh, J.; Choi, J. W. Anode-Less All-Solid-State Batteries: Recent Advances and Future Outlook. *Mater. Futur.* **2023**, *2* (1), 013502. https://doi.org/10.1088/2752-5724/acb3e8.

(209) Heubner, C.; Maletti, S.; Auer, H.; Hüttl, J.; Voigt, K.; Lohrberg, O.; Nikolowski, K.; Partsch, M.; Michaelis, A. From Lithium-Metal toward Anode-Free Solid-State Batteries: Current Developments, Issues, and Challenges. *Adv. Funct. Mater.* **2021**, *31* (51), 2106608. https://doi.org/10.1002/ADFM.202106608.

(210) Chen, S.; Jingxuan Zhang; Lu Nie; Xiangchen Hu; Yuanqi Huang; Yi Yu; Wei Liu. All-solid-state Batteries with a Limited Lithium Metal Anode at Room Temperature Using a Garnet-based Electrolyte. *Adv. Mater.* **2020**, *33* (1), 2002325.

(211) Zhang, J. G. Anode-Less. *Nat. Energy 2019 48* **2019**, *4* (8), 637–638. https://doi.org/10.1038/s41560-019-0449-4.

(212) Nanda, S.; Gupta, A.; Manthiram, A.; Nanda, S.; Gupta, A.; Manthiram, A. Anode-Free Full Cells: A Pathway to High-Energy Density Lithium-Metal Batteries. *Adv. Energy Mater.* **2021**, *11* (2), 2000804. https://doi.org/10.1002/AENM.202000804.

(213) Lewis, J. A.; Sandoval, S. E.; Liu, Y.; Nelson, D. L.; Yoon, S. G.; Wang, R.; Zhao, Y.; Tian, M.; Shevchenko, P.; Martínez-Pañeda, E.; McDowell, M. T. Accelerated Short Circuiting in Anode-Free Solid-State Batteries Driven by Local Lithium Depletion. *Adv. Energy Mater.* **2023**, *13* (12), 2204186.

(214) Lee, Y. G.; Fujiki, S.; Jung, C.; Suzuki, N.; Yashiro, N.; Omoda, R.; Ko, D. S.; Shiratsuchi, T.; Sugimoto, T.; Ryu, S.; Ku, J. H.; Watanabe, T.; Park, Y.; Aihara, Y.; Im, D.; Han, I. T. High-Energy Long-Cycling All-Solid-State Lithium Metal Batteries Enabled by Silver–Carbon Composite Anodes. *Nat. Energy 2020 54* **2020**, *5* (4), 299–308. https://doi.org/10.1038/s41560-020-0575-z.

(215) *Solid State Battery Technology*. QuantumScape. https://www.quantumscape.com/battery-technology/ (accessed 2024-09-08).

(216) QuantumScape. *Third-Party Test Results*. QuantumScape. https://www.quantumscape.com/press-release/quantumscape-releases-third-party-test-results/ (accessed 2024-09-08).

(217) Salvatierra, R. V.; Chen, W.; Tour, J. M. What Can Be Expected from “Anode-Free” Lithium Metal Batteries? *Adv. Energy Sustain. Res.* **2021**, *2* (5), 2000110.

(218) Sharafi, A.; Yu, S.; Naguib, M.; Lee, M.; Ma, C.; Meyer, H. M.; Nanda, J.; Chi, M.; Siegel, D. J.; Sakamoto, J. Impact of Air Exposure and Surface Chemistry on Li–Li 7 La 3 Zr 2 O 12 Interfacial Resistance. *J. Mater. Chem. A* **2017**, *5* (26), 13475–13487. https://doi.org/10.1039/c7ta03162a.

(219) Li, X.; Liang, J.; Luo, J.; Banis, M. N.; Wang, C.; Li, W.; Deng, S.; Yu, C.; Zhao, F.; Hu, Y. Air-Stable Li3InCl6 Electrolyte with High Voltage Compatibility for All-Solid-State Batteries. *Energy Env. Sci* **2019**, *12*, 2665.

(220) Dunn, B. Effect of Air Exposure on the Resistivity of Sodium Beta and Beta Aluminas. *J. Am. Ceram. Soc.* **1981**, *64* (3), 125–128. https://doi.org/10.1111/j.1151-2916.1981.tb10241.x.

(221) Fertig, M. P.; Dirksen, C.; Schulz, M.; Stelter, M. Humidity-Induced Degradation of Lithium-Stabilized Sodium-Beta Alumina Solid Electrolytes. *Batteries* **2022**, *8* (9). https://doi.org/10.3390/batteries8090103.

(222) Wang, S.; Barks, E.; Lin, P.-T.; Xu, X.; Melamed, C.; McConohy, G.; Nemšák, S.; Chueh, W. C. Effect of H+ Exchange and Surface Impurities on Bulk and Interfacial Electrochemistry of Garnet Solid Electrolytes. *Chem. Mater.* **2024**, *36* (14), 6849–6864. https://doi.org/10.1021/acs.chemmater.4c00738.

(223) Li, Y.; Chen, X.; Dolocan, A.; Cui, Z.; Xin, S.; Xue, L.; Xu, H.; Park, K.; Goodenough, J. B. Garnet Electrolyte with an Ultralow Interfacial Resistance for Li-

Metal Batteries. *J. Am. Chem. Soc.* **2018**, *140* (20), 6448–6455. https://pubs.acs.org/doi/full/10.1021/jacs.8b03106.
(224) Jin, S.; Ye, Y.; Niu, Y.; Xu, Y.; Jin, H.; Wang, J.; Sun, Z.; Cao, A.; Wu, X.; Luo, Y.; Ji, H.; Wan, L. J. Solid-Solution-Based Metal Alloy Phase for Highly Reversible Lithium Metal Anode. *J. Am. Chem. Soc.* **2020**, *142* (19), 8818–8826. https://doi.org/10.1021/jacs.0c01811.
(225) Jeong, M.-G.; Hatzell, K. B.; Banerjee, S.; Vishnugopi, B. S.; Mukherjee, P. P. Temperature Impact on Lithium Metal Morphology in Lithium Reservoir-Free Solid-State Batteries. *PRX Energy* **2024**, *3* (2), 023003. https://doi.org/10.1103/PRXEnergy.3.023003.
(226) Siniscalchi, M.; Liu, J.; Gibson, J. S.; Turrell, S. J.; Aspinall, J.; Weatherup, R. S.; Pasta, M.; Speller, S. C.; Grovenor, C. R. M. On the Relative Importance of Li Bulk Diffusivity and Interface Morphology in Determining the Stripped Capacity of Metallic Anodes in Solid-State Batteries. *ACS Energy Lett.* **2022**, *7* (10), 3593–3599. https://pubs.acs.org/doi/full/10.1021/acsenergylett.2c01793.
(227) Kim, S.; Jung, C.; Kim, H.; Thomas-Alyea, K. E.; Yoon, G.; Kim, B.; Badding, M. E.; Song, Z.; Chang, J.; Kim, J. The Role of Interlayer Chemistry in Li-Metal Growth through a Garnet-Type Solid Electrolyte. *Adv Energy Mater* **2020**, *10*, 1903993.
(228) Yan, K.; Lu, Z.; Lee, H.-W.; Xiong, F.; Hsu, P.-C.; Li, Y.; Zhao, J.; Chu, S.; Cui, Y. Selective Deposition and Stable Encapsulation of Lithium through Heterogeneous Seeded Growth. *Nat Energy* **2016**, *1*, 16010.
(229) Spencer Jolly, D. Interfaces between Metal Anodes and Solid Electrolytes in Solid-State Batteries. http://purl.org/dc/dcmitype/Text, University of Oxford, 2021. https://ora.ox.ac.uk/objects/uuid:d5aaa1f6-fc35-4739-a151-b053d44dc4ef (accessed 2024-08-26).
(230) *Which format do the major battery cell manufacturers bet on? Prismatic, cylindrical or pouch?* https://cicenergigune.com/en/blog/format-battery-cell-manufacturers-prismatic-cylindrical-pouch (accessed 2024-11-07).
(231) Zhu, J.; Wang, Y.; Huang, Y.; Bhushan Gopaluni, R.; Cao, Y.; Heere, M.; Mühlbauer, M. J.; Mereacre, L.; Dai, H.; Liu, X.; Senyshyn, A.; Wei, X.; Knapp, M.; Ehrenberg, H. Data-Driven Capacity Estimation of Commercial Lithium-Ion Batteries from Voltage Relaxation. *Nat. Commun.* **2022**, *13* (1), 2261. https://doi.org/10.1038/s41467-022-29837-w.
(232) Smith, A.; Stüble, P.; Leuthner, L.; Hofmann, A.; Jeschull, F.; Mereacre, L. Potential and Limitations of Research Battery Cell Types for Electrochemical Data Acquisition. *Batter. Supercaps* **2023**, *6* (6), e202300080. https://doi.org/10.1002/batt.202300080.
(233) Murray, V.; Hall, D. S.; Dahn, J. R. A Guide to Full Coin Cell Making for Academic Researchers. *J. Electrochem. Soc.* **2019**, *166* (2), A329. https://doi.org/10.1149/2.1171902jes.
(234) Doerrer, C.; Capone, I.; Narayanan, S.; Liu, J.; Grovenor, C. R. M.; Pasta, M.; Grant, P. S. High Energy Density Single-Crystal NMC/Li6PS5Cl Cathodes for All-Solid-State Lithium-Metal Batteries. *ACS Appl. Mater. Interfaces* **2021**, *13* (31), 37809–37815. https://pubs.acs.org/doi/full/10.1021/acsami.1c07952.
(235) Boaretto, N.; Garbayo, I.; Valiyaveettil-SobhanRaj, S.; Quintela, A.; Li, C.; Casas-Cabanas, M.; Aguesse, F. Lithium Solid-State Batteries: State-of-the-Art and Challenges for Materials, Interfaces and Processing. *J. Power Sources* **2021**, *502*, 229919. https://doi.org/10.1016/j.jpowsour.2021.229919.
(236) *Thin-Film Batteries and the Use of PVD Explained.* https://korvustech.com/thin-film-batteries/ (accessed 2024-10-28).

(237) Selvakumar, N.; Barshilia, H. C. Review of Physical Vapor Deposited (PVD) Spectrally Selective Coatings for Mid- and High-Temperature Solar Thermal Applications. *Sol. Energy Mater. Sol. Cells* **2012**, *98*, 1–23. https://doi.org/10.1016/j.solmat.2011.10.028.

(238) Powell, C. F.; Oxley, J. H.; Blocher, J. M.; Klerer, J. Vapor Deposition. *J. Electrochem. Soc.* **1966**, *113* (10), 226–269. https://doi.org/10.1149/1.2423765.

(239) Mahan, J. E. Physical Vapor Deposition of Thin Films. **2000**, 312.

(240) *What Is PVD Coating? Physical Vapor Deposition Coatings*. https://www.semicore.com/what-is-pvd-coating (accessed 2024-09-23).

(241) *Cleaning with plasma*. https://www.plasma.com/en/cleaning-with-plasma/ (accessed 2024-08-26).

(242) Fridman, A. *Plasma Chemistry*; Cambridge University Press, 2008.

(243) Kim, M. C.; Yang, S. H.; Boo, J.-H.; Han, J. G. Surface Treatment of Metals Using an Atmospheric Pressure Plasma Jet and Their Surface Characteristics. *Surf. Coat. Technol.* **2003**, *174–175*, 839–844. https://doi.org/10.1016/S0257-8972(03)00560-7.

(244) Plasma Cleaning - Henniker Plasma. https://plasmatreatment.co.uk/pt/plasma-technology-overview/plasma-cleaning.

(245) *What is Plasma?*. Harrick Plasma. https://harrickplasma.com/plasma-cleaning/what-is-plasma/ (accessed 2024-08-26).

(246) Brown, M. *Plasma Cleaning Process | Inseto Knowledge Base Document*. Inseto UK. https://www.inseto.co.uk/explanation-of-low-pressure-plasma-cleaning-ikb-014/ (accessed 2024-10-28).

(247) *Let's Talk About… getting to know your plasma - Henniker Plasma*. https://plasmatreatment.co.uk/knowledge-base/knowledge-articles/160-let-s-talk-about-getting-to-know-your-plasma (accessed 2024-08-28).

(248) *Henniker Plasma Treatment - Henniker Plasma*. https://plasmatreatment.co.uk/ (accessed 2024-08-25).

(249) *Physics of Plasma*. Harrick Plasma. https://harrickplasma.com/plasma-cleaning/physics-of-plasma/ (accessed 2024-08-26).

(250) Das, R.; Ali, M.; Abd Hamid, S. B. Current Applications of X-Ray Powder Diffraction - A Review. *Rev. Adv. Mater. Sci.* **2014**, *38*, 95–109.

(251) Khan, H.; Yerramilli, A. S.; D'Oliveira, A.; Alford, T. L.; Boffito, D. C.; Patience, G. S. Experimental Methods in Chemical Engineering: X-Ray Diffraction Spectroscopy—XRD. *Can. J. Chem. Eng.* **2020**, *98* (6), 1255–1266. https://doi.org/10.1002/cjce.23747.

(252) Clegg, W. X-Ray Crystallography in Practice. *X-Ray Crystallogr.* **2015**, 33–70.

(253) He, B. B. Introduction to Two-Dimensional X-Ray Diffraction. *Powder Diffr.* **2003**, *18* (2), 71–85. https://doi.org/10.1154/1.1577355.

(254) *X-ray Diffraction : XRD | Commissioned Analysis and Research | Technical Information*. Toray Research Center. https://www.toray-research.co.jp/en/technical-info/analysis/XRD.html (accessed 2024-11-09).

(255) Stan, C.; Beavers, C.; Kunz, M.; Tamura, N. X-Ray Diffraction under Extreme Conditions at the Advanced Light Source. *Quantum Beam Sci.* **2018**, *2*. https://doi.org/10.3390/qubs2010004.

(256) *Figure 4.20: Schematic diagram of Bragg's law in vector form.* ResearchGate. https://www.researchgate.net/figure/Schematic-diagram-of-Braggs-law-in-vector-form_fig56_343151817 (accessed 2024-11-09).

(257) Hull, A. W. A New Method of Chemical Analysis. *J. Am. Chem. Soc.* **1919**, *41* (8), 1168–1175. https://doi.org/10.1021/ja02229a003.

(258) Epp, J. X-Ray Diffraction (XRD) Techniques for Materials Characterization. In *In Materials characterization using nondestructive evaluation (NDE) methods*; Woodhead Publishing, **2016**; p (pp. 81-124).

(259) Herrmann, H.-G.; Huebschen, G.; Tschuncky, R.; Altpeter, I. X-Ray Diffraction (XRD) Techniques for Materials Characterization; Elsevier Science & Technology: United Kingdom, **2016**. https://doi.org/10.1016/B978-0-08-100040-3.00004-3.

(260) *What is SEM Analysis and Why Is It Important?*. Secat, Inc. https://secat.net/sem-analysis-use-importance/ (accessed 2024-09-19).

(261) Abd Mutalib, M.; Rahman, M. A.; Othman, M. H. D.; Ismail, A. F.; Jaafar, J. Chapter 9 - Scanning Electron Microscopy (SEM) and Energy-Dispersive X-Ray (EDX) Spectroscopy. In *Membrane Characterization*; Hilal, N., Ismail, A. F., Matsuura, T., Oatley-Radcliffe, D., Eds.; Elsevier, **2017**; pp 161–179. https://doi.org/10.1016/B978-0-444-63776-5.00009-7.

(262) Ul-Hamid, A. *A Beginners' Guide to Scanning Electron Microscopy*; Springer International Publishing: Cham, **2018**. https://doi.org/10.1007/978-3-319-98482-7.

(263) *Ul-Hamid, Anwar. "Introduction." A Beginners' Guide to Scanning Electron Microscopy. Cham: Springer International Publishing, **2018**. 1–14. Web.*

(264) Yao, N. Introduction to the Focused Ion Beam System. In *Focused Ion Beam Systems*; Cambridge University Press, **2007**; pp 1–30. https://doi.org/10.1017/CBO9780511600302.002.

(265) *Ion Extractor in FIB*. https://www.globalsino.com/EM/page2487.html (accessed 2024-12-06).

(266) Temiz, C. Scanning Electron Microscopy. In *Electron Microscopy*; IntechOpen, **2022**. https://doi.org/10.5772/intechopen.103956.

(267) *Virtual Labs*. https://emb-iitk.vlabs.ac.in/exp/sem-basics/theory.html (accessed 2024-12-06).

(268) Károly Havancsák. *High-Resolution Scanning Electron Microscopy*. Technoorg-Linda. https://www.technoorg.hu/news-and-events/articles/high-resolution-scanning-electron-microscopy-1/ (accessed 2024-12-06).

(269) *Introduction to components - FIB*. https://myscope.training/FIB_Introduction_to_components (accessed 2024-12-06).

(270) Kuba, J.; Mitchels, J.; Hovorka, M.; Erdmann, P.; Berka, L.; Kirmse, R.; König, J.; De Bock, J.; Goetze, B.; Rigort, A. Advanced Cryo-Tomography Workflow Developments – Correlative Microscopy, Milling Automation and Cryo-Lift-Out. *J. Microsc.* **2021**, *281* (2), 112–124. https://doi.org/10.1111/jmi.12939.

(271) Rubanov, S.; Munroe, P. R. Investigation of the Structure of Damage Layers in TEM Samples Prepared Using a Focused Ion Beam. *J. Mater. Sci. Lett.* **2001**, *20* (13), 1181–1183. https://doi.org/10.1023/A:1010950201525.

(272) Sergey, G.; Denis, K.; Ava, H.; Gediminas, G.; Viola, O.; L, K. O.; H.p, L. R.; O', B. M.; Roger, P.; C, W. J.; Alex, de M. Oxygen Plasma Focused Ion Beam Scanning Electron Microscopy for Biological Samples. bioRxiv October 31, **2018**, p 457820. https://doi.org/10.1101/457820.

(273) Smith, N. S.; Skoczylas, W. P.; Kellogg, S. M.; Kinion, D. E.; Tesch, P. P.; Sutherland, O.; Aanesland, A.; Boswell, R. W. High Brightness Inductively Coupled Plasma Source for High Current Focused Ion Beam Applications. *J. Vac. Sci. Technol. B Microelectron. Nanometer Struct. Process. Meas. Phenom.* **2006**, *24* (6), 2902–2906. https://doi.org/10.1116/1.2366617.

(274) Berger, C.; Dumoux, M.; Glen, T.; Yee, N.; Mitchels, J. M.; Patáková, Z.; Darrow, M. C.; Naismith, J. H.; Grange, M. Plasma FIB Milling for the Determination of

Structures in Situ. *Nat. Commun.* **2023**, *14* (1), 629. https://doi.org/10.1038/s41467-023-36372-9.

(275) *Thermo Fisher Helios G4 PFIB UXe – Michigan Center for Materials Characterization*. https://mc2.engin.umich.edu/techniques/fei-helios-g4-pfib-uxe/ (accessed 2024-11-02).

(276) Nanakoudis, A. *EDX Analysis with SEM: How Does it Work?*. Advancing Materials. https://www.thermofisher.com/blog/materials/edx-analysis-with-sem-how-does-it-work/ (accessed 2024-10-30).

(277) Gaston, B.; Protter, C. *Energy-Dispersive X-ray Spectroscopy (EDS)*. https://chem.libretexts.org/Courses/Franklin_and_Marshall_College/Introduction_to_Materials_Characterization__CHM_412_Collaborative_Text/Spectroscopy/Energy-Dispersive_X-ray_Spectroscopy_(EDS) (accessed 2024-09-20).

(278) Lee, J. Z.; Wynn, T. A.; Schroeder, M. A.; Alvarado, J.; Wang, X.; Xu, K.; Meng, Y. S. Cryogenic Focused Ion Beam Characterization of Lithium Metal Anodes. *ACS Energy Lett.* **2019**, *4* (2), 489–493. https://pubs.acs.org/doi/full/10.1021/acsenergylett.8b02381.

(279) Agrawal, M.; Prasad, V.; Nijhawan, G.; Jalal, S. S.; Rajalakshmi, B.; Dwivedi, S. P. A Comprehensive Review of Electron Microscopy in Materials Science: Technological Advances and Applications. *E3S Web Conf.* **2024**, *505*, 01029. https://doi.org/10.1051/e3sconf/202450501029.

(280) *Principles and Fundamentals of Energy-Dispersive Spectroscopy*. Rocky Mountain Labs. https://rockymountainlabs.com/principles-and-fundamentals-of-energy-dispersive-spectroscopy/ (accessed 2024-09-20).

(281) *EDS Principle | West Campus Materials Characterization Core*. https://ywcmatsci.yale.edu/edx-principle (accessed 2024-12-10).

(282) Suga, S.; Sekiyama, A.; Tusche, C. Bulk and Surface Sensitivity of Photoelectron Spectroscopy. *Springer Ser. Surf. Sci.* **2021**, *72*, 111–118. https://doi.org/10.1007/978-3-030-64073-6_4.

(283) Watts, J. F.; Wolstenholme, John. An Introduction to Surface Analysis by XPS and AES. **2003**, 212.

(284) Hüfner, S. *Photoelectron Spectroscopy: Principles and Applications*; Springer Verlag, **1995**.

(285) Measurlabs. *X-Ray Photoelectron Spectroscopy | XPS Analysis | Measurlabs*. https://measurlabs.com/methods/x-ray-photoelectron-spectroscopy-xps/ (accessed 2024-10-30).

(286) Stevie, F. A.; Donley, C. L. Introduction to X-Ray Photoelectron Spectroscopy. *J. Vac. Sci. Technol. A* **2020**, *38* (6), 063204. https://doi.org/10.1116/6.0000412.

(287) Magdy, M. X-Ray Techniques Dedicated to Materials Characterization in Cultural Heritage. *ChemistrySelect* **2023**, *8* (33), e202301306. https://doi.org/10.1002/slct.202301306.

(288) Zhang, L.; Yao Dai; Chao Li; Yuzhen Dang; Runguo Zheng; Zhiyuan Wang; Yuan Wang et al. Recent Advances in Electrochemical Impedance Spectroscopy for Solid-State Batteries. *Energy Storage Mater. 2024* **2024**, 103378. https://doi.org/10.1016/j.ensm.2024.103378.

(289) *Basics of EIS: Electrochemical Research-Impedance Gamry Instruments*. https://www.gamry.com/application-notes/EIS/basics-of-electrochemical-impedance-spectroscopy/ (accessed 2024-09-24).

(290) Barsoukov, E.; Macdonald, J. R. *Impedance Spectroscopy: Theory, Experiment, and Applications*, 3rd ed.; Wiley: Hoboken, New Jersey, **2018**.

(291) Larfaillou, S.; Guy-Bouyssou, D.; Le Cras, F.; Franger, S. Comprehensive Characterization of All-Solid-State Thin Films Commercial Microbatteries by Electrochemical Impedance Spectroscopy. *J. Power Sources* **2016**, *319*, 139–146.

(292) Gamry Instruments. *Measuring Batteries using the Right Setup (Application Note)*.

(293) Irvine, J. T. S.; Sinclair, D. C.; West, A. R. Electroceramics Characterized by Impedance Spectroscopy. *Adv. Mater.* **1990**, *2* (3), 132–138. https://doi.org/10.1002/adma.19900020304.

(294) *Anode-less Solid-State Batteries: higher energy, more efficient, safer and cheaper batteries*. https://cicenergigune.com/en/blog/anodeless-solid-state-batteries-cicenergigune (accessed 2024-10-14).

(295) Kim, J.-S.; Yoon, G.; Kim, S.; Sugata, S.; Yashiro, N.; Suzuki, S.; Lee, M.-J.; Kim, R.; Badding, M.; Song, Z.; Chang, J.; Im, D. Surface Engineering of Inorganic Solid-State Electrolytes via Interlayers Strategy for Developing Long-Cycling Quasi-All-Solid-State Lithium Batteries. *Nat. Commun.* **2023**, *14* (1), 782. https://doi.org/10.1038/s41467-023-36401-7.

(296) Sandoval, S. E.; Lewis, J. A.; Vishnugopi, B. S.; Nelson, D. L.; Schneider, M. M.; Cortes, F. J. Q.; Matthews, C. M.; Watt, J.; Tian, M.; Shevchenko, P.; Mukherjee, P. P.; McDowell, M. T. Structural and Electrochemical Evolution of Alloy Interfacial Layers in Anode-Free Solid-State Batteries. *Joule* **2023**, *7* (9), 2054–2073. https://doi.org/10.1016/j.joule.2023.07.022.

(297) Kim, S.; Yoon, G.; Jung, S.-K.; Park, S.; Kim, J.-S.; Yoon, K.; Lee, S.; Kang, K. High-Power Hybrid Solid-State Lithium–Metal Batteries Enabled by Preferred Directional Lithium Growth Mechanism. *ACS Energy Lett.* **2022**, 9–20. https://pubs.acs.org/doi/full/10.1021/acsenergylett.2c02150.

(298) Stan, M. C.; Becking, J.; Kolesnikov, A.; Wankmiller, B.; Frerichs, J. E.; Hansen, M. R.; Bieker, P.; Kolek, M.; Winter, M. Sputter Coating of Lithium Metal Electrodes with Lithiophilic Metals for Homogeneous and Reversible Lithium Electrodeposition and Electrodissolution. *Mater. Today* **2020**, *xxx* (xx), 1–9. https://doi.org/10.1016/j.mattod.2020.04.002.

(299) Lewis, J. A.; Cavallaro, K. A.; Liu, Y.; McDowell, M. T. The Promise of Alloy Anodes for Solid-State Batteries. *Joule* **2022**, *6* (7), 1418–1430. https://doi.org/10.1016/J.JOULE.2022.05.016.

(300) Sandoval, S. E.; Cortes, F. J. Q.; Klein, E. J.; Lewis, J. A.; Shetty, P. P.; Yeh, D.; McDowell, M. T. Understanding the Effects of Alloy Films on the Electrochemical Behavior of Lithium Metal Anodes with Operando Optical Microscopy. *J. Electrochem. Soc.* **2021**, *168* (10), 100517. https://doi.org/10.1149/1945-7111/AC2D11.

(301) Connell, J. G.; Fuchs, T.; Hartmann, H.; Krauskopf, T.; Zhu, Y.; Sann, J.; Garcia-Mendez, R.; Sakamoto, J.; Tepavcevic, S.; Jürgen Janek. Kinetic versus Thermodynamic Stability of LLZO in Contact with Lithium Metal. *Chem Mater* **2020**, *2020*, 34. https://doi.org/10.1021/acs.chemmater.0c03869.

(302) Luntz, A. C.; Voss, J.; Reuter, K. Interfacial Challenges in Solid-State Li Ion Batteries. *Journal of Physical Chemistry Letters*, **2015**, *6*, 4599–4604. https://doi.org/10.1021/acs.jpclett.5b02352.

(303) Tong, Z.; Bazri, B.; Hu, S. F.; Liu, R. S. Interfacial Chemistry in Anode-Free Batteries: Challenges and Strategies. *J. Mater. Chem. A* **2021**, *9* (12), 7396–7406. https://doi.org/10.1039/D1TA00419K.

(304) Ning, Z.; Spencer Jolly, D.; Li, G.; De Meyere, R.; Pu, S. D.; Chen, Y.; Kasemchainan, J.; Ihli, J.; Gong, C.; Liu, B.; Bonnin, A.; Magdysyuk, O.; Adamson, P.; Hartley, G. O.; Monroe, W.; James Marrow, T.; Bruce, P. G. Visualising Plating-

Induced Cracking in Lithium Anode Solid Electrolyte Cells 1 2. *Nat. Mater.* **2021**, *20*, 1121–1129. https://doi.org/10.1038/s41563-021-00967-8.

(305) Suzuki, J.; Sekine, K.; Takamura, T. Evaluation of the Diffusion Coefficient of Li in Ag Using a Li+ Sensor Electrode Mounted in a Bipolar Cell. *Electrochemistry* **2006**, *74* (4), 303–308. https://doi.org/10.5796/electrochemistry.74.303.

(306) Yang, C.; Yao, Y.; He, S.; Xie, H.; Hitz, E.; Hu, L. Ultrafine Silver Nanoparticles for Seeded Lithium Deposition toward Stable Lithium Metal Anode. *Adv. Mater.* **2017**, *29* (38), 1702714. https://doi.org/10.1002/adma.201702714.

(307) Wang, Z.; Zhao, J.; Zhang, X.; Rong, Z.; Tang, Y.; Liu, X.; Zhu, L.; Zhang, L.; Huang, J. Tailoring Lithium Concentration in Alloy Anodes for Long Cycling and High Areal Capacity in Sulfide-Based All Solid-State Batteries. *eScience* **2023**, *3* (1), 100087. https://doi.org/10.1016/j.esci.2022.100087.

(308) Gu, X.; Jing Dong; Chao Lai. Li-containing Alloys Beneficial for Stabilizing Lithium Anode: A Review. *Eng. Rep.* **2021**, *3* (1), e12339.

(309) Armstrong, R. D.; Brown, O. R.; Ram, R. P.; Tuck, C. D. Lithium Electrodes Based upon Aluminium and Alloy Substrates I. Impedance Measurements on Aluminium. *J. Power Sources* **1989**, *28* (3), 259–267. https://doi.org/10.1016/0378-7753(89)80054-0.

(310) Taillades, G.; Sarradin, J. Silver: High Performance Anode for Thin Film Lithium Ion Batteries. *J Power Sources* **2004**, *125*, 199.

(311) Li, M.; Zhou, D.; Wang, C.; Weng, W.; Jiang, M.; Liu, G.; Yao, X.; He, H. Situ Formed Li−Ag Alloy Interface Enables Li 10 GeP 2 S 12-Based All-Cite This. *ACS Appl Mater Interfaces* **2021**, *13*, 50082. https://doi.org/10.1021/acsami.1c16356.

(312) Li, B.; Sun, Z.; Lv, N.; Hu, Y.; Jiang, L.; Zhang, Z.; Liu, F. Dual Protection of a Li−Ag Alloy Anode for All-Solid-State Lithium Metal Batteries with the Argyrodite Li 6 PS 5 Cl Solid Electrolyte. *ACS Appl Mater Interfaces* **2022**, *14*. https://doi.org/10.1021/acsami.2c09013.

(313) Wang, M. J.; Carmona, E.; Gupta, A.; Albertus, P.; Sakamoto, J. Enabling "Lithium-Free" Manufacturing of Pure Lithium Metal Solid-State Batteries through in Situ Plating. *Nat. Commun. 2020* **2020**, *11* (1), 1–9. https://doi.org/10.1038/s41467-020-19004-4.

(314) Lee, J. H.; Oh, S.-H.; Yim, H.; Lee, H.-J.; Kwon, E.; Yu, S.; Kim, J. S.; Song, J.; Koo, J.; Cho, J.; Kim, S. H.; Ryu, A.; Choi, S. H.; Kim, Y.; Im, G.; Choi, J.-W.; Yu, S.-H. Interfacial Stabilization Strategy via In-Doped Ag Metal Coating Enables a High Cycle Life of Anode-Free Solid-State Li Batteries. *Energy Storage Mater.* **2024**, *69*, 103398. https://doi.org/10.1016/j.ensm.2024.103398.

(315) Ting, L. K. J.; Gao, Y.; Wang, H.; Wang, T.; Sun, J.; Wang, J. Lithium Sulfide Batteries: Addressing the Kinetic Barriers and High First Charge Overpotential. *ACS Omega* **2022**, *7* (45), 40682–40700. https://doi.org/10.1021/acsomega.2c05477.

(316) Haslam, C. G.; Fuchs, T.; Liao, D. W.; Becker, J.; Dasgupta, N. P.; Janek, J.; Sakamoto, J. The Effect of Alloying Interlayers on Lithium Anode Morphology and Microstructure in "Anode-Free" Solid-State Batteries. *ACS Energy Lett.* **2025**, *10* (5), 2285–2291. https://doi.org/10.1021/acsenergylett.5c00149.

(317) Thomas, J.; Behara, S. S.; Van der Ven, A. Thermodynamic and Kinetic Properties of the Lithium–Silver System. *Chem. Mater.* **2024**, *36* (18), 8936–8948. https://doi.org/10.1021/acs.chemmater.4c01903.

(318) *Unlocking the Potential of Li–Ag Alloys: Phase Selection and Practical Application | Energy Material Advances*. https://spj.science.org/doi/10.34133/energymatadv.0108 (accessed 2025-09-07).

(319) Pavlyuk, V. V.; Dmytriv, G. S.; Tarasiuk, I. I.; Chumak, I. V.; Pauly, H.; Ehrenberg, H. Polymorphism of LiAg. *Solid State Sci.* **2010**, *12* (2), 274–280. https://doi.org/10.1016/J.SOLIDSTATESCIENCES.2009.11.006.

(320) Pei, A.; Zheng, G.; Shi, F.; Li, Y.; Cui, Y. Nanoscale Nucleation and Growth of Electrodeposited Lithium Metal. *Nano Lett* **2017**, *17*, 1132.

(321) Cheng, X.-B.; Zhang, R.; Zhao, C.-Z.; Zhang, Q. Toward Safe Lithium Metal Anode in Rechargeable Batteries: A Review. *Chem Rev* **2017**, *117*, 10403.

(322) Kazyak, E.; Wang, M. J.; Lee, K.; Yadavalli, S.; Sanchez, A. J.; Thouless, M. D.; Sakamoto, J.; Dasgupta, N. P. Understanding the Electro-Chemo-Mechanics of Li Plating in Anode-Free Solid-State Batteries with Operando 3D Microscopy. *Matter* **2022**, *5* (11), 3912–3934. https://doi.org/10.1016/J.MATT.2022.07.020.

(323) Liu, S.; Ma, Y.; Wang, J.; Zuo, P.; Du, C.; Yin, G.; Gao, Y. Regulating Li Deposition by Constructing Homogeneous LiF Protective Layer for High-Performance Li Metal Anode. *Chem. Eng. J.* **2022**, *427*, 131625. https://doi.org/10.1016/J.CEJ.2021.131625.

(324) Su, L.; Charalambous, H.; Cui, Z.; Manthiram, A. High-Efficiency, Anode-Free Lithium-Metal Batteries with a Close-Packed Homogeneous Lithium Morphology.

(325) Pang, B.; Gan, Y.; Xia, Y.; Huang, H.; He, X.; Zhang, W. Regulation of the Interfaces Between Argyrodite Solid Electrolytes and Lithium Metal Anode. *Front. Chem.* **2022**, *10*, 3.

(326) Liu, J.; Bao, Z.; Cui, Y.; Dufek, E. J.; Goodenough, J. B.; Khalifah, P.; Li, Q.; Liaw, B. Y.; Liu, P.; Manthiram, A. Pathways for Practical High-Energy Long-Cycling Lithium Metal Batteries. *Nat Energy* **2019**, *4*, 180.

(327) Kato, A.; Kowada, H.; Deguchi, M.; Hotehama, C.; Hayashi, A.; Tatsumisago, M. XPS and SEM Analysis between Li/Li3PS4 Interface with Au Thin Film for All-Solid-State Lithium Batteries. *Solid State Ion.* **2018**, *322*, 1.

(328) Choi, H. J.; Kang, D. W.; Park, J.-W.; Park, J.-H.; Lee, Y.-J.; Ha, Y.-C.; Lee, S.-M.; Yoon, S. Y.; Kim, B. G. In Situ Formed Ag-Li Intermetallic Layer for Stable Cycling of All-Solid-State Lithium Batteries. *Adv. Sci.* **2022**, *9* (1), 2103826. https://doi.org/10.1002/advs.202103826.

(329) Zhao, N.; Fei, X.; Cheng, X.; Yang, J. Synthesis of Silver/Silver Chloride/Graphene Oxide Composite and Its Surface-Enhanced Raman Scattering Activity and Self-Cleaning Property. *IOP Conf. Ser. Mater. Sci. Eng.* **2017**, *242* (1), 012002. https://doi.org/10.1088/1757-899X/242/1/012002.

(330) Zhai, P.; Liu, L.; Gu, X.; Wang, T.; Gong, Y. Interface Engineering for Lithium Metal Anodes in Liquid Electrolyte. *Adv. Energy Mater.* **2020**, *10* (34), 2001257. https://doi.org/10.1002/aenm.202001257.

(331) Liang, Z.; Xiang, Y.; Wang, K.; Zhu, J.; Jin, Y.; Wang, H.; Zheng, B.; Chen, Z.; Tao, M.; Liu, X.; Wu, Y.; Fu, R.; Wang, C.; Winter, M.; Yang, Y. Understanding the Failure Process of Sulfide-Based All-Solid-State Lithium Batteries via Operando Nuclear Magnetic Resonance Spectroscopy. *Nat. Commun.* **2023**, *14* (1), 259. https://doi.org/10.1038/s41467-023-35920-7.

(332) Jiang, Y.; Ye, F. Dead Lithium in Lithium Metal Batteries: Formation, Characterization and Strategies. *Chem. – Eur. J.* **2024**, *30* (43), e202400424. https://doi.org/10.1002/chem.202400424.

(333) Li, Y.; Li, Y.; Pei, A.; Yan, K.; Sun, Y.; Wu, C.-L.; Joubert, L.-M.; Chin, R.; Koh, A. L.; Yu, Y.; Perrino, J.; Butz, B.; Chu, S.; Cui, Y. Atomic Structure of Sensitive Battery Materials and Interfaces Revealed by Cryo–Electron Microscopy. *Science* **2017**, *358* (6362), 506–510. https://doi.org/10.1126/science.aam6014.

(334) Li, H.; Yamaguchi, T.; Matsumoto, S.; Hoshikawa, H.; Kumagai, T.; Okamoto, N. L.; Ichitsubo, T. Circumventing Huge Volume Strain in Alloy Anodes of Lithium Batteries. *Nat. Commun.* **2020**, *11* (1), 1–8. https://doi.org/10.1038/s41467-020-15452-0.

(335) Wang, J.; Wang, H.; Xie, J.; Yang, A.; Pei, A.; Wu, C. L.; Shi, F.; Liu, Y.; Lin, D.; Gong, Y.; Cui, Y. Fundamental Study on the Wetting Property of Liquid Lithium. *Energy Storage Mater.* **2018**, *14* (March), 345–350. https://doi.org/10.1016/j.ensm.2018.05.021.

(336) Meier, A.; Javernick, D. A.; Edwards, G. R. Ceramic-Metal Interfaces and the Spreading of Reactive Liquids. *Jom* **1999**, *51* (2), 44–47. https://doi.org/10.1007/s11837-999-0209-1.

(337) Hu, Y.; Li, H.; Chen, Z.; Cen, W.; Wang, Q.; Chen, Y.; Davoodi, A.; Liu, W. Li-Alloy Texture Creates in-Built Li(110) Epitaxy in a Thin Li-Metal Anode Allowing High Depth-of-Discharge Cycling in Carbonate Electrolyte. *Chem. Eng. J.* **2023**, *466*, 143084. https://doi.org/10.1016/j.cej.2023.143084.

(338) *Epitaxy | Crystal Growth & Characteristics | Britannica*. https://www.britannica.com/science/epitaxy (accessed 2024-11-03).

(339) He, Y.; Ren, X.; Xu, Y.; Engelhard, M. H.; Li, X.; Xiao, J.; Liu, J.; Zhang, J.-G.; Xu, W.; Wang, C. Origin of Lithium Whisker Formation and Growth Under Stress. *Nat Nanotechnol* **2019**, *14*, 1042.

(340) Cao, J.; Shi, Y.; Gao, A.; Du, G.; Dilxat, M.; Zhang, Y.; Cai, M.; Qian, G.; Lu, X.; Xie, F.; Sun, Y.; Lu, X. Hierarchical Li Electrochemistry Using Alloy-Type Anode for High-Energy-Density Li Metal Batteries. *Nat. Commun.* **2024**, *15* (1), 1354. https://doi.org/10.1038/s41467-024-45613-4.

(341) Cao, J.; Qian, G.; Lu, X.; Lu, X. Advanced Composite Lithium Metal Anodes with 3D Frameworks: Preloading Strategies, Interfacial Optimization, and Perspectives. *Small* **2023**, *19* (10), 2205653. https://doi.org/10.1002/smll.202205653.

(342) Aksay, I. A.; Hoge, C. E.; Pask, J. A. Wetting under Chemical Equilibrium. *J Phys Chem* **1973**, *i*, 1178–1183.

(343) Han, S. Y.; Lee, C.; Lewis, J. A.; Yeh, D.; Liu, Y.; Lee, H. W.; McDowell, M. T. Stress Evolution during Cycling of Alloy-Anode Solid-State Batteries. *Joule* **2021**, *5* (9), 2450–2465. https://doi.org/10.1016/J.JOULE.2021.07.002.

(344) Wu, B.; Wang, S.; Lochala, J.; Desrochers, D.; Liu, B.; Zhang, W.; Yang, J.; Xiao, J. The Role of the Solid Electrolyte Interphase Layer in Preventing Li Dendrite Growth in Solid-State Batteries. *Energy Environ. Sci.* **2018**, *11* (7), 1803–1810. https://doi.org/10.1039/c8ee00540k.

(345) Nitta, N.; Yushin, G. High-Capacity Anode Materials for Lithium-Ion Batteries: Choice of Elements and Structures for Active Particles. *Part. Part. Syst. Charact.* **2014**, *31* (3), 317–336. https://doi.org/10.1002/ppsc.201300231.

(346) Hong, C. S.; Han, S. M. Mechanical Properties of Electrochemically Lithiated Sn. *Extreme Mech. Lett.* **2020**, *40*, 100907. https://doi.org/10.1016/j.eml.2020.100907.

(347) Hertzberg, B.; Benson, J.; Yushin, G. Ex-Situ Depth-Sensing Indentation Measurements of Electrochemically Produced Si-Li Alloy Films. *Electrochem. Commun.* **2011**, *13* (8), 818–821. https://doi.org/10.1016/j.elecom.2011.05.011.

(348) Lu, Y.; Zhao, C. Z.; Yuan, H.; Cheng, X. B.; Huang, J. Q.; Zhang, Q. Critical Current Density in Solid-State Lithium Metal Batteries: Mechanism, Influences, and Strategies. *Adv. Funct. Mater.* **2021**, *31* (18), 2009925. https://doi.org/10.1002/ADFM.202009925.

(349) Feng, W.; Dong, X.; Li, P.; Wang, Y.; Xia, Y. Interfacial Modification of Li/Garnet Electrolyte by a Lithiophilic and Breathing Interlayer. *J Power Sources* **2019**, *419*, 91.

(350) Zhao, N.; Fang, R.; He, M.-H.; Chen, C.; Li, Y.-Q.; Bi, Z.-J.; Guo, X.-X. Cycle Stability of Lithium/Garnet/Lithium Cells with Different Intermediate Layers. *Rare Met* **2018**, *37*, 473.

(351) Electrolyte, S. Effect of Gold Layer on Interface Resistance between Lithium Metal. **2017**. https://doi.org/10.1149/2.0471706jes.

(352) Lu, Y.; Huang, X.; Ruan, Y.; Wang, Q.; Kun, R.; Yang, J.; Wen, Z. An in Situ Element Permeation Constructed High Endurance Li–LLZO Interface at High Current Densities. *J Mater Chem A* **2018**, *6*, 18853.

(353) Tsai, C.-L.; Roddatis, V.; Chandran, C. V.; Ma, Q.; Uhlenbruck, S.; Bram, M.; Heitjans, P.; Guillon, O. Li7La3Zr2O12 Interface Modification for Li Dendrite Prevention. *ACS Appl Mater Interfaces* **2016**, *8*, 10617.

(354) Luo, W.; Gong, Y.; Zhu, Y.; Li, Y.; Yao, Y.; Zhang, Y.; Fu, K. K.; Pastel, G.; Lin, C.-F.; Mo, Y. Reducing Interfacial Resistance between Garnet-Structured Solid-State Electrolyte and Li-Metal Anode by a Germanium Layer. *Adv Mater* **2017**, *29*, 1606042.

(355) Fu, K. K.; Gong, Y.; Fu, Z.; Xie, H.; Yao, Y.; Liu, B.; Carter, M.; Wachsman, E.; Hu, L. Transient Behavior of the Metal Interface in Lithium Metal–Garnet Batteries. *Angew. Chem. Int. Ed.* **2017**, *56* (47), 14942–14947. https://doi.org/10.1002/ANIE.201708637.

(356) He, M.; Cui, Z.; Chen, C.; Li, Y.; Guo, X. Formation of Self-Limited, Stable and Conductive Interfaces between Garnet Electrolytes and Lithium Anodes for Reversible Lithium Cycling in Solid-State Batteries. *J Mater Chem A* **2018**, *6*, 11463.

(357) V. Alexander, G.; V. Sreejith, O.; S. Indu, M.; Murugan, R. Interface-Compatible and High-Cyclability Lithiophilic Lithium–Zinc Alloy Anodes for Garnet-Structured Solid Electrolytes. *ACS Appl. Energy Mater.* **2020**, *0* (0). https://doi.org/10.1021/acsaem.0c01430.

(358) Grimsmann, F.; Brauchle, F.; Gerbert, T.; Gruhle, A.; Knipper, M.; Parisi, J. Hysteresis and Current Dependence of the Thickness Change of Lithium-Ion Cells with Graphite Anode. *J. Energy Storage* **2017**, *12*, 132–137. https://doi.org/10.1016/j.est.2017.04.006.

(359) Schweidler, S.; De Biasi, L.; Schiele, A.; Hartmann, P.; Brezesinski, T.; Janek, J. Volume Changes of Graphite Anodes Revisited: A Combined Operando X-Ray Diffraction and in Situ Pressure Analysis Study. *J. Phys. Chem. C* **2018**, *122* (16), 8829–8835. https://pubs.acs.org/doi/full/10.1021/acs.jpcc.8b01873.

(360) Xing, X.; Li, Y.; Wang, S.; Liu, H.; Wu, Z.; Yu, S.; Holoubek, J.; Zhou, H.; Liu, P. Graphite-Based Lithium-Free 3D Hybrid Anodes for High Energy Density All-Solid-State Batteries. *ACS Energy Lett.* **2021**, *6* (5), 1831–1838. https://pubs.acs.org/doi/full/10.1021/acsenergylett.1c00627.

(361) Takada, K.; Inada, T.; Kajiyama, A.; Sasaki, H.; Kondo, S.; Watanabe, M.; Murayama, M.; Kanno, R. Solid-State Lithium Battery with Graphite Anode. *Solid State Ion.* **2003**, *158* (3–4), 269–274. https://doi.org/10.1016/S0167-2738(02)00823-8.

(362) Futscher, M. H.; Amelal, T.; Sastre, J.; Müller, A.; Patidar, J.; Aribia, A.; Thorwarth, K.; Siol, S.; Romanyuk, Y. E. Influence of Amorphous Carbon Interlayers on Nucleation and Early Growth of Lithium Metal at the Current Collector-Solid Electrolyte Interface. *J. Mater. Chem. A* **2022**, *10* (29), 15535–15542. https://doi.org/10.1039/D2TA02843C.

(363) Doerrer, C.; Metzler, M.; Matthews, G.; Bu, J.; Spencer-Jolly, D.; Bruce, P. G.; Pasta, M.; Grant, P. S. Spraying Li6PS5Cl and Silver-Carbon Multilayers to Facilitate

Large-Scale Fabrication of All-Solid-State Batteries. *Device* **2024**, *2* (8), 100468. https://doi.org/10.1016/j.device.2024.100468.

(364) Seymour, I. D.; Ainara Aguadero. Suppressing Void Formation in All-Solid-State Batteries: The Role of Interfacial Adhesion on Alkali Metal Vacancy Transport. *J. Mater. Chem. A* **2021**, *9* (35), 19901–19913. https://doi.org/10.1039/D1TA03254B.

(365) Ning, Z.; Li, G.; Melvin, D. L. R.; Chen, Y.; Bu, J.; Spencer-Jolly, D.; Liu, J.; Hu, B.; Gao, X.; Perera, J.; Gong, C.; Pu, S. D.; Zhang, S.; Liu, B.; Hartley, G. O.; Bodey, A. J.; Todd, R. I.; Grant, P. S.; Armstrong, D. E. J.; Marrow, T. J.; Monroe, C. W.; Bruce, P. G. Dendrite Initiation and Propagation in Lithium Metal Solid-State Batteries. *Nature* **2023**, *618* (7964), 287–293. https://doi.org/10.1038/s41586-023-05970-4.

(366) Höltschi, L.; Borca, C. N.; Huthwelker, T.; Marone, F.; Schlepütz, C. M.; Pelé, V.; Jordy, C.; Villevieille, C.; Kazzi, M. E.; Novák, P. Performance-Limiting Factors of Graphite in Sulfide-Based All-Solid-State Lithium-Ion Batteries. *Electrochimica Acta* **2021**, *389*, 138735 (10 pp.)-138735 (10 pp.).

(367) Dahn, J. R. Phase Diagram of Li_xC_6. *Phys. Rev. B* **1991**, *44*. https://doi.org/10.1103/PhysRevB.44.9170.

(368) Fujimoto, H.; Yamaki, T.; Shimoda, K.; Fujinami, S.; Nakatani, T.; Kano, G.; Kawasaki, M.; Ogumi, Z.; Abe, T. Phase Diagram of Li-Graphite Intercalation Compound Formed by the Charge/Discharge Reaction in Li-Ion Battery. *J. Electrochem. Soc.* **2022**, *169* (7), 70507. https://doi.org/10.1149/1945-7111/AC7E77.

(369) Missyul, A.; Bolshakov, I.; Shpanchenko, R. XRD Study of Phase Transformations in Lithiated Graphite Anodes by Rietveld Method. *Powder Diffr.* **2017**, *32* (S1), S56–S62. https://doi.org/10.1017/S0885715617000458.

(370) Freeth, W. E.; Raynor, G. V. The Constitution of the System Silver-Lithium. *J. Inst. Met.* **1953**, *82*, 569–574.

(371) Persson, K.; Sethuraman, V. A.; Hardwick, L. J.; Hinuma, Y.; Meng, Y. S.; Van Der Ven, A.; Srinivasan, V.; Kostecki, R.; Ceder, G. Lithium Diffusion in Graphitic Carbon. *J. Phys. Chem. Lett.* **2010**, *1* (8), 1176–1180. https://pubs.acs.org/doi/full/10.1021/jz100188d.

(372) Xie, H.; Yang, C.; Ren, Y.; Xu, S.; Hamann, T. R.; Mcowen, D. W.; Wachsman, E. D.; Hu, L. Amorphous-Carbon-Coated 3D Solid Electrolyte for an Electro-Chemomechanically Stable Lithium Metal Anode in Solid-State Batteries. *Nano Lett.* **2021**. https://doi.org/10.1021/acs.nanolett.1c01748.

(373) Suzuki, N.; Yashiro, N.; Fujiki, S.; Omoda, R.; Shiratsuchi, T.; Watanabe, T.; Aihara, Y. Highly Cyclable All-Solid-State Battery with Deposition-Type Lithium Metal Anode Based on Thin Carbon Black Layer. *Adv. Energy Sustain. Res.* **2021**, *2* (11), 2100066. https://doi.org/10.1002/AESR.202100066.

(374) Allart, D.; Montaru, M.; Gualous, H. Model of Lithium Intercalation into Graphite by Potentiometric Analysis with Equilibrium and Entropy Change Curves of Graphite Electrode. *J. Electrochem. Soc.* **2018**, *165* (2), A380–A387. https://doi.org/10.1149/2.1251802JES/XML.

(375) Fertig, M. P.; Skadell, K.; Wegner, K.; Schulz, M.; Stelter, M. A Medium-Temperature All-Solid-State Sodium Battery Utilizing Sodium-Beta Alumina and a Polymeric Composite Positive Electrode. *J. Electrochem. Soc.* **2023**, *170* (5), 050501. https://doi.org/10.1149/1945-7111/accf39.

(376) Flor, G.; Marini, A.; Massarotti, V.; Villa, M. Reactivity of β-Aluminas with Water. *Solid State Ion.* **1981**, *2* (3), 195–204. https://doi.org/10.1016/0167-2738(81)90179-X.

(377) Will, F. G. Effect of Water on Beta Alumina Conductivity. *J. Electrochem. Soc.* **1976**, *123* (6), 834. https://doi.org/10.1149/1.2132943.

(378) Spencer Jolly, D.; Ning, Z.; Darnbrough, J. E.; Kasemchainan, J.; Hartley, G. O.; Adamson, P.; Armstrong, D. E. J.; Marrow, J.; Bruce, P. G. Sodium/Na B″ Alumina Interface: Effect of Pressure on Voids. *ACS Appl. Mater. Interfaces* **2020**, *12* (1), 678–685. https://doi.org/10.1021/acsami.9b17786.

(379) Tian, Y.; Shi, T.; D. Richards, W.; Li, J.; Chul Kim, J.; Bo, S.-H.; Ceder, G. Compatibility Issues between Electrodes and Electrolytes in Solid-State Batteries. *Energy Environ. Sci.* **2017**, *10* (5), 1150–1166. https://doi.org/10.1039/C7EE00534B.

(380) Lewis, J. A.; Cortes, F. J. Q.; Boebinger, M. G.; Tippens, J.; Marchese, T. S.; Kondekar, N.; Liu, X.; Chi, M.; McDowell, M. T. Interphase Morphology between a Solid-State Electrolyte and Lithium Controls Cell Failure. *ACS Energy Lett* **2019**, *4*, 591.

(381) Zhang, W.; Zhao, C. D.; Wu, X. L. Research Progresses on Interfaces in Solid-State Sodium Batteries: A Topic Review. *Adv. Mater. Interfaces* **2020**, *7* (23), 2001444. https://doi.org/10.1002/ADMI.202001444.

(382) Dai, H.; Chen, Y.; Xu, W.; Hu, Z.; Gu, J.; Wei, X.; Xie, F.; Zhang, W.; Wei, W.; Guo, R.; Zhang, G. A Review of Modification Methods of Solid Electrolytes for All-Solid-State Sodium-Ion Batteries. *Energy Technol.* **2021**, *9* (1), 2000682. https://doi.org/10.1002/ENTE.202000682.

(383) Cuesta, A. F.; Dickson, S. A. M.; Naden, A. B.; Lonsdale, C.; Irvine, J. T. S. Influence of Electrode Processing and Electrolyte Composition on Multiwall Carbon Nanotube Negative Electrodes for Sodium Ion Batteries. *J. Phys. Energy* **2023**, *5* (1), 015004. https://doi.org/10.1088/2515-7655/acb3fc.

(384) Yoon, G.; Kim, S.; Kim, J.-S. Design Strategies for Anodes and Interfaces Toward Practical Solid-State Li-Metal Batteries. *Adv. Sci.* **2023**, *10* (27), 2302263. https://doi.org/10.1002/advs.202302263.

(385) Otto, S.-K.; Fuchs, T.; Moryson, Y.; Lerch, C.; Mogwitz, B.; Sann, J.; Janek, J.; Henss, A. Storage of Lithium Metal: The Role of the Native Passivation Layer for the Anode Interface Resistance in Solid State Batteries. *ACS Appl. Energy Mater.* **2021**, *4* (11), 12798–12807. https://doi.org/10.1021/acsaem.1c02481.

(386) *Plasma Treatment Explained in Simple Terms - Henniker Plasma*. https://plasmatreatment.co.uk/pt/plasma-technology-overview/plasma-treatment-explained (accessed 2024-08-26).

(387) *Auger Peaks and the Auger Parameter*. http://www.xpsfitting.com/2012/08/auger-peaks-and-auger-parameter.html (accessed 2024-10-28).

(388) Huey, M. *Argon vs. Nitrogen Purging for Atmospheric Inerting*. Nitrogen & Gas Solutions. https://www.generon.com/argon-vs-nitrogen-purging-for-inerting/ (accessed 2024-08-28).

(389) Talebizadeh, P.; Babaie, M.; Brown, R.; Rahimzadeh, H.; Ristovski, Z.; Arai, M. The Role of Non-Thermal Plasma Technique in NOx Treatment: A Review. *Renew. Sustain. Energy Rev.* **2014**, *40*, 886–901. https://doi.org/10.1016/j.rser.2014.07.194.

(390) Penetrante, B. M.; Brusasco, R. M.; Merritt, B. T.; Vogtlin, G. E. Environmental Applications of Low-Temperature Plasmas. *Pure Appl. Chem.* **1999**, *71* (10), 1829–1835. https://doi.org/10.1351/pac199971101829.

(391) *Plasma Surface Modification of Polymers: Relevance to Adhesion*; Mittal, K. L., M, Lyons, Eds.; CRC Press: London, **1994**. https://doi.org/10.1201/b12019.

(392) El-Hossary, F. M.; Ghitas, A.; El-Rahman, A. M. A.; Shahat, M. A.; Fawey, M. H. The Effective Reduction of Graphene Oxide Films Using RF Oxygen Plasma

Treatment. *Vacuum* **2021**, *188*, 110158. https://doi.org/10.1016/j.vacuum.2021.110158.

(393) Begley, A.; Oganesyan, I.; Mrđenović, D.; Smok, I.; Leitner, A.; Zenobi, R. Low-Temperature Plasma Jet Treatment Generates Reactive Oxygen Species in Solution That Leads to Peptide Oxidation and Protein Aggregation. *J. Phys. Appl. Phys.* **2024**. https://doi.org/10.1088/1361-6463/ad211c.

(394) Tang, B.; Jaschin, P. W.; Li, X.; Bo, S. H.; Zhou, Z. Critical Interface between Inorganic Solid-State Electrolyte and Sodium Metal. *Mater. Today* **2020**, *41*, 200–218. https://doi.org/10.1016/J.MATTOD.2020.08.016.

8 Appendix

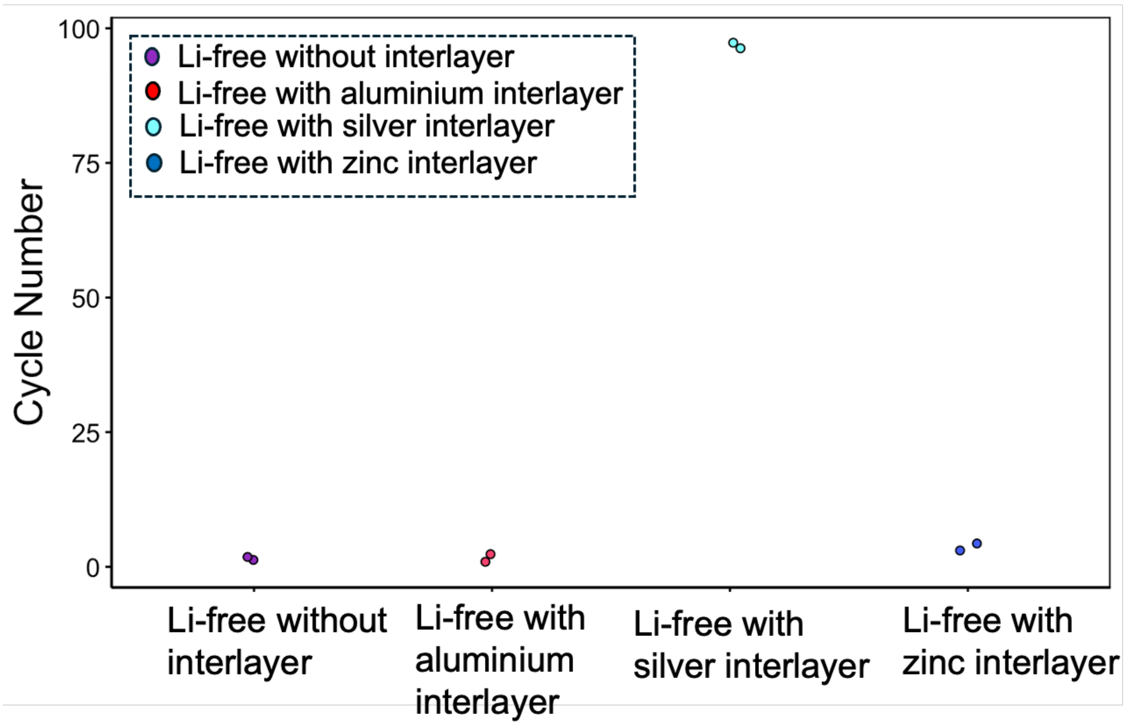

Figure A.1. Graph showing cycle number of Li-free full cell without metal interlayer (purple) in comparison with Li-free cell with aluminium metal interlayer (red), silver metal interlayer (teal) and zinc metal interlayer (blue). Silver metal interlayer shows high cycling performance.

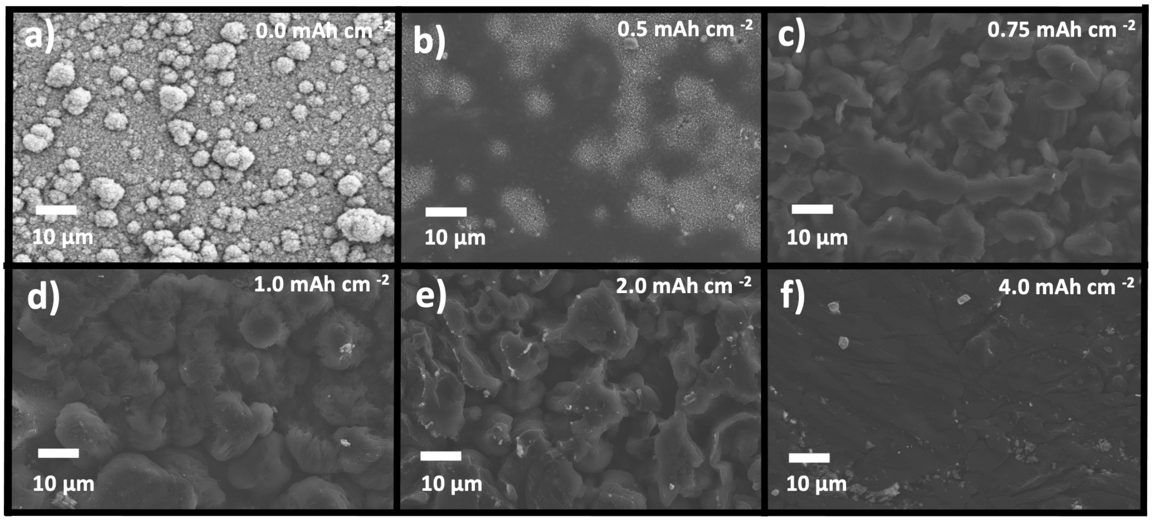

Figure A.2. Top-view SEMs of half-cells with zinc metal interlayer on sulphide solid electrolyte after removal of current collector. Each panel shows a separate cell SEM arrested at a different point in charge after a) 0.0 mAh cm^{-2}, b) 0.5 mAh cm^{-2}, c) 0.75 mAh cm^{-2}; d) 1 mAh cm^{-2}; e) 2.0 mAh cm^{-2} and d) 4.0 mAh cm^{-2}. These SEM images show the morphology after passing different amounts of Li metal. In case of pristine i.e, a) the morphology of zinc metal interlayer is shown and as Li metal is passed, it shows pillar like morphology and at 4.0 mAh cm^{-2} i.e, f) homogenous deposition of Li-Zn alloy is observed.

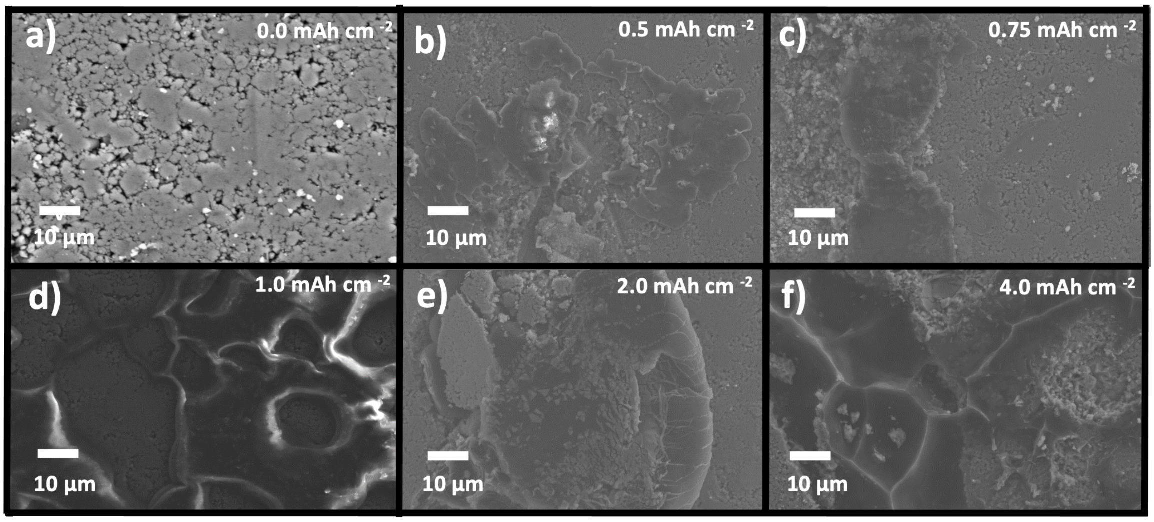

Figure A.3. Top-view SEMs of half-cells with aluminium metal interlayer on sulphide solid electrolyte after removal of current collector. Each panel shows a separate cell SEM arrested at a different point in charge after a) 0.0 mAh cm^{-2}; b) 0.5 mAh cm^{-2}; c) 0.75 mAh cm^{-2}; d) 1 mAh cm^{-2}; e) 2.0 mAh cm^{-2} and d) 4.0 mAh cm^{-2}. These SEM images show the morphology after passing different amounts of Li metal. In case of pristine i.e, a) the morphology of aluminium metal interlayer is shown and as Li metal is passed i.e, b, c, d, e, f, it shows inhomogeneous deposition of Li metal and alloy.

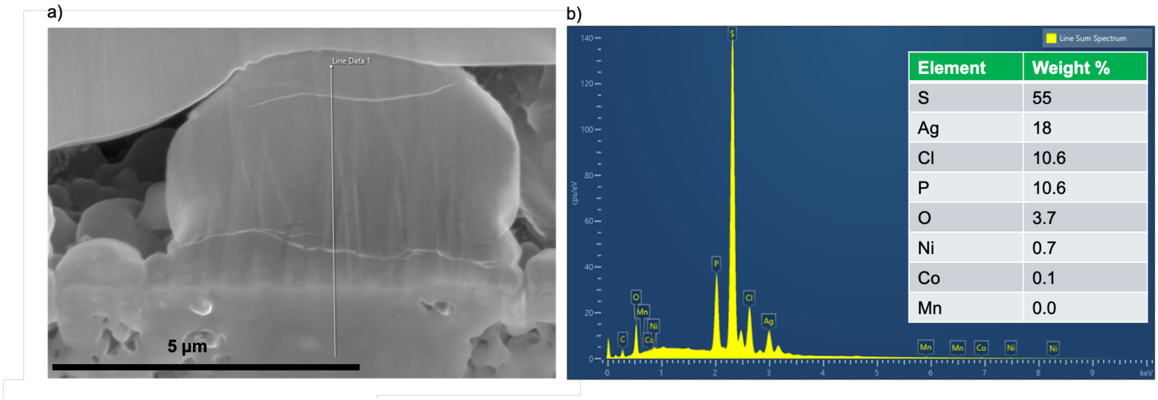

Element	Weight %
S	55
Ag	18
Cl	10.6
P	10.6
O	3.7
Ni	0.7
Co	0.1
Mn	0.0

Figure A.4. Quantative analysis of EDX data, where a) shows the electron image with line data in white; b) shows the element with weight % analysed by Aztec software.

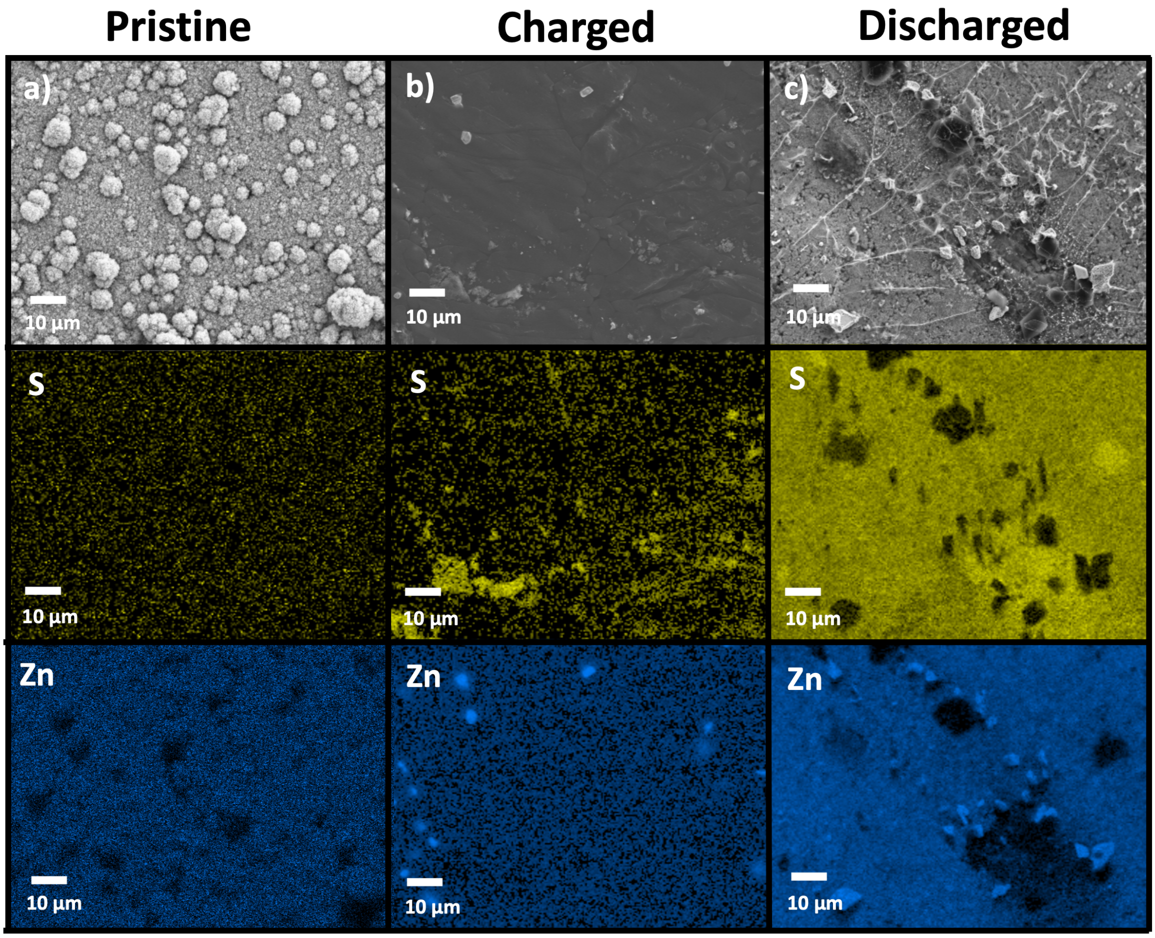

Figure A.5. Top-view SEM/EDX colour maps of Li-free ASSBs with zinc metal interlayer surfaces after charge and discharge at 4 mAhcm^{-2} at 60°C at 0.05 mA cm^{-2} current density after the careful removal of stainless-steel current collector. (a) Li-free pristine with zinc metal interlayer b) after charging; and (c) after discharge with corresponding EDX maps. Yellow shows sulphur and blue shows the presence of zinc metal interlayer. (b) shows homogenous deposition of Li-Zn alloy after charging, however after discharge, globules of Li metal are left behind as dead lithium, which can be observed due to the absence of zinc signal in the corresponding EDX maps.

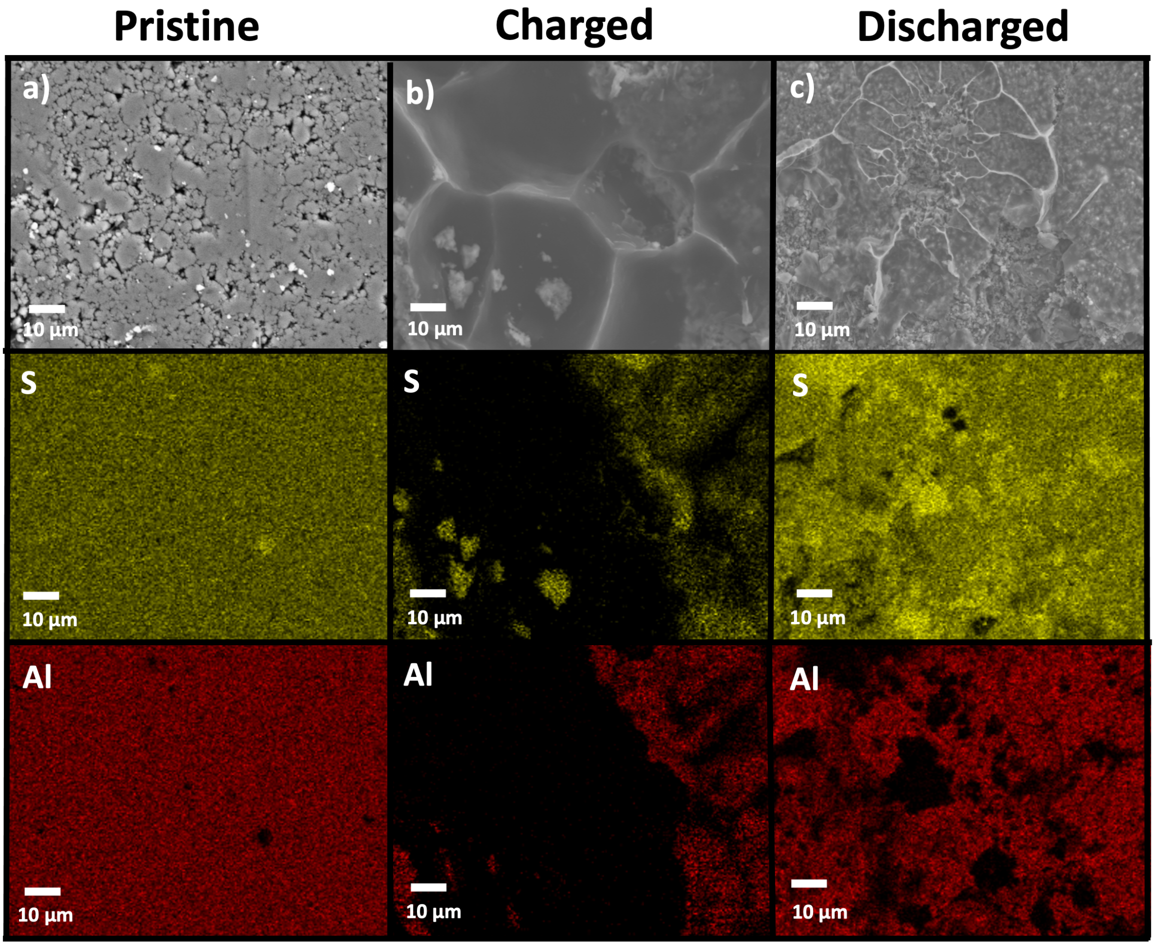

Figure A.6. Top-view SEM/EDX colour maps of Li-free ASSBs with aluminium metal interlayer surfaces after charge and discharge at 4 mAhcm^{-2} at 60°C at 0.05 mA cm^{-2} current density after the careful removal of stainless-steel current collector. (a) Li-free pristine with aluminium metal interlayer b) after charging; and (c) after discharge with corresponding EDX maps. Yellow shows sulphur and red shows the presence of aluminium metal interlayer. (b) shows inhomogeneous deposition of Li-Al alloy after charging, c) shows Li metal left behind as dead lithium, which can be observed due to the absence of aluminium signal in the corresponding EDX maps.

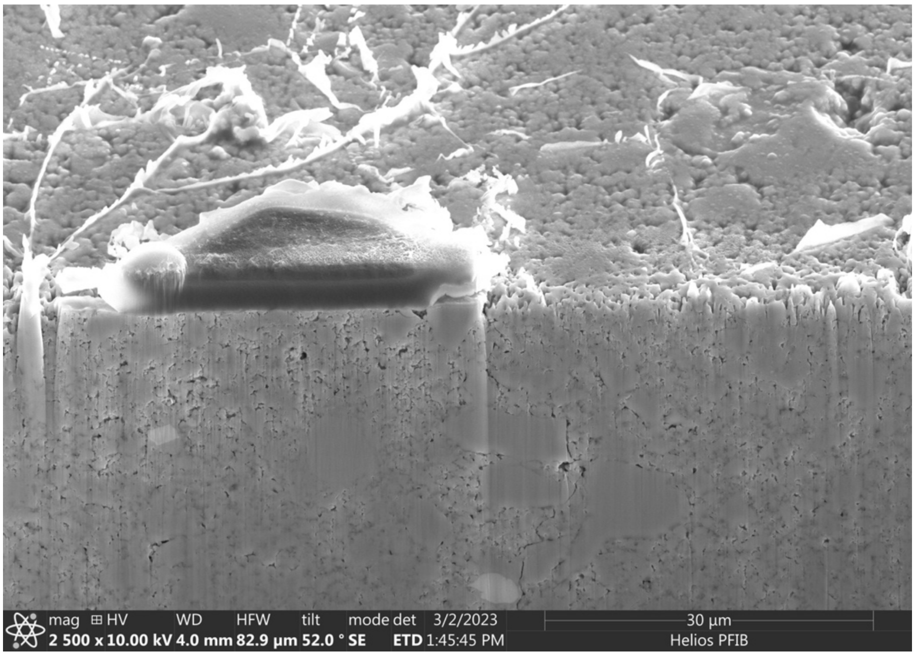

Figure A.7. Raw image for Li-free ASSB after discharge.

Table A.1. For silver XPS analyses, a survey scan of 0 to 1100 eV was collected. Shirley background with cross section area as 299, 542 , 275 , 9.3 was fixed. LA (50) lineshape was utilised.

For **Ag 3d spectra** are analysed as doublets 3d$^{5/2}$ and 3d$^{3/2}$, the position was fixed at 368.36 and 374.36 eV. Two regions were defined. Each had two components and were analysed with LA (50) lineshape. RSF value was 18.04 for all components.

	LiAg 3d$^{5/2}$	**LiAg 3d$^{3/2}$**	**Ag$_2$S 3d$^{5/2}$**	**Ag$_2$S 3d$^{3/2}$**
Position	368.36	378.317	369.06	375.07
Area Constraint	0.0 , 603467.9	0.0 , 670289.0	0.0 , 670289.0	0.0 , 670289.0
FWHM constraint	0.19 , 4.75	0.19 , 4.75	0.3811 , 9.527	0.2662 , 6.656
% atomic concentration	50.57	33.60	9.59	6.23

For **S 2p spectra** are analysed as doublets 2p$^{3/2}$ and 2p$^{1/2}$, 3 components were analysed with LA(50) lineshape and position constraint of 165.37, 157.86 (this is the start and end of the region). RSF value was 1.677 for all components.

	S-Li$_6$PS$_5$Cl 2p$^{3/2}$	**S-Li$_6$PS$_5$Cl 2p$^{1/2}$**	**Li$_2$S 2p$^{3/2}$**	**Li$_2$S 2p$^{1/2}$**	**Ag$_2$S 2p$^{3/2}$**	**Ag$_2$S 2p$^{1/2}$**
Position	162.34	163.37	161.056	162.0016	162.063	163.077
Area Constraint	0.0, 126730.0	S-Li$_6$PS$_5$Cl 2p$^{3/2}$ *0.5	0.0, 126730.0	Li$_2$S 2p$^{3/2}$ *0.5	0.0, 127276.9	Ag$_2$S 2p$^{3/2}$ *0.5
FWHM constraint	0.29, 7.25	S-Li$_6$PS$_5$Cl 2p$^{3/2}$ *1	0.4318, 10.8	Li$_2$S 2p$^{3/2}$ *1	0.263, 6.575	Ag$_2$S 2p$^{3/2}$ *1
% atomic concentration	42.53	21.26	10.10	5.05	14.04	7.02

For **P 2p spectra** are analysed as doublets 2p$^{3/2}$ and 2p$^{1/2}$, 133.21eV position was fixed. 2 components were analysed with LA(50) lineshape. All of them had a position constraint of

137.696, 128.527 (this is the start and end of the region). RSF value was 1.192 for all components.

	P- Li_6PS_5Cl $2p^{3/2}$	**P- Li_6PS_5Cl $2p^{1/2}$**	**Li_3P $2p^{3/2}$**	**Li_3P $2p^{1/2}$**
Position	133.0233	133.5503	134.2875	134.7739
Area Constraint	0.0 , 26726.0	P- Li_6PS_5Cl $2p^{3/2}$ *0.5	0.0 , 26726.0	Li_3P $2p^{3/2}$ *0.5
FWHM constraint	0.38 , 9.5	P- Li_6PS_5Cl $2p^{3/2}$ *1	0.4677 , 11.69	Li_3P $2p^{3/2}$ *1
% atomic concentration	63.58	31.79	3.09	1.54

For **Cl 2p spectra** are analysed as doublets $2p^{3/2}$ and $2p^{1/2}$, 199.46eV position was fixed. 3 components were analysed with LA(50) lineshape. Position constraint of 203.535 , 194.724 (this is the start and end of the region). RSF value was 2.285 for all components.

	Cl - Li_6PS_5Cl $2p^{3/2}$	**Cl-Li_6PS_5Cl $2p^{1/2}$**	**LiCl $2p^{3/2}$**	**LiCl $2p^{1/2}$**	**AgCl $2p^{3/2}$**	**AgCl $2p^{1/2}$**
Position	199.3282	200.9905	200.0840	201.3139	199.2976	199.7968
Area Constraint	0.0 , 38249.0	Cl-Li_6PS_5Cl $2p^{3/2}$ *0.5	0.0 , 38249.0	LiCl $2p^{3/2}$ *0.5	0.0 , 38249.0	AgCl $2p^{3/2}$ *0.5
FWHM constraint	0.26 , 6.5	Cl-Li_6PS_5Cl $2p^{3/2}$ *1	0.3415 , 8.538	LiCl $2p^{3/2}$ *1	0.3069 , 7.672	AgCl $2p^{3/2}$ *1
% atomic concentration	52.71	26.35	10.33	5.16	3.63	1.81

Now **for pristine Ag_2S sample , for Ag 3d spectra** 368.90 and 374.91eV position was fixed and are analysed as doublets $3d^{5/2}$ and $3d^{3/2}$. 2 regions were defined, similar to above. 1 components were analysed with LA (50) lineshape. RSF value was 18.04 for all components.

	Ag_2S $3d^{5/2}$	**Ag_2S $3d^{3/2}$**
Position	368.9076	374.91
Area Constraint	0.0 , 2462403.0	0.0 , 2462403.0
FWHM constraint	0.19 , 4.75	0.19 , 4.75
% atomic concentration	59.60	40.40

For S 2p spectra are analysed as doublets $2p^{3/2}$ and $2p^{1/2}$**,** 162.07eV position was fixed. 1 components were analysed with LA(50) lineshape and position constraint of 166.991, 158.40 (this is the start and end of the region). RSF value was 1.677 for all components.

	Ag_2S $2p^{3/2}$	**Ag_2S $2p^{1/2}$**
Position	162.033	163.23
Area Constraint	0.0 , 132066.0	Ag_2S $2p^{3/2}$ *0.5
FWHM constraint	0.19 , 4.75	Ag_2S $2p^{3/2}$ *1
% atomic concentration	66.67	33.33

For **pristine LiAg sample, the Ag 3d spectra** 368.39 and 374.39eV position was fixed and are analysed as doublets $3d^{5/2}$ and $3d^{3/2}$. 2 regions were defined. 2 components were analysed with LA (50) lineshape. RSF value was 18.04 for all components.

	LiAg $3d^{5/2}$	**LiAg $3d^{3/2}$**
Position	368.4347	374.4512
Area Constraint	0.0 , 275747.0	0.0 , 275747.0
FWHM constraint	0.16 , 4	0.16 , 4
% atomic concentration	62.00	38.00

Table A.2. For all three NBA combined samples consisting of air-exposed, heat treatment and plasma treatment, a survey scan of 0 to 1100 eV was conducted. Shirley background with cross section 299 , 542 , 275 , 9.3 was used with LA (50) lineshape.

Air-exposed

For **C 1s spectra**, 284.8eV position was fixed. 3 components were analysed. All of them had an area constraint of 0.0, 65895.0 (default) and position constraint of 293.877, 280.545. (this is the start and end of the region). There was no FWHM constraint, default was used. RSF value was 1 for all components.

	C-C/C-H	**C-OH/O-C=O**	**Na_2CO_3**
Position	284.877	285.886	289.0855
% atomic concentration	56.56	31.48	11.96

For **O 1s spectra**, 530.95 eV position was fixed. 4 components were analysed. All of them had an area constraint of 0.0, 661940.0 (default) and position constraint of 538.892, 525.781. (this is the start and end of the region). There was no FWHM constraint, default was used. RSF value was 2.93 for all components.

	C-O/C-O=O	**$Al(OH)_3$**	**Na_2CO_3**	**NBA_O**
Position	532.6358	532.029	531.5892	530.70
% atomic concentration	2.60	28.25	7.03	62.12

For **Al 2p spectra**, 74.25 eV position was fixed. 4 components were analysed. All of them had an area constraint of 0.0 , 163070.0 (default) except AlOH, which had an area constraint of 0.5 * Al $2p^{3/2}$ and position constraint of 66.2162 , 60.6921 (this is the start and end of the region) for NBA and Na_2CO_3 and 78.5578, 59.9384 for Al 2p and AlOH. There was FWHM constraint for AlOH as 1* Al $2p^{3/2}$. RSF value was 0.5371 for all components.

	NBA_Na	**Na_2CO_3**	**Al-O $2p^{3/2}$**	**AlOH $2p^{1/2}$**
Position	63.6665	63.4559	74.0026	74.9007
Area Constraint	0.0 , 163070.0	0.0 , 36032.6	0.0 , 163070.0	Al-O $2p^{3/2}$ *0.5
FWHM constraint	0.4969 , 12.42	0.4572 , 11.43	0.4385 , 10.96	Al $2p^{3/2}$ *1
% atomic concentration	4.57	5.67	59.84	29.92

Heat Treated

For **C 1s spectra**, 284.8 eV position was fixed. 3 components were analysed. All of them had an area constraint of 0.0, 65895.0 (default) and position constraint of 294.617 , 280.018. (this is the start and end of the region). There was no FWHM constraint, default was used. RSF value was 1 for all components.

	C-C/C-H	**C-OH/O-C=O**	**Na_2CO_3**
Position	284.8432	286.2223	289.9737
FWHM constraint	0.39 , 9.75	1.006 , 25.16	0.44 , 11
% atomic concentration	61.98	13.69	24.32

For **O 1s spectra**, 530.81 eV position was fixed. 4 components were analysed. All of them had an area constraint of 0.0, 723557.0 (default) and position constraint of 539.305, 526.592 (this is the start and end of the region). There was no FWHM constraint, default values were used. RSF value was 2.93 for all components.

	C-O/C-O=O	**$Al(OH)_3$**	**Na_2CO_3**	**NBA_O**
Position	532.5804	531.5265	532.0136	530.6969
FWHM constraint	0.63, 15.75	1.09, 27.25	1.09, 27.25	0.46, 11.5
% atomic concentration	5.44	15.40	16.70	62.46

For Al 2p spectra, 73.75 eV position was fixed. 4 components were analysed.

RSF value was 0.5371 for all components.

	NBA_Al	**Na_2CO_3**	**Al-O 2p$^{3/2}$**	**AlOH 2p$^{1/2}$**
Position	63.5562	63.7960	73.6319	74.42
Position constraint	67.0039, 60.3235	67.0039, 60.3235	78.1635, 59.9724	78.1635, 59.9724
Area constraint	0.0 , 188485.0	0.0 , 50366.2	0.0 , 188485.0	Al-O 2p$^{3/2}$ *0.5
FWHM constraint	0.722, 18.05	0.4359, 10.9	0.441, 11.02	Al-O 2p$^{3/2}$ *1
% atomic concentration	11.20	2.71	57.39	28.69

Plasma Cleaned

For **C1s spectra**, 284.8 eV position was fixed. 3 components were analysed. All of them had an area constraint of 0.0, 78959.0 (default) and position constraint of 291.469, 280.976. (this is the start and end of the region). There was no FWHM constraint, default values were used. RSF value was 1 for all components.

	C-C/C-H	**C-OH/O-C=O**	**Na_2CO_3**
Position	284.6972	285.8278	288.6803
FWHM constraint	0.35 , 8.75	0.34 , 8.5	1.252 , 31.3
% atomic concentration	69.90	25.33	4.77

For **O 1s spectra**, 530.60 eV position was fixed. 4 components were analysed. All of them had an area constraint of 0.0, 830944.0 (default) and position constraint of 538.741, 526.375 (this is the start and end of the region). There was no FWHM constraint, default values were used. RSF value was 2.93 for all components.

	C-O/C-O=O	**$Al(OH)_3$**	**Na_2CO_3**	**NBA_O**
Position	532.9961	531.3885	530.9919	530.5207
FWHM constraint	0.35, 8.75	0.4712, 11.78	0.5382, 13.46	0.4, 10
% atomic concentration	0.22	13.87	9.64	76.27

For **Al 2p spectra**, 73.85 eV position was fixed. 4 components were analysed. RSF value was 0.5371 for all components.

	NBA_Na	**Na_2CO_3**	**Al-O $2p^{3/2}$**	**AlOH $2p^{1/2}$**
Position	63.5899	63.7085	73.6547	74.3877
Position constraint	78.8346 , 60.712	78.8346 , 60.712	78.8346 , 60.712	78.8346 , 60.712
Area constraint	0.0 , 210967.5	0.0 , 210967.5	0.0 , 210967.5	Al-O $2p^{3/2}$ *0.5
FWHM constraint	0.6874, 17.19	0.3881, 9.703	0.4203, 10.51	Al-O $2p^{3/2}$ *1
% atomic concentration	2.17	4.47	62.24	31.12